AC & DC Zeeman Interferometric Sensing with Ultracold Trapped Atoms on a Chip

Shuangli Du

Beijing, China

Master of Science, College of William & Mary, 2016
Bachelor of Science, Renmin University of China, 2014

A Dissertation presented to the Graduate Faculty
of The College of William & Mary in Candidacy for the Degree of
Doctor of Philosophy

Department of Physics

College of William & Mary
August 2021

©2021
Shuangli Du
All rights reserved.

APPROVAL PAGE

This Dissertation is submitted in partial fulfillment of
the requirements for the degree of

Doctor of Philosophy

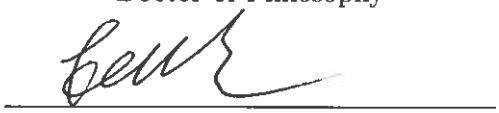

Shuangli Du

Approved by the Committee July 2021

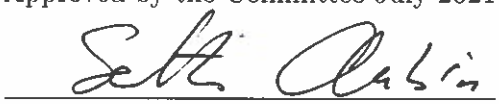

Committee Chair
Seth Aubin, Associate Professor, Physics
College of William & Mary

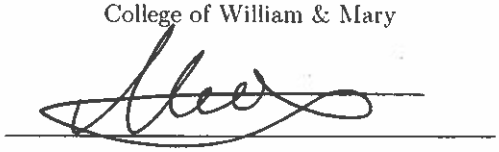

Eugeniy Mikhailov, Associate Professor, Physics
College of William & Mary

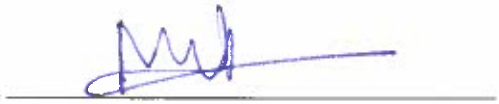

Mumtaz Qazilbash, Associate Professor, Physics
College of William & Mary

Todd Averett, Professor, Physics
College of William & Mary

Charles Sukenik, Professor, Physics
Old Dominion University

ABSTRACT

This thesis presents progress in developing a trapped atom interferometer on a chip, based on AC Zeeman potentials. An atom interferometer is a high-precision measuring tool that can detect various types of forces and potentials. The trapped atom interferometer introduced in this thesis targets the shortcomings of traditional ballistic atom interferometers, which are t ypically meter-scale in height. Notably, a trapped atom interferometer has a localized atomic sample, a potentially longer interferometric phase accumulation time, and the prospect of being the basis for a more compact instrument. This thesis presents multiple projects in the development of a trapped atom interferometer based on the AC Zeeman potentials and traps: 1) production of ultracold potassium on a chip, 2) the theory of potential roughness in chip traps, 3) microwave chip trap design, and 4) a trapped atom interferometer with rubidium atoms, based on a laser dipole trap and an AC Zeeman force. (1) Potassium is a good candidate for the atom interferometer due to its bosonic and fermionic isotopes, multiple "magic" magnetic fields, and the convenience of RF and microwave trapping. The laser cooling and trapping system were upgraded to improve the temperature and population of potassium atoms in the chip trap. On-chip cooling resulted in a significant inelastic loss, which prevented the production of a potassium Bose-Einstein condensate. (2) Numerical simulations of chip wire defects predict that the AC Zeeman trapping potential should be substantially smoother than its DC Zeeman counterpart: the suppression of the roughness is due to magnetic polarization selection rules and the AC skin effect. (3) Furthermore, the thesis presents a number of studies on the straight and curved microstrip transmission lines that form the building blocks of the microwave atom chip for the AC Zeeman trap. (4) Finally, we constructed a rubidium-based Ramsey interferometer that can be converted to an atom interferometer by applying a spin-dependent AC Zeeman force: the interferometer was used to measure DC and AC Zeeman energy shifts and fringes were observed with an AC Zeeman force.

TABLE OF CONTENTS

ACKNOWLEDGMENTS

Many people support this work, and it is impossible to achieve this work without their help.
First, my thanks to my parents, Xiaoyong Du and Jin Li, and brother, Shuangjie Du, who support me in various aspects to pursue the dream of physics research. And also my other family members that helped me.
In the academy:
Seth Aubin advises me on my projects and provides enormous help on my academic English writing.
Megan, Austin, Charlie, and AJ set up the apparatus so that we can stand on their shoulder.
Andrew Rotunno works with me for almost my entire Ph.D. career. It is a good time to collaborate with him.
William Miyahira takeover and continue my project.
Eugeniy Mikhailov advise my research during my first Ph.D. summer.
William Henninger helps a lot with the machine shop.
Eric with William & Mary Research Computing provides computational resources and technical support for our lab. Their patient tutorial helps us to start our simulation with HPC easier.
All the W&M faculty and staff that support my career.
And the Funding for this project, W&M, DTRA, NSF, and VMEC.
After I started my new life in a foreign country:
John Delos, as my academic advisor, helps me to ramp up with the academic learning process.
As one of the only two Chinese students in the class, including me, Hua Zhang helped me a lot to get over a hard time before getting used to the life in the U.S.
Mi Zhang and Zhiying Cui share their time with me to make my Ph.D. not monotonic.
And Wenjun Chen always shares with me his dramatic life.

For those who like this thesis.

LIST OF TABLES

LIST OF FIGURES

CHAPTER 1

Introduction

This thesis presents my research work in developing a trapped atom interferometer based on spin-dependent AC Zeeman potentials generated by an atom chip [1–8]. This thesis work includes several projects, both experimental and theoretical, that are all directed towards the development of a trapped atom interferometer. These projects include the development of an atom interferometer based on a Ramsey interferometer (i.e. atom clock), theoretical work on understanding atom chip potential roughness for both AC and DC Zeeman potentials, simulations for a microwave atom chip, and work on a laser cooling and trapping apparatus for generating ultracold potassium gases on a chip. In order to understand the motivation and context for all of these projects, this introductory chapter explains the motivations for developing a trapped atom interferometer and the importance of the AC Zeeman effect. The chapter begins by providing a brief summary of the physics of atom interferometry and the state of the field.

1.1 Atom interferometer background

The atom interferometer is a high-precision tool for measuring various types of forces and potentials, including inertial forces, such as the acceleration [9], rotation [10–12], and gravity [13–20], as well as fundamental constants [21–25]. As shown in Fig. 1.1, much like a laser interferometer, an atom interferometer simultaneously directs an atom along two distinct paths before recombining it. While following these two paths, the atom acquires a phase due to the different energies (potential or kinetic) associated with these paths. However, unlike a photon, various types of forces and potentials can affect an atom. The interferometric signal, i.e. the phase difference $\Delta\phi$ that accumulates between the two paths, is given by $\Delta\phi = \frac{\Delta T \Delta E}{\hbar}$, where ΔE is the energy difference between the two paths, and ΔT is the time during which the atom travels along two distinct paths. This equation shows that an atom interferometer is primarily sensitive to energy differences, as well as the duration of the phase evolution. However, a change in potential energy over a distance (e.g. the path separation) implies a potential gradient and thus a force, and so the interferometer is sensitive to external force, e.g. gravity.

The typical atom interferometer uses laser cooled ultracold atom in a vacuum cell [26–30]. Generally, the colder the atoms the better, in order to limit the initial velocity spread of the atomic sample, so a Bose-Einstein condensate (BEC) is sometimes used [31–34], though it comes at the cost of a smaller atomic sample and a more complex apparatus. The interferometer operations (e.g. separation along different paths, recombinations, phase readout) are typically implemented via optical laser pulses and laser traps, and DC and AC magnetic fields (including RF and microwaves).

The traditional atom interferometer is the ballistic atom interferometer, and the one in the Kasevich group at Stanford University is a flagship apparatus and

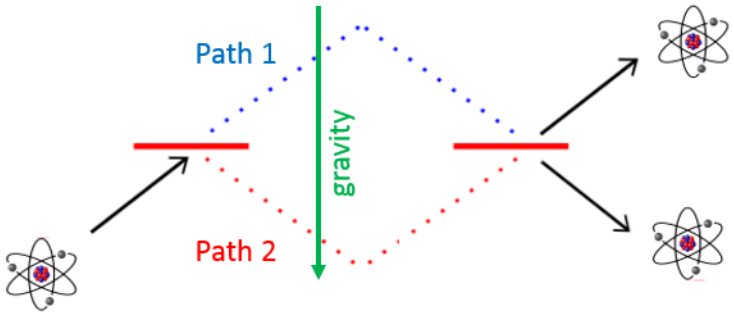

FIG. 1.1: Basic atom interferometer scheme. The atom interferometer works by directing atoms at a beamsplitter (red horizontal line), which then puts each atom in a quantum superposition of traveling along path 1 and path 2, simultaneously. The two paths are recombined on the second beamsplitter, which erases "which path" information and directs the atoms to the two output ports. The path phase difference $\Delta\phi$ (i.e. the interferometer signal) is readout from the population ratio for the two ports. This figure uses the gravity as the external force that generates a potential energy difference ΔE between path 1 and path 2, which is turn generates the phase difference $\Delta\phi$.

a representative design for this type of interferometer. The Stanford atom interferometer [35] prepares a laser cooled ultracold gas of atoms at the bottom of a 8.2 m tower vacuum system. The atoms are then launched on an upward trajectory, and a first beamsplitting laser pulse is applied to direct the atoms along two different ballistic upwards paths. The atoms follow a fountain-like trajectory, and the second "beamsplitting" laser pulse is applied when the two paths cross during the downward portion of their trajectories. This fountain design maximizes the Ramsey time ΔT in order to maximize the accumulated phase $\Delta\phi$ and thus the interferometer sensitivity. The Stanford ballistic atom interferometer has measured local acceleration of gravity, g, at a sensitivity of $3 \times 10^{-11} g/\sqrt{\text{Hz}}$ with 1.4 cm arm separation. The primary drawback of these ballistic atom interferometers is that longer phase accumulation times, which are needed to improve sensitivity, also require much taller fountains and vacuum towers.

Due to their extreme sensitivity, other groups are pursuing ballistic interferometers with large effective fountain heights. The MAGIS-100 experiment at Fermi

National Laboratory [36] is building an interferometer in a 100-meter deep shaft. Since the key requirement is that the atoms in a ballistic interferometer are in free flight, the Institute of Quantum Optics (Leibniz University, Germany) plans to use a high altitude rocket to operate their interferometer for six minutes in a microgravity enviroment [37]. The Jet Propulsion Lab (JPL, part of NASA) is constructing their atom interferometer on the International Space Station [38], where the atoms can be in permanent free fall. The above schemes will improve the atom interferometer by extend the Ramsey time, but at a substantial cost.

1.2 Motivation for trapped atom interferometry

The trapped atom interferometer targets the shortcomings of the ballistic atom interferometer, which are its limited phase accumulation time and the large space that the atoms traverse during the Ramsey time.

As its name implies, the atoms remain confined in a trapped atom interferometer with the path controlled by the trapping potential. This benefit of this approach is that the Ramsey time not determined by the available free fall space, and in principle can be quite long for improved sensitivity. Ultimately, the Ramsey time is limited by the coherence time, which depends on the interferometry design and noise source. Indeed, the Ramsey interferometer in atom chip traps can obtain coherence times in the range of 1-60 s [39,40]. Furthermore, the sensitivity of the atom interferometer increases linearly with the phase accumulation time, which is very efficient. As a comparison, the average of multiple independent measurements only increases the sensitivity with the square root of the total number of measurements, i.e. basically the square root of the total summed phase accumulation times, which is much less efficient.

The trapped atom interferometer also has a localized sample and can potentially

be the basis for a compact instrument. The localized sample will improve the spatial resolution, and thus allow operating the interferometer as a "force microscope" for measurements of forces at the sub-mm and micron scale close to a surface, such as the Casimir-Polder force [41] or gravity from a small test at sub-mm distance, e.g. to test the $1/d^2$ law for gravity at short distance d [42]. Finally, a more compact instrument makes the interferometer more portable so that it can be used to map out small forces or force variations, e.g. as a gravimeter for searching gravitational anomalies (due to hidden minerals, subterranean structures).

The trapped atom interferometer also faces several challenges, and the principal physics challenge is from atom-atom interactions. In a trap, the atoms are typically close enough to each other that they will collide, i.e. they will interact with each other, which manifests itself as mean field energy (a sort of collective potential energy). This mean field energy is affected by the atomic density, and it contributes to the accumulated phase of the interferometer. This mean field energy can limit the accuracy of the interferometer and also affect its precision, since quantum fluctuations in the interactions will generate fluctuations in the phase, leading to the phase diffusion. In a ballistic atom interferometer, the atoms are generally too far apart for interactions to play a role. Reducing the atom number N is one strategy to suppress the atom interactions [43], but it also reduces the signal to noise ratio: the quantum projection on the phase is $\delta\phi \approx \frac{1}{\sqrt{N}}$ [44].

An alternative approach is to suppress atom-atom interactions by using identical fermions, which essentially do not interact at ultracold temperatures [45]. Also, one can use ultracold thermal bosons instead of a BEC, since thermal bosons have a smaller collisional cross-section and tend to be less dense (i.e. since they are warmer and thus populate a larger volume). Both fermion and thermal boson-based trapped atom interferometers are multi-mode devices. When sufficiently cooled, an ultracold gas of identical fermions becomes a degenerate fermi gas (DFG), in which each state

(or level) of the trapping potential is occupied by a single atom, due to the Pauli exclusion principle. While thermal bosons do not obey the Pauli exclusion principle, the atoms are still distributed among different trap energy states.

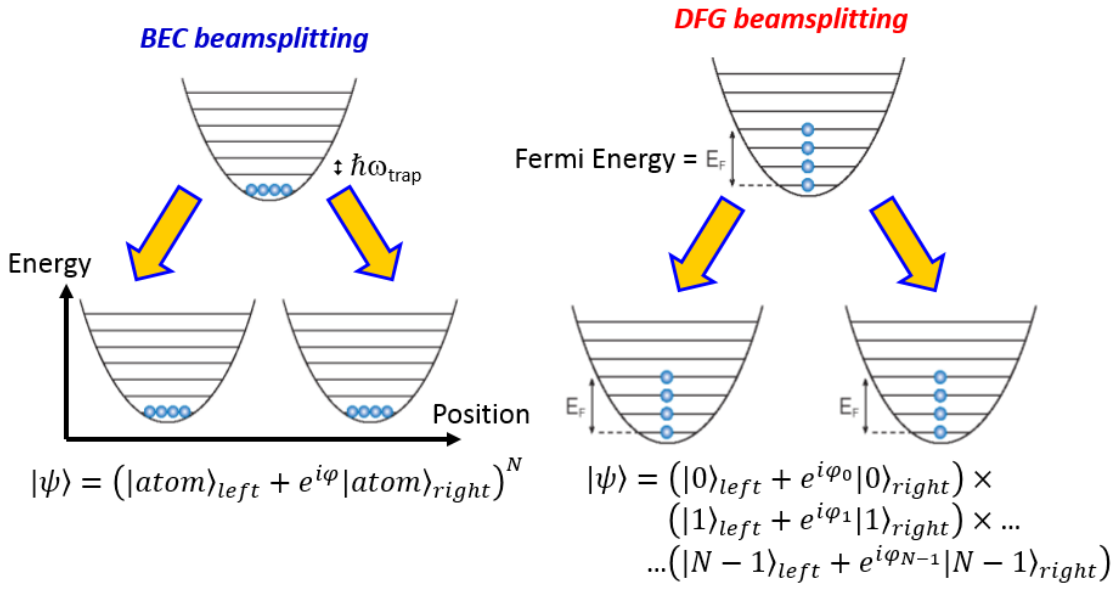

FIG. 1.2: Trapped BEC and DFG beamsplitting. Since all the BEC atoms share the same ground state wavefunction, there is only one splitting phase φ between atoms in a superposition of left and right traps. In the case of DFG, each atom is in a different trap state, so when the beamsplitting occurs, each atom is in superposition of being in the left and right traps, then there is splitting phase φ_n associated with each trap state n: If these splitting phase are all different, then the interferometer phase will be different for each atom, and the total interferometer signal will wash out. The only way to avoid this washing out effect is to make sure that the splitting phases are the same for all atoms and all trap states ($\varphi_1 = \varphi_2 = ... = \varphi_{N-1}$). As part of this process, the left and right trap frequencies and shapes should remain the same. This figure is made by S. Aubin.

The multi-mode trapped atom interferometer has a stringent requirement on the trap quality during the Ramsey time. The fermions (or thermal bosons) are in different trap states, and there is a possibility that beam splitting process will result in different splitting phases for each these trap states. As shown in Fig. 1.2, we need to make sure that the beam splitting process is designed to result in identical splitting phases for all of the different trap states (and atoms), much like in a white light interferometer. The technique for the trapped Bose-Einstein condensate

that deforms the harmonic trap into a double-well [6] will result in different splitting phases for a multi-mode interferometer. Furthermore, in order to ensure that the two paths do not accumulate a phase difference because of differing trap state energies (trap state energy = $n\hbar\omega_{trap}$, n = trap energy level number), the traps for the two paths should have the same trapping frequencies ($\omega_{trap,left} = \omega_{trap,right}$).

In order to ensure a common splitting phase for all trap states (independent of energy), the lab is pursuing scheme based on a spin-dependent interferometer, as shown in Fig. 1.3. Each atom will be prepared into a $|\psi\rangle = \frac{1}{\sqrt{2}}(|\uparrow\rangle + |\downarrow\rangle)$ superposition state. The basic idea is give the spin-up $|\uparrow\rangle$ state and the spin-down $|\downarrow\rangle$ state their own individual traps (i.e. spin-dependent traps): these two traps are identical in shape and overlap each other at the start of the interferometry process. The beamsplitting process is implemented by adiabatically translating the two traps away from each other. A simulation shows if a harmonic trap is translated adiabatically (smooth acceleration, constant velocity, and then smooth deceleration), then the phase of each trap state will remain the same. This spin-dependent interferometer can be considered as an atomic clock (i.e. Ramsey interferometer) with spatially separated spin states.

An additional advantage of using a spin-dependent interferometer is that spin-squeezing techniques can be used. In particular, spin squeezing can be used to reduce the quantum projection noise on the phase uncertainty $\delta\phi$ to below the standard quantum limit (i.e. $1^{\sqrt{N}}$) [3,46]. Notably, the atom-atom interactions that we ultimately interested in avoiding can also be used to provide spin squeezing [3].

1.3 Motivation for AC Zeeman force

We use the AC Zeeman effect [47–53] to generate the spin-dependent potentials and forces for our spin-dependent interferometer. The AC Zeeman potentials and

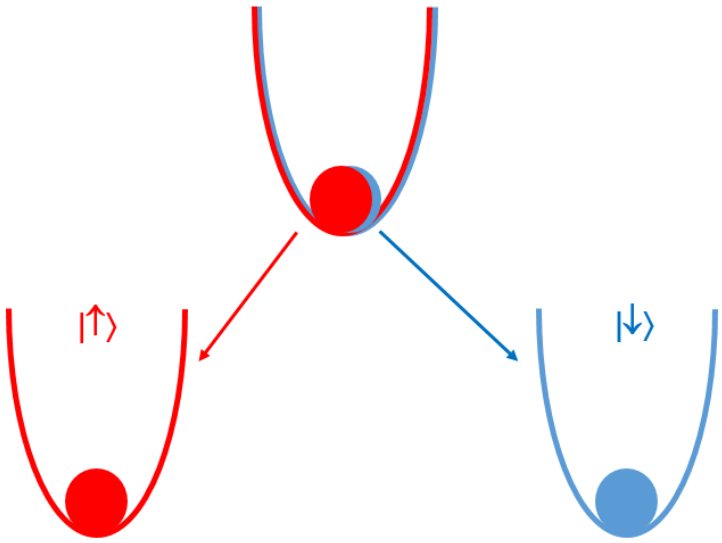

FIG. 1.3: Adiabatic spin-dependent beamsplitter. We prepared each atom in the $|\phi\rangle = \frac{1}{\sqrt{2}}(|\uparrow\rangle + |\downarrow\rangle)$ state, with two spin dependent trap, one for each spin state (spin-up is shown in red, and spin-down is in blue). These two traps are identical in shape (same trap frequencies) and overlap each other, so the condition will be the same as if the atoms are in a spin-independent trap. Finally, the atoms are beamsplit by adiabatically translating the spin-up and spin-down traps apart, while keeping their shapes identical. If the process is sufficiently adiabatic, then each trap level (state) will experience the same splitting phase.

forces only affect the states that are involved in the transition targeted by the applied AC magnetic field (generally in the RF or microwave). In order to generate a sufficiently strong force to manipulate atoms, the AC magnetic field must have a strong gradient. Since the AC magnetic fields for the AC Zeeman potentials are in the RF and microwave, they have wavelengths on the order meters to centimeters. Since this is the length scale to which these fields can be focused in the far field, strong gradients require very high beam power (i.e. kW). However, an atom chip can generate very strong AC field gradients [51] because it operates in the near field, where the characteristic length scale is given by the chip wire features (wire width, wire spacing) not wavelength. While atom chips are not typically designed for RF and microwave frequencies (at least not yet), AC Zeeman potentials generated by atom chip near fields have many useful features for spin dependent trapping and interferometry:

1) The AC Zeeman force is robust to the environment noise. Since the environment noise typically drops off as the reciprocal of the frequency (i.e. "1/f" noise), the AC Zeeman force, which operates in a radio frequency (MHz level) to microwave frequency (GHz level), experience much smaller environmental noise than its DC Zeeman counterpart.

2) The AC Zeeman force is spin-specific and can target multiple states simultaneously with independent potential. Only transition states that are targeted by a near-resonant AC magnetic field are affected. We can use two different frequencies to drive two non-related transitions simultaneously and thus generate independent AC Zeeman traps for each state of the atom interferometer.

3) The detuning can control the strength of the AC Zeeman trap (in addition to the AC current), thus we have an additional parameter for controlling the trapping potential.

4) The AC Zeeman force can trap any spin state. The AC Zeeman force for

the $|\uparrow\rangle$ and $|\downarrow\rangle$ states can be reversed if we flip the detuning sign to switch a state between low field seeker and high field seeker.

5) AC Zeeman trap has no spontaneous emission. The AC Zeeman effect works on ground state hyperfine transitions, in which the energy difference is small. The lifetime of these states is on the order of months to years, so there is essentially no spontaneous emission on our experimental time scale (milliseconds to seconds).

6) The AC Zeeman force can work at any DC magnetic field. The DC magnetic field will change the hyperfine splitting, but we can always adjust the AC magnetic field frequency to match the modified transition energy. Therefore, we can choose the DC magnetic field most suitable for the atom interferometer experiment, such as at a magnetic Feshbach resonance or at a "magic" magnetic field, which results in transition that are insensitive to magnetic field noise.

7) AC Zeeman traps are expected to suppress the magnetic roughness in the trapping potential due to wire imperfections, as compared to their DC Zeeman counterparts (see Chapter 5).

8) AC Zeeman trap can only be produced by the near field of an atom chip, e.g. with parallel 2-wire or 3-wire configurations [54], while a DC Zeeman trap can be made with an atom chip or with microscopic magnetic coils.

1.4 Atom chip

This thesis describes research and results on four distinct projects that all support the long term objective of constructing a trapped atom interferometer based on spin-dependent AC Zeeman potentials, forces, and traps. Here is a brief preview of how these projects support this long term trapped interferometry goal.

i. Potassium laser cooling and trapping system (Chapter 3)

I made a major upgrade to an existing laser cooling and trapping system in order to load large ultracold potassium samples onto the lab's atom chip, simultaneously with rubidium. The lab would like to conduct interferometry experiments with potassium isotopes (instead of bosonic rubidium) due to their many Feshbach resonances and "magic" magnetic fields, small hyperfine splittings, and the fermionic isotope ^{40}K.

ii. AC and DC Zeeman trapping potential roughness (Chapter 5)

I made a computational study that shows that the AC Zeeman trapping potential roughness on a chip should be strongly suppressed with respect to its DC Zeeman counterpart. This magnetic roughness is due to chip wire imperfections and could impact the performance of the AC Zeeman traps for interferometer.

iii. Trapped atom Ramsey interferometer (Chapter 6)

This chapter contains my main results. I developed a trapped atom Ramsey interferometer, which will serve as a cornerstone for the trapped atom interferometer. Notably, the Ramsey interferometer successfully observed DC and AC Zeeman potentials, and operation with spatially spin states was initiated.

iv. Curved microstrips for microwave atom chip design (Chapter 7)

I conducted numerous microwave simulations to characterize and design curved microstrip trace for the lab's new microwave atom chip, which will generate the spin-dependent AC Zeeman traps for the atom interferometer. This work includes the first simulations of the trapping microwave field for the chip.

The thesis also includes several chapters that provide supporting information to understand the key thesis results: Chapter 2 describes the main ultracold atom apparatus, Chapter 4 presents the theory of the AC Zeeman effect, and Chapter 8 concludes by summarizing the main thesis results and providing an outlook for future work.

CHAPTER 2

Apparatus

The ultracold AMO lab in the College of William and Mary is located on the basement floor of the Small Hall. Since Small Hall is located on the side of a small hill, parts of the "basement" floor are still above the ground, and part of the wall is exposed to the sunshine. This lab condition makes temperature control more difficult, which is important for a sensitive and complex ultracold atom experimental apparatus. Fortunately, the lab wall is thick, the lab is windowless to prevent sunshine, and the HAVC system helps stabilize the lab temperature to within around 1°F/ 0.5 °C. The temperature drifting during the day is not negligible, but the experiment is not affected too much by this temperature drifting (with one exception discussed in chapter 6).

In the lab, there is a regular classroom size space for the experimental apparatus. More than half of this space is occupied by two optics tables, the "laser table" and the "science table." On the "laser table," we prepare laser light for the experiment, which goes through optical fibers to the "science table". On the "science table," there is our vacuum system, magneto-optical trap, and atom chip, which is where all the experiments happen. Figure 2.1 shows an overview of the vacuum system of our

laser cooling and trapping apparatus. All the previous Ph.D. students contributed to various parts of this apparatus, which can be found in more detail in their respective theses [54–58].

This chapter provides an apparatus overview in section 2.1, and then introduces the experiment cycle in section 2.2. The basic experiment cycle elements are the magneto-optical trap and molasses (subsection 2.2.1), optical pumping (subsection 2.2.2), the transportation trap (subsection 2.2.3), the chip trap (subsection 2.2.4), evaporative cooling (subsection 2.2.5), the experiment stage (subsection 2.2.6), and the imaging stage (subsection 2.2.7).

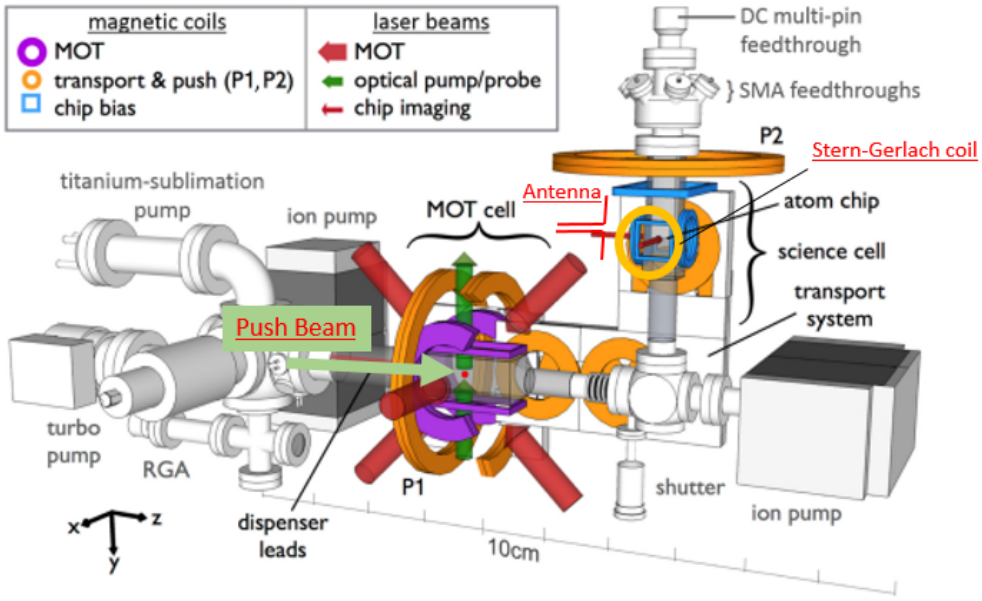

FIG. 2.1: Vacuum system apparatus. The figure is modified from Austin Ziltz's thesis [56] with some extra instruments added for my projects: potassium push beam, microwave antenna, and DC Stern-Gerlach coil.

2.1 Apparatus overview

As shown in Fig. 2.1, the vacuum system in our lab has two different cells, one of which is the magneto-optical trap (MOT) cell, the other one is the science

cell. The MOT cell is where we use the MOT to collect and cool atoms, and the science cell is where we operate the atom chip-related experiment. The two cells are connected with an L shape tunnel to transport atoms. In the original design, the two cells have a different level of vacuum. The science cell should have a higher vacuum than the MOT cell, and the size of the tunnel is designed to keep the science cell at a better vacuum from the worse vacuum level in the MOT cell. However, in our measurement, the science cell has not reached a better vacuum level than the MOT cell, possibly due to virtual leaks from the large number kapton-coated cables in the science cell.

In the upper half of the science cell, there is an atom chip with multiple wires on it. The side of the chip with wires on it points down to generate a micro-magnetic trap and various magnetic near fields in the vacuum to support our experiment.

Outside of the vacuum cell and connection tunnel, there are several electromagnetic coils to provide the magnetic fields necessary for the MOT, magnetic trap, transportation magnetic trap, and the chip trap.

Next to the science cell, there are two cameras used to image the ultracold atom cloud from the "radial" and "axial" directions. Both directions are defined by the atom shape in our chip trap. Atoms in the chip trap are generally in a cigar shape along the chip wire direction. The "radial" camera is oriented in the direction along the long axis of the cigar to obtain radial information on the atom cloud, and the "axial" camera view the long axis of the cigar.

Most of the apparatus is controlled by a sequencer called the "Adwin" (Adwin-pro II). The Adwin provides multiple programmed analog and digital signals with a timing resolution of 10 μs for the experiment. Some of the instruments for the atom interferometer experiment require a much higher timing resolution and accuracy, and for these we use a pulse generator system to provide more accurate timing the control after receiving a trigger from the Adwin. Details of the pulse generator

system are discussed in chapter 6.

2.2 Basic experiment cycle

This section introduces the basic experimental cycle used for ultracold atom experiments in our lab. Most of the cold atom experiments follows a similar process, including the rubidium BEC cooling (Ziltz [56]), AC Zeeman force measurement (Fancher [57]), quantum pumping experiment (Pyle [58]), AC Zeeman trap experiment (Rotunno [54]) and the atom interferometer (this thesis). Each experiment has a roughly 30 s cycle time, starting with the MOT to collect the atoms, then a molasses cooling stage, and optical pumping to increase the atom population spin purity for efficient loading of the magnetic trap for transporting atoms to the chip trap. After reaching the chip trap, evaporative cooling reduces the atom temperature to the level that the experiment requires. At this point the specific experiment can begin, and each experiment has its own process, but all share the setup and the final imaging process. Figure 2.2 shows the running time, atom number, and atom temperature for each stage.

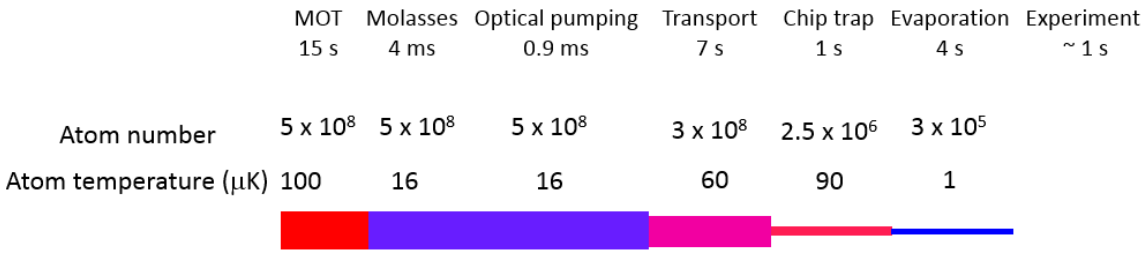

FIG. 2.2: Basic cooling and trapping sequence for ^{87}Rb with atom number and temperature for each stage. The line at the bottom qualitatively shows the atoms' condition for each stage. Color represents atom sample temperature, and thickness represents atom number.

2.2.1 Magneto-optical trap (MOT)

The experimental cycle starts with the magneto-optical trap (MOT). The MOT has six laser cooling beams directed at the center of the anti-Helmholtz coils along three roughly perpendicular axes (each axis has two counter propagating beams). Each beam contains two different laser frequencies, which we refer to the "trap light" and the "repump light." As shown in Fig. 2.3, both the trap and repump light drive the D2 electric dipole transition $5S_{1/2} \rightarrow 5P_{3/2}$ at 780 nm. The trap light drives the $\left|5S_{1/2}, F=2\right\rangle \leftrightarrow \left|5P_{3/2}, F=3\right\rangle$ transition, and the repump light drives the $\left|5S_{1/2}, F=1\right\rangle \leftrightarrow \left|5P_{3/2}, F=2\right\rangle$ transition. Since the excited state of trap light transition $\left|5P_{3/2}, F=3\right\rangle$ can only drop back to $\left|5S_{1/2}, F=2\right\rangle$ state via spontaneous emission, the trap light transition is closed and can be used for laser cooling and trapping (cycling transition). The excited state of the repump light transition $\left|5P_{3/2}, F=2\right\rangle$, can drop to the $\left|5S_{1/2}, F=2\right\rangle$ and $\left|5S_{1/2}, F=1\right\rangle$ states; thus the repump light is used for pumping atoms in the $\left|5S_{1/2}, F=1\right\rangle$ state back to the $\left|5S_{1/2}, F=2\right\rangle$ state where they can be trapped and cooled with trap light.

The trap light in the MOT has two different functions. The first function is to provide the Doppler cooling, and the other function is to trap the atoms.

Doppler cooling, as illustrate in Fig. 2.4, cools the atoms via the Doppler effect. The trap beam is red detuned with respect to the cycling transition and, and thus is not scattered too much by stationary atom. Meanwhile, the Doppler effect will increase the effective frequency of the trap beam for those atoms that are moving towards the trap beam, and thus these atoms will closer to resonance: Atoms moving towards the trap beam will absorb photon and be pushed backward, and hence they will slowed down (i.e. their temperature decreases). Doppler cooling has a limit because spontaneous emission will recoil and heat the atoms. The Doppler limit is $T_D = \dfrac{\hbar\Gamma}{2k_B}$: For rubidium, the decay rate on this transition is $\Gamma = 2\pi \times 6$ MHz, and

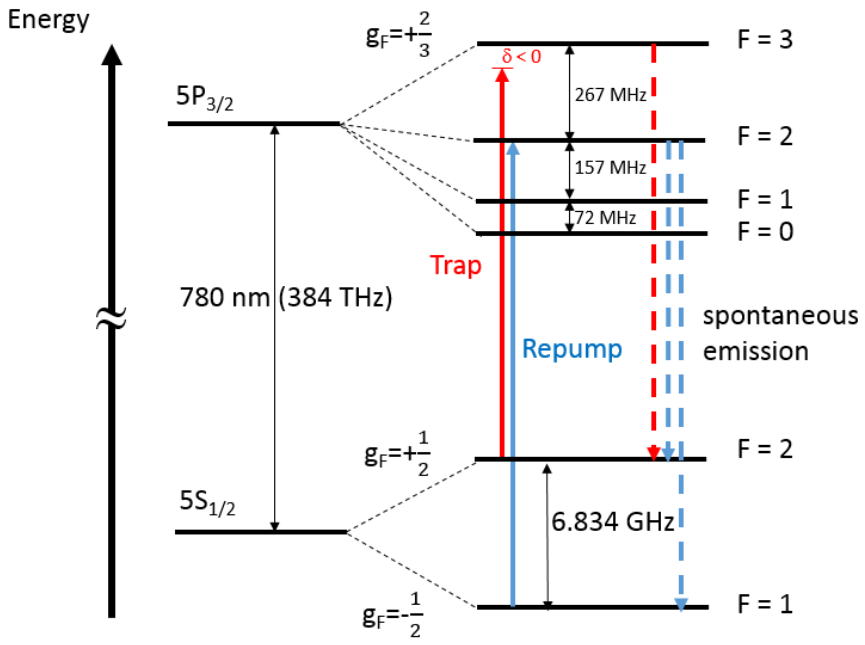

FIG. 2.3: Rubidium 87 energy structure with the trap and repump laser transitions. The trap laser operates on the $|5S_{1/2}, F = 2\rangle \rightarrow |5P_{3/2}, F = 3\rangle$ transition with a red detuning δ = - 20 MHz to perform the cooling and trapping in the MOT. The repump laser operates on the $|5S_{1/2}, F = 1\rangle \rightarrow |5P_{3/2}, F = 2\rangle$ transition to pump the atoms back to $|5S_{1/2}, F = 2\rangle$ for the trap light transition [59].

so we have $T_D = 144\ \mu$K. For further cooling, we need sub-Doppler cooling, such as the molasses cooling, which is implemented immediately after the MOT stage.

The trap beam is also used to trap atoms in the MOT. As shown in Fig. 2.5, the magnetic field generates a Zeeman splitting of the excited states. In the figure, we use $F = 0$ for ground state and $F = 1$ for the excited states, accroding their mF value. As an example, the trap beam has a red detuning to the $|g, m_F = 0\rangle \rightarrow |e, m_F = 0\rangle$ transitions, and is not resonant at the center of the trap where the magnetic field is zero. Once the atom moves away from the center, the magnetic field shifts the excited state, and for the x positive direction, the $|e, m_F = -1\rangle$ states becomes closer to resonance with the trap laser beam. We also adjust the laser to be σ^- polarization for the beam that comes from the right direction to maximize the transition of $|g, m_F = 0\rangle \rightarrow |e, m_F = -1\rangle$ and hence the trap beam pushes atoms

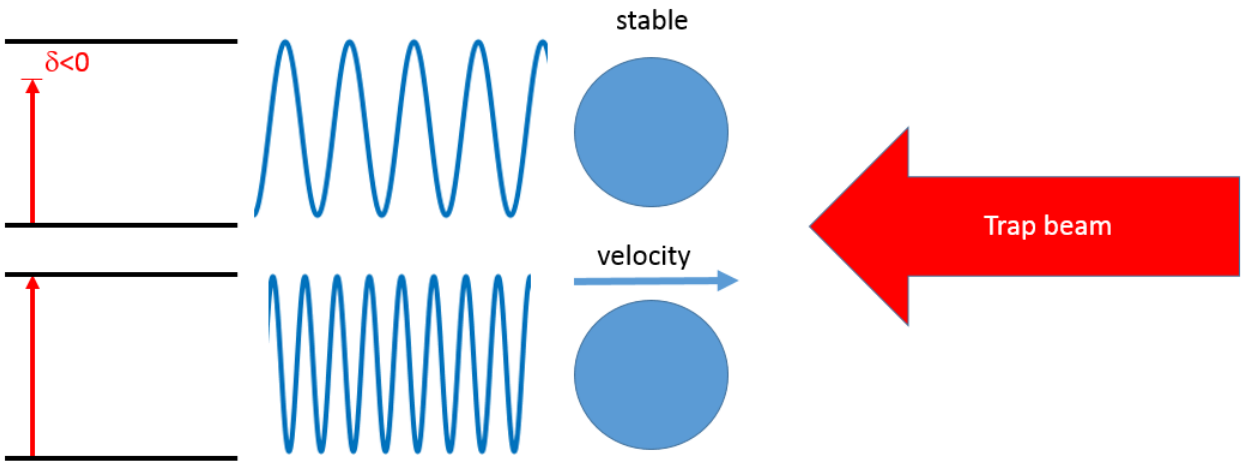

FIG. 2.4: Doppler cooling. The effective trap light frequency increases in the reference frame of an atom moving towards the trap light and compensate for the red detuning ($\delta < 0$). Hence, trap light photons are absorbed by atoms that are moving towards it which decelerates them, and thus cools them.

back to the center. Meanwhile, the beam from the opposite direction with opposite polarization does not affect it.

After the MOT stage, the optical molasses stage starts. The optical molasses stage operates with no anti-Helmholtz magnetic field, and cool the atom with only the optic laser to the atom temperature 10-30 μK. Since there is no trapping in the molasses stage, so this stage must be short (2-10 ms), and 4 ms for our standard cycle.

2.2.2 Optical pumping

The magnetic trap is designed to only trap atoms in the $|F = 2, m_F = 2\rangle$ state. The optical molasses stage operates at zero magnetic field and the m_F states of the atoms are scrambled. After the magnetic field turns back on, it will randomly quantize the m_F state, and all the atoms with the "wrong state" will be lost from the trap. To avoid this loss, we operate the optical pumping with a single vertically oriented circular-polarized beam and vertical magnetic field to pump the atom into

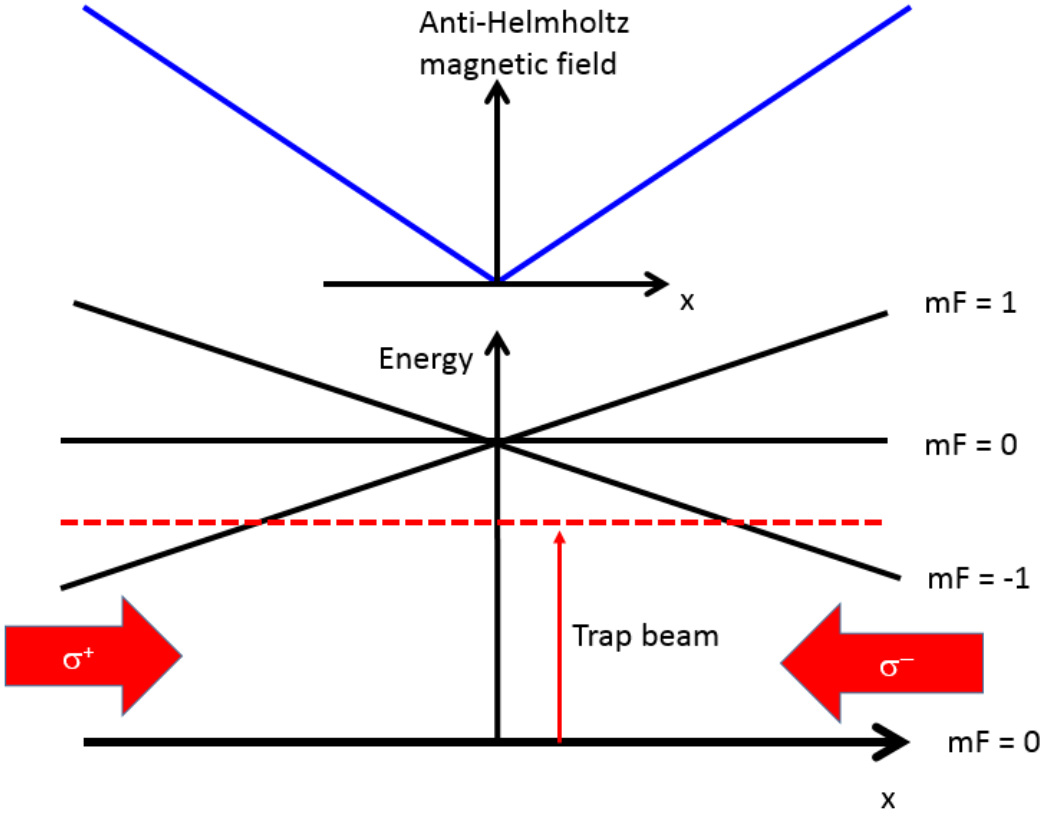

FIG. 2.5: MOT cooling and trapping physics diagram. The magnetic field generates the excited state DC Zeeman splitting, and thus atoms further from the center have more of an energy shift. This DC energy shift compensates for the red detuning of the trap beam the atoms away from the center and pushes them back to the center with the trap beam with the correct polarization.

the $|F = 2, m_F = 2\rangle$ state. The optical pumping beam is a mix of optical pumping light and repump light, the optical pump light is resonant with the transition $|5S_{1/2}, F = 2\rangle \leftrightarrow |5P_{3/2}, F' = 2\rangle$ to maximize the optical pumping process. Figure 2.6 shows the trap and repump beam power and frequency and the magnetic field current setting in the Adwin pannel.

2.2.3 Transportation trap

Next, atoms are transferred into a transportation trap, which is formed by a series of anti-Helmholtz coils along the L shape tunnel, with up to 150 Amps of

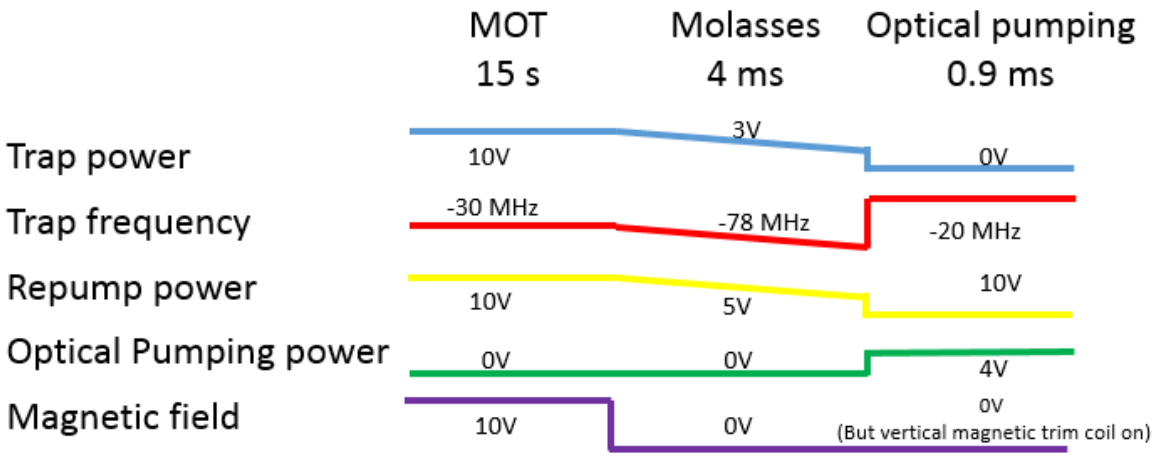

FIG. 2.6: Laser cooling and trapping cycle in the MOT cell. This diagram shows the change of trap laser power, trap laser frequency, repump laser power, optical pumping laser power and the magnetic coil strength during these various stages.

current running in a designed sequence through these coils to generate and move the magnetic trap along the tunnel to the science cell. The transportation trap is a linear magnetic trap with a magnetic zero point at the middle. Atoms at this zero point will suffer from Majorana loss: Atoms passing near the zero have their m_F state scrambled and they can be lost from the trap. In practice, the atoms are warm enough that they do not spend sufficient time near the center of the trap and so there is very little Majorana loss during the 7 s transportation process.

2.2.4 Chip trap

After the transportation trap reaches the top of the science cell, atoms are loaded into the chip trap by a smooth handover from one magnetic trap to the other. Since the transportation trap is much larger than the chip trap, the loading process is very inefficient, and about 1% of atoms are loaded into the chip trap.

As shown in Fig. 2.7 (top), the chip trap is formed with four different magnetic fields: the chip near field, the hold field, the vertical trim field, and the Ioffe field.

The chip center Z wire generates a high gradient, high curvature near field. The hold field is a uniform magnetic field and has a direction counter to the chip near field under the Z wire. As shown in Fig. 2.7 (bottom), the chip near field and hold field form a magnetic minimum point, which can trap atoms.

The Ioffe field is a uniform field perpendicular to the chip near field and hold field. The purpose of the Ioffe field is to add a magnetic field background to eliminate the magnetic zero point (to avoid Majorana losses). The vertical trim field will horizontally shift the chip trap position. The vertical trim is useful when we need to load the atoms into the optical dipole trap (ODT), which may not be exactly under the Z wire.

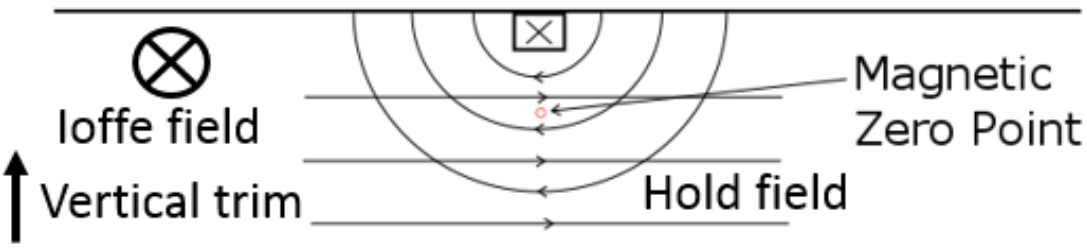

FIG. 2.7: Micro-magnetic chip trap has four different magnetic fields. The chip near field and the hold field form a magnetic minimum point. The Ioffe field eliminates the magnetic zero point. The vertical trim field is used when we need to move the chip trap horizontally.

2.2.5 Evaporation cooling

During the long journey from the MOT to the chip trap, the atoms have suffered substantial heating, and we need to cool them in the chip trap before the experiment.

The method we use for chip trap cooling is evaporative cooling. The idea of evaporative cooling is simple: Just like a hot coffee, atoms with a high temperature evaporate and escape from the trap, and the remaining atoms will be colder.

We use a RF frequency magnetic field to evaporate the high temperature ultracold atoms. The chip trap can only trap low-field seeking atoms, and for our ^{87}Rb species, we use $|F = 2, m_F = 2\rangle$ (abbreviated as $|2, 2\rangle$) and $|2, 1\rangle$ state. Let us assume there are only $|2, 2\rangle$ atoms, and their trap energy will follow the shape of the chip trap, which is harmonic in shape. For a low magnetic field, the energy splitting between the m_F states is proportional to the magnetic field. This property means that atoms at the edge of the atom cloud, are hotter, and they also have a higher transition frequency to an anti-trapped state. As shown in Fig. 2.8, if we sweep the RF frequency from high to low, the hotter atoms will first hit the transition frequency and transform to a high-field seeking state, which is then ejected from the trap.

If the assumption above, i.e. that there are only atoms in the $|2, 2\rangle$ state, is not true, and some $|2, 1\rangle$ atoms are present, e.g. generated in the transportation stage by the atom re-quantized by the magnetic zero point then an additional step is required: We can operate a process called "$|2, 1\rangle$ remover" to eliminate the $|2, 1\rangle$ state atom. The $|2, 1\rangle$ remover is similar to the evaporative cooling process, but we use a microwave knife to evaporate all the $|2, 1\rangle$ state atoms.

2.2.6 Experiment stage

After all the preparation processes above, the atoms are finally ready for the experiment. The experiment process will be different for each project: For example, the rubidium BEC project will further evaporate the atoms; the AC Zeeman force experiment will load atoms into the optical-dipole trap (ODT). The atom interferometer project in chapter 6 also starts by loading atoms into the ODT, and then applies several microwave pulses in sequence for the experiment stage.

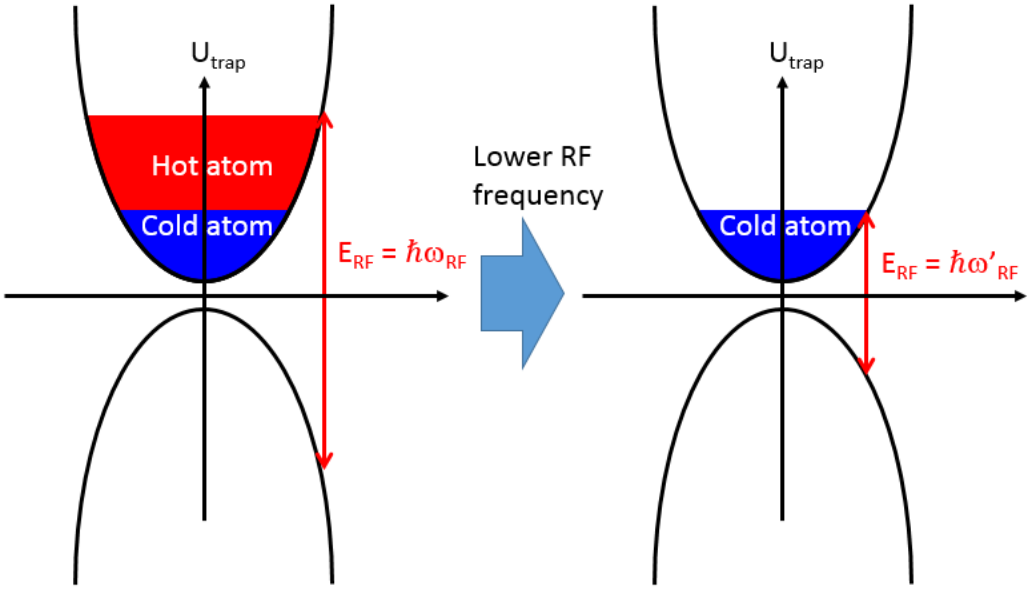

FIG. 2.8: Cartoon of the evaporation process. The evaporative cooling uses RF frequency magnetic field as a knife to selectively eject the high temperature atoms: The remaining atoms are thus colder.

2.2.7 Imaging

After the experiment, we need to image the atom cloud to extract data. Currently, in our lab, the atom cloud image is the only experimental output, and all the properties of the atom cloud are determined from the images.

The laser for the image probe beam is on resonance with the $\left|5S_{1/2}, F = 2, m_F = 2\right\rangle \rightarrow \left|5P_{3/2}, F = 3, m_F = 3\right\rangle$ transition, so this image laser can only image atoms in the $|2, 2\rangle$ state effectively. To image all the atom, we need a "pre-pulse" process with both trap and repump laser on, and sweep the trap laser frequency across all m_F state transitions. The "pre-pulse" is a type of optical pumping running and it will pump all the atom into the $|2, 2\rangle$ state for the imaging pulse. On the contrary, if we do not operate the "pre-pulse", then we largely image the $|2, 2\rangle$ state atoms.

The imaging method is called absorption imaging. The absorption image does not work well if the atomic density is too high, so we have a few ms of time of flight (TOF) to let the atom cloud fall and expand before we take the image. As shown in

Fig. 2.9, each absorption image of an atom cloud involves two camera images: an "atom" image with the atoms present, and a background laser image with the atom absent. The laser image is taken 0.5 s after the atom image when all the atoms have already fallen out of the camera region. Both of the camera images are taken with the probe laser on, and by dividing one image with the other (pixel by pixel), the probe laser is removed in the final processed image. This processed image is an image of the optical depth given by $OD = -ln(\frac{I_{Image}}{I_{Laser}})$, where I is the intensity of the image data or laser data. The optical depth has a linear relation to the atom number, $N_{Atom,pixel} = OD \times AtomCountFactor$. The "atom count factor" is given by the equation: $AtomCountFactor = \frac{A_{pixel}}{\sigma_0}(1 + (\frac{2\delta}{\gamma})^2)$ [57], where A_{pixel} is the area of the CCD pixel, $\sigma_0 = \frac{3\lambda}{2\pi}$ is on-resonance atomic cross section ($\lambda = 780$ nm for ^{87}Rb), γ is the natural linewidth of the targeted transition (6 MHz for ^{87}Rb), and δ is the detuning of the imaging beam (typically we use $\delta = 0$).

Next, we fit the processed image data with a Gaussian distribution. Since the 2D-Gaussian fitting is not very stable, we sum up the optical depth along the x or y axis and fit with a 1D-Gaussian along the other axis. The parameters provided by Gaussian fits can help calculated multiple pieces of experimentally useful information. From the amplitude and width, we can calculate atom number, from the width, we can calculate the atom temperature, and from the center position, we can determine the atom state in combination with a Stern-Gerlach pulse, or the trap frequency from atom oscillations in the trap.

In our atom interferometer experiment, we need to image two different atomic spin states separately at the same time. We add a single coil next to the science cell to provide a high gradient magnetic field, and the DC Stern-Gerlach effect will separate the atoms with different m_F states. The Stern-Gerlach coil will pulse on for 7 ms typically during the TOF to fully separate the atoms with different m_F

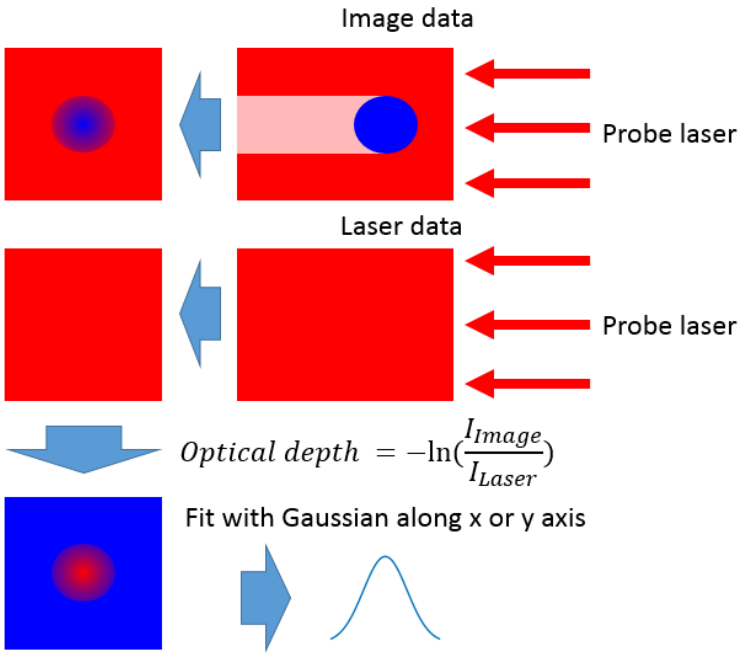

FIG. 2.9: The absorption imaging procedure. There are two images for each experimental cycle: one for image data with atoms, and another one for laser data with no atoms. The intensity of the image data and laser data can be use to calculate the optical depth, which is proportional to the atom number. Fitting the optical depth with a Gaussian distribution provide multiple pieces of information for the atom cloud (e.g. atom number, temperature).

states. Notably, there are three pairs of states, $|2,1\rangle$ and $|1,-1\rangle$, $|2,0\rangle$ and $|1,0\rangle$, and $|2,-1\rangle$ and $|1,-1\rangle$ that have the same DC energy shift at low magnetic field and we can not distinguish them with only the DC Stern-Gerlach coil.

CHAPTER 3

Potassium cooling apparatus

The first few years of my Ph.D. involved work on a project to cool potassium isotopes for chip trap experiments. As with the rubidium in our lab, the plan was to trap potassium atoms in the chip trap and cool it to BEC. This project pushed forward the cooling process significantly but has not yet reached a BEC. To further improve the potassium cooling, we need some new instruments, which will take a long time to prepare. As a result, we paused this project and moved our focus back to the rubidium atom interferometer.

3.1 Motivation

There are several advantages of using ultracold potassium atoms for trapped atom interferometry, and spin-specific AC Zeeman trap and potentials.

First, the potassium isotopes have smaller hyperfine splittings relative to rubidium-87. The three isotopes of potassium ^{39}K, ^{40}K, and ^{41}K have hyperfine splittings from 254 MHz to 1.3 GHz. The smaller hyperfine splitting results in a lower operating frequency for an AC Zeeman trap, which in turn results in better coupling to our existing atom chip.

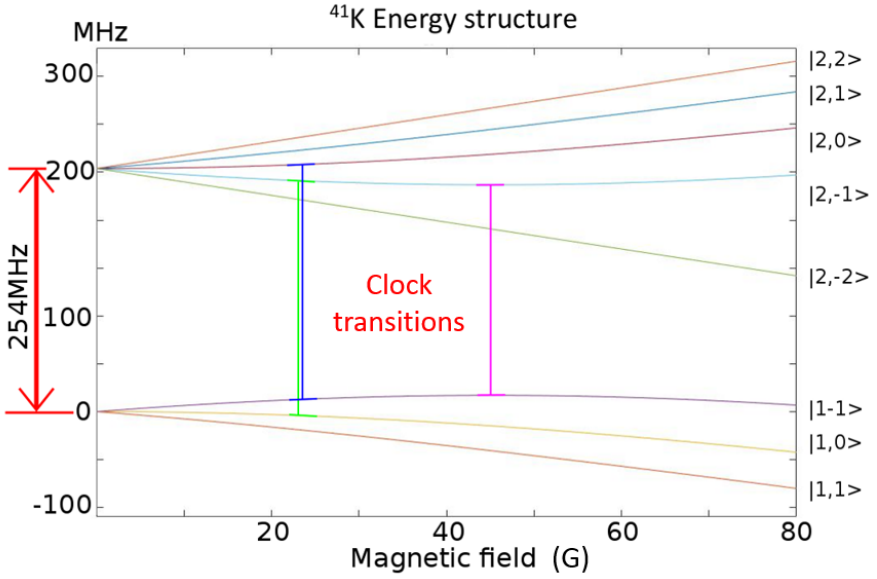

FIG. 3.1: Breit-Rabi plot for the $4S_{1/2}$ ground level of ^{41}K. Showing the energy of the hyperfine levels as a function of magnetic field. The clock transitions indicate the "magic" magnetic fields and their associated states and transition.

Second, potassium has a fermion isotope, ^{40}K. Cooling the fermion to ultracold temperatures (sub-μK), will produce a degenerate Fermi gas (DFG) rather than a BEC. In a DFG, each atom must be in a different trap state, in order to satisfy the Pauli exclusion principle. In contrast, all the atoms in a BEC are in the same trap state. Since a DFG is a multi-state gas, an interferometer based on a DFG must be a multi-mode interferometer similar to a white light interferometer. The benefit of using a DFG is that, remarkably, the fermions barely interact, thus leading to a more accurate and stable interferometer.

Third, due to its small hyperfine splittings, potassium has many accessible "magic" magnetic field states, i.e. a magnetic field strength at which two states have the same DC Zeeman shift. At a "magic" magnetic field, the transition energy between the two states is insensitive to small variations in the DC magnetic field.

Table 3.1 shows the "magic" magnetic field for ^{41}K, ^{40}K, and ^{87}Rb. The ^{87}Rb has a single magic magnetic field at 3.23 G (all the others are many hundred Gauss). In contrast, ^{40}K and ^{41}K have 3 "magic" magnetic fields each between 20 G and

80 G. Importantly, magic magnetic fields are necessary for operating an atom interferometer that is insensitive to environmental and technical magnetic field noise. Finally, the mid-scale strength of the "magic" magnetic fields result in Zeeman splitting between neighboring states that are an order of magnitude larger than in ^{87}Rb, thus limiting cross-talk between AC Zeeman transitions.

species	Transition	Magic field	Zeeman splitting (MHz)
^{41}K	$\|1,0\rangle \leftrightarrow \|2,-1\rangle$	24.28 G	17
	$\|1,-1\rangle \leftrightarrow \|2,-1\rangle$	45.32 G	32
	$\|1,-1\rangle \leftrightarrow \|2,0\rangle$	24.29 G	15
^{40}K	$\left\|\frac{9}{2},-\frac{5}{2}\right\rangle \leftrightarrow \left\|\frac{7}{2},\frac{7}{2}\right\rangle$	93.04 G	32
	$\left\|\frac{9}{2},-\frac{3}{2}\right\rangle \leftrightarrow \left\|\frac{7}{2},\frac{5}{2}\right\rangle$	63.55 G	20
	$\left\|\frac{9}{2},\frac{1}{2}\right\rangle \leftrightarrow \left\|\frac{7}{2},\frac{1}{2}\right\rangle$	50.96 G	15
^{87}Rb	$\|1,-1\rangle \leftrightarrow \|2,1\rangle$	3.23 G [60]	2

TABLE 3.1: The useful "magic" magnetic fields and associated states for ^{41}K, ^{40}K, and ^{87}Rb. Potassium has multiple "magic" magnetic fields from 20 G to 100 G, while rubidium has only one at 3.23 G. "Zeeman splittings" refers to the energy splittings with states neighboring the transition states.

Finally, potassium has multiple magnetic Feshbach resonance that can be used to tune atom-atom interactions. We can use the Feshbach resonance to enhance or suppress interactions, and study their effect on the interferometer.

3.2 Choice of ^{39}K and ^{41}K

We started the potassium cooling project with ^{39}K, because the ^{39}K is the most abundant isotope. Our potassium dispenser uses natural abundance potassium (SAES Getters), with 93.26% of ^{39}K, 6.73% of ^{41}K, and 0.01% of ^{40}K. Using the large abundance of ^{39}K made the MOT stage easier to collect many atoms without increasing the background vacuum pressure too much. However, due to some unknown problem (possibly due to AOM broadcast noise, see section 3.6.3), the

^{39}K laser cooling and trapping system was not very stable in the number of atoms loaded into the chip trap, and also, the lifetime in the chip trap was very short. The instability in the atom number made the system difficult to use. The short lifetime limited the maximum operation time in the chip trap and was insufficient for evaporative cooling. Moreover, ^{39}K has a negative scattering length (attractive interaction), which strongly limits the ability to make a BEC. Given the above problems, we chose to switch our working potassium isotope to ^{41}K.

Despite the lower natural abundance of ^{41}K (13 times less than) ^{39}K, we were able to collect enough atoms to the MOT. The main advantage of ^{41}K is that it has a positive scattering length (repulsive interaction), which means that it can be cooled to BEC. Furthermore, several groups have successfully made a ^{41}K BEC [61–65]. While the BEC is not necessary for our atom interferometer experiment, it is a handy tool to check the proper operation for our apparatus every day. Furthermore, a trapped atom interferometer requires ultracold "near-BEC" temperatures. The original potassium laser cooling system for ^{39}K is presented in this refernce [56, 66].

3.3 Laser preparation

The laser preparation for the potassium system is similar to the rubidium system in our lab, which has been presented in Dr. Austin Ziltz's thesis [56] and in Megan's RSI 2014 paper [66]. In this section we focus on the differences with the rubidium laser system.

3.3.1 Injection laser for potassium

The master and injection laser system of potassium is similar to the rubidium system, but the potassium system uses a second injection laser for the repump laser. This change allow us to sweep the potassium repump frequency during the

experiment, while, in contrast, the rubidium repump feedback system is not fast enough to modify the frequency during the experiment.

As shown in Fig. 3.2, the frequency of potassium trap and repump laser is around 767 nm, and there is some frequency difference between the ^{39}K and ^{41}K. This difference makes it difficulty to switch between the ^{39}K and ^{41}K, because we need to change an AOM setting and realign the laser.

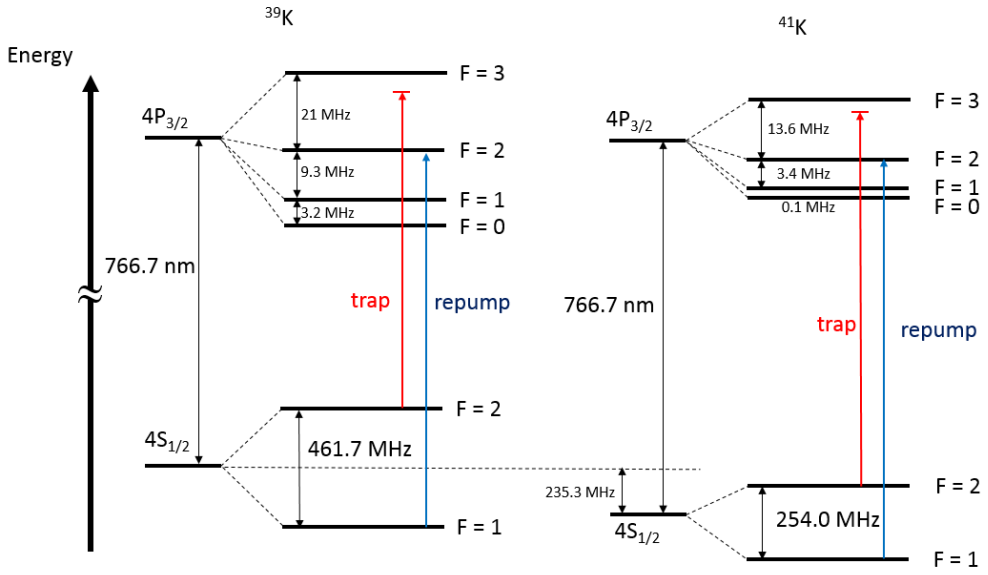

FIG. 3.2: ^{39}K and ^{41}K energy levels for laser cooling and trapping [67].

3.3.2 Daisy chained tapered amplifier

Due to the low power of our injection lasers, the potassium laser cooling system has too little laser power with just one tapered amplifier (TA). Therefore, we have set up a "daisy chain" of two TAs to amplify the potassium injection laser. As shown in Fig. 3.3, the first TA amplifies the injection laser from the 7 mW to 100 mW maximum. The output of the first TA has some of its light picked off by a polarizing beam splitter (PBS) for the optical pumping beam and push beam, and the remain is directed to the "science" table via an optical fiber. The output of the

fiber will be around 20 mW and amplified by the second TA to the maximum 400 mW to the MOT.

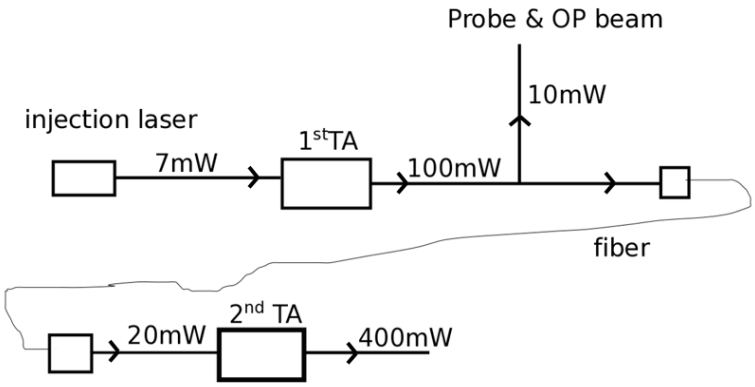

FIG. 3.3: Daisy chain of two tapered amplifiers (TAs). The laser power from the injection laser is around 7 mW before the first TA. The first TA amplifies the power to 100 mW. The output power from first TA is partially split off to the probe and optical pumping beams. After loss from the fiber, only 20 mW reaches the second TA. The second TA amplifies the power to 400 mW, which is enough for the ^{41}K MOT.

3.3.3 Push beam

After the first TA output, we use a PBS to take some of the laser power for the push beam and optical pumping beam.

The push beam does not exist in the rubidium laser system and is disabled in potassium-only laser cooling. The push beam is used when operating a dual species Rb-K MOT. The push beam shoots into the MOT with an angle different from the six MOT beams to push the potassium atoms off from magnetic minimum of the anti-Helmholtz coils. We use this push beam when we trap the rubidium and the potassium together in the MOT: The large number of atoms in the rubidium MOT conspire with the Rb and K cooling light to reduce the potassium MOT population (possibly via light induced collisions). However, once we load both the ^{41}K and ^{87}Rb into the magnetic transport trap, we are able to sympathetically cool the potassium

by force evaporation of rubidium (RF and microwave knives both work). To load the maximum potassium and rubidium atoms together in the chip trap, we use the push beam to shift the potassium MOT location away from the rubidium MOT to avoid the competition between them.

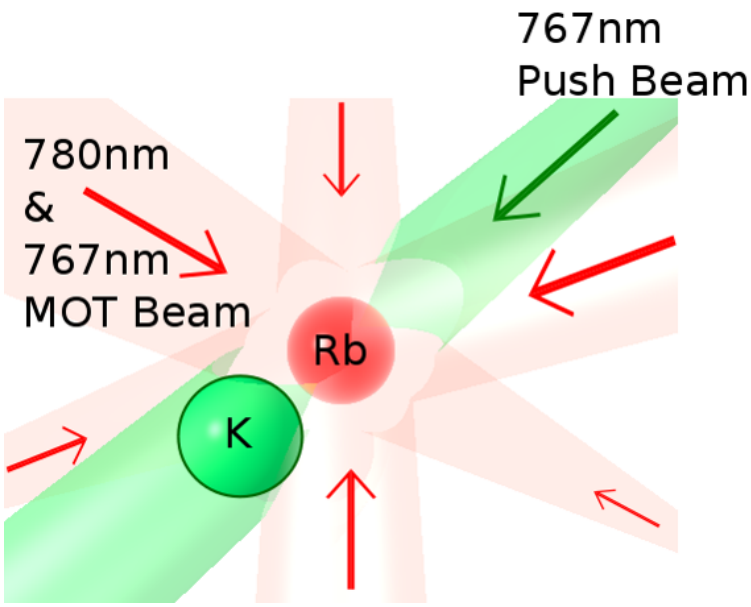

FIG. 3.4: The push beam is a mix of potassium trap and repumper light, the same as the potassium MOT light. The push beam will slightly offset to the potassium MOT from rubidium MOT to avoid the competition between these two species in the MOT.

3.3.4 Optical pumping beam

The optical pumping beam shares the same power and frequency control as the trap laser, since we just use detuned trap light for the optical pump (the $4P_{3/2}$ hyperfine structure of ^{41}K is much more compact than the $5P_{3/2}$ hyperfine structure of ^{87}Rb). We use the optical shutters to block the MOT beam or optical pumping beam when one of them is not needed.

3.3.5 Injection laser box

The injection lock requires the injection laser to have a specific current and temperature setting along with a very good master laser alignment. Unfortunately, the temperature required for the potassium laser is so low that it reaches the dew point in summer, which is harmful to the performance of the diode laser source. Notably, the lab humidity is around 20% in winter and safe from the dew point, while the humidity in summer is around 50%. Unfortunately, the HVAC system does not controls the lab humidity. To deal with this problem, we set up a sealed metal box with some open windows and inject a slow bleed of dry air into the box, as shown in Fig. 3.5, Dr. Drew Rotunno constructed an Arduino-based temperature and humidity monitor for the box. This metal box keeps the humidity at a level that is below the Arduino humidity sensor detection range.

This potassium injection laser box helps us avoid the dew point. However, its closed environment tends to accumulate heat slowly inside the box, resulting in a drift in the current requirement for the injection lock. We need to adjust the potassium injection laser current once an hour to deal with this drifting. It does not stop the experiment but still causes much trouble to our experiment. A high school lab member, Finn Hulse, and a physics major, Bennett Atwater, had a project to build a temperature feedback system for this potassium injection laser box, but this project has not yet been finished.

3.4 Laser cooling

This section will presents the laser cooling potassium system and compares it to the rubidium one.

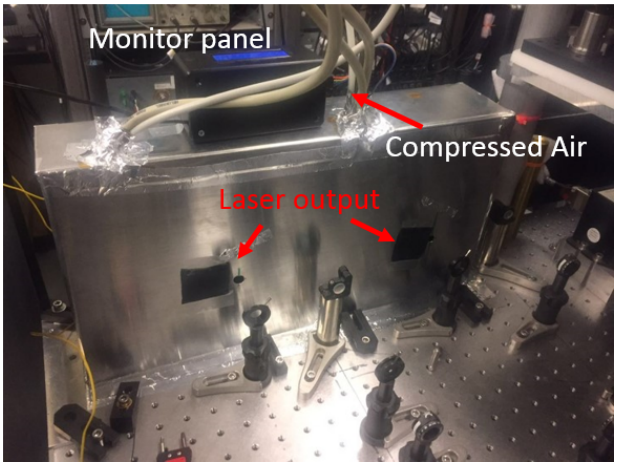

FIG. 3.5: Injection laser box. A sealed metal box with dry compressed air slowly inject into it keeps the humidity inside of box at a low level to prevent condensation on the laser diode when the temperature is below the dew point. At the front of the laser box there are two holes for the trap and repump laser outputs. There is an Arduino sensor with a monitor panel to display the temperature and humidity in real time.

3.4.1 MOT

The potassium laser cooling process for the MOT stage is shown in Fig. 3.6. There are some differences with the rubidium MOT cooling process. In addition to detuning and power differences, there are three significant modifications. First, the MOT period extends for 20 s, due to the lower abundance of ^{41}K, and thus more time is needed to collect the atoms. Second, the potassium MOT includes a compression stage for 20 ms at the end of the MOT period. Third, due to the higher sensitivity of potassium laser lock system to the turn off the MOT coils, there is a 2.1 ms waiting time after the magnetic coil turned off, and the molasses cooling time shrinks from 4 ms in rubidium system to 2 ms in potassium system to compensate for this waiting time.

3.4.2 Optical pumping and spin distillation

The last process in the MOT cell is the optical pumping stage to pump the atoms into the ground state $|F = 2, m_F = 2\rangle$ state. This process is the same as in

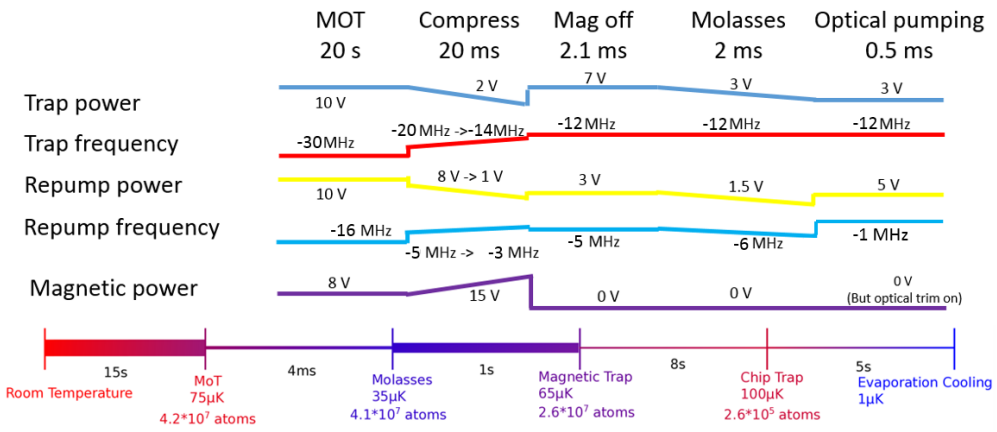

FIG. 3.6: Potassium cooling sequence in the MOT cell (with ^{87}Rb MOT on simultaneously). Not shown: before the optical pumping stage there is a shutter to shut the optical pumping laser into the MOT cell, and after the optical pumping stage the optical pumping shutter will open, and the MOT beam shutter will close. The line at the bottom shows the temperature and atom number for each potassium cooling process.

the rubidium system, but the requirements are different. For the rubidium system, the optical pumping only improves the atom number in the MOT. Because the magnetic trap is set to a value that is not strong enough to trap the $|2,1\rangle$ state atoms against gravity, since this state only feels half of the trapping potential of the $|2,2\rangle$ state atoms. However, if we trap the rubidium $|2,2\rangle$ state atoms, then the trap automatically traps both the $|2,2\rangle$ and $|2,1\rangle$ potassium atoms, and we cannot remove the potassium $|2,1\rangle$ atoms anymore. Since the mass of the potassium is less than half of the rubidium, the magnetic field that is able to trap rubidium $|2,2\rangle$ atoms will also trap potassium $|2,1\rangle$. The quality of the potassium optical pumping is critical to the purity of the atom states, since it must ensure that all $|2,1\rangle$ potassium atoms are pumped into the $|2,2\rangle$ state. Figure 3.7 shows the spin distillation experiment for potassium atoms in the MOT cell magnetic trap.

The spin distillation measurement is used to determine the spin population in a magnetic population trap. The spin distillation method is applied by lowering the magnetic field current after loading the atoms into the MOT cell magnetic trap (after the optical pumping stage). As the strength of the linear magnetic potential

is lowered, at some point it will no longer counteract gravity, and the atoms will become untrapped. Importantly, atoms in the $|2,2\rangle$ state experience twice magnetic potential strength of atoms in the $|2,1\rangle$ (or $|1,-1\rangle$ state), so the $|2,1\rangle$ atoms will be removed from the trap before the $|2,2\rangle$ atoms. As shown in Fig. 3.7, around 20 A, the atom population signal has a stair up from zero, which means the magnetic trap starts to trap the $|2,2\rangle$ state atom. If we keep increasing the current (i.e. the end current at which we stop lowing the current), there will be another stair around 30 A shows the magnetic field traps the $|2,1\rangle$ atoms. The ratio of the first stair to the second stair shows the atom population ratio of $|2,2\rangle$ atoms to the total atom number in the magnetic trap. Figure 3.7 on the top shows the spin distillation result before we optimize the optical pumping beam, and the bottom figure shows the result after the optimization: The atom ratio for $|2,2\rangle$ has improved from 60% to 80%, which shows that the quality of the optical pumping has improved. Naively, one would expect that the $|2,1\rangle$ atoms would be removed at 40 A (since $|2,2\rangle$ atoms are removed at 20 A). However, since the Zeeman shift of the $|2,1\rangle$ state is not linear even at low magnetic field, we find empirically that it is removed at a lower current (i.e. lower magnetic gradient), 30 A.

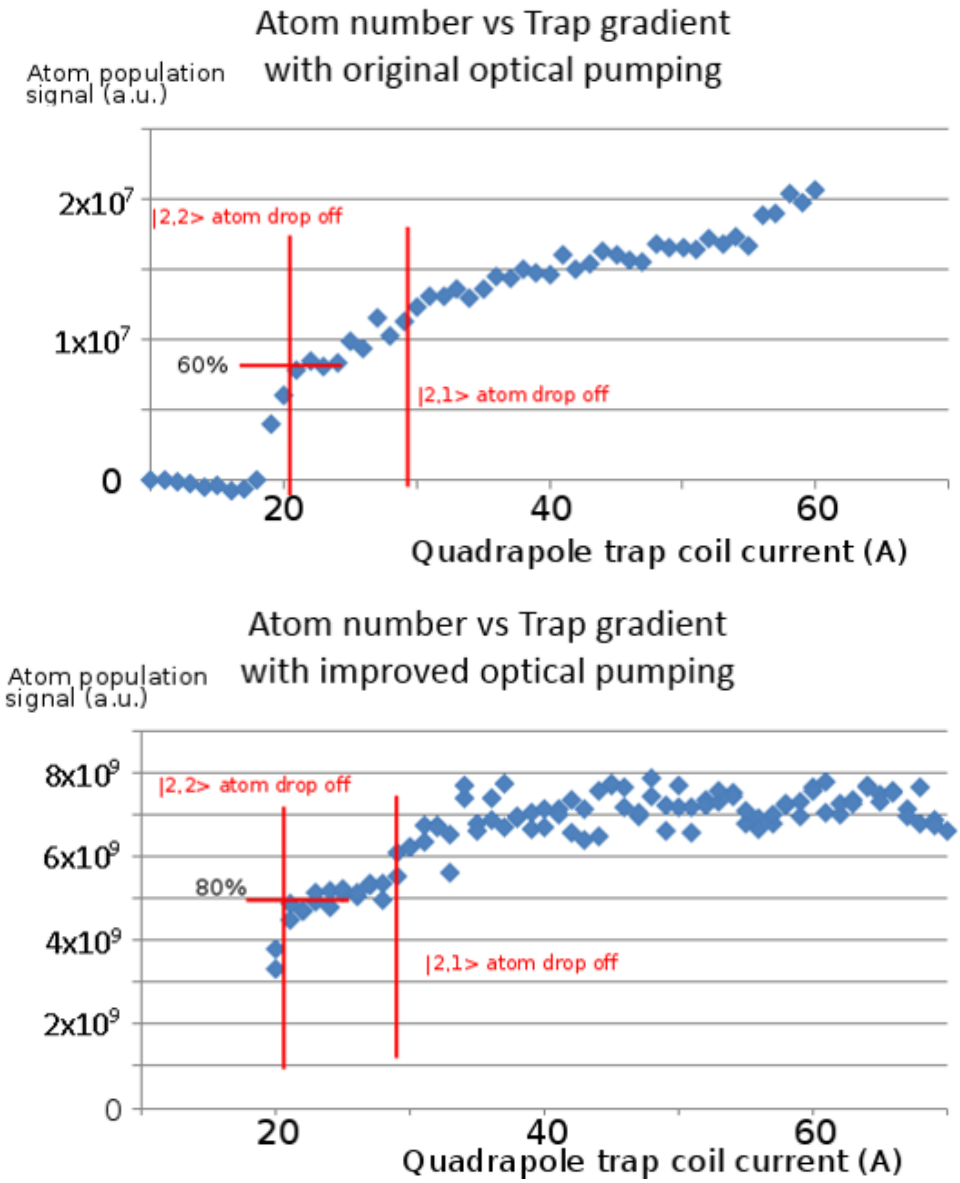

FIG. 3.7: Potassium spin distillation experiment. The top figure shows the spin distillation experiment with original optical pumping, which result in 60% of the atoms in the $|2,2\rangle$ state. The bottom figure shows the spin distillation experiment with improved optical pumping, and around 80% of the atom are in the $|2,2\rangle$ state.

3.4.3 Tranportation stage

The atoms are transferred by the transportation magnetic trap to the science cell after the molasses cooling. In the science cell, the atoms are loaded into the chip trap. As shown in Fig. 3.8 (left top), the size of the chip trap cloud is much

smaller than the transportation trap cloud: the loading process is not very efficient, and we lose most of the atom (around 1% of atoms load into the chip trap).

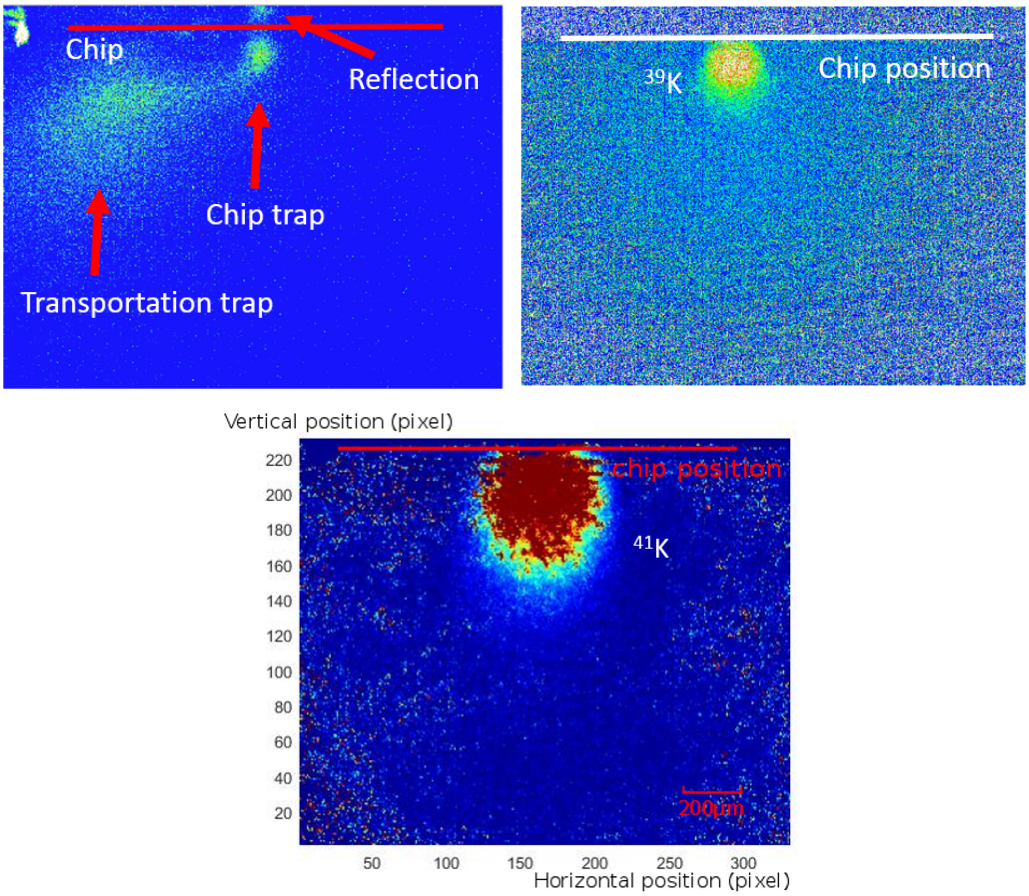

FIG. 3.8: Images of potassium in the chip trap. Left top: ^{39}K loaded into the chip trap from the transportation trap (florescence image). Right-top: ^{39}K atoms in the atom chip micro-magnetic trap (absorption image). Bottom: ^{41}K atoms in the atom chip micromagnetic trap (absorption image). Notably, the loading figure is taken by the fluorescence imaging with 1D MOT technique [56], and the chip figure is taken by absorption image with few ms of time of flight.

3.5 Potassium chip trap cooling

After we load the atom into the chip trap, we used forced evaporation to cool the potassium atoms, either directly or indirectly.

The initial idea is to follow the same step as the rubidium evaporation cooling scheme, i.e. use the RF knife to selectively remove the hot potassium atoms. How-

ever, the potassium atom number in the chip trap is initially much lower than in the rubidium case: evaporating the potassium atoms directly is not likely to achieve a BEC (or at least a large enough BEC).

3.5.1 Sympathetic cooling

The alternative method is to trap the rubidium with the potassium in the chip trap and evaporate the rubidium atoms. The colder rubidium will elasitcally collide with potassium and sympathetically cool the potassium in the same trap. This method can cool the potassium without losing any potassium atoms in principle.

The sympathetic cooling idea requires us to trap the rubidium and potassium simultaneously, from the MOT stage to the chip trap. In the experiment, we found that even without sympathetic cooling in the chip, trapping the rubidium and potassium together already improves the potassium quality (lower temperature and higher atom number) in the chip trap. In the MOT and transportation stage, the rubidium has a lower temperature than the potassium and thus sympathetically cools the potassium during these stages. The colder potassium results in an improved loading efficiency on to the chip and an improved lifetime in the chip trap.

However, use of the rubidium is not a win for all the aspects of the potassium cooling process. The first problem is that the potassium number in the MOT decreases when trapping with rubidium. To avoid the competition between the rubidium and potassium MOTs, we set up the push beam as shown in Fig. 3.4 to push the potassium MOT off-center and separate it from the rubidium MOT. The improvement from the push beam is summarized in Table 3.2: The push beam helps the system to reach its largest potassium population, the same as without rubidium, and with the lowest temperature as with rubidium.

	Atom signal in Mag trap (a.u.)	Temperature (μm)
Without Rb	8×10^7	75
With Rb	4×10^7	35
With Rb & push beam	8×10^7	35

TABLE 3.2: Improvements in ^{41}K atom number and temperature in the magnetic trap with rubidium ^{87}Rb and push beam.

3.5.2 Inelastic collisions

Unfortunately, we ran into a problem with the rubidium sympathetic cooling approach: the potassium lifetime in the chip trap decreases when rubidium co-trapped. We implemented $|2,1\rangle$ state remover for both rubidium and potassium, but the problem still remains (we had a hard time diagnosing the fraction of ^{41}K $|2,1\rangle$ atoms on the chip). The $|2,1\rangle$ state remover is similar to the evaporation cooling, but target on the $|2,1\rangle$ state related transition and sweep the frequency until all the $|2,1\rangle$ state atoms is been removed. This phenomenon hints that there are inelastic collisions [65] between the rubidium and potassium. As shown in Fig. 3.9, the potassium lifetime with Rb in the chip trap has only around 1.6 s, while the lifetime without Rb is around 10 times longer (18 s).

This inelastic collision problem brings us a dilemma that a tighter trap improves the cooling efficiency by direct evaporation or sympathetic, but shortens the lifetime significantly by improve the collision rate with Rb. A weaker trap holds the potassium in the chip trap for longer but then result in a longer cooling time. Moreover, due to the atom chip safety purposes, there is a time interlock to limit the maximum time of running current through the chip (7 seconds at 1 A). The cooling in a weaker trap may not be effective enough to reach a potassium BEC before this time limit.

Fig. 3.10 shows the temperature and the collision rate for potassium only (single species collision) and potassium with rubidium (inter-species collision) in our experiment for some other groups. It shows that the condition for our experiment

is not far from other groups, and that we should be able to reach a BEC. Moreover, this data implies that our atom preparation to the chip trap is good enough, but some other problems, such as inelastic collisions and chip trap operation time limit us.

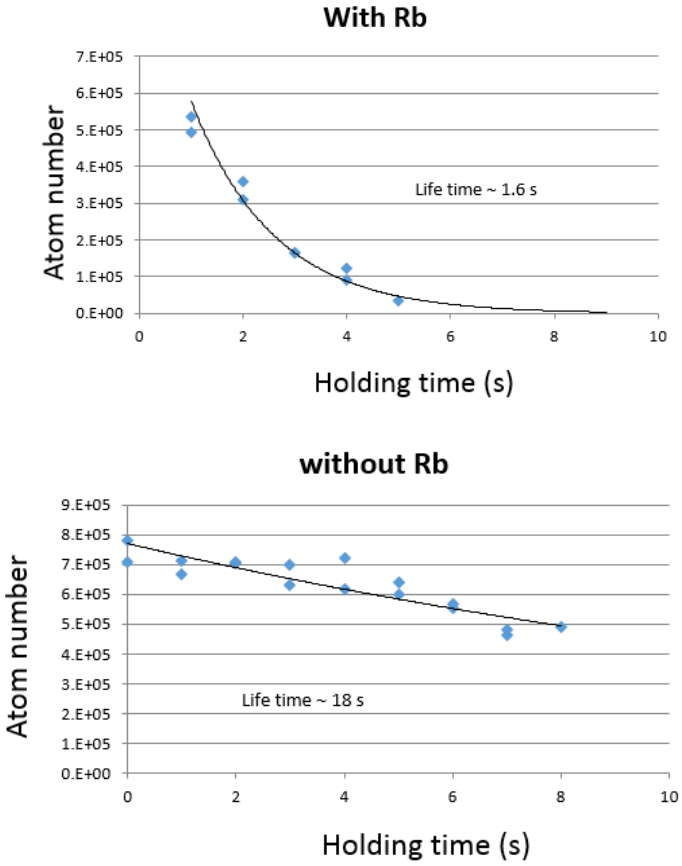

FIG. 3.9: Potassium lifetime measurement with low trap frequency (2 V hold field), high trap frequency (3.45 V hold field), and with a rubidium remover. The first two data shows the potassium lifetime with rubidium in the trap for different trap frequency. The their curve is that we remove the rubidium first and measure the potassium lifetime.

3.5.3 Sympathetic cooling in the transportation trap

Considering the two points we discussed above, sympathetic cooling and inelastic collisions, another approach to potassium cooling is to evaporate the rubidium and sympathetically cool the potassium during the transportation from MOT cell

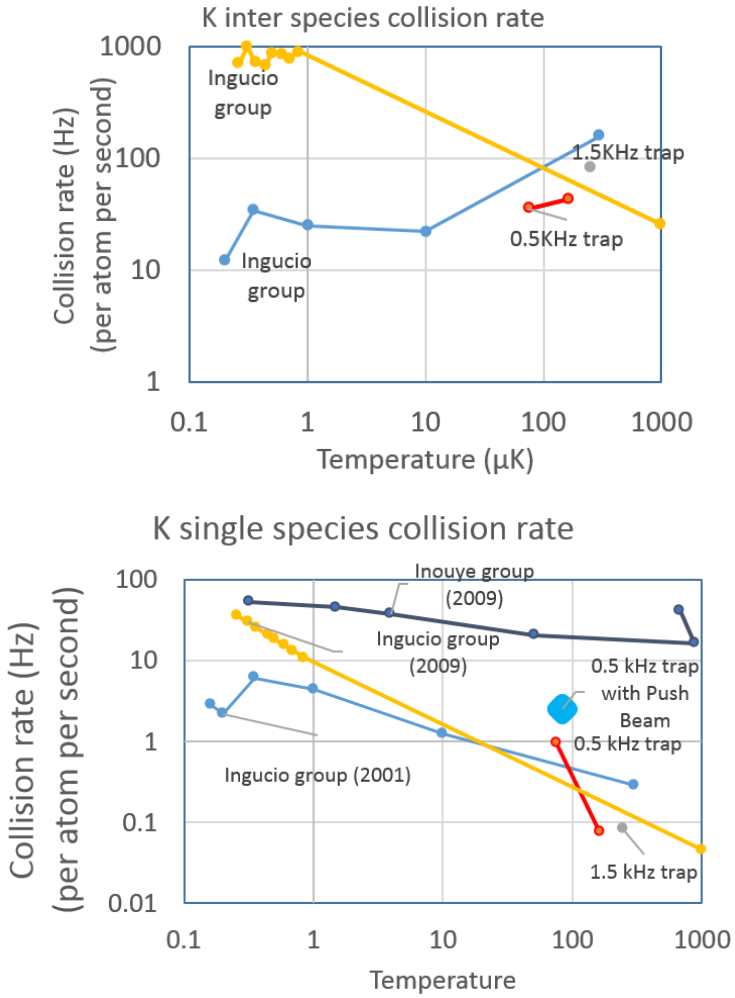

FIG. 3.10: The single species (bottom) and inter-species (top) collision rate for potassium cooling. The data shows the atom condition in the chip trap is not far from other groups, who achieved potassium chip trap BEC. These groups are the Ingucio group [61, 62], and the Inouye group [63].

to science cell (in the transport magnetic trap). We expect that the sympathetic cooling in the transportation trap will increase the potassium loading into the chip trap and reduce the temperature: In this manner, we may be able to load potassium into the chip trap without rubidium (it will already be evaporated), and then we can evaporate potassium directly to get BEC. Using this approach, we improved the ^{41}K atom number in the chip trap from 1.47×10^5 to 1.6×10^6, and the lifetime improve from 3 s to 7.4 s.

However, this improvement is still not enough to reach a ^{41}K BEC, and some problems prevent us from improving the cooling in the transportation trap. A first problem is that the transportation trap is a linear trap with a magnetic zero at its center. Atoms passing through this magnetic zero will have their spin state scrambled and transform some of there atom into the high field seekers, which cannot be trapped in the tranportation trap. This loss is called "Majorana loss", and it worsens as the cloud cools since colder atoms tend to concentrate at the center of the trap, i.e. at the zero point. A second problem is that the transportation trap also has a time limit: The transportation coils are more robust than the chip wires, but there are roughly 100 A of current running in the transportation coils during the transportation stage, which is much higher than the chip wire. There is a significant risk that the transportation coils will overheat and damage the apparatus, vacuum system, and optics. Moreover, the trap frequency of the transportation trap is lower than the chip trap, and it requires a longer time to cool the potassium sympathetically.

As shown in Fig. 3.11, evaporative cooling of ^{87}Rb in the transport trap improves the atom number and phase space density (PSD) of potassium in the chip trap, with some loss of rubidium atom number as a cost. However, even if we cool the rubidium to lower temperature in the transportation trap, we can only remove more rubidium, but not improve the potassium atom number and PSD. This performance shows that as long as we try to evaporate rubidium, we quickly reach a maximum PSD and atom number for ^{41}K.

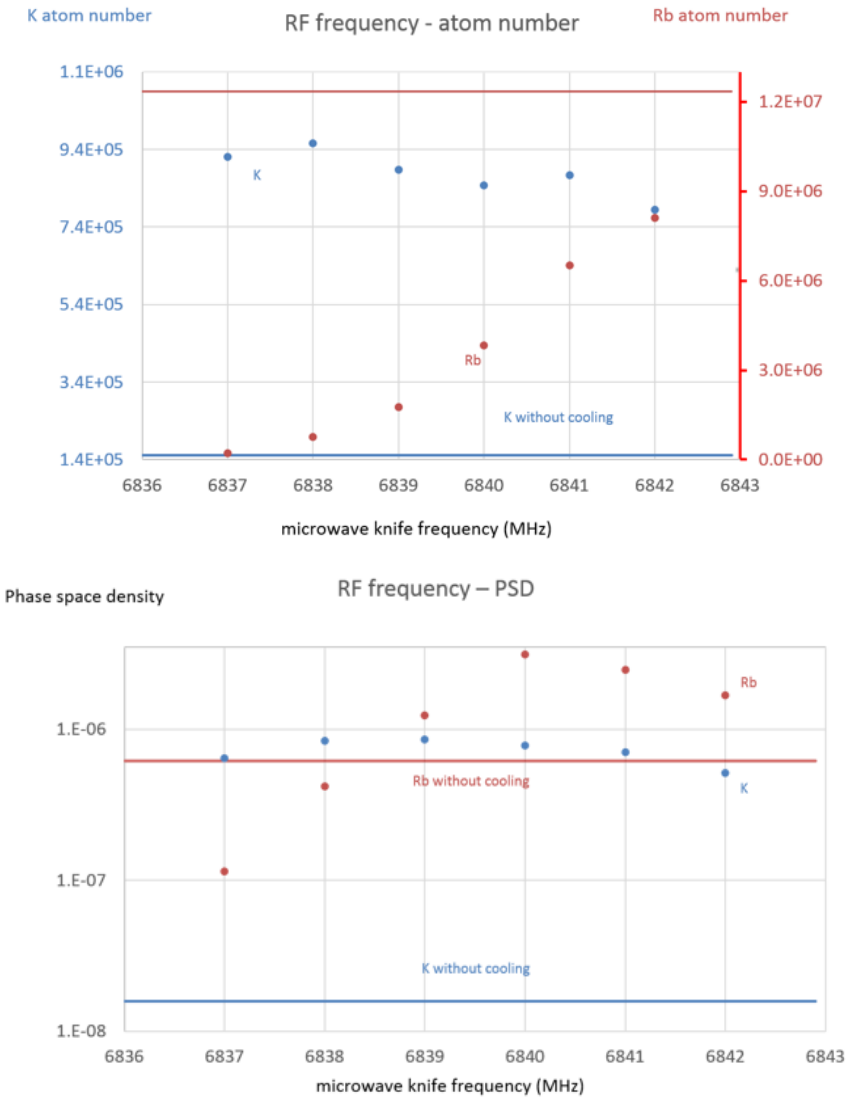

FIG. 3.11: The atom number and phase space density (PSD) in the chip trap improves with sympathetic cooling with ^{87}Rb in the transportation trap. The data shows that as long as we operate the sympathetic cooling in the transportation trap, the atom number and PSD will increases. However, cooling rubidium to lower temperature does not further improve the ^{41}K PSD significantly.

3.5.4 Best potassium chip trap cooling in our lab

With all the efforts we discussed above, the best potassium cooling that we achieved in the chip trap is shown in Fig. 3.12. We start with 1.5×10^6 potassium atom with PSD $\approx 3 \times 10^{-6}$ (no ^{87}Rb present). The RF evaporative cooling improves

the PSD, but the efficiency is not as sufficient, and by the 12^{th} cooling phase, the PSD starts to drop. Clearly, we are still far from reaching a BEC (PSD = 2.6) and need further improvements to achieve it.

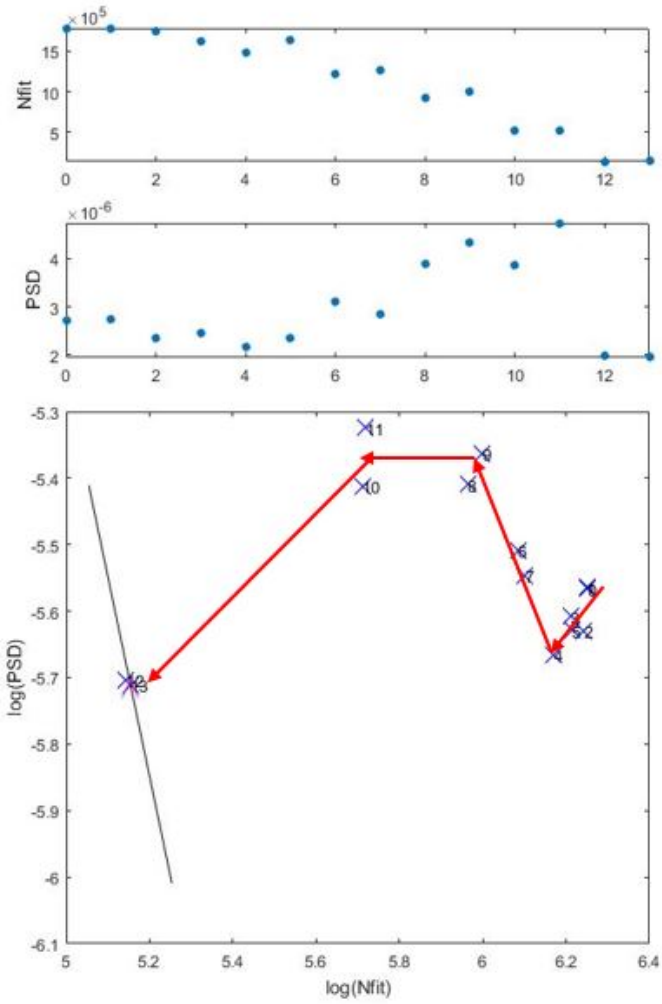

FIG. 3.12: The best potassium chip trap cooling result in this project (no ^{87}Rb present). The PSD improves with each RF cooling stage, but the slope is not as high as the rubidium case (black slope line). At the 12^{th} cooling stage the PSD starts to drop and so this evaporation path is not viable from BEC.

3.5.5 Further cooling idea

While evaporative cooling of ^{41}K in the chip trap has generally been difficult, sympathetic cooling with ^{87}Rb in the transportation trap has worked relatively well

until running into Majorana losses. Furthermore, inelastic losses in the transportation trap have been negligible. A possible path forward is to try to cool further in the transportation trap, while finding a way to suppress Majorana losses.

In order to further cool the potassium before the chip trap, the time orbital potential (TOP) trap may be a good candidate. The TOP trap is a linear trap with an orbiting trap bottom. Since the trap bottom is orbiting, there will be no magnetic zero points on average and so Majorana loss should be suppressed. The TOP trap can be operated with existing coils and power supplies, though it may be necessary to extend the time limit of safety interlocks. Further improving the sympathetic cooling efficiency may require an increase in trap frequency. The problem with the TOP trap is that the TOP trap has to be some distance away from the chip, and we cannot load the atom from the TOP trap to the chip trap directly, due to the rotation magnetic fields of the TOP trap and the static magnetic fields of the chip trap. Instead, the TOP trap atoms can be loaded into the optical dipole trap (ODT) rather than the chip trap. However, regardless of whether we then load the atoms from the ODT to the chip trap or directly apply the atom interferometer experiment to the ODT, the ODT must be moved closer to the atom chip.

Another idea is to construct a transportation-ODT hybrid trap [68]. This idea will use the ODT to avoid the Majorana loss and control the trap frequency, by placing the ODT just off center of the magnetic zero in the transportation magnetic trap. This hybrid trap can also loading the atoms directly into the ODT. However, as we discussed with the TOP trap, the ODT will have to move closer to the chip trap after the hybrid trap stage.

William Miyahira, a new lab member, is working on a moving ODT with a rotational stage to rotate a thick glass window to translate the ODT vertically next to the chip.

3.6 Notes on the potassium cooling and trapping apparatus

This section discusses some issues that have come up in developing the potassium laser cooling and trapping system.

3.6.1 Double pass TA system

Before setting up the daisy chain of two tapered amplifiers (TAs), the potassium laser cooling system originally used a double pass TA system to amplify the potassium laser twice, which is described in Austin Ziltz's thesis [56]. The double pass TA system sends input backwards into the TA, from the output to the input direction, and then reflects the amplified beam with a mirror to direct it through the TA again in the forward direction. This double-pass system will amplify the laser beam at roughly the same level as with using two daisy-chained TAs. However, this double pass TA system will generate a standing wave between the TA and mirror, and the peak laser intensity of the standing wave will threaten the TA crystal. As a result, our TA crystal was fatally damaged in this configuration, and we have to replace the TA crystal. The double pass TA system is risky, and we should avoid using it.

3.6.2 Potassium trap and repump laser competition

The potassium and repumper light is amplified twice by the two daisy chained TAs. However, we find that there is some competition in the amplification of these two optical frequencies. This problem is unsolved and contributes to the instability of the potassium laser system power.

This problem is visible on our MOT Fabry-Perot cavity monitor, and Fig. 3.13

shows an oscilloscope image of this monitor. The two peaks at the edge are the trap and repump laser, and they go through two TAs before they reach the MOT. The monitor shows that the amplitude of the trap and repump laser are randomly jumping up and down: the amplitude of these two lasers are anti-correlated in that one jumps up while another jumps down. If we block one of the beams, the peak of the other beam will be higher and without the amplitude instability. This phenomenon shows there is some competition between the trap and repump laser in the TA. In particular, the second TA has a saturated input power, and a little jitter on the laser power or the alignment will affect the balance of the laser amplification ratio between the two lasers.

If we have enough budget, this problem can be solved easily. We only need to add two more TAs, so that each laser has its own two-TA system to amplify its power without competition.

However, it will be hard to deal with this problem without additional TAs because the jitter on the laser power or the alignment is too easily affected by multiple factors, such as the laser current stability, lab temperature stability, or even the airflow in the lab.

As a result, we left this problem as it is and continue the experiment, since it is not a show stopper. Hopefully, in the future, our lab will have enough budget to solve this problem.

3.6.3 AOM broadcast noise

Another problem in the experimental apparatus is that one of the acousto-optic modulators (AOMs) is broadcasting noise. Figure 3.14 shows the noise on the frequency feedback signal for saturation spectroscopy on the rubidium and potassium master laser when the rubidium double-pass AOM scans from 90 MHz to 100 MHz.

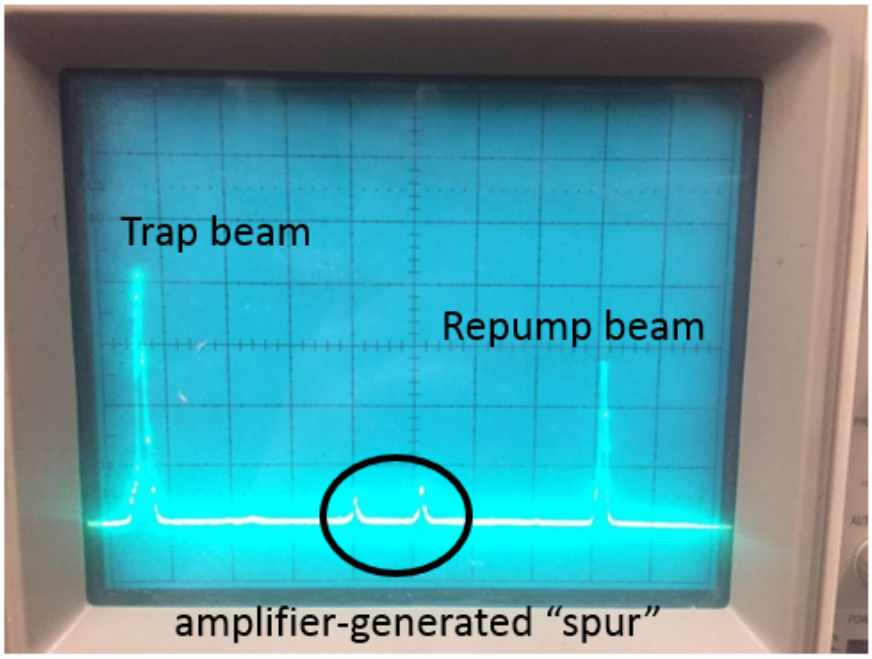

FIG. 3.13: ^{39}K MOT amplifier competition between trap beam and repump beam. The trap and repump beam amplitudes are noisy and anti-correlated. The power ratio between the trap and repump beam will effect the MOT and Molasses quality. There are also two amplifier generated “spurs” between them.

Channel 1 shows a trigger pulse, and channel 2 is the feedback noise signal. The master laser for both rubidium and potassium are always locked on a saturation spectroscopy peak. The AOM only modifies the laser frequency after the master laser output, so the AOM should not affect the laser lock signal.

However, based on Fig. 3.14, the AOM generates noise in the spectroscopy feedback signal and especially disruptive to the potassium laser lock signal: The potassium noise is much bigger and lasts longer than the rubidium. This difference might be because the rubidium feedback system is more robust than the potassium feedback system, or perhaps the noise source couple better to the potassium laser system.

Figure 3.14 also shows the error signals for the rubidium and potassium laser locks when the problematic AOM is not swept through the 89-100 MHz frequency range. This figure shows that even without the problematic AOM, some noise still

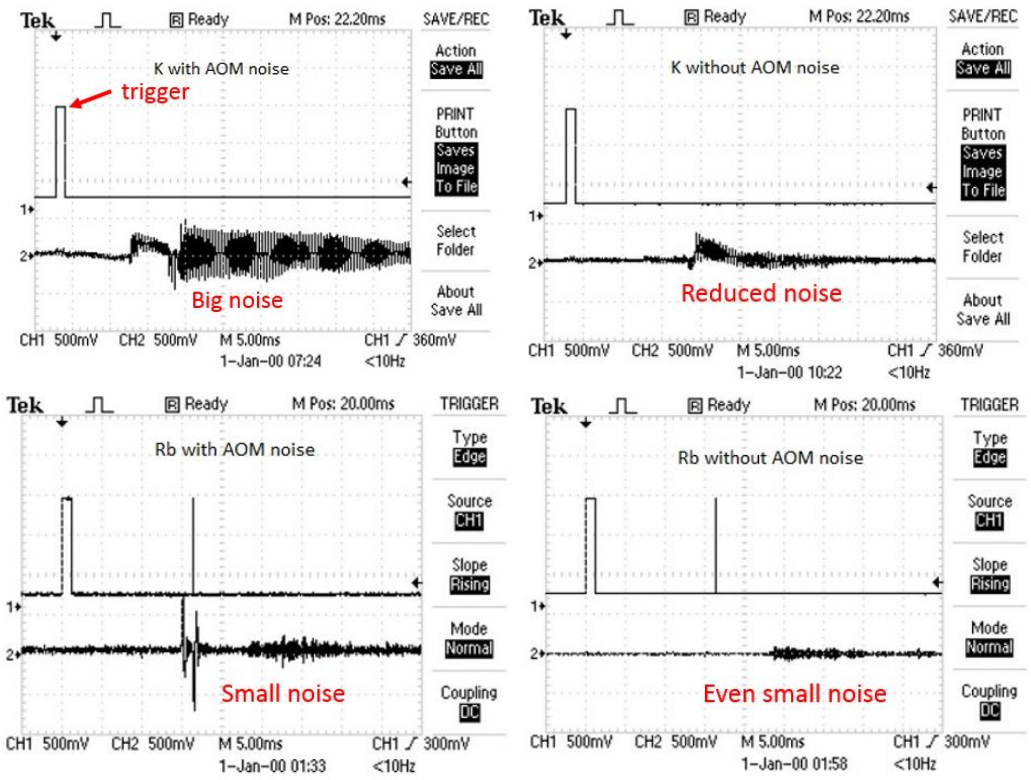

FIG. 3.14: The noise on the saturation spectroscopy feedback error signal when one of the Rb AOM scans through the 90 MHz to 100 MHz frequency region. Even without the problematic AOM, there still some noise, but much smaller. Clearly, the potassium laser lock signal is more sensitive to this noise.

affects the master laser feedback signal, but the noise much smaller than with the problematic AOM.

We tried to solve this problem in several ways, such as replacing the problematic AOM, and adding an attenuator to reduce the reflection from the AOM. The noise did get smaller with these improvements, but it did not go away. To make further improvements, we might have to open up the AOM amplifier and frequency source system. This will be considerable work, and will stop the entire lab experiment for a long time, so we chose to stop the debugging at this level.

3.7 Conclusion and future plan

In conclusion, we have made substantial progress on the potassium cooling and trapping apparatus. We converted the potassium apparatus from ^{39}K to ^{41}K, used a push beam to maximize the rubidium and potassium atom number in the MOT, used evaporative cooling of rubidium to improve the loading efficiency for the potassium into the chip trap. Our progress on the potassium cooling system improved the atom number and reduced the temperature of potassium in the chip trap. However, the progress in the potassium cooling system was not sufficient enough for us to reach the ^{41}K BEC, due in large part to inelastic losses (Rb-K).

The next step in the potassium cooling project will be improving the cooling before loading into the chip trap. This step requires a new trap at the end of the transportation stage, a TOP trap or a hybrid optical-magnetic trap. Considering that atom cloud size in the transportation trap is much larger than the chip trap, the new trap has to be in a location far from the chip, and so we need a movable ODT to further the ^{41}K experiments on the chip.

CHAPTER 4

AC and DC Zeeman trap Theory

This chapter introduces the theory of DC Zeeman and AC Zeeman traps base on an atom chip. Both DC Zeeman and AC Zeeman potential are generated by the Zeeman interaction Hamiltonian, which is given by:

$$H_{Zeeman} = -\vec{\mu} \cdot \vec{B} \tag{4.1}$$

where the $\vec{\mu}$ is the magnetic moment of the atom and $\vec{B}$ is the external magnetic field. The external magnetic field $\vec{B}$ could be static (DC) or oscillating (AC). The magnetic moment for an alkali atom, without considering the nuclear spin, is given by $\vec{\mu} = (2\mu_B/\hbar)\vec{S}$, where μ_B is the Bohr magneton, $\hbar$ is Planck's constant over 2π, and the $\vec{S}$ is the spin operator of the valence electron.

This chapter first discusses the DC Zeeman trap theory in section 4.1 and then AC Zeeman trap theory in section 4.2. This chapter is modified from the not submitted paper [69] on roughness in AC Zeeman traps that in preparation.

4.1 DC Zeeman trap theory

In an ultracold atom experiment, the atoms' temperature is very low, and atomic motion is very slow compared to magnetic precession. Under these conditions, the magnetic moment of the atom follows the direction of the local static magnetic field ($\vec{B}_{DC}$) and keeps the same angle between $\vec{\mu}$ and $\vec{B}_{DC}$. The total angular momentum of the atom $\vec{F} = \vec{I} + \vec{S}$ is a good quantum number at low magnetic fields, where $\vec{I}$ is the nuclear spin and $\vec{S}$ is the electron spin. The projection of the angular momentum $\vec{F}$ on the static magnetic field $\vec{B}_{DC}$ is m_F, which keeps the same value in the magnetic field. Under the conditions above, the DC Zeeman energy E_{DCZ} is given by:

$$E_{DCZ} = m_F g_F \mu_B |B_{DC}| \tag{4.2}$$

which is linear with the magnetic field magnitude. Here g_F is the Landé g-factor: $g_F = (F(F+1) - S(S+1) - I(I+1))/(F(F+1))$. E_{DCZ} is the energy shift of the atom's internal state, and also the atom's potential energy when the atom is in a magnetic field. Earnshaw's theorem prevents the existence of magnetic maxima in a free space, but the magnetic field can form magnetic minima (Fig. 4.1 (a)) to trap the "low field seeker" states ($m_F g_F > 0$).

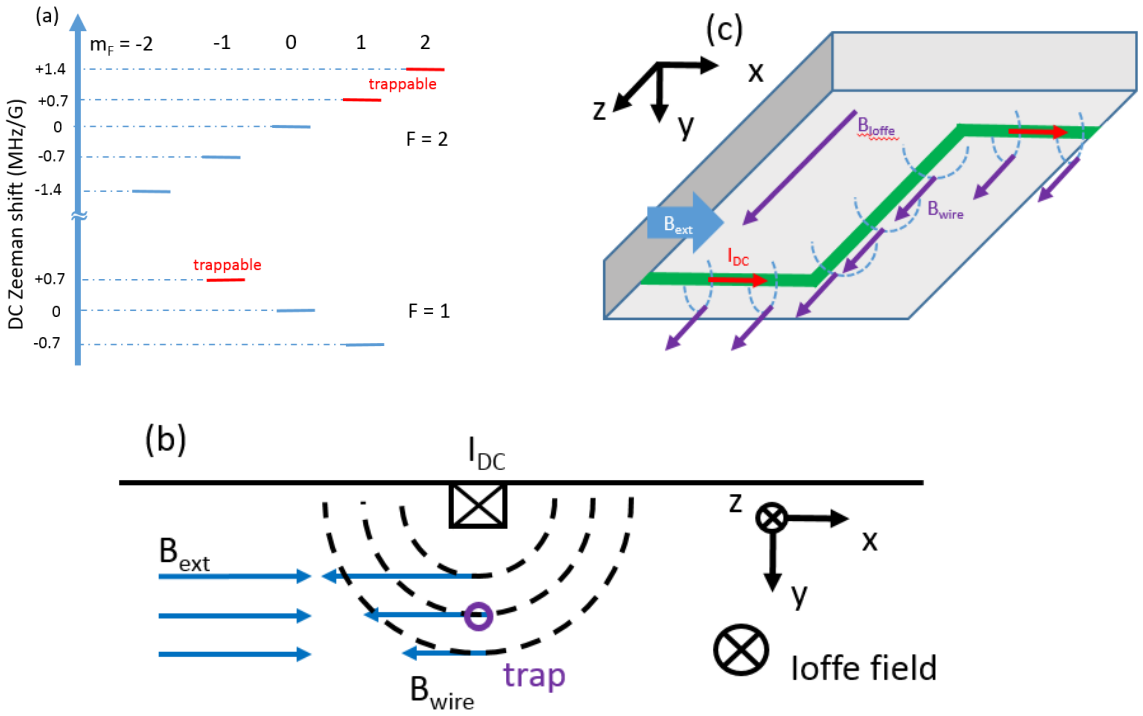

FIG. 4.1: Basic physics of a DC Zeeman Z-wire trap on an atom chip. (a) DC Zeeman energy shift E_{DCZ} for alkali atoms that have nuclear spin I = 3/2, with $F = 1$ and $F = 2$ states, e.g. ^{39}K, ^{41}K, and ^{87}K. Since the energy shift is linear with the magnetic field and atoms move towards the lower energy position, the states with positive E_{DCZ} will be trapped in a magnetic minimum, and we call these states "low field seeker". (b) Diagram of the magnetic fileds of a DC Zeeman chip trap. The DC Zeeman trap is formed with B_{wire}, which is generated by the chip current I_{DC}, and the external uniform magnetic field B_{ext}, which has the opposite direction to B_{wire} in the horizontal direction. Since the source of the B_{wire} is very close to the target trap position and has a high gradient, there is a point where B_{ext} and B_{wire} have exactly the same value but opposite directions, and this is the magnetic minimum point (trap position). The Ioffe field B_{Ioffe} is in the same direction as the current I_{DC} and removes the magnetic zero point. (c) The Ioffe field B_{Ioffe} is an external uniform magnetic field, and the direction of the Ioffe field depends on the end cap of the Z-shaped wire (green). As shown in the plot, the end cap of the magnetic field will generate a magnetic field perpendicular to the B_{ext}. If the end cap magnetic field has the same direction of B_{Ioffe}, which is the same direction as I_{DC} in the center segment of the Z-shaped wire, then the magnetic field z-axis component is larger next to the end cap, and thus provide axial confinement. Figure adapted in part from [69] and S. Aubin.

For a DC Zeeman trap on an atom chip, the magnetic field minimum is generated by canceling the B_{ext} and B_{wire} magnetic fields, as shown in Fig. 4.1(b). We denote the location of the magnetic field minimum (we call it the "trap bottom") as the position $\vec{r}_0$. The Ioffe field B_{Ioffe} is perpendicular to the B_{ext} and B_{wire}

and has the same direction as I_{DC}, providing a magnetic background to prevent the magnetic field zero point. As long as the external magnetic field B_{ext} is uniform, the magnetic field in the vicinity of the trap bottom is quadrupolar and harmonic in magnitude to lowest order. The total magnetic field is given by:

$$\vec{B}_{DC}(x,y) \simeq \frac{B_{wire}}{h}(\Delta y\hat{x}) + \Delta x\hat{y}) + B_{\text{Ioffe}}\hat{z} \tag{4.3}$$

$$|B_{DC}(x,y)| \simeq |B_{\text{Ioffe}}| + \frac{B_{wire}(\vec{r}_0)^2}{2h^2|B_{\text{Ioffe}}|}(\Delta x^2 + \Delta y^2) \tag{4.4}$$

where Δx and Δy is the position with respect to the trap minimum ($\vec{r}_0$), and h is the distance of the trap bottom to the wire. In the case of an infinite thin wire, the distance can be easily derived from Ampere's law, $h = \mu_0 I_{DC}/2\pi B_{ext}$, where μ_0 is the permeability of the free space. Equation 4.4 describes the field that provides radial confinement in the xy plane.

Other than the radial confinement shows above, the atom chip also provides axial confinement. The axial confinement is typically provided by the "end cap" wires of the Z-shaped wire, as shown in Fig.4.1(c). The end cap current generates an end cap magnetic field along the z-axis with the same direction as B_{Ioffe}. Therefore, the magnetic field at the end of the center segment will be larger and thus provides the axial confinement.

4.2 AC Zeeman trap theory

The AC Zeeman effect uses RF or microwave magnetic fields driven near resonance to an atomic hyperfine transition to generate a spin-specific energy shift [49, 50]. The AC Zeeman effect is generated by the same Zeeman Hamiltonian (eq. 4.1) as the DC Zeeman effect. However, the AC Zeeman effect happens between two hyperfine states, say $|g\rangle$ and $|e\rangle$, which are separated in energy by $E_{eg} = \hbar\omega_{eg}$

$= \hbar(\omega_e - \omega_g)$. When an AC magnetic field B_{AC} is driven near resonance on this transition, the Hamiltonian for this two-level system with N microwave photons with driving frequency ω_{AC} in the dressed atom basis $\{|g, N\rangle, |e, N-1\rangle\}$ is given by:

$$H = H_0 + H_{\mu W} + H_{interaction} \tag{4.5}$$

$$= \hbar \begin{bmatrix} \omega_g & 0 \\ 0 & \omega_e \end{bmatrix} + \hbar\omega_{AC} \begin{bmatrix} N & 0 \\ 0 & N-1 \end{bmatrix} + \frac{\hbar}{2} \begin{bmatrix} 0 & \Omega \\ \Omega^* & 0 \end{bmatrix} \tag{4.6}$$

where the Ω in the interaction term is the Rabi frequency. For simplicity, we ignore the nuclear spin and let the orbital spin $L = 0$, and then the magnetic moment will be the valence electron spin, which is $\vec{\mu} = (\frac{g_s \mu_B}{\hbar})\vec{S}$, where the μ_B is the Bohr magneton and g_s is the electron gyromagnetic factor ($g_s = 2$ in our case). The Rabi frequency is thus:

$$\Omega = \langle g| - \vec{\mu} \cdot \vec{B}_{AC} |e\rangle \tag{4.7}$$

$$= -\frac{\mu_B}{\hbar^2} \langle g| S_+ B_- + S_- B_+ + 2S_z B_{AC,z} |e\rangle \tag{4.8}$$

where the $S_\pm = S_x \pm iS_y$, $B_\pm = B_{AC,x} \pm iB_{AC,y}$. This equation shows that the Rabi frequency depends on the polarization of B_{AC} and the transition states: the first two terms are the $\sigma^\pm$ transitions, and the last term is the π transition. $B_\pm$ can only drive $\sigma^\pm$ transitions such that $\Delta m_F = \pm 1$, and $B_{AC,z}$ can only drive π transitions such that $\Delta m_F = 0$. The polarization selection rules are shown in Fig. 4.3(b).

If we subtract $\hbar\omega_g + \hbar\omega_{AC}$ from eq. 4.6, the Hamiltonian becomes:

$$H = \hbar \begin{bmatrix} 0 & \Omega/2 \\ \Omega^*/2 & -\delta \end{bmatrix} \tag{4.9}$$

where $\delta = \omega_{AC} - \omega_{eg}$ is the detuning. From this Hamiltonian, we find that the eigenenergies and the eigenstates are:

$$E_\pm = \frac{\hbar}{2}(-\delta \pm \sqrt{\delta^2 + |\Omega|^2}) \tag{4.10}$$

$$|+\rangle = cos(\theta)\,|g, N\rangle + sin(\theta)\,|e, N-1\rangle \tag{4.11}$$

$$|-\rangle = -sin(\theta)\,|g, N\rangle + cos(\theta)\,|e, N-1\rangle \tag{4.12}$$

where $cos(\theta) = \Omega/\zeta$, $sin(\theta) = (\Omega' - \delta)/\zeta$, $\Omega' = \sqrt{\delta^2 + |\Omega|^2}$, and $\zeta = \sqrt{(\Omega' - \delta)^2 + |\Omega|^2}$. The eigenenergies of this Hamiltonian are the energy of the $|+\rangle$ and $|-\rangle$ eigenstates. As shown in Fig. 4.2 (left), the eigenstate energy in the vicinity of the resonance is far away from the bare state energy ($|g, N\rangle$ and $|e, N-1\rangle$). This energy difference is the AC Zeeman energy shift and is given by:

$$E_{ACZ,\pm} = \pm\frac{\hbar}{2}(-|\delta| + \sqrt{\delta^2 + |\Omega|^2}) \tag{4.13}$$

This equation is shown in Fig. 4.2 (right). Similar to the DC Zeeman energy shift, the AC Zeeman energy shift is linear in the magnetic field on resonance ($\delta = 0$). Far off resonance ($|\delta| \gg |\Omega'|$) the shift is proportional to $|B_{AC}|^2$. The $|+\rangle$ state has a positive energy shift, and it is a "low-field seeker," while the $|-\rangle$ state has a negative energy shift, and it is a "high-field seeker."

Moreover, as shown in Fig. 4.2 (left), and eq. 4.11 and eq. 4.12, the fraction of the bare state in the eigenstate changes with detuning. If we sweep the driving frequency adiabatically, e.g. the detuning changes from far negative to far positive,

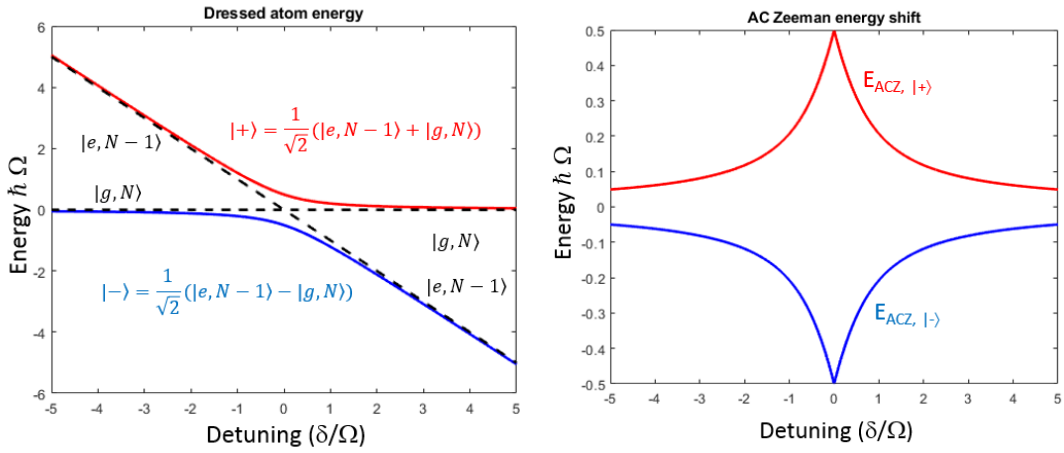

FIG. 4.2: Diagram of dressed atom energies and eigenenergies (left) based on eq. 4.10, and the AC Zeeman energy shift (right).

then the atom will follow the blue $|-\rangle$ line to transform the atom state from $|g\rangle$ into $|e\rangle$. In contrast, if we sweep the frequency adiabatically from high to low frequency, the atom will stay in the red $|+\rangle$ line and transform the atom from $|g\rangle$ into $|e\rangle$. This process is called an adiabatically rapid passage, which we abbreviate as "ARP". The ARP process is a very important tool in our atom interferometer experiment (Chapter 6) for manipulating and transferring spin states..

As shown in Fig. 4.2 (left), in the far-detuned limit ($|\delta| \gg |\Omega|$), the bare states ($|g\rangle$ and $|e\rangle$) can be identified with the dress state ($|+\rangle$ and $|-\rangle$). The AC energy shift in this case can be simplified to $E_{g,e} = \pm\frac{\hbar|\Omega|^2}{4\delta}$ (with "+" for $|g\rangle$ and "−" for $|e\rangle$).

4.2.1 AC polarization selection

Fig. 4.3(b) shows the transition polarizations. Due to the angular momentum selection rule and transition detuning, often only one polarization of the AC magnetic field provides a AC Zeeman energy shift to the $|F, m_F\rangle$ spin state. For example, the ^{87}Rb $F = 1$ and $F = 2$ hyperfine manifolds can be host intra-manifold hyperfine transitions ($\Delta F = 0$) with only $\sigma^{\pm}$ transition ($\Delta m_F = \pm 1$). Therefore,

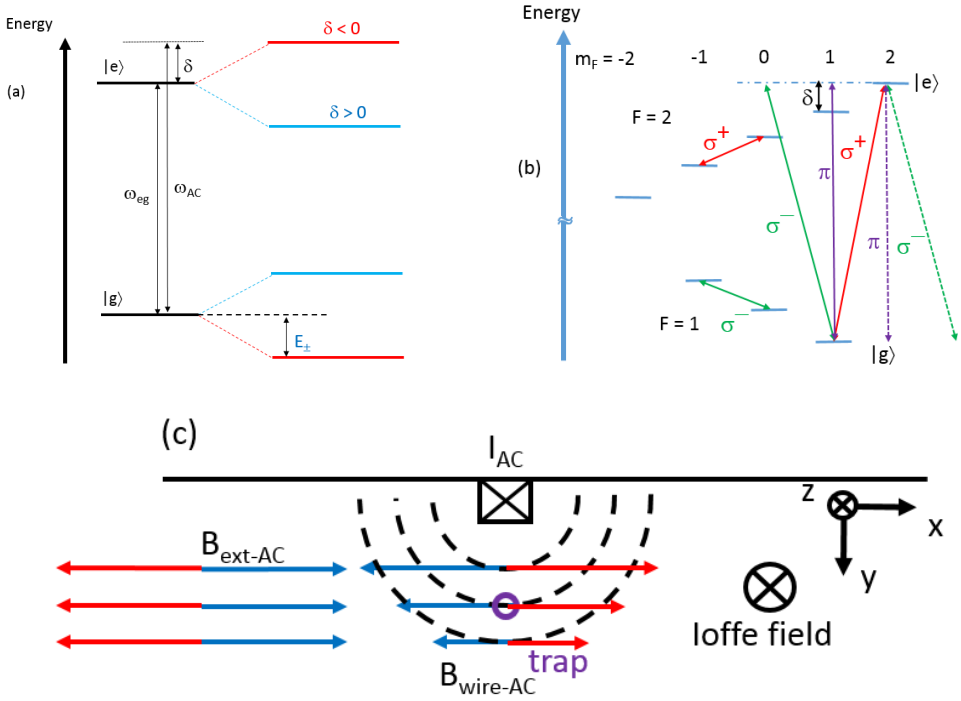

FIG. 4.3: Basic physics of an AC Zeeman chip trap. (a) AC Zeeman shift $E_{\pm}$ in a 2-level system with a near-resonant AC magnetic field. This figure is similar to Fig. 4.2 without the detuning information. This figure is in a similar format to a well-used AC Stark energy shift diagram. The AC Zeeman energy shift is similar to the DC Zeeman energy shift but only affects the near resonance transition states with the energy shifting direction controlled by the detuning. (b) The AC Zeeman transition polarization selection. We use an alkali atom with F = 1 and F = 2 as an example. Each transition is driven by one of the three different types of polarization (σ^+, σ^-, π). Once the driving frequency is near resonance to a transition, this driving frequency will be far detuned from other transitions. (c) The AC Zeeman trap is formed in a similar manner to the DC Zeeman trap. The AC magnetic field $B_{wire-AC}$ is generated by the AC current I_{AC}, which is canceled at the trap location by an external in-sync opposite direction uniform magnetic field B_{ext-AC}. The Ioffe field B_{Ioffe} is a DC magnetic field that provides a DC Zeeman shift to separate the hyperfine states. Figure adapted from reference [69].

only the left-circularity or right-circularity polarized component of the MHz-level driving magnetic field can affect the intra-manifold hyperfine transition. The inter-manifold transitions ($\Delta F = \pm 1$ at 6.8 GHz), with a moderate DC magnetic field, can use σ^+, σ^-, or π polarized microwave fields to drive transitions. For example, the $|e\rangle = |F = 2, m_F = 2\rangle$ state can only affected by the σ^+ transition connected with the $|g\rangle = |F = 1, m_F = 1\rangle$ state. However, $|g\rangle = |F = 1, m_F = 1\rangle$ state, can be affected by three different polarizations: σ^+ transition for $|e\rangle = |2, 2\rangle$, π transition for $|e\rangle = |2, 1\rangle$, and σ^- transition for $|e\rangle = |2, 0\rangle$. However, the three different transitions have different transition frequencies, and once the AC magnetic field is near resonance to one of the transition, the other two are sufficiently off-resonance. Therefore, the inter-manifold transitions are effective 2-level system over a narrow range of driving frequencies or a purely polarized driving field.

4.2.2 AC Zeeman trapping scheme

The AC Zeeman trapping scheme is similar to the DC Zeeman trapping scheme. As shown in Fig. 4.3 (c), the AC Zeeman trap is formed by the chip AC current magnetic field $B_{wire-AC}$, the external uniform AC magnetic field B_{ext-AC} and a DC magnetic field B_{Ioffe}. The AC magnetic near field $B_{wire-AC}$ is in-sync with, but in the opposite direction of B_{ext-AC}, which results in a magnetic minimum point (trap), where the two fields cancel each other. The trap distance from the wire is $h = \dfrac{\mu_0 I_{AC}}{2\pi B_{ext-AC}}$, if we assume the wire is an infinite thin wire. In practice, the external uniform field B_{ext-AC} can actually be provided by additional chip wires parallel to the central one shown in Fig. 4.3 (c). The DC Ioffe field B_{Ioffe} is used to separate the hyperfine spin-state energies and provide a convenient quantization axis. Notably, in this arrangement, the $B_{wire-AC}$ and B_{ext-AC} fields can only drive $\sigma^{\pm}$ transitions.

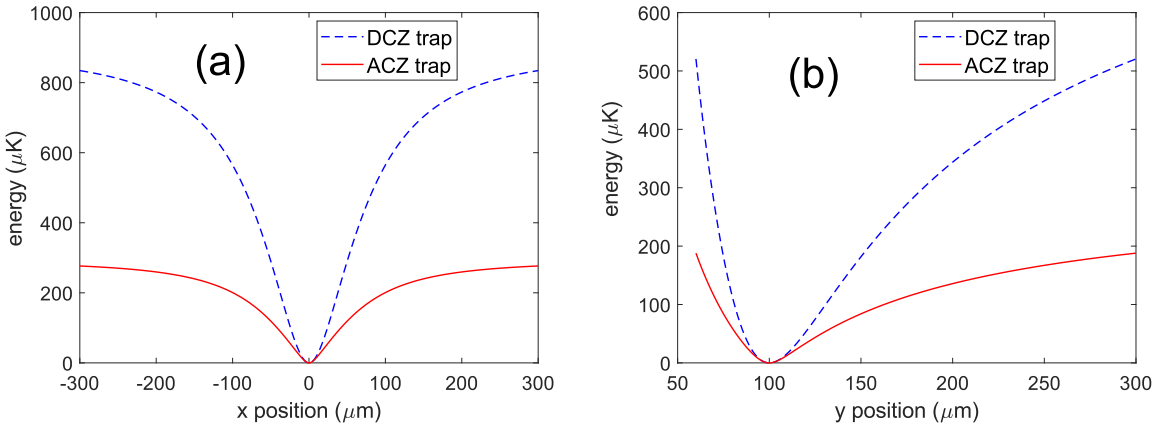

FIG. 4.4: Comparison of similar AC Zeeman and DC Zeeman chip traps. Both trap have the same harmonic trapping frequency $\omega_{trap} = 2\pi\times$ 1 kHz for ^{87}Rb and are located at the same trap position, which is $h = 100$ μm away from the wire. In order to match the AC Zeeman and DC Zeeman trap frequencies, the two traps have different settings for the current and external magnetic field. The DC Zeeman trap has $I_{DC} = 0.8796$ A, $B_{ext} = 17.592$ G, and $B_{Ioffe} = 5$ G. For convenience, we subtract the energy offset caused by B_{Ioffe}, and set the energy at the trap bottom to be 0. The AC Zeeman trap operates on the ^{87}Rb $|2,2\rangle \leftrightarrow |1,1\rangle$ transition (around 6.8 GHz), and uses $I_{AC} = 0.543$ A ($I_{AC-rms} = 0.384$ A), $B_{ext-AC} = 10.86$ G, detuning $\delta = 2\pi\times$ 1 MHz and $B_{Ioffe} = 5$ G. These trap settings are also used for all the traps in Chapter 5. (a) Trapping potentials versus x for $y = 100$ μm. (b) Trapping potentials versus y for $x = 0$ μm. Figure from reference [69].

As long as the trap distance h is much smaller than the wavelength $\lambda_{AC} = \frac{2\pi c}{\omega_{AC}}$ (c is the speed of light), then $B_{wire-AC}$ can be treated as a near field and is identical to the DC near field but with a time oscillating term $B_{wire-AC} = B_{wire}e^{i\omega_{AC}t}$. In this case, the magnetic maximum is again impossible by Earnshaw's theorem, and hence the AC Zeeman trap can only be a magnetic minimum (for low field seekers).

In this AC Zeeman trap scheme, the AC magnetic field at the trap bottom $B_{Bottom-AC} = 0$, and hence $\Omega = 0$. Therefore, the atom is in the far-detuned limit ($|\delta| \gg |\Omega|$) at the trap bottom. If we set $|\delta| = |\Omega|$ in eq. 4.13, we can see that the trapped atom is in the far detune limit as long as the temperature is much less than $T \simeq 0.21\hbar|\delta|$. For example, the detuning of $|\delta| = 2\pi\times1$ MHz requires atoms with temperature lower than $T \simeq 10$ μK for the far-detuned limit, and thus the $|+\rangle$ eigenstate is primarily in one of the $|F, m_F\rangle$ spin states.

Both DC Zeeman and AC Zeeman trap produce harmonic potentials at the bottom of the trap. Fig. 4.4 shows similar DC Zeeman and AC Zeeman traps: both traps have the same trap position ($h = 100$ μm) and the same trap frequency ($\omega_{trap} = 2\pi \times 1$ kHz) for ^{87}Rb. The two energy curves for the DC Zeeman and AC Zeeman trap looks different and have significantly different trap depths, but at the trap bottom they are identical. We will use these two traps extensively in chapter 5 for comparisons of AC and DC Zeeman trap roughness.

The endcaps for the AC Zeeman trap can provide some axial confinement, it is smaller than the DC Zeeman trap, since the atoms are insensitive to the π polarized field generated by the endcaps. An alternative method is to use a standing wave or microwave lattice. We can direct two microwaves at each other at the same frequency from both ends of the wire to generate a standing wave in the middle to provide the axial confinement. If these additional microwaves are at a different detuning from the primary trapping microwave frequency, then the two microwave

fields will provide independent trapping. Moreover, the phase of the standing wave can be used to control the longitudinal position of the trap.

CHAPTER 5

AC potential roughness

5.1 Introduction

This chapter discusses the theoretical and computational research on the suppression of magnetic roughness due to the imperfection of atom chip wire in AC Zeeman traps, in comparison with their DC Zeeman counterparts. This chapter is based on the draft of a paper that I am writing, which will be submitted to Physical Review A [69].

Atom chips have several advantages for cold atom experiment: 1) small in size, 2) low power, 3) able to integrate multiple function wires on the same atom chip, 4) the ability sculpt complex near field potentials. These advantages make the atom chip a good candidate for providing magnetic fields, electric fields, RF fields, and optical fields [70]. Furthermore, the photolithography can be used to fabricate atom chips with complicated wire layouts.

A number of research groups have used atom chips to generate the Bose-Einstein condensates (BEC) [71], degenerate Fermi gases (DFG) [45], 1D gases [72], as well as to build atom interferometers [6, 51, 73]. Atom chips have also used to study

atom-surface interactions [74]. Moreover, some commercial cold atom apparatus are based on atom chips, e.g. ColdQuanta, Kelvin Nanotechnology. Finally, The cold atom apparatus on the International Space Station [75].

Even though atom chips have multiple advantages, they have not been widely adopted by the AMO community. One of the main reason is imperfections in an atom chip's wires result in magnetic field roughness, which will be substantial for a magnetic trap with an ultracold atom cloud (especially a BEC) close to the chip wire [76]. Evaporative deposition improves the atom chip wire quality and reduces the imperfections [77], but there are still some imperfections that remain, such as small conductivity variations that result in magnetic roughness albeit reduced. The atom chip in our group also has some magnetic roughness, which is observed even at an atom-wire distance of 100 μm for a 1 A level current [66]. Research shows that kHz-scale AC fields and currents can be used to suppress this roughness by generating a smoother time averaged trapping potential, though this approach requires a more complicated apparatus [78].

Currently, most atom chips use the DC Zeeman effect for trapping. However, the AC Zeeman effect is also suitable for atom chip-based traps [54]. The AC Zeeman effect uses RF or microwave magnetic fields to drive hyperfine transitions to generate a spin-specific energy shift [49, 50] (see Chapter 4). At present, RF and microwave near fields have been used to manipulate and trap atoms with the AC Zeeman effect [51, 53, 54].

This chapter presents theoretical research that shows that AC Zeeman traps should substantially suppress potential roughness due to imperfections in a current carrying wire, as compared to similar DC Zeeman traps generated by the same wire. The sources of this suppression are: 1) the physics of the AC Zeeman effect, such as its magnetic polarization dependence, and 2) the AC skin effect, i.e. AC currents hug the edges of wires.

This roughness research builds on the work of Dr. Austin Ziltz in his thesis [56], which uses calculations based on a toy model with non-realistic parameters, i.e. proof-of-principal research. In contrast, the research in this chapter is fully numeric with realistic parameters. We also extend our research to include trap position roughness, trap frequency roughness, and roughness in a microstrip transmission line. This microwave transmission line is a potential building block for our future atom chip, and is suitable for driving a high-frequency AC current. We use FEKO, a commercial electromagnetic simulation software to build a microstrip model with two different types of imperfections to research the resulting magnetic and current roughness.

This chapter explains the physics of the AC Zeeman roughness suppression in section 5.2. Next, section 5.3 presents numerical results on roughness suppression based on a thin wire toy model. Finally, section 5.4 describes how the AC skin effect can suppress or worsen roughness in a microstrip transmission line.

5.2 AC Zeeman roughness suppression

We consider two types of wire trace imperfection: 1) a local variation in wire conductivity (conductivity patch), and 2) a indent or a bump in the side of the wire (Fig. 5.1(a)). These two types of imperfection can cause a small deviation in the current path. The DC Zeeman trap potential roughness comes from such current deviations, and the manufacturing improvements with evaporation deposition have reduced these imperfections and reduced the magnetic roughness. However, even with these improvements, a conductivity patch can still cause the current deviate on the order of 0.1 mrad over a distance of 100 μm [79]. The main source of current deviations is conductivity patches, and these deviations are much larger than those that caused by the edge defects, due to the size of the imperfections.

Tabel 5.1 shows the current deviation parameters and wire defect parameters from atom chips manufactured by evaporation deposition. Fig. 5.2 shows a scanning electron microscope (SEM) image of our atom chips. This broken atom chip snapped in the middle of the AlN substrate, but the wires are still representative of traces manufactured by evaporation deposition. In this SEM picture, the bottom left is the chip wire trace (Ag with Au coating), and we can see the grain-like microstructure. The gain size in Fig. 5.2 is about 100 μm, which is comparable with the size reported in Table 5.1. We note that the conductivity patches are not identified with grains and are typically larger. Conductivity patches can also be identified with slightly thicker or thinner portions of a trace.

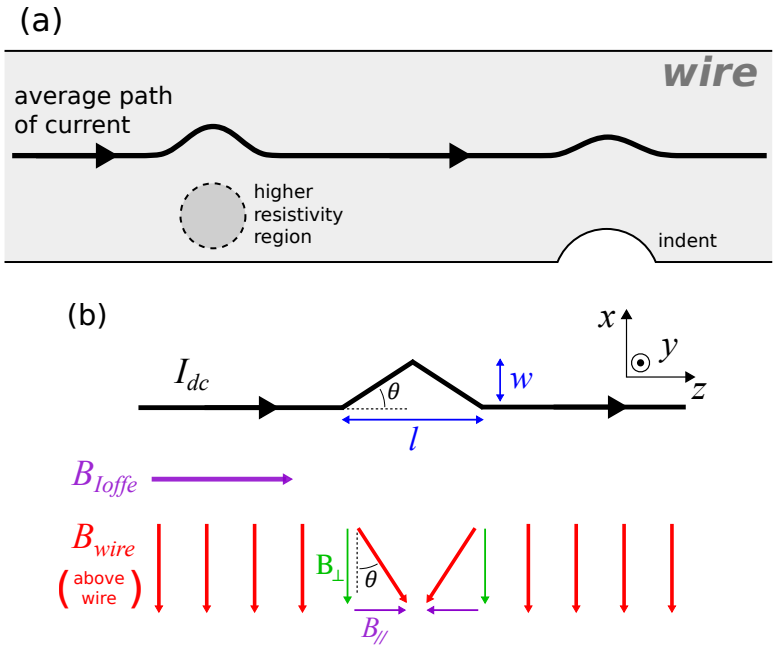

FIG. 5.1: Average path of the current with wire imperfections. (a) Diagram for the average path of the current deviation due to the two types of imperfection: conductivity patch and the indent edge defect (bump is similar). (b) 1D current deviation model and the corresponding magnetic field. We integrate the two different types of imperfection into the same DC current deviation model: a straight current has a "bump" deviation with an angle θ, amplitude w and a length l. For simplicity, we use a "bump" with a triangular shape. The straight current generates a magnetic field B_{wire} (red), which is perpendicular to the current. However the current in the "bump" generate a magnetic field with a parallel component ($B_{//}$), which is thus parallel to the Ioffe field direction (B_{Ioffe}, purple). In the case of an AC current I_{AC}, all of the magnetic field are AC except B_{Ioffe}.

Defect Parameter	Average Value	Range
grain size	90 nm	30-70 nm [79, 80] 100 nm [81], < 100 nm [76] 70 nm [82]
edge defect	100 nm	< 100 nm [81], 100 nm [83]
bump angle θ	0.1 mrad	0.04-0.16 mrad rms [79] 0.1-0.4 mrad pk-pk [79] < 0.1 mrad [76]
bump length l	100 μm	10-50, 79, 90, 300 μm [79]

TABLE 5.1: Table of experimental current deviation parameters and wire defect parameters for atom chips manufactured by evaporation deposition.

As shown in Fig. 5.1(b), a current deviation bump with an angle θ from the original current propagation direction $\hat{z}$, generates a magnetic field B_{wire} with longitudinal component $B_{/\!/} = B_{wire} \sin\theta\hat{z}$. This longitudinal component $B_{/\!/}$ adds linearly to the Ioffe field B_{Ioffe}. In the small angle limit ($\sin(\theta) \approx \theta$), the current deviations longitudinal component is $B_{wire}\theta$. In contrast, the current deviation reduces the magnetic field in the x-axis direction by only a small amounts $B_{wire}\theta^2/2$ in small angle limit.

For the DC Zeeman trapping potential shown in Fig. 4.4, we apply a 0.1 mrad current deviation with length $l = 100$ μm to generate a potential bump and valley around sub-100 nK in amplitude, as shown Fig. 5.3 (a) blue curve, which is around the BEC transition. The blue curve shows the potential energy along the trace (z-axis) at the designed trap position (i.e. the trap position without current deviation). The trap parameters are the same as in Fig. 4.4. In Fig. 5.1(b), we

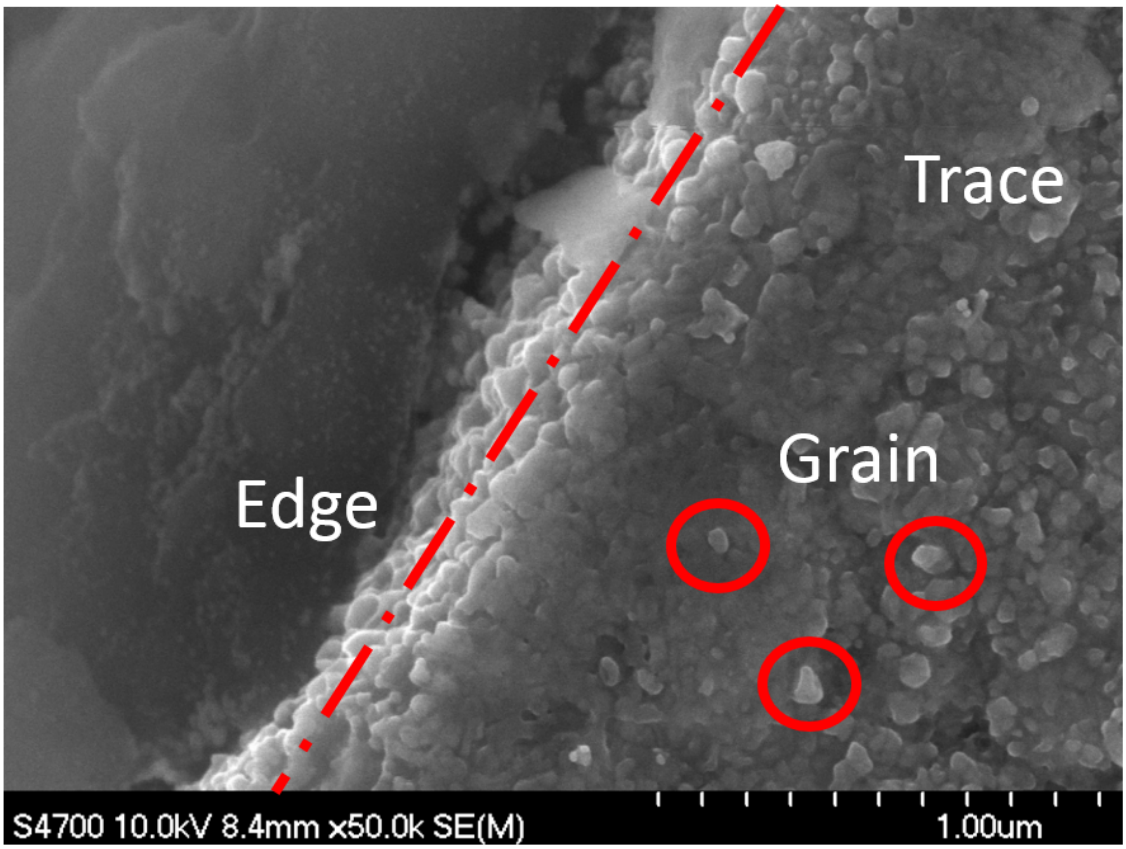

FIG. 5.2: SEM picture for a broken atom chip in our group. The left bottom side is the wire, AlN substrate supporting Ag traces with thin Au layer. On the wire there are a lot of grain-like microstructure, and this microstructure caused the bumpiness on the side. The grain size in this picture is comparable to that listed in Table 5.1, This chip has 50 μm wide Ag traces (4 μm thick) in the central section of the chip. In the legend, neighboring tick marks are separate by 100 μm.

shows the roughness with a bigger current deviation ($\theta = 0.1$ rad and $l = 100$ μm). The positive and negative angles of the current deviation generate a bump and valley pair in the DC Zeeman magnetic trapping potential.

For the AC Zeeman trapping potential, the magnetic roughness longitudial component $B_{/\!/} \simeq B_{wire,AC}\theta\hat{z}$ can only drive a π transition, which follows the angular momentum selection rule $\Delta m_F = 0$. If we operate on $\sigma^{\pm}$ transitions, which is the case for our AC Zeeman trap design, then the π transition will be far off-resonance and will not contribute to the AC Zeeman trapping potential. Furthermore, the trapped atomic state might not have π transition available, e.g. the $|e\rangle$ level in

Fig. 4.3 (b), and so the longitudinal component of the AC magnetic field cannot contribute to the AC trapping potential.

Furthermore, in the case of an AC Zeeman trap based on intra-manifold hyperfine transitions (RF), there are no π transitions that can be driven by spurious $B_{/\!/}$ components.

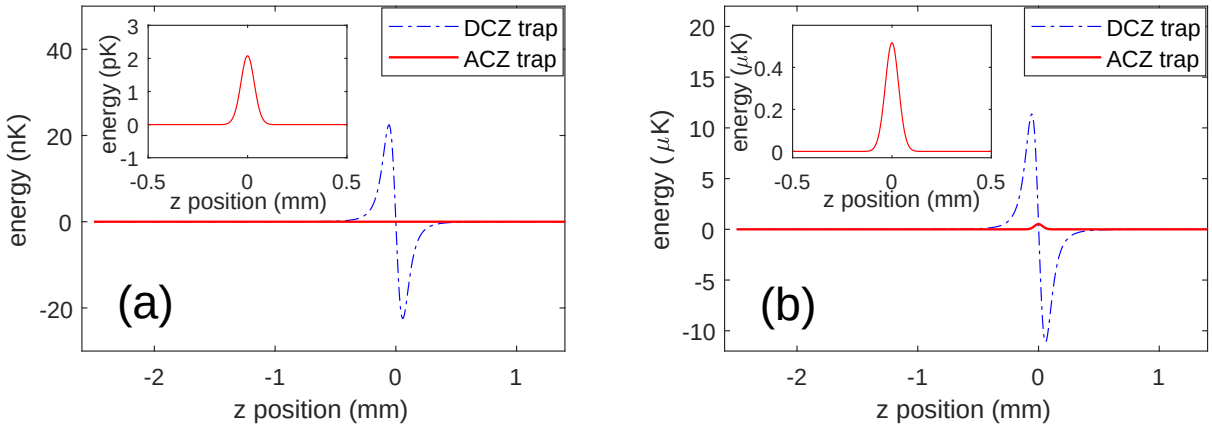

FIG. 5.3: Trapping potential roughness at the designed trap location due to a single defect. (a) DC Zeeman and AC Zeeman trapping potential roughness for a small current distortion, which has $w = 5$ nm, $l = 100$ μm with distortion angle at 0.1 mrad. This model uses parameters based on Table 5.1. (b) DC Zeeman and AC Zeeman trapping potential roughness for a large current distortion, which has $w = 2.5$ μm, $l = 100$ μm with distortion angle at 0.1 rad. The AC Zeeman trap has much smaller roughness than the equivalent DC Zeeman trap. *Blue: DC Zeeman trap. Red: AC Zeeman trap.*

5.3 1D wire model

We use a 1D wire toy model to simulate the roughness in the AC and DC trapping potentials for both single defects and multiple defects. This model will ignore all the details about the wire trace (or microstrip transmission line) and only focus on the relation between the current deviation and the trapping potential roughness. In order to compare AC Zeeman and DC Zeeman traps, we use the traps in Fig. 4.4, which have the same height and the same radial trap frequency (but different trap depth).

As shown in Fig. 5.1 (b), we assume that the current deviation has a triangular shape in the plane of the trace (chip) for simplicity. This simple shape allows us to use the Biot-Savart law for a finite segment wire to calculate the magnetic field. For a segment starting from position (a, b, c) with length L and with an angle θ to the z-axis in the z-x plane (wire is along x-axis for $\theta = 0$), the magnetic field that this segment generates at (x, y, z) is given by the equation:

$$\begin{aligned}\overrightarrow{\mathrm{B}}(x, y, z) = \frac{\mu_0 I}{4\pi} \frac{1}{y_0^2 + x_0^2} (x_0 \hat{y} - y_0 \cos(\theta)\hat{x} + y_0 \sin(\theta)\hat{z}) \\ \times \left(\frac{z_0}{\sqrt{z_0^2 + x_0^2 + y_0^2}} + \frac{L - z_0}{\sqrt{(L - z_0)^2 + x_0^2 + y_0^2}}\right)\end{aligned} \tag{5.1}$$

where we have used the variable x_0, y_0, z_0, which have the following definitions:

$$z_0 = (z - c)\cos(\theta) + (x - a)\sin(\theta) \tag{5.2}$$

$$x_0 = -(z - c)\sin(\theta) + (x - a)\cos(\theta) \tag{5.3}$$

$$y_0 = y - b \tag{5.4}$$

In order to make the model imitate the current deviation reported in Table 5.1, the length of the current deviation is set at l set a $l = 100$ μm, and the deviation angle is set a $\theta = 0.1$ mrad, which corresponds to bump width of $w = 5$ nm. We use these parameters for our standard single defect model.

In addition to studying the single current deviation model, we are also interested in the roughness for multiple such current deviations. The research model for multiple current deviations, which we call the multiple defect model, is shown in Fig. 5.6 (a). Each current deviation has the same parameters as a single defect model, and we place all the defects next to each other without any separation. All the defect stays in the same plane perpendicular to the trap height direction (z direction), and each defect has the opposite direction to the one next to it.

5.3.1 Single defect

The numerical simulation results of the trapping potential deviation for a single defect located at $z = 0$ are shown at in Fig. 5.3. The plots show the trapping potential deviation (AC Zeeman and DC Zeeman) roughness, which is the difference in the trapping potential between the single defect model and the no defect model (i.e. an infinitely long straight current that has no deviation). The trapping potential deviation is calculated at the intended trap position, at $y = 100$ μm above the current wire and perpendicular to the plane where the current deviation is located.

The simulation shows that the AC Zeeman trap has much better performance than the DC Zeeman trap and suppresses the potential roughness. The simulation in Fig. 5.3 (a) is for a current defect with angle $\theta = 0.1$ mrad and length $l = 100$ μm, which follows Table 5.1. The magnetic roughness of the DC Zeeman trap has a peak around 20 nK in amplitude, while the AC Zeeman trap has only 2 pK amplitude peak. The roughness on the AC Zeeman trap is around 10^4 times smaller than the DC Zeeman trap. Fig. 5.3 (b) shows the deviation for the trapping potential with current defect angle $\theta = 0.1$ rad, which is much bigger than the current defect angle in (a). In this model, the potential roughness for the DC Zeeman trap has a peak around 12 μK, while the AC Zeeman trap only has a peak of 0.5 μK. AC Zeeman trap still has a better performance than the DC Zeeman trap, but with a bigger defect size, the roughness suppression only a factor better. Finally, the shape of the AC Zeeman roughness is qualitatively different from the DC Zeeman roughness: The AC Zeeman trapping potential deviation is only positive and has even symmetry. The DC Zeeman potential deviation is bipolar and has odd symmetry (it always has a zero crossing).

We also research how the trap minimum in the x-y plane shifts with the current deviation. As shown in Fig. 5.4, the trap minimum for the AC Zeeman trap only

shifts along the x-axis, the same as the current deviation direction. Similarly, the DC Zeeman trap minimum is also shifted along the x-axis by the same amount as the AC Zeeman trap. However, the DC Zeeman trap minimum is also shifted along the y-axis to produce a spiral-like shape in the x-y plane.

Moreover, we have trapping potential at each minimum point (see inset plot of Fig. 5.4). These two potential energy curve are the raw potential energy without subtracting the potential energy for the no defect case. The plot shows that the potential energy at the minimum for the distorted AC Zeeman trap remains at zero. In contrast, the trapping potential at bottom of the distorted DC Zeeman trap varies significantly. In the case of a BEC, we expect the AC Zeeman trap will have a similar shape as the original trap but a small dimple that mimics the current defect. In contrast, the DC Zeeman trap will change its shape into a spiral, and the atom cloud in it will not keep a uniform density due to the variations of trapping potential minimum.

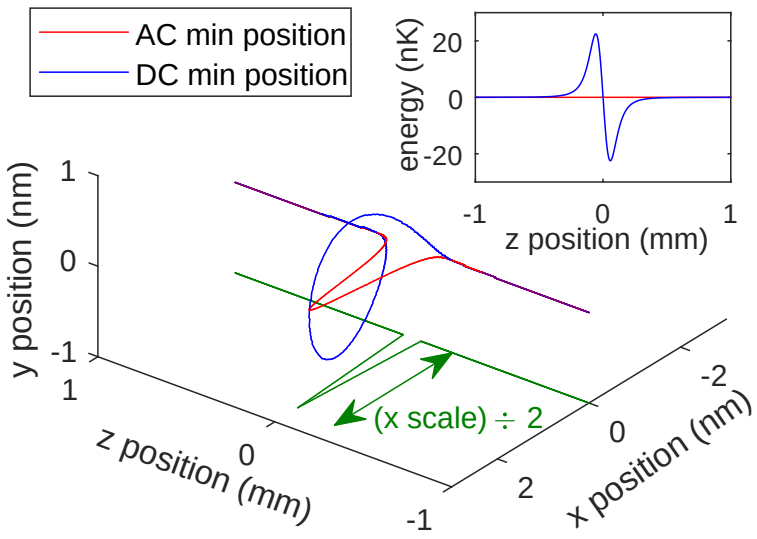

FIG. 5.4: Trap location shift (energy minimum point for each x-y plane) in 3D due to a single defect. This plot uses the same defect model as Fig. 5.3 (a), w = 5 nm, l = 100 μm. *Blue: DC Zeeman trap. Red: AC Zeeman trap. Green: current path, which located at y = -100 μm position, and the scale of the x-axis shrunk by 2 for illustrative purposes*

Finally, we look at the change in trap frequency included by the current deviation. Figure 5.5 shows the trap frequency deviation with the single defect model, i.e. transverse trap frequency with defect minus trap frequency without defect. Both the AC Zeeman and DC Zeeman trap have more trap frequency deviation in the x-direction than the y-direction. The trap frequency deviation in the AC Zeeman trap is at the 10^{-5} Hz level with a quadratic like shape, while the DC Zeeman trap frequency deviation is at the 10^{-2} Hz level with a more complicated bipolar shape.

The trapping potential roughness for the DC Zeeman trap are oddly symmetric along the z-axis, centered on the defect, which means the trapping potential deviation is always bipolar and always has a zero crossing. In contrast, the AC Zeeman potential deviation is always positive and has even symmetry along the z-axis (centered on defect).

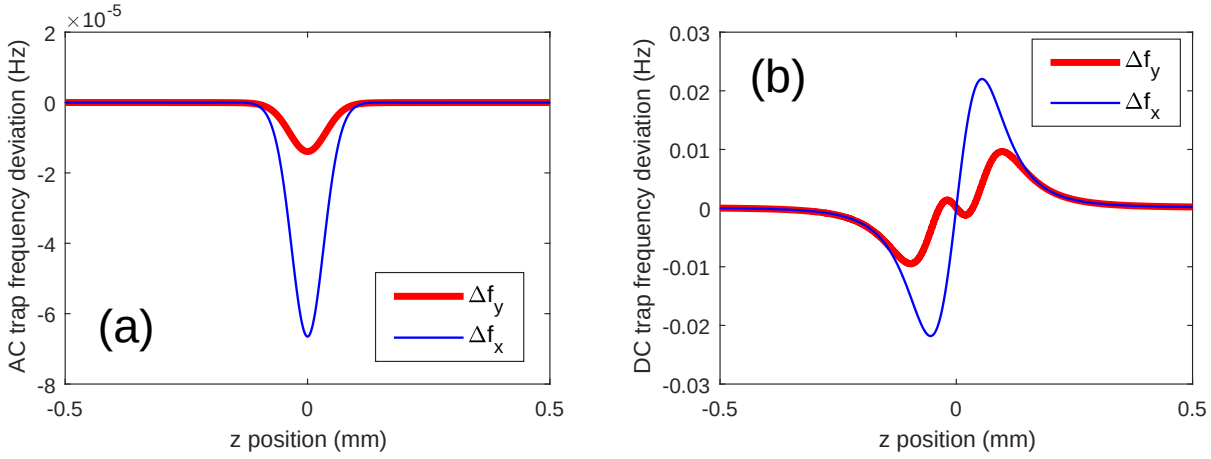

FIG. 5.5: Trap frequency deviation due to a single defect. The trap frequency deviation is $\Delta f = (\omega_{defect} - \omega_{original})/2\pi$. The defect parameters are the same as in Fig. 5.3 (a). The trap frequency deviation is strongest in the transverse x direction. The trap frequency deviation for the AC Zeeman case is around 500 times smaller than the DC Zeeman case.

5.3.2 Multiple defects

Since the potential roughness shown in Fig. 5.3 spans the z-axis for a few hundred microns, which is wider than the defect length $l = 100$ μm, there is a strong possibility that the potential roughness is affected by neighboring defects. In order to investigate this possibility, we set up a multiple defect model by concatenating 50 single defects one next to the other without separation and with alternating defect directions, as shown in Fig. 5.6 (a). Each of the defects has the same parameters as in Fig. 5.3 (a).

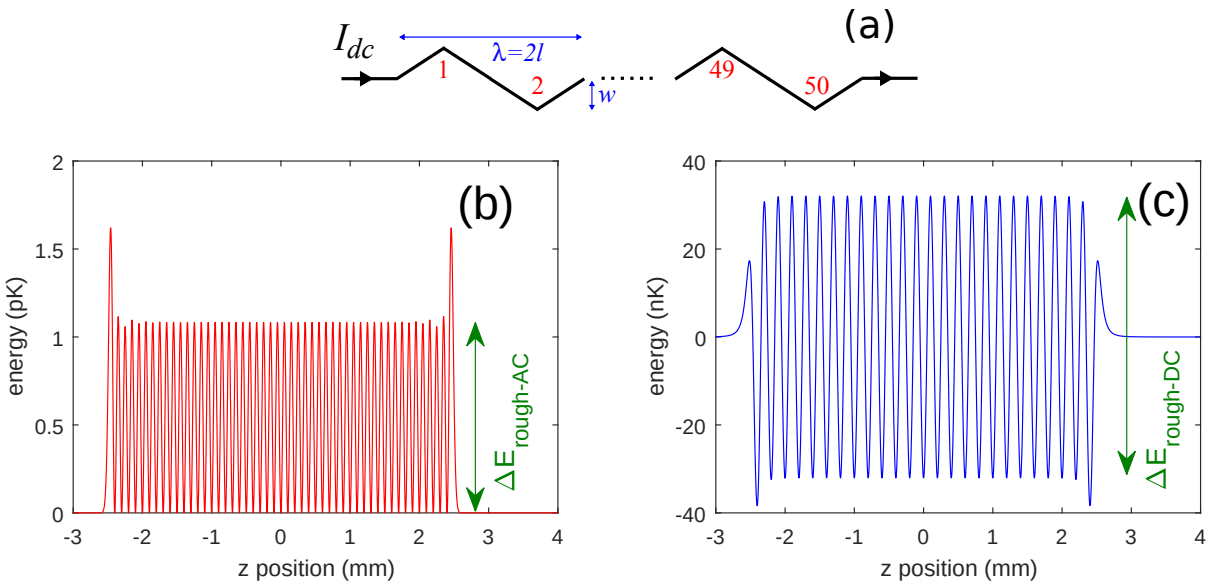

FIG. 5.6: Trap potential roughness due to multiple (50) defects at the original trap location. The parameter for each defect follows Fig. 5.3 (a). The defects are arranged in a chain with alternative bump directions with no space between them. The potential roughness for the AC Zeeman case (b) is 3×10^4 time smaller than DC Zeeman case (c). *Blue: DC Zeeman trap. Red: AC Zeeman trap.*

Figures 5.6 (b) and (c) shows the multiple defects model simulation results for both the AC Zeeman and DC Zeeman trapping potentials. As expected from the single defect simulations, the AC Zeeman trap suppresses the roughness more than the DC Zeeman trap. The AC Zeeman trap potential roughness also has 50 peaks, the same number as the current, but each peak has only around half of the amplitude

of the single defect case ignoring the end peaks: neighboring defects are suppressing each others. In the DC Zeeman case, each defect generates a peak and a valley in the trapping potential according to the sign of the defect angle. Two neighboring defects will share a single long wire segment (length = l) with a given angle ($\pm\theta$) which results in a higher potential deviation peak and a neighboring lower potential deviation valley.

To quantify the advantage of the AC Zeeman trap versus the DC Zeeman trap in suppressing potential roughness, we define a new variable called the "Suppression factor":

$$\text{Suppression factor} = \frac{\Delta E_{rough-DC}}{\Delta E_{rough-AC}} \tag{5.5}$$

Since we will trap the atom at the middle of the trace, we only need to focus on the amplitude at the center (i.e. we ignore the behavior of the two ends of defect chain). $\Delta E_{rough-AC}$ and $\Delta E_{rough-DC}$ are the amplitudes of the potential roughness.

We run sets of simulations to study how the suppression factor changes with the trap height h (the distance from atom chip to trap position) and the current deviation length l (we keep the current deviation width $w = 5$ nm constant). We have two sets of models in this part, single defect model and multiple defect model. The multiple defect model has 500 bumps to avoid the effect of roughness at the edge. Notably, we keep the AC Zeeman and DC Zeeman trap frequency the same, even as h is varied ($\omega_{AC,trap} = \omega_{DC,trap} = 2\pi \times 1$ kHz).

The plot in Fig. 5.7 (a) shows the suppression factor as a function of trap height h, while in Fig. 5.7 (b) is the plot shows the relation between the suppression factor and current deviation length l for various trap heights. In these simulations, the width w of the defect is kept at $w = 5$ nm, and since the bump length l is much longer than w, the deviation angle θ remains very small (in the small-angle limit $\theta = 2w/l$). Figure 5.7 (a) shows that the suppression factor will increase with the

trap heights. The trap potential roughness decreases with increasing trap height for both the AC Zeeman trap and DC Zeeman trap cases, but the roughness in the AC Zeeman trap decreases faster than for the DC Zeeman trap. Also, the multiple defect case has a higher suppression factor than a single defect case: This advantage increases for higher trap heights. The multiple bump case has a similar suppression factor for small trap heights, but at a trap height of 100 μm, the suppression factor for the single defect case is around 10^4, while in the multiple defect case it is 5 times larger.

Figure 5.7 (b) shows that the suppression factor decreases as the current bump length increases. This plot also shows that the suppression factor for multiple defect cases is better than a single defect case, which means the multiple defects will further suppress the potential roughness in an AC Zeeman trap. The suppression factor is largest (10^8 level) for short bump lengths and large heights, and it is smalled for long bump length and small heights. Suppose we convert the x-axis from bump length l into $1/l$, it will shows a linear relation for a single defect case, which means the suppression factor is reciprocal to the bump length (Suppression Factor $\propto 1/l$) for single defect case.

5.4 Role of the AC skin effect

The previous section discusses the performance of the AC Zeeman and DC Zeeman potential roughness for a same current deviation. However, the AC and DC currents have very different current distributions within a wire trace due primary to the AC skin effect: In a alternating current (AC) the current hugs the inner edge of the wire. Furthermore, this effect gets stronger as the frequency increases. Figure 5.8 (a) shows the AC skin effect in a microstrip transmission line trace. The skin depth is given by $\delta = \sqrt{\frac{2}{\sigma\mu\omega}}$, where σ is the conductivity of the wire conductor, μ

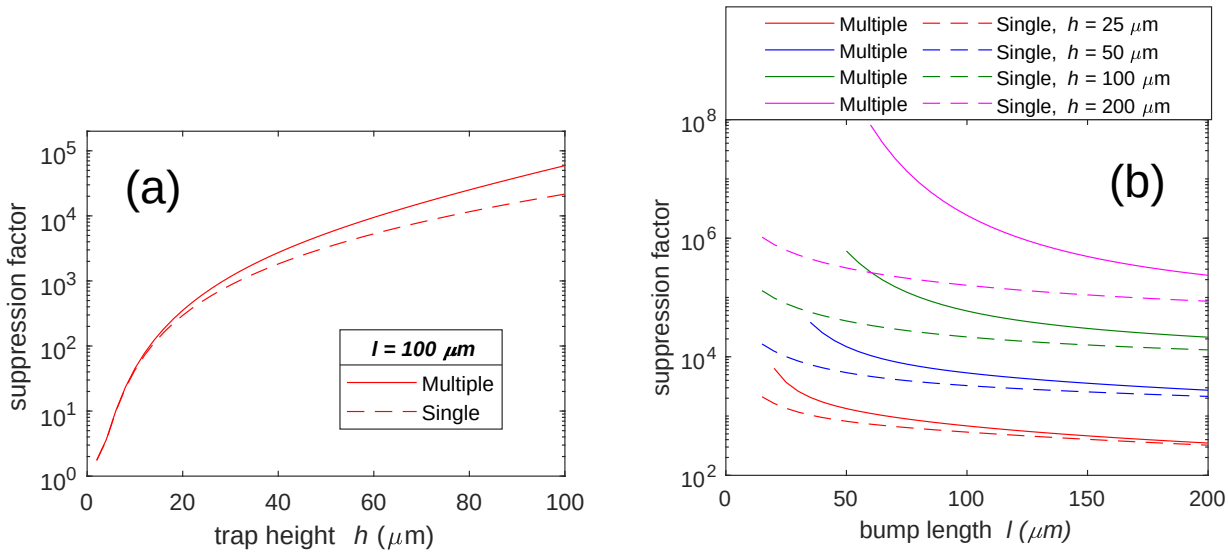

FIG. 5.7: The suppression factor relation with trap height h and bump length l. These simulations use 500 bumps to supress edge effects. (a) Suppression factor as a function of trap height. (b) Suppression factor as a function of l for different trap heights h.

is its magnetic permeability, and ω is the frequency of the AC current in radius/s.

In section 5.2, we introduced the two main types of imperfections in atom chip wire traces: the conductivity patch and the edge defect. These two types of imperfection have different impacts on the AC Zeeman trap and the DC Zeeman trap. A DC current tends to flow uniformly throughout the wire, and the effect of the two imperfection will mainly depend on the size and the conductivity differences of the imperfection. However, for an AC current the case is more complicated, since the position of the conductivity patch will matter: a conductivity patch in the middle of a microstrip trace has a limited effect due to the low current density there, while the conductivity patch on the edge of trace will result in a competition between the conductivity change and the skin effect.

In order to research the role of AC skin effect on this roughness problem, we will use FEKO, an electromagnetic simulation software, to build a microstrip trace model with different types of imperfections. The microstrip is the fundamental

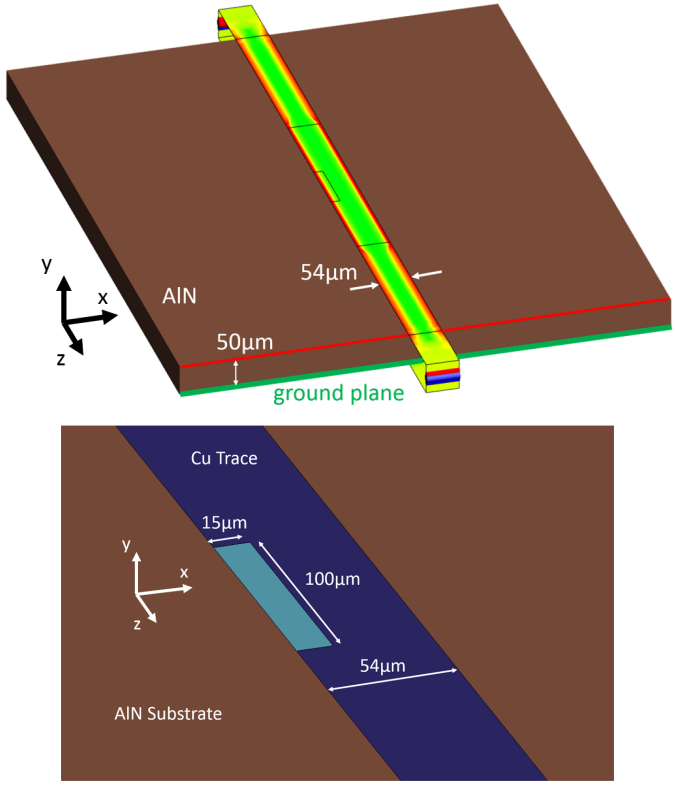

FIG. 5.8: FEKO conductivity patch model. Top: microstrip transmission line design and current distribution. The microstrip consists of a 50 μm thick aluminum nitride substrate ($\epsilon = 8.9$) with copper ground plane and 54 μm wide copper trace. The microstrip has an impedance of 50 Ω. The current density in the trace shows the current hugging the trace edges due to the AC skin effect. The rectangle in the middle of the trace is the conductivity patch. Bottom: Close view of conductivity patch. The length of the conductivity patch is 100 μm with a width of 15 μm.

element of our microwave atom chip. A microstrip is a simple type of transmission line that can carry current up to GHz level and generates an AC magnetic near field that can be used to trap atoms.

We use the FEKO simulations to model the current deviation and magnetic roughness for AC and DC currents. Unfortunately, FEKO cannot use true DC currents, so we have to set the frequency at 1 MHz, which does not have a noticeable skin effect: when we refer to DC performance in this section, we are really referring to performance in the low frequency limit. The results in this section are not really of the form AC Zeeman vs DC Zeeman, but instead show a continuum of behavior as

the frequency of the current is varied. Therefore in this section, we do not compute the trapping potential, but instead study the roughness in the magnetic field as a function of frequency.

The FEKO microstrip model shown in Fig. 5.8 (a) has a 1 mm long trace and 5 μm thick copper trace ($\sigma = 5.813 \times 10^7$ $(\Omega\ \mathrm{m})^{-1}$) on a 1 mm $\times$ 0.8 mm $\times$ 50 μm AlN substrate ($\epsilon = 8.9$ and dielectric loss tangent = 0.0005). There is a copper ground plane with the same thickness as the trace on the other side of the substrate, covering the entire substrate surface. To set up the voltage source, load, and connect the trace and ground plane, we set up a 0.1 mm long feed line elongated from the end of the trace, and the FEKO "edge port" has been set in the middle of this perpendicular connection to the ground plane. We set the voltage source on one side of the "edge port" to 1V with a 50 Ω source impedance, and the load is set on the other side to 50 Ω. The setting of 50 Ω is to match the standard impedance used in the RF system in our lab. The width of the microstrip trace is 54 μm to match the 50 Ω requirement. To reduce the simulation burden, we set different mesh sizes for different parts of the microstrip. The middle part, which includes our imperfection models has the finest mesh, and both sides of the microstrip trace have a medium mesh size, and others sections, such as feedline, ground plane, and AlN substrate, have a coarse mesh size. The difference in the mesh size is why the AC current shown in Fig. 5.8 has a different skin effect distribution along the trace, since the computing resolution changed with the mesh size, while the skin depth remains the same.

5.4.1 Conductivity patch model

In this subsection, we investigate magnetic roughness due to the conductivity patch. The model shown in Fig. 5.8, and (b) is the detail of the conductivity patch.

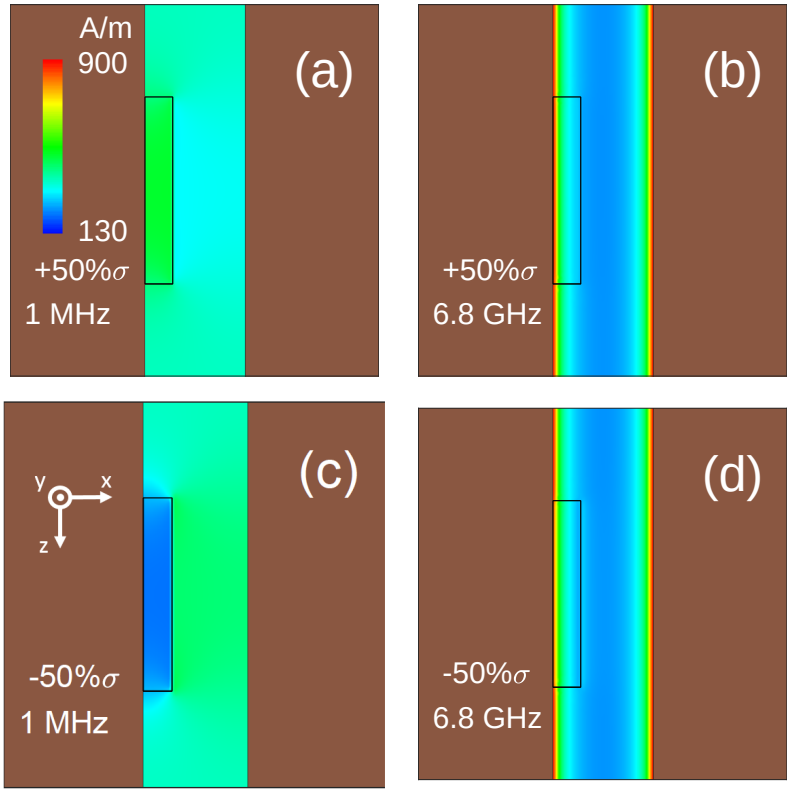

FIG. 5.9: The current distribution in a copper microstrip due to the conductivity patch defect. For illustrative purposes, the conductivity of the patch is ±50% different from normal ($\sigma \pm 50\%\sigma$). Moreover, the voltage source across the microstrip is 1 V, which corresponding to 20 mA current and 50 Ω in impedance at 1 MHz and 19 mA current and 53 Ω impedance at 6.8 GHz. From the plot, we can see that the current distribution has been affected quite a lot at low frequency but has not been affected at high frequency. (a): Low-frequency current distribution for a +50% conductivity patch. (b): High-frequency current distribution for a +50% conductivity patch. (c): Low-frequency current distribution for a -50% conductivity patch. (d): High-frequency current distribution for a -50% conductivity patch.

Previous research [79] shows that the conductivity variations occur mainly for two reasons: an actual variation in conductivity and the thickness of the trace varies in the patch . This previous research did not show the actual variation of conductivity, but it list the fractional thickness variation at around 0.6 - 1.7 $\times 10^{-3}$, i.e. about 0.1%. So we set the conductivity for this conductivity patch as ±0.1% different from the copper trace, which should be close to the actual case. Based on Table. 5.1, and the parameters that we used in the 1D wire model simulations (section 5.3), the bump length is $l = 100$ μm. The bump angle is $\theta = 0.1$ mrad, which corresponds to

a deviation width of $w = 5$ nm. We set the length of the conductivity patch as 100 μm to match the bump length and the width as 15 μm, which will shift the center of current (COC) by roughly 5 nm at low frequency. We define the COC as the average transverse position of the current in the conductivity patch section of the microstrip. Due to the difficulty to cleanly extract the current data from the FEKO output data; we use transverse component of the surface magnetic field (x-axis, B_x), which is gathered 20 nm above the trace, to compute the current density $J(x)$.

The simulation result shows that the current deviation (i.e. center-of-current deviation) gets weaker with increasing frequency. As shown in Fig. 5.10, the current deviation is around 6 nm at 1 MHz, and begins to drop above 10 MHz. The deviation finally reaches the sub-nm level around 500 MHz. Figure 5.9 shows the current distortion for 1 MHz and 6.8 GHz for conductivity differences of $\pm 50\%$ (chosen for illustrative purposes). In this figure, we can see that the current distribution is strongly affected by the conductivity patch at low frequency, but at high frequency, the skin effect dominates and pushes the current to the trace edges; hard to see a effect from the conductivity patch.

The magnetic roughness due to the conductivity patch has a similar behavior as COC deviation. The magnetic roughness in each axis component is shown in Fig. 5.11 (a). The magnetic field ($B_{x,y,z}$) is measured at $h = 100$ μm. The magnetic roughness of B_z is minimal compared to all the other components. The B_x and B_y components have a behavior similar to the COC deviation, which is high at low frequency and drops close to zero at high frequency. The y component has around 10 times the magnetic roughness as the x component: the B_y component has a magnetic deviation of 6×10^{-5} at low frequency which less than 1×10^{-5} at high frequency.

However, since the AC Zeeman potential is typically based on the circularly polarized components $B_\pm$ (recall: $B_\pm = B_x \pm iBy$), we also plot the deviations of

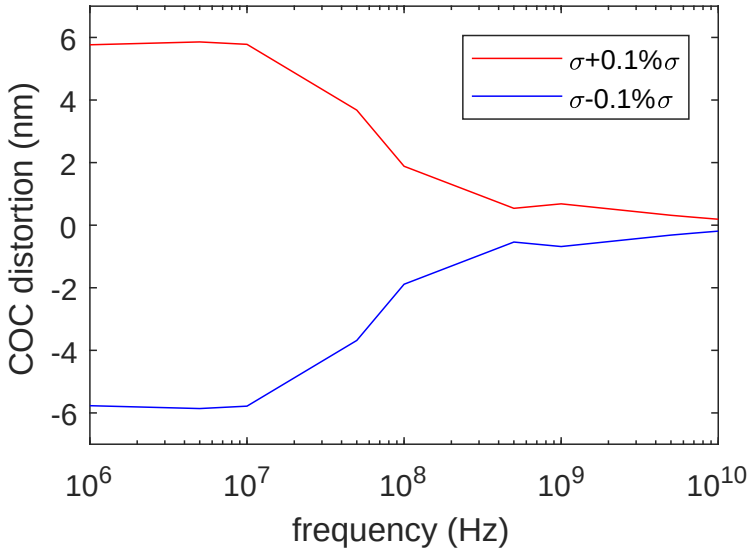

FIG. 5.10: Center-of-current (COC) deviation with a conductivity patch. Both the "$\sigma + 0.1\%\sigma$" case and "$\sigma - 0.1\%\sigma$" cases have a 6 nm COC deviation at low frequency, which drops to almost zero at high frequency.

B_+ and B_-. As shown in Fig. 5.11 (b), the magnetic roughness for B_+ and B_- follows the trend of B_x and B_y, i.e. the magnetic roughness level drops from low frequency to high frequency. The roughness level around 10 GHz is only 1/10 of the level around 1 MHz.

The x,y, and z components of the magnetic roughness are given by the magnitude of the difference of the complex magnetic field value between the defect case and the no defect case:

$$B_{x,\text{roughness}} = |\widetilde{B}_{x,\text{Defect}} - \widetilde{B}_{x,\text{No Defect}}| \tag{5.6}$$

We use tilde to present the complex value, such as $\widetilde{B}$.

The magnetic roughness for B_+ and B_- is also calculated as the magnitude of the difference between the complex value of $B_\pm$ field for defect case and no defect case.

$$B_{+,roughness} = |\widetilde{B}_{+,Defect} - \widetilde{B}_{+,NoDefect}| \tag{5.7}$$

where we use the following definitions:

$$\widetilde{B}_{+,Defect} = \widetilde{B}_{x,Defect} + i\widetilde{B}_{y,Defect} \tag{5.8}$$

$$\widetilde{B}_{+,NoDefect} = \widetilde{B}_{x,NoDefect} + i\widetilde{B}_{y,NoDefect} \tag{5.9}$$

B_- is calculated in the same manner.

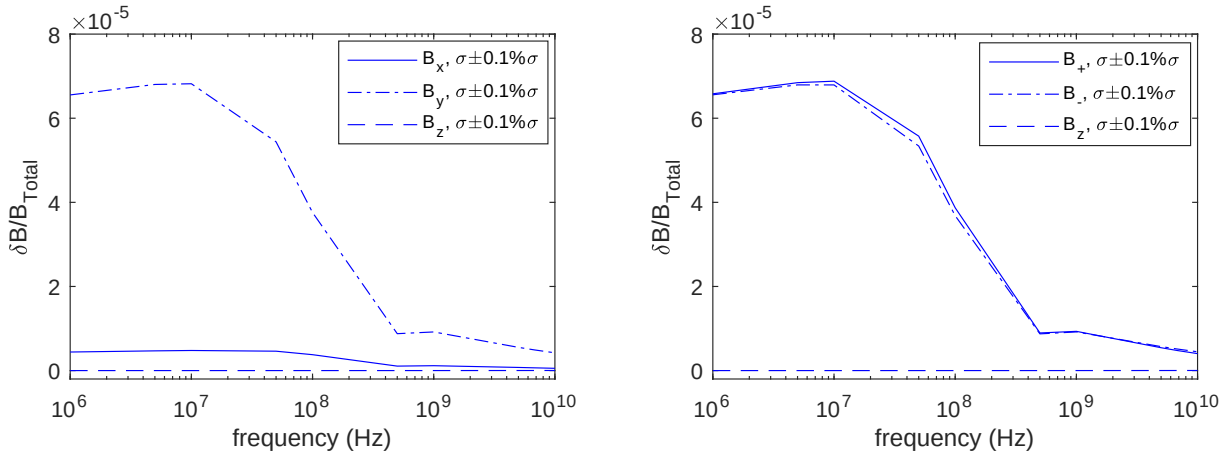

FIG. 5.11: Magnetic field distortion at the trap position versus frequencies for the conductivity patch defect. We define the trap position as the center of the trace and 100 μm above. Left: The plot shows that the magnetic roughness for the z component δB_z is minimal compared to other components. The x component, δB_x, is also tiny and less than 1 $\times 10^{-5}$ for low frequency and drops at higher frequency. The y component, δB_y is the largest one, and has a deviation of 6.5 $\times 10^{-5}$ level for low frequency but drops to 1 $\times 10^{-5}$ at high frequency. Right: Plot of the magnetic distortion in the $B_\pm$ circular polarization components. Since δB_y is much larger than δB_x, δB_y dominates the magnetic roughness level of B_+ and B_-, decreasing with increasing frequency. The performances of opposite conductivity patches, i.e. "$\sigma + 0.1\%\sigma$" and "$\sigma - 0.1\%\sigma$" are almost the same.

5.4.2 Edge defect model

Next, we simulate an edge defect. Again, we use Table 5.1, which indicates a typical size of 100 nm for the defect. For simplicity, we use a square edge defect as shown in Fig. 5.12. Since the scale of the edge defect is much smaller than the microstrip trace, we only show the defective position in Fig. 5.12. The edge defect comes in two different types. If The trace has a missing section at the edge, then we refer to it as a "defect in". If the trace has a section that sticks out of the edge, then we refer to it as a "defect out".

In this type of defect, the skin effect will not be helpful anymore since the "skin" will be distorted by the edge defect. However, we are still interested in the resulting current and magnetic field distortion.

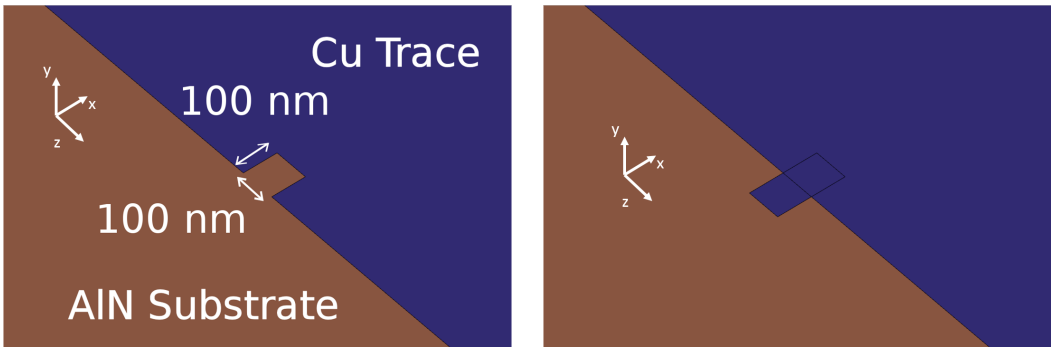

FIG. 5.12: Microstrip edge defect models. The shape of the edge defect is a rectangular square with a 100 nm edge length. Left: is the "defect in" model microstrip trace with an inward-facing edge defect. Right: is the "defect out" model microstrip trace with an outward-facing edge defect.

The current deviation for the edge defect has a different behavior from the conductivity patch. As shown in Fig. 5.14, the "defect in" and "defect out" cases cause different scale COC distortions from each other: The "defect in" case has a much stronger effect than the "defect out" case. Figure 5.13 illustrates this difference as well: for the "defect in" case, the current has to go around the defect, and will thus quite distorted, while for the "defect out" case, the current does not have enough space to "squeezed in" and fully hug the edge of the defect due to the 100

nm scale of the defect compare with skin depth at 1 MHz & 6.8 GHz.

Moreover, Fig. 5.14 shows that both of the "defect in" and "defect out" case at low frequency performs better than at high frequency: The COC distortion at high frequency is around two times bigger than at low frequency. Figure 5.13 also shows this trend: Due to the skin effect, at high frequency there is more current at the edges and thus near the defect, and so the defect can distort the current more.

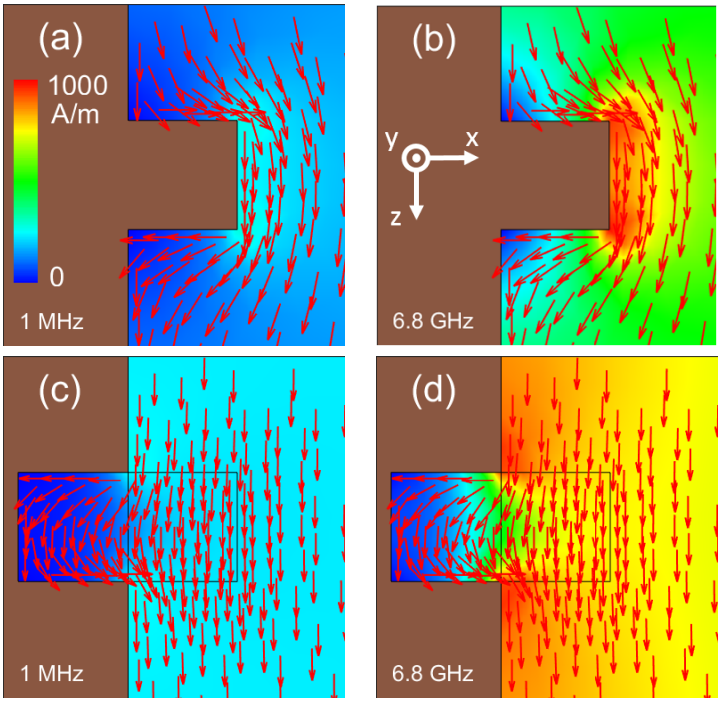

FIG. 5.13: Current distribution in a copper microstrip due to a square shape edge defect. a) and b) Edge defect protrudes out of trace. c) and d) Edge defect protrudes into the trace. a) and c) are at low frequency (1 MHz) and b) and d) are at high frequency (6.8 GHz). Defect dimensions are given in Fig. 5.12.

After the COC, we will look at the magnetic field roughness in Fig. 5.15. The magnetic field roughness calculations follow the same magnetic deviation definition as the conductivity patch (Eq.5.6 to Eq.5.9). The color bands represent the range of results from multiple different mesh types.

The magnetic field distortion are computed at the trap location ($h = 100\ \mu$m $= y$). The magnetic roughness for the edge defects has a different scale for "defect

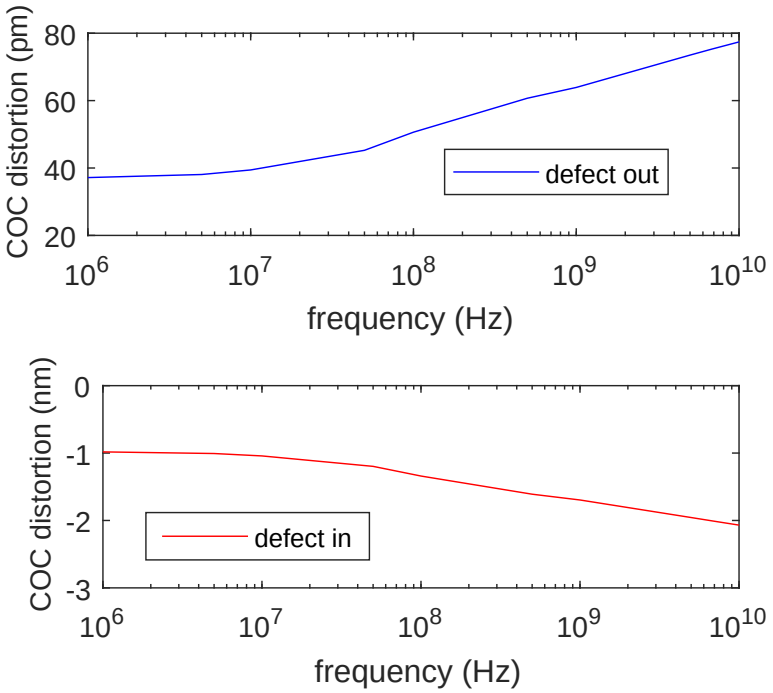

FIG. 5.14: COC distortion for the edge defect cases. The COC at low frequency has only half of the level than at high frequency. The COC distortion for the defect out case is around 25 times smaller than the defect in case.

in" and "defect out" cases: the fractional magnetic roughness of B_+, B_-, B_x and B_y are all at the 10^{-6} level for "defect in " case, while the "defect out" case is only at the 10^{-8} level. All the above components do not have a strong trend from low frequency to high frequency, but the roughness at high frequency is slightly bigger than at low frequency. The z component is a little bit special: it remains close to zero for both defect cases, from 1 MHz to around 1 GHz, but them starts to increase around 1 GHz and reaches the 2 $\times 10^{-8}$ level at 10 GHz.

The edge defects generally show less distortion at low frequency than at high frequency, in both COC and magnetic field roughness. However, this variation is much smaller than for the conductivity patch defect: High frequency suppress the $\delta B_\pm$ by around 6 times than low frequency for conductivity patch, while the $\delta B_\pm$ of high frequency is only around 10% - 50% higher than low frequency. Also, compared to the conductivity patch, which is not simply visible, the edge defect is visible under

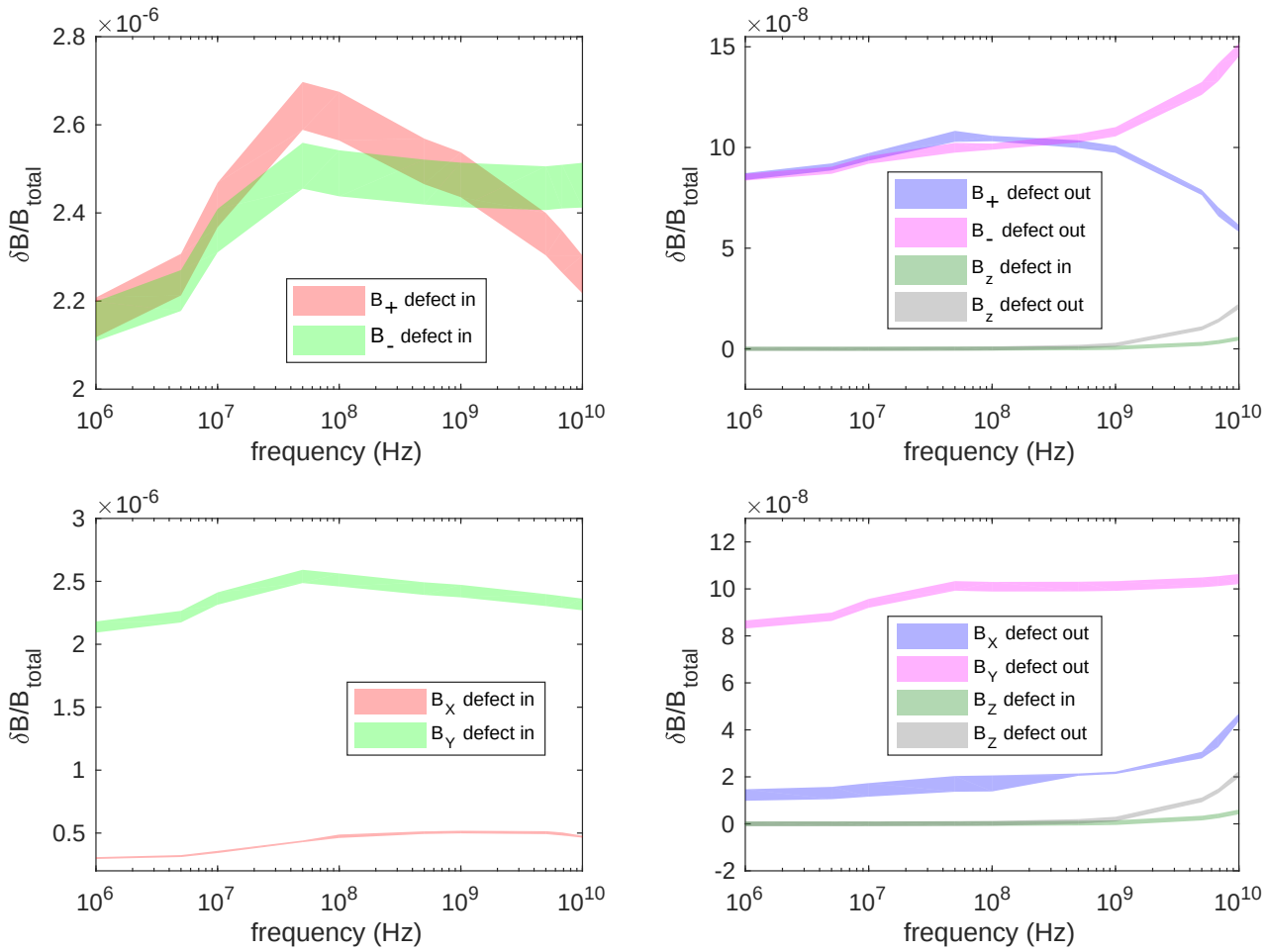

FIG. 5.15: Magnetic roughness at the trap position ($y = 100$ μm) for edge defects. The magnetic roughness at low frequency has a smaller roughness than at high frequency, but the difference is quite modest.

a microscope, so building or selecting a better chip, which has a smaller edge defect or that has more "defect out" defects than "defect in" ones can lead to improved roughness performance.

5.5 Conclusion

This chapter shows an AC Zeeman trap is expected to suppress trapping potential roughness much more than a comparable DC Zeeman trap. We used a 1D wire model to simulate the AC Zeeman and DC Zeeman trapping potentials single and

multiple defects, and used FEKO to simulate the magnetic field for conductivity patch and edge defects in a microstrip transmission line.

For the 1D wire simulations, the AC Zeeman trap clearly suppresses the trapping potential roughness more than the DC Zeeman traps, and the associated suppression factor can be large for multiple defect cases: The suppression factor increases with the trap height and decreases with the defect length.

The FEKO simulations show that the the AC skin effect will dominate the current distribution at high frequency, thus suppressing roughness generated by a conductivity patch defect. The FEKO simulations also show that edge defects perform better at low frequency. However, the advantage of low frequency for edge defects is not as large as the advantage of high frequency for the conductivity patch. Finally, conductivity patches are not visible under a microscope so they cannot be screened before installation in a ultracold atom apparatus. However, we can always use a microscope to choose a microstrip with fewer and smaller edge defects.

We have naively multiply up the roughness suppression effect for all the condition above, and show it in Table. 5.2. This naive combination table just multiply all the suppression factor for each frequency together. We are not claiming the value in this table is correct, but still indicative. The low frequency AC current have a suppression factor around 10^4, and the high frequency AC current have a suppression factor around 5×10^4.

$\frac{\text{Roughness}_{\text{DC}}}{\text{Roughness}_{\text{AC}}}$	DC	Low frequency (20 MHz)	High frequency (6.8 GHz)
1D wire	1	10^4	10^4
Conductivity patch	1	1	10
Edge defect	1	1	0.5
Naive combination	1	10^4	5×10^4

TABLE 5.2: Naive combination for all the roughness effect.

CHAPTER 6

Atom Interferometer

This chapter discusses one of the main results of this thesis: a trapped atom Ramsey interferometer, and progress on the development of an atom interferometer, which is the long term objective of the project.

This chapter begins with the introduction of the basic theory of a Ramsey interferometer at section 6.1. Next, section 6.2 introduces the apparatus instrumentation used for conducting the interferometry measurements, including the ultracold atom preparation in the ODT (subsection 6.2.1), the microwave and RF sources (subsection 6.2.5), safety interlock (subsection 6.2.6), microwave monitoring system (subsection 6.2.7), and the control system (subsection 6.2.8). Section 6.3 describes the basic experimental scheme. The measurement of the two-photon transition is described in section 6.4 along with the microwave scan experiment (subsection 6.4.1) and Rabi flop experiment (subsection 6.4.2). In the two-photon transition experiment, we found that the resonance frequency will shift with the driving microwave power, which is described in subsection 6.4.3. Section 6.5 presents the Ramsey interferometer experiment with an application of this measurement, the Ioffe magnetic field calibration in subsection 6.5.1. Section 6.6 presents a proof-of-principle

measurement of DC (subsection 6.6.1) and AC Zeeman shift using the Ramsey interferometer, including the attempt at using the interferometer as spatial atom interferometer (subsection 6.6.2). Section 6.7 reviews the data fitting process for the camera data, while the section 6.8 reviews the experiment issues. Finally the chapter concludes in section 6.9.

6.1 Basic theory

The Ramsey interferometer core of the atom interferometer operates on the $|2,1\rangle \leftrightarrow |1,-1\rangle$ transition [39]. This transition needs two photons to operate: the $|2,1\rangle \leftrightarrow |2,0\rangle$ transition with around 3 MHz RF frequency and the $|2,0\rangle \leftrightarrow |1,-1\rangle$ transition with around 6.8 GHz microwave frequency. Based on their frequencies, we call the first one RF transition and the second one microwave transition.

In order to drive the $|2,1\rangle \leftrightarrow |1,-1\rangle$ transition without polulating the unwanted intermediate state $|2,0\rangle$, we operate the RF and microwave drive frequencies at a common detuning from this intermediate state [39]. To complete the 2-photon transition, we need the sum of the two driving frequencies to be equal to the total energy change of the $|2,1\rangle \leftrightarrow |1,-1\rangle$ transition (on-resonance), which requires the detuning of the two single-photon transitions to be the same value (magnitude) but in different directions (opposite signs). Under this condition, we can treat the 2-photon transition involving three levels as an effective two-level system, i.e. omitting the intermediate level.

6.1.1 Ramsey interferometer

The spatial atom interferometer is essentially a Ramsey interferometer with spatially separated states. The development of the interferometer is thus divided into two main milestones: 1) The construction and operation of the Ramsey in-

terferometer, and 2) the addition of a spin-dependent potential that affects the two spin states of the interferometer differently. Ultimately, this last component will be configured as a spin-dependent potential with a gradient, so as to impart a spin-dependent force, which will then spatially separate the two spin states of the interferometer into two distinct spatial arms.

The Ramsey interferometer consists of two identical $\frac{\pi}{2}$ pulses with a time interval between them. This time interval is called the Ramsey time, or phase accumulation time. The Ramsey interferometer experiment scans the Ramsey time to generate the interferometer fringe signal, i.e. the fractional population of a given spin state oscillates between 0 and 1 as the Ramsey time is varied. The fringe oscillation frequency is the detuning of the combined 2-photon drive fields from the transition resonance.

The $\frac{\pi}{2}$ pulse uses the two-photon transition by applying the RF and microwave driving fields for a time that corresponds to a phase of $\frac{\pi}{2}$ of the Rabi flopping cycle, i.e. a quarter Rabi period. The first $\frac{\pi}{2}$ pulse will transform the atom from a pure state, for example the $|1,-1\rangle$ state, into a 50/50 superposition of the $|2,1\rangle$ and $|1,-1\rangle$ states, i.e. $\frac{1}{\sqrt{2}}|1,-1\rangle - \frac{i}{\sqrt{2}}|2,1\rangle$ [28]. The second $\frac{\pi}{2}$ pulse returns the atom from the 50/50 superposition to a state decided by the phase accumulated in the interferometer time.

The Bloch sphere explanation of this interferometer scheme is easier to understand. As shown in Fig. 6.1, The atom starts in the $|\uparrow\rangle = |2,1\rangle$ state, which is represented by an arrow pointing up along the z-axis. The two-photon transition will make the arrow rotate around an axis in the equatorial plane. Let us call it the y-axis. This two-photon transition "rotation" will stop when the arrow reaches the equatorial plane (for detuning $\delta = 0$), which is $\frac{1}{4}$ of the rotation circle, so we call it a $\frac{\pi}{2}$ pulse. Next, the arrow will precess in the equatorial plane during the Ramsey time, when the interferometer accumulates the phase. The phase accu-

mulation is the source of the interferometer signal, and different experiments have different operations during this stage. After the Ramsey time, we apply another $\frac{\pi}{2}$ pulse, and the arrow rotates around the y-axis for another quarter turn. After the second $\frac{\pi}{2}$ pulse, the arrow's final orientation (i.e. atom's final state) is determined by the angle between the arrow and y-axis at the time of the second $\frac{\pi}{2}$ pulse. The interferometer signal is the ratio of the atomic state population to the total atom number, i.e. the vertical z-axis component of the arrow (plus $\frac{1}{2}$).

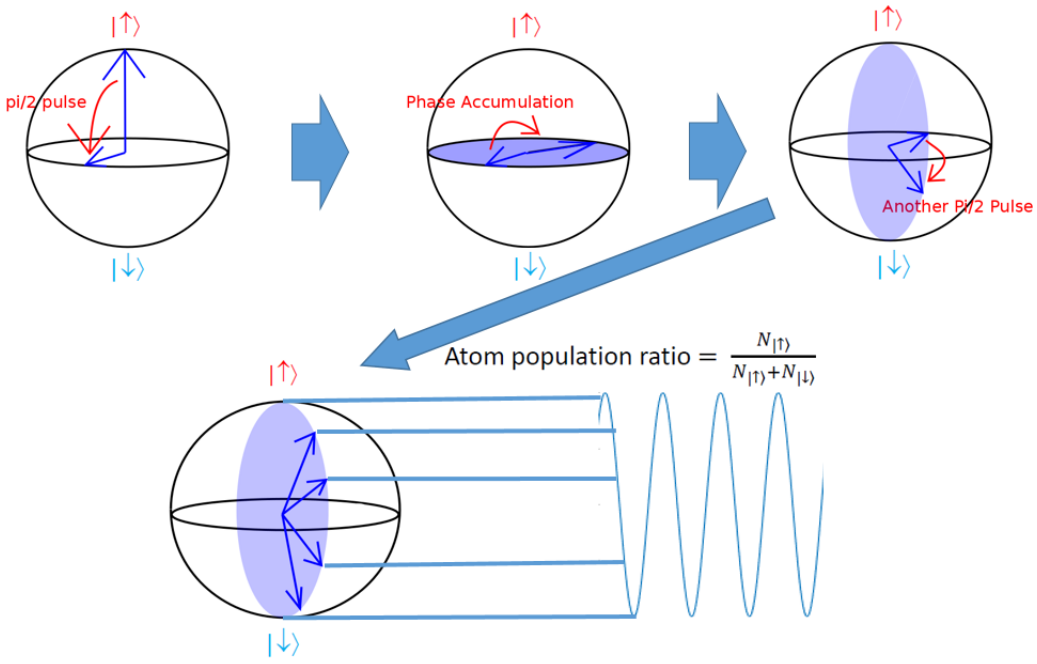

FIG. 6.1: Bloch sphere explanation for a Ramsey interferometer. In our Ramsey interferometer experiment, the $|\uparrow\rangle$ is the $|2,1\rangle$, and the $|\downarrow\rangle$ is the $|1,-1\rangle$. The first $\frac{\pi}{2}$ pulse will move the arrow to the equatorial plane, and the arrow will process in the equatorial during the Ramsey time to accumulate the phase. The procession frequency is the frequency difference between the energy gap between the $|\uparrow\rangle$ and $|\downarrow\rangle$ state $E_{\uparrow,\downarrow}$ and the driving transition frequency, which in our experiment will be the two photon transition frequency $f_{2-\gamma}$, for $|2,1\rangle \leftrightarrow |1,-1\rangle$. The second $\frac{\pi}{2}$ pulse will return the arrow to the vertical plane, and the atomic population ratio is determined by the vertical z-axis component of the final arrow position.

The two-photon transition performs a critical role in the interferometer experiment. The precession rate of the Bloch sphere arrow during the Ramsey time is the frequency difference between the two-photon transition driving frequency $f_{2-\gamma}$ and

the transition energy $E_{|2,1\rangle \leftrightarrow |1,-1\rangle}$. Based on this fact, we can control the interferometer signal frequency with the two-photon transition. Notably, if the two-photon transition frequency is the same as the transition energy, the interferometer signal will be at 0 Hz, and so the Ramsey fringes disappear, i.e. there are no oscillations in interferometer signal as the Ramsey time is varied. Since the two-photon transition directly controls the atom interferometer signal, the quality of the two-photon transition driving fields (and associated sources) will limit the precision of the atom interferometer. In other words, we should choose the best RF source and microwave source as we can for the two-photon transition, i.e. sources with very low phase noise.

6.1.2 Enabling spatial interferometry: adding a spin-dependent potential or force

In order to convert the Ramsey interferometer into an atom interferometer, the two spin states ($|1,-1\rangle$ and $|2,1\rangle$) must be spatially separated. We choose to separate these two states by applying a spin-dependent AC Zeeman potential and force.

In the case of a spatially flat AC Zeeman potential, the energy difference between the two states is changed, resulting in a change in the Ramsey fringe frequency. However, the two spin states remain in the same location. In this scenario, the Ramsey fringe signal can be used to determine the energy difference created by AC Zeeman potential.

As shown in Fig. 6.2, in the case of an AC Zeeman potential with a spatial gradient, a spin-dependent force (AC Zeeman force) is generated, which can spatially separate the two spin states. However, in order to observe Ramsey interference fringes, the two states must be made to overlap spatially at the end of the Ramsey

time (when the second $\frac{\pi}{2}$ pulse is applied). While the two spin states are spatially separated, they can acquire a phase due to spatial variations in the potential energy (AC Zeeman or other).

Note: in principle, the two states could be separated via a DC Zeeman potential and force. However, the experiment is explicitly designed so that the atoms are insensitive to external DC magnetic fields, so this approach is impractical. By operating at 3.23 G, the $|1,-1\rangle$ and $|2,1\rangle$ states are at "magic" magnetic field condition, such that they experience the same DC Zeeman energy shift (and the same force if there is a field gradient): a DC magnetic field cannot apply a spin-dependent energy or force unless it is quite large.

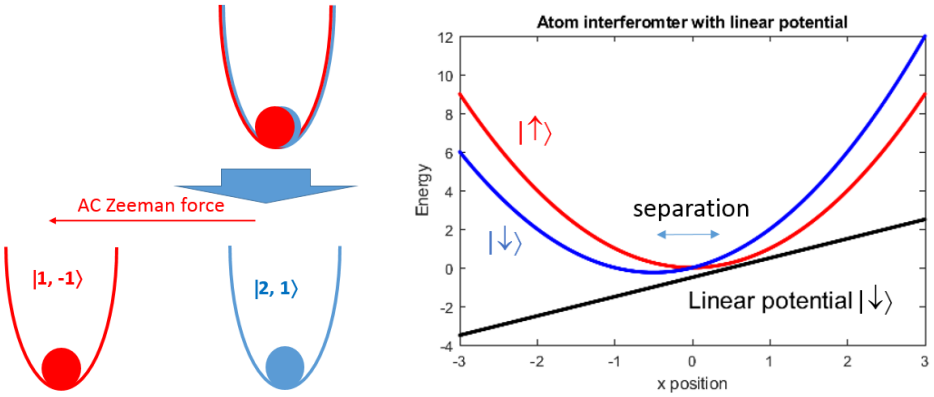

FIG. 6.2: Spatial atom interferometer with AC Zeeman force. The spin-dependent AC Zeeman force shifts the corresponding state's trap and spatially separates the two spin states.

6.2 Apparatus setup

This section presents the main components of the interferometry setup that have been added to the main ultracold atom apparatus for the atom interferometry experiments. We start by describing the atom preparation procedure (subsection 6.2.1) and then explain the optical dipole laser trap setup (subsection 6.2.2). The

high quality RF and microwave sources and related systems are described in subsection 6.2.5 and later subsections.

6.2.1 Atom preparation

The ultracold atoms for the trapped atom interferometer experiment are prepared largely by same process as the BEC. We cool and collect ^{87}Rb atoms in the MOT and then load them into a magnetic trap for transport to the atom chip, which is located in another vacuum cell. Once the atoms are loaded into the micromagnetic chip, they are then are evaporatively cooled to sub-μK temperatures.

In contrast with the BEC production process, we stop the evaporative cooling a little before the onset of BEC. Moreover, the atom interferometer experiment includes an additional step: the atoms are loaded from the chip trap into an optical dipole trap (ODT). Since the loading process will heat the atom, cooling the atom to BEC in the chip trap will only reduce the available atom number in the ODT, but not make them any colder. In practice, we optimize the ultracold atom population in the ODT by finding the optimum temperature at which to stop evaporative cooling in the chip trap.

Ideally, the ODT trap position is the same as the chip trap position, so the loading process is to ramp up the ODT power while reducing the chip trap current: the ODT adiabatically replaces the chip trap. Notably, some of the atom interferometer experiments involve an ODT located under the U wire (instead of the Z wire), where the ODT does not overlap with the standard chip trap. In this case, we add a vertical trim magnetic field to move the chip trap position horizontally to the ODT position and then transfer the atoms into the ODT.

6.2.2 ODT setup

The atoms are trapped by the ODT directly below the atom chip, as shown in Fig. 6.3. The two beams of the optical dipole trap are perpendicular to each other with unbalanced power. The one with higher power is called the main beam, and the one with weaker power is called the transverse beam. Furthermore, the main beam is a little more tightly focused than the transverse beam: the power imbalance and different beam sizes results in an atomic cloud that is elongated along the main beam axis, which is the same direction as the center wires on the chip, and the DC external magnetic field, i.e. the "Ioffe" field.

6.2.3 DC magnetic field

We also have two DC magnetic field sources for the experiment. One of them is the Ioffe field, which will provides the magic magnetic field for the duration of the experiment and also provides a convenient quantization axis. The Ioffe coil is a Helmholtz-style coil pair set around the vacuum chamber to provide a uniform DC magnetic field. The second DC magnetic field is the Stern-Gerlach (S-G) field, which spatially separates an atom's spin states at the end of an experimental cycle in order to image the different spin states. To spatially separate the different spin states with the S-G effect, we need a high gradient field, so the S-G coil is a single coil right next to the vacuum chamber, only a few centimeters away from the atoms. The Ioffe field and the S-G field are perpendicular to each other, and in the coordinate system shown in Fig. 6.3, the Ioffe field is in the z-axis direction and the S-G field is in the x-axis direction.

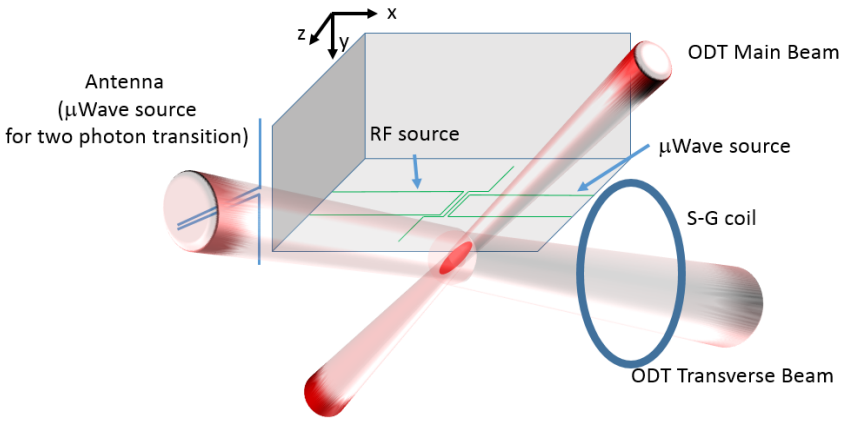

FIG. 6.3: Schematic of the apparatus setup at the atom chip showing the optical dipole trap (ODT) and the microwave sources used in the atom interferometry experiments. S-G coil refers to the Stern-Gerlach magnetic coil used for separating spin states after release from the trap for imaging.

6.2.4 RF and microwave sources

Our experiment has two microwave sources, which generate frequencies around 6.8 GHz, as well as two RF sources that generate MHz range frequencies.

One of the microwave sources uses the Holzworth HSM4001AS, the top quality source in our lab. The Amaterasu amplifier system, generally referred to as "Amaterasu", amplifies the Holzworth source to 20 W. The output of the Amaterasu connects to the antenna to drive the microwave transition part of the two-photon transition. As shown in Fig. 6.3 and Fig. 6.4, the antenna is a half wave antenna, set outside of the vacuum cell, a few cm away from the atom cloud, in an attempt to provide a rough plane wave, so as to suppress field curvature and gradient that could affect the quality of the interferometer.

The second microwave source uses a direct digital synthesis (DDS, based on a AD9910 chip) source operating at around 107 MHz, which is sent to the Dr. Watts amplifier system, generally referred to as "Dr. Watts". The details of the "Dr. Watts" design are covered in Charlie Fancher's thesis [57]. The "Dr. Watts"

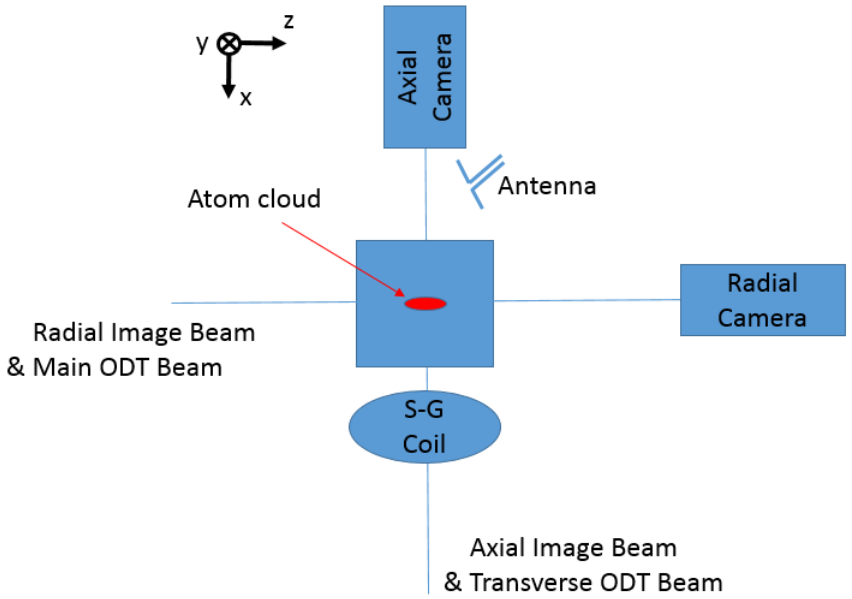

FIG. 6.4: Top view of the apparatus setup in the vicinity of the atom chip. The diagram shows the imaging cameras in relation to the ODT trapping beams and the atomic cloud. S-G coil refers to the Stern-Gerlach magnetic coil used as part of the imaging process.

multiplies the input frequency 64 times to around 6.8 GHz using a SynthNV device ($\times$32 phase-lock loop) and a frequency doubler ($\times$2), and then amplifies the power up to 3.3 W. The quality of this microwave source is lower than the Holzworth, so we use it on jobs that do not require very high quality, such as when we need to conduct an adiabatic rapid passage (ARP) from one atomic spin state to another.

We have an excellent RF source provided by a DDS (based on a AD9910 chip), which is then amplified and directed to the U wire of the atom chip. We use this excellent RF source to drive the RF transition of the two-photon transition. The RF transition is around 3 MHz, and if we generate 3 MHz from the DDS, the harmonic at 6 MHz might affect the experiment. To suppress this harmonic, we generate 53 MHz with the DDS and mix it down with a 50 MHz signal from a Siglent SDG6022X arbitrary waveform generator to create the 3 MHz RF frequency and reduce the harmonic.

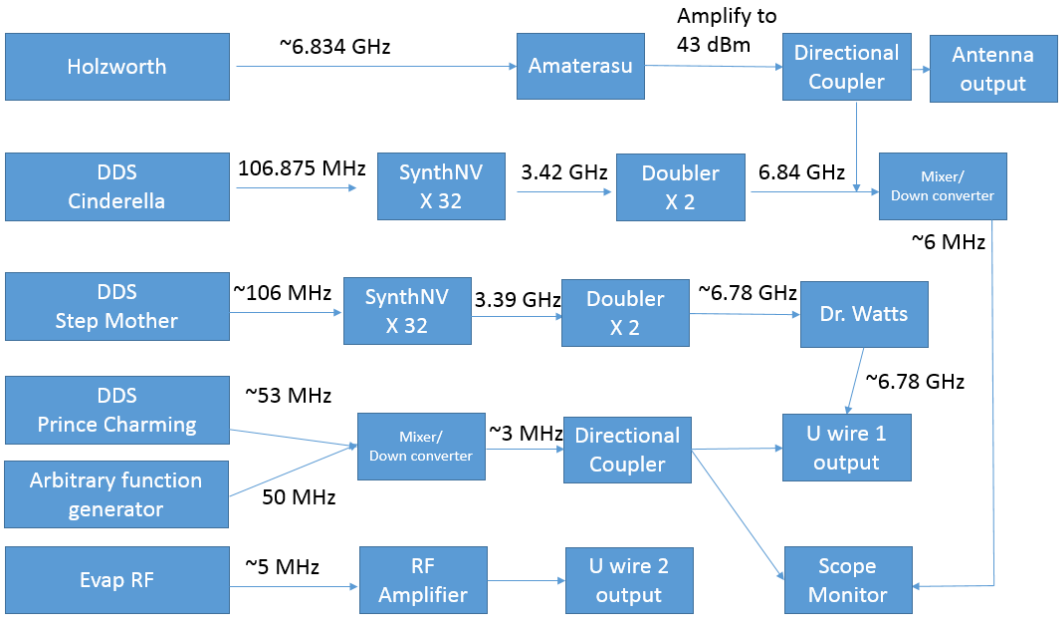

FIG. 6.5: Diagram of the microwave and RF systems used in the atom interferometry experiments.

A second RF source is used for forced RF evaporative cooling of atoms in the atom chip's micromagnetic trap. The source is based on the Berkeley Nucleonics model 645 function generator and is generally referred to as the "Evap RF". This source is not digitally controlled nor is it connected to the lab's main 10 MHz reference clock, and instead its frequency is adjusted using an analog voltage. We reuse the Evap RF to ARP the atoms from $|1,1\rangle$ to $|1,-1\rangle$ in the atom state preparation stage. While the phase noise of this RF source is not as good as the others, the APR process is not affected.

The amplified output of all of the sources is sent to the atom chip wires (see Fig. 6.6), except for the Holzworth source (amplified by Amaterasu), whose output is directed to the microwave antenna. Figure 6.5 shows a diagram of the RF and microwave systems, and how they are interconnected. The Cinderella DDS has its frequency multiplied by a SynthNV and then doubled to around 6.8 GHz. Our monitoring system mixes down the Amaterasu output to under 10 MHz for easy real-time monitoring on an oscilloscope. The DDS Step Mother also has its frequency

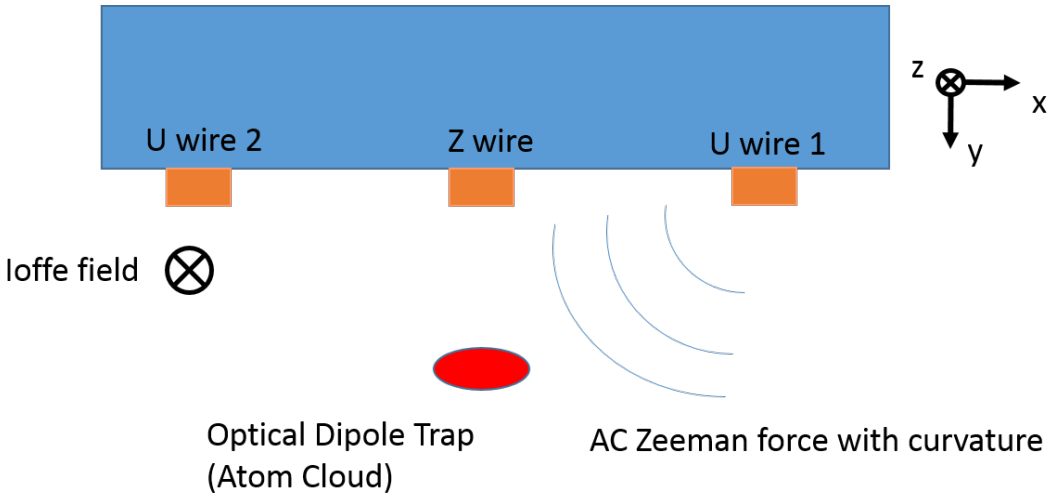

FIG. 6.6: Diagram of the chip wire layout. The center wire is the Z wire and both sides are U wires. The left U wire, referred as "U wire 2" connects the Evap RF source and the right U wire, referred as "U wire 1" connects the Dr. Watts microwave source and DDS Prince Charming RF source. The ODT is below the Z wire, and the microwave near field from the U wire 1 has a 45° angle for the gradient. The Ioffe field is along the same direction as the wire.

multiplied by a SynthNV and then doubled to around 6.8 GHz and amplified by Dr. Watts. The output of the Dr. Watts connect to the atom chip U wire (U wire 1 shown in Fig. 6.6). The DDS Prince Charming and arbitrary function generator output frequencies around 50 MHz that are then mixed down to generate a 3 MHz signal, which is then directed to the same atom chip U wire as Dr. Watts (U wire 1); a small part of this signal goes to a monitor system. The Evap RF generates a frequency under 10 MHz, which is amplified before going to the other atom chip U wire (U wire 2), different from the Dr. Watts.

6.2.5 Amplifier system

In this subsection, we discuss our microwave amplifier system. We have three microwave amplifier systems in our lab, the "Dr. Watts" amplifier system, the Amaterasu amplifier system, and the Baku amplifier system. Amaterasu is the Sun God in Japanese mythology, and is a suitable name for a high power amplifier. Baku is a

creature in Japanese tales that consumes human nightmares. The "Baku" name for the amplifier was chosen to represent our success overcoming the engineering difficulty with the "Dr. Watts" amplifier (see subsection 6.2.7), which was a nightmare for us.

The "Dr. Watts" amplifier system is presented in Charlie Fancher's thesis [57]. The maximum output power of the "Dr. Watts" is 3.3 W, much weaker than the Amaterasu and Baku. The "Dr. Watts" cannot support the power requirements of future experiments and will be replaced by Baku or a similar amplifier system.

Amaterasu and Baku follows the same microwave amplifier system design. Baku was built after Amaterasu, and so its board layout features some organizational improvements.

We will use the Amaterasu as an example to introduce our new microwave amplifier system. The Amaterasu has three different system blocks: the power system, the microwave system, and the control signal system.

The power system (grey box in Fig. 6.9) is straightforward. We have two power supplies: one provides ± 15 V with respect to ground, and the other one provides +30 V. The 30 V power supply supports the amplifier, and the ± 15 V goes to the power box, which regulate the voltage to ± 12 V, ± 7 V, and ± 5 V to support all the other elements on the Amaterasu board.

The microwave system (white box in Fig. 6.9) receives a 3.4 GHz microwave signal from the Holzworth, which is then directed through a switch, doubler, and voltage variable attenuators (VVAs). The resulting 6.8 GHz signal is then amplified to 20 W and sent to the antenna.

The switch (ZASWA-2-50DR+) can only support a range of DC to 5 GHz, so it is located before the doubler. The doubler (mini-circuits ZX90-2-36-S+) doubles the frequency from 3.4 GHz to 6.8 GHz. Notably, the doubler is not a linear device, and it will largely not function if the microwave power is too low: this property of

the doubler helps to block the leakage through the switch.

After the doubler, there is a daisy chain of two voltage variable attenuators (VVA). The attenuation curve for a single VVA as shown in Fig. 6.7: the total attenuation is 45 dB at -8.5 V, while at maximum transmission at -4 V, the insertion attenuation is 5 dB. For convenient analog control of the VVA, we use an inverting amplifier (op-amp based) to flip the sign of the control voltage, and thus use a positive control voltage. Figure 6.8 shows the output power after a single VVA, if we apply a control voltage with a Gaussian shape from -9.9 V to -7.5 V. In this case, the output microwave signal has clear step in amplitude right after the turn on of the switch. At this time, the control voltage is still around -9.9 V for maximum attenuation. This amplitude step indicates that a single VVA is insufficient to adjust the Amaterasu output power smoothly and is leaking microwaves. To deal with the problem of a single VVA, we daisy chain two VVAs one after the other to suppress the amplitude step.

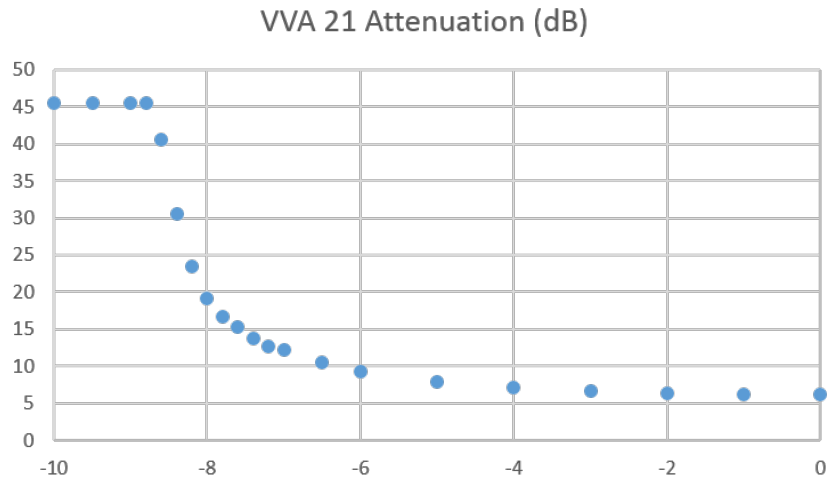

FIG. 6.7: VVA voltage attenuation curve for a signal VVA.

After passing through the switch, the doubler, and the two VVAs, the microwaves are sent to the power amplifier (CTT inc. GaN Amplifier 6.4-8.5 GHz, Psat=43 dBm, Part # AGW/085-4346). This amplifier will amplify the microwaves

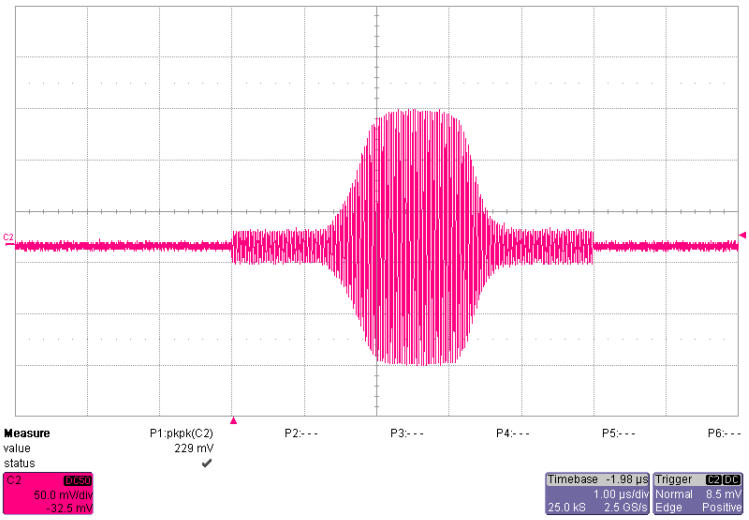

FIG. 6.8: The real-time power output of single VVA with a Gaussian control voltage.

up to 20 W. After the amplifier, we use a circulator (Nova Microwave, part #0680CES) to prevent spurious reflections (e.g. from the atom chip or from a poorly terminated output) from damaging the amplifier. One arm of the circulator connects to a 50 Ω power terminator with a large heatsink (Aeroflex Weinschel 1458-1), and the other arm goes to the antenna.

We use two directional couplers (ZADC-13-73-S+ for 3.4 GHz, and 4014C-30 for 6.8 GHz) to pick off a tiny amount of the microwave signal. The first directional coupler is located before the switch to pick off the 3.4 GHz Holzworth input and send it to a frequency counter to monitor the operating frequency. The second directional coupler is located after the circulator and picks off a tiny amount of microwave power, and then directs it to a power splitter (ZX10-2-183-S+). One arm of the splitter goes to the Ramsey interferometer monitor system, and another arm goes to a power detector (Herotek DZR124AA) to convert the microwave power into a DC voltage and then send it to the safety interlock system. The Ramsey interferometer monitor system will mix the input microwave with a 6.8 GHz reference frequency generated by the SRS SG384 signal generator, around 10 MHz away from the input signal. The output of the mixer will be around 10 MHz and goes to an oscilloscope for

real-time monitoring. Since we pick off the microwaves right before they goes to the antenna, the oscilloscope will show the microwave behavior during the $\frac{\pi}{2}$ pulse, as shown in Fig. 6.8.

The control signal system, shown in the yellow box of Fig. 6.9, receives two digital signals from the pulse generator SRS DG535 and an analog signal from a Siglent SDG5122 arbitrary waveform generator. The digital signal controls the amplifier and switch, and the analog signal controls the VVA pair. The control signal will first go to the isolator box to prevent ground loops. In the isolator box, the digital signal is isolated via opto-isolation, and the analog signal is isolated by an op-amp differential amplifier. The analog signal will go to the VVAs directly after the isolator box, while the digital signal goes to the safety interlock before it goes to the amplifier and switch.

The safety interlock gathers the digital control signal and power detector voltage to determine whether the amplifier can be operated without damaging the atom chip. The power detector voltage goes through a proportional-integrator circuit to limit the maximum output power and also to limit the maximum continuous power output time of Amaterasu.

The safety interlock protects the chip wire from thermal damage when we attach Amaterasu to the atom chip. However, currently, Amaterasu connects to the antenna, and the antenna has no risk of thermal damage due to its size, so we bypass the safety interlock.

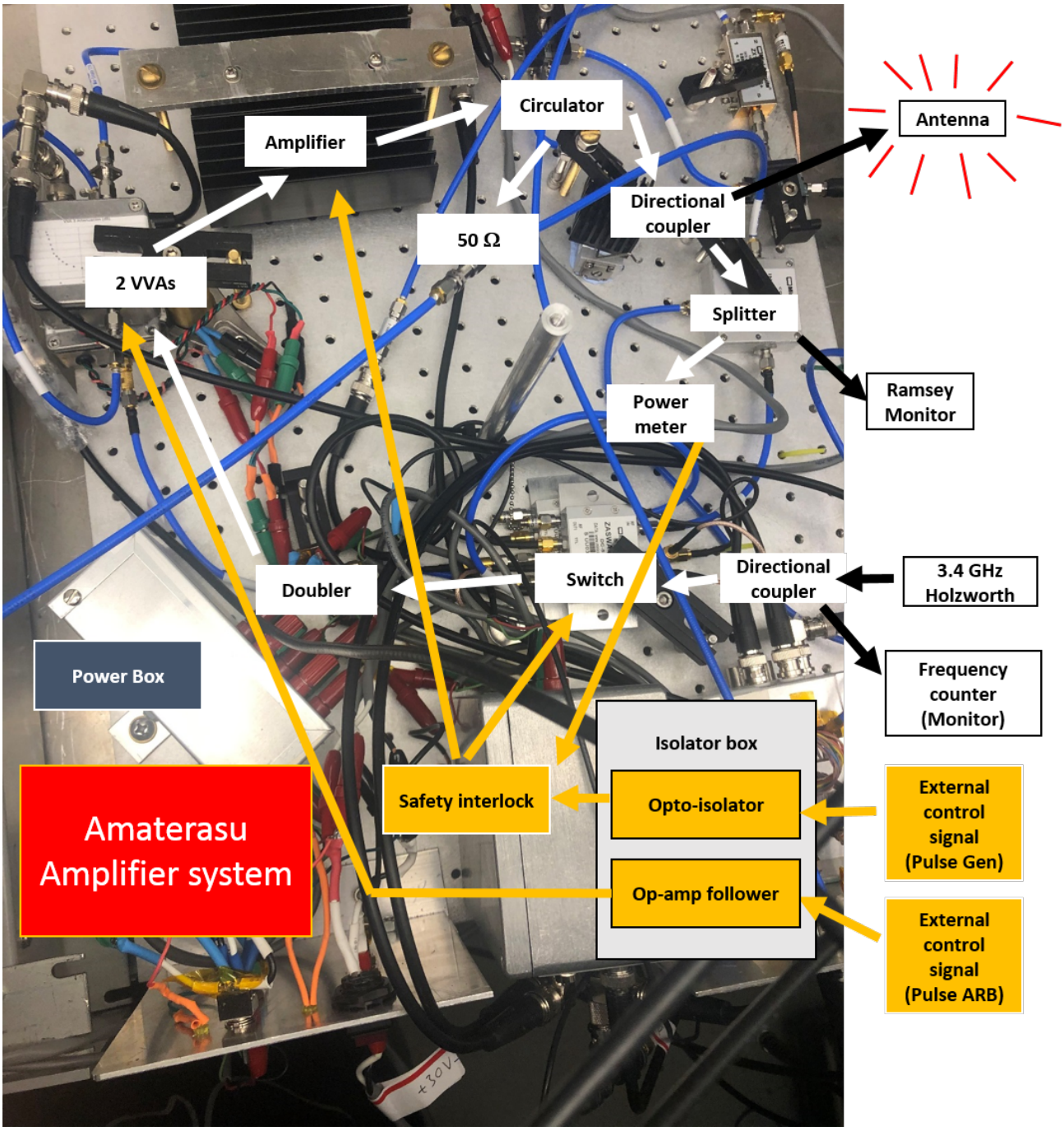

FIG. 6.9: Amaterasu amplifier system layout.

6.2.6 Safety interlock

Figure 6.10 shows the detailed design of the safety interlock. The "RF in" on the left top indicates the RF power detector voltage input. An op-amp follower conditions the input voltage to ensure that it has a sufficient source impedance. After this follower, we set up a monitor point, which is mainly used for debugging, and we also isolate it by an op-amp follower.

Next, the safety signal goes through a PI circuit system, with an inverting amplifier, an integrator, and two voltage comparators. The inverting amplifier limits the maximum amplifier power output, i.e. it prevents Amaterasu from outputting a power higher than its designed value, 20 W. The integrator limits the microwave power that accumulates as heat on the chip over time. Finally, there are several logic gates that ensure that the amplifier system will only output power when the control signal, proportional trigger, and integrator trigger all allow it.

In practice, the integrator needs "bleeding" to reset the integrator voltage for each experiment cycle. This design has a built-in risk to the system that if the microwave leakage is too tiny to integrate the voltage in the integrator, but is meanwhile too large to dissipate all the heat, then the integrator cannot protect the atom chip anymore. To deal with this risk, we add another integrator with constant input, 5 V, to limit the maximum microwave amplifier running time regardless of its output power. However, this upgrade only applies to the Baku but not Amaterasu yet.

Additionally, the power detector's power-voltage curve has a logarithm shape. This non-linear relation adds extra difficulty to adjusting the safety interlock value. We use a special chip AD633 analog multiplier to square the voltage before the input of the safety interlock, and the power-voltage relation becomes largely linear. This modification only applies to Baku, and we should apply it to Amaterasu in the

future.

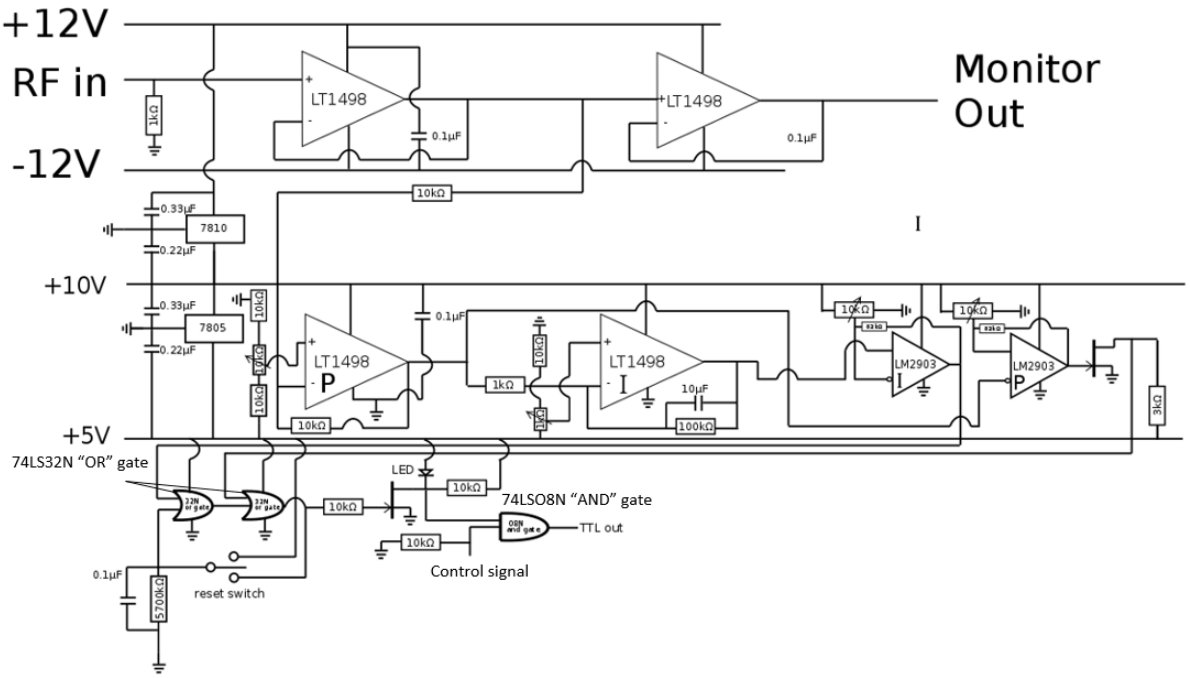

FIG. 6.10: Safety interlock design.

6.2.7 Microwave monitor system

The microwave monitor system in our atom interferometer experiment includes frequency counters and the Ramsey interferometer monitor system.

The frequency counters monitor the frequencies output by all the DDS units, the Holzworth, the SynthNV, and the "Dr. Watts". The primary purpose of the frequency counter is to check whether the frequency is at the requested value. The DDS and SynthNV sometimes fail to lock to their frequency when we touch the cable, and the connection gets unstable. The worst experience is on the "Dr. Watts" that will randomly have no output. This problem existed for more than a year, and finally we found that one of the voltage regulators in the "Dr. Watts" was not soldered to its cables but attached to the cables with a plastic board pressed on it

it. We solve this problem by soldering the cable to the voltage regulator.

The frequency counters only update their display around once per second, and they do not have a time log. Thus the frequency counters cannot help us to monitor the power and frequency during the experiment, either in real-time or post measurement. However, The Ramsey interferometer monitor system does help us to monitor the two-photon transition sources during the experiment.

The Ramsey interferometer monitor system uses a directional coupler to pick off some of the output of the Amaterasu and RF amplifiers and send them to an oscilloscope. The microwave at 6.8 GHz is too fast for the scope, so we mix the frequency down with a reference source to output a beatnote around a few MHz. The reference sources are provided by the DDS "Cinderella" with 64 times frequency multiplication or the SRS SG384 signal generator.

The Ramsey monitor will display the two-photon transition sources as shown in Fig. 6.31. We can check the two-photon transition running time on it. If we zoom in on the scope display, we can also check the frequency.

6.2.8 Control system

Our apparatus has two control system, the Adwin system and Ramsey time control system. The Adwin system controls most of the apparatus in our experiment, and the Ramsey time control system controls the two-photon transition $\frac{\pi}{2}$ pulses, i.e. the switch, the VVA, and the amplifiers for the microwave and RF transition.

The Ramsey time control system has two SRS DG535 pulse generators and a Siglent SDG 5122 arbitrary function generator. As shown in Fig. 6.11, the first pulse generator receives a trigger from the Adwin to start the Ramsey interferometer process and then outputs two brief pulses to trigger each $\frac{\pi}{2}$ pulse. The time interval between the two trigger is the $T_{Ramsey} + T_{\pi/2\,pulse}$.

The second pulse generator will keep its output voltage at high for $T_{\pi/2\,pulse}$, after receiving a trigger from first pulse generator. This signal will control the switches for both the microwave and RF systems, and the RF amplifier.

Meanwhile, the arbitrary function generator will start a negative square pulse after receiving the trigger of first pulse generator. This is an analog signal with high level at 10 V and low level at 7.5 V. This analog signal controls the VVA attenuation.

The last control signal for the Ramsey time control system is the Adwin signal for the Amaterasu amplifier. Since the Amaterasu amplifier needs to unmute long time before the Ramsey time (discussed in subsection 6.8.5), it will be hard to control by the pulse generator, but it also does not require a very high precision. The Adwin control signal will turn on few second before the Ramsey time and turn off after it.

The three signals (pulse generator switch control, arbitrary function generator VVA control, and the Adwin amplifier control) are sent into the microwave and RF amplifier systems. In the Amaterasu amplifier system, these three control signals are directed into the yellow external control signal block in Fig. 6.9.

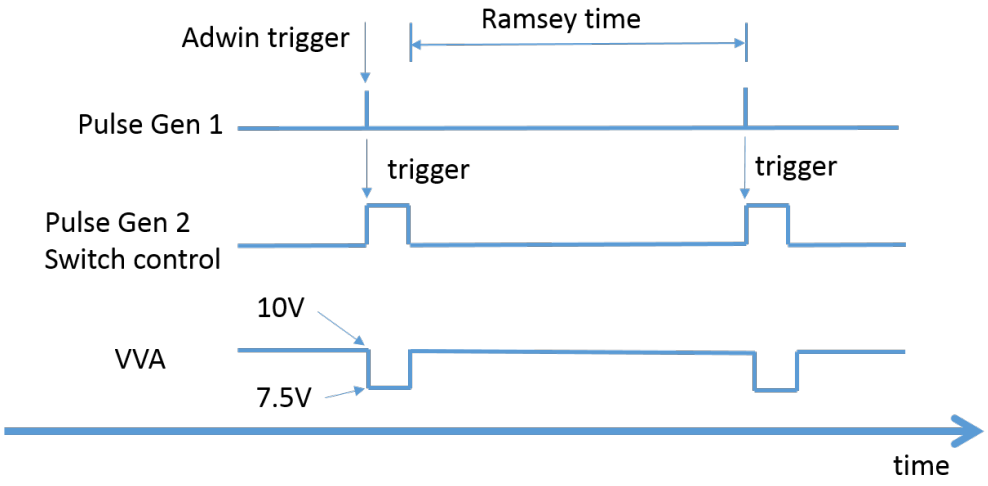

FIG. 6.11: Basic timing diagram for the Ramsey interferometer.

6.3 Experiment setup

We operate our experiment in the ODT, with the Ioffe field at 3.23 G, which is the magic magnetic field for the $|1,-1\rangle \leftrightarrow |2,1\rangle$ two photon transition.

In the ODT, the atom are initially in the $|2,2\rangle$ state, while our two-photon transition operates between $|1,-1\rangle$ and $|2,1\rangle$. We need a process to prepare our atoms into one of the two-photon transition states to start our atom interferometer experiment.

Fig. 6.12 shows the process for our atomic state preparation. We start from $|2,2\rangle$ and conduct an adiabatic rapid passage (ARP) to $|1,1\rangle$ with "Dr. Watts". Then, we use the Evap RF source to ARP the atoms into the $|1,-1\rangle$ state, which is our initial state for the atom interferometer experiment.

After the atom interferometer experiment, our atoms should be in a superposition of $|2,1\rangle$ and $|1,-1\rangle$ states. However, under the Stern-Gerlach push, the $|2,1\rangle$ state and the $|1,-1\rangle$ state have the same response (especially at the "magic" magnetic field), and we can not spatially separate these two states because both states have the same positive DC Zeeman energy shift. Instead, we apply an extra ARP process to transform the $|1,-1\rangle$ state component into the $|2,-2\rangle$ state, which has a negative Zeeman energy shift, somewhat opposite to that of $|2,1\rangle$. At this point, we can use a Stern-Gerlach push to separate the atomic spin states.

Since the ARP process does not require a very high quality microwave source, we use our "Dr. Watts" and Evap RF, which are less good, to operate the ARP process. The high-quality microwave source, Amaterasu, and the high-quality RF source, DDS prince charming, are used for the two-photon transition.

Fig. 6.13 shows the detail of the experimental process. We start with Dr. Watts to run the $|2,1\rangle$ remover and thus eliminate the remaining $|2,1\rangle$ state atoms in the ODT. The $|2,1\rangle$ remover scans from 6843.73632 MHz to 6836.98624 MHz for 400

ms and crosses the $|2,1\rangle$ to $|1,1\rangle$ transition resonance frequency to provide an AC Zeeman pushing force larger than the ODT trapping force, while leaving the $|2,2\rangle$ state atoms undisturbed. Next, we use "Dr. Watts" to operate the $|2,2\rangle$ to $|1,1\rangle$ ARP for 2 ms with a frequency scan from 6844.56064 MHz to 6846.73152 MHz. The next process is the ARP of $|1,1\rangle$ to $|1,-1\rangle$ transition. This transition is an RF level frequency transition, and we use the Evap RF source to scan the frequency from 6 MHz to 10 MHz for 100 ms. At this point, all of our atoms are initialized in $|1,-1\rangle$ for the atom interferometer experiment.

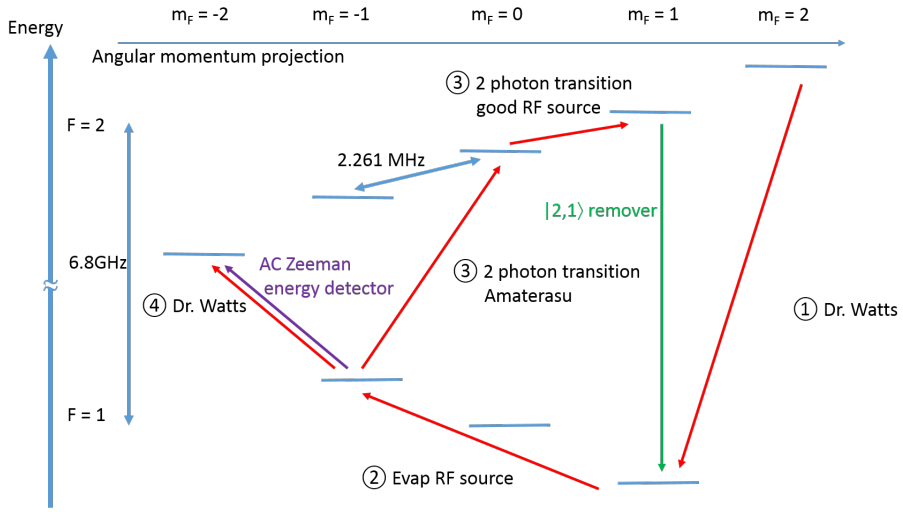

FIG. 6.12: Atom state preparation process.

The main atom interferometer experiment starts and ends with identical $\frac{\pi}{2}$ pulses on the two-photon transition (2-γ). As discussed in section 6.1, the frequency sources for the two-photon transition will directly affect the atom interferometer signal, which requires the quality to be as high as possible. We use the Holzworth and DDS Prince Charming, which are the best quality microwave frequency source and RF source in our lab, respectively. Based on the research of Andrew Rotunno, The DDS Prince Charming frequency peak has a FWHM around 2 Hz (measured with Anritsu MS2038C spectrum analyzer) after we multiply the DDS frequency by 64 times to the 6.8 GHz. The frequency settings of both the Holzworth and the DDS

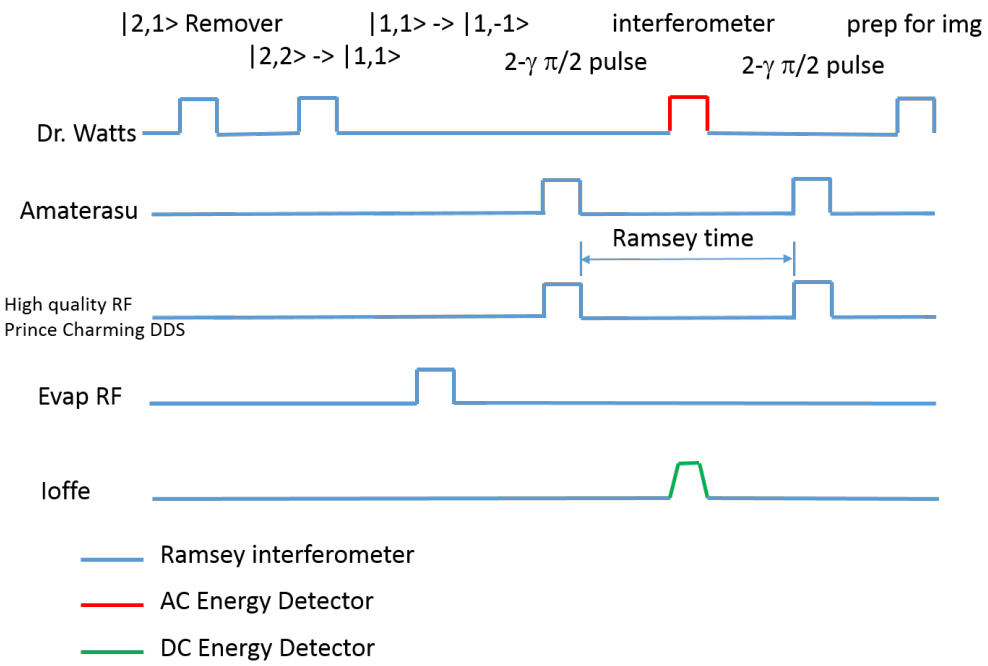

FIG. 6.13: Ramsey interferometer experiment timing diagram.

Prince Charming are determined every day by running a microwave scan experiment and a Rabi flop experiment. In the microwave scan experiment, shown in Fig. 6.15, we run the two-photon transition for a few seconds to make sure the Rabi flopping fully decoheres, and we scan one of the frequency sources, microwave or RF, to find the peak atom ratio. The resonance frequency for the two-photon transition should be at this peak, with amplitude 50% of the atom ratio $(\frac{N_{|\uparrow\rangle}}{N_{|\uparrow\rangle}+N_{|\downarrow\rangle}})$.

Next, we run a Rabi flopping experiment to determine the $\frac{\pi}{2}$ pulse time. The Rabi flop experiment runs the two-photon transition with the resonance frequency that we found in the microwave scan experiment and scans the two-photon transition driving time. The $\frac{\pi}{2}$ pulse time of the two-photon transition is the time it takes for the first Rabi flop to reach a ratio of 50%.

It is necessary to run the microwave scan and Rabi flop experiment every day because the signal drifting is severe in our apparatus. This drifting problem will be discussed in section 6.8, in which we found that the atom interferometer is drifting

with time, and this is very obvious even in the data recorded on the same day. Even though there is a signal drift, we cannot update the $\frac{\pi}{2}$ pulse setting multiple times within a day in practice, so we compromise to update the two-photon transition setting every morning and suffer the drifting during the day.

Our atom interferometer apparatus can be operated in three different modes: Ramsey interferometer, DC Zeeman energy detector, and AC Zeeman energy detector. We note that this last mode of operation becomes a spatial atom interferometer, if the AC Zeeman energy potential has a sufficient gradient (i.e. force) to spatially separate the Ramsey spin states.

Ramsey interferometer: The Ramsey interferometer has the simplest design, its basic timing operation is given by the blue lines in Fig. 6.13: In this case, during the Ramsey time between the two $\frac{\pi}{2}$ pulses no extra operations occur, and we scan the Ramsey time interval to observe the interferometer fringes. The phase of the atom interferometer signal evolves as $e^{i\frac{\Delta E}{\hbar}t}$, and in this mode of operation the energy difference between the states ΔE remains constant over the duration of the Ramsey time. The interferometer signal (i.e. the spin state population ratio) comes from the scan of t, the Ramsey time interval: the oscillation frequency is the detuning between the $\frac{\pi}{2}$ two-photon driving frequency and the two-photon transition energy.

DC Zeeman energy detector: The Ramsey interferometer can be operated as a DC energy detector by adding a DC magnetic field pulse (provided by the Ioffe field) during the Ramsey time, as shown by the green line in Fig. 6.13. In this case, the Ramsey time interval is kept constant, and the duration t_{DC} of the DC magnetic field pulse is scanned. Since the Ioffe field is already at the "magic" value (3.23 G), it is pulsed to a lower value. This temporary change in Ioffe field will shift the transition energy between the two states. The DC Zeeman energy detector signal is the atomic spin population ratio (i.e. Ramsey signal) that oscillates as the DC

magnetic field pulse duration t_{DC} is scanned. The oscillation frequency is equal to the change in DC Zeeman energy, $f_{DC} = \Delta E_{DC}/h$.

AC Zeeman energy detector: Similar to the DC Zeeman energy detector, the AC Zeeman energy detector applies a magnetic field pulse during the Ramsey time, but uses a microwave magnetic field instead. This microwave field is provided by Dr. Watts, and the associate timing is shown with the red line in Fig. 6.13. The AC magnetic field has a frequency that is resonant with the $|1,-1\rangle \leftrightarrow |2,-2\rangle$ transition. This AC magnetic field will shift the energy level for $|1,-1\rangle$ state and hence shift the transition energy between the two interferometer states, $|2,1\rangle$ and $|1,-1\rangle$. We scan the time t_{AC}, during which we apply the AC magnetic field, and this AC Zeeman energy shift will show up as an accumulated phase shift: when we scan t_{AC} the Ramsey signal (i.e. spin state population ratio) oscillates, with a frequency equal to the energy shift $\Delta E_{AC}/h$.

After the Ramsey interferometry procedure (or the AC/DC Zeeman energy detector variations on it), we need to spatially separate the different spin states so we can image them and count spin populations. The Stern-Gerlach force is a common mechanism for separating atoms with different spin states. However, we cannot use it directly, because as shown in Fig. 6.12, the DC Zeeman energy shift for both $|2,1\rangle$ and $|1,-1\rangle$ states is positive with almost the same value, and thus the Stern-Gerlach effect (force) cannot separate the two states. Instead, we use the Dr. Watts microwave source to run another ARP sweep to transfer the $|1,-1\rangle$ state into the $|2,-2\rangle$ state, which experiences a negative DC Zeeman energy shift, thus can be spatially separated from the $|2,1\rangle$ state via the Stern-Gerlach effect for imaging. This Stern-Gerlach separation process is a applied after the atoms are released from the ODT.

6.4 Two photon transition

This section presents the core part of the Ramsey interferometer: the two-photon transition. As shown in Fig. 6.14, the two-photon transition operates between the $|2,1\rangle$ to $|1,-1\rangle$ state. However, in order to not populate the middle $|2,0\rangle$ state, via a single photon transition, we operate with microwave and RF drive fields detuned by 1.35 MHz from this middle state. The value of the detuning can be a different number, but if the detuning is too small, then there is a risk of single-photon transitions. On the other hand, if the detuning is too large, then the two-photon transition will be very weak (small Rabi frequency) and very narrow, and thus hard to find. Empirically, we find that the 1.35 MHz detuning is the most convenient for our current apparatus. The remaining properties of the two-photon transition are very similar to the single-photon transition.

The Rabi frequency of two-photon transition $\Omega_{2-\gamma}$ is determined by the Rabi frequency of RF transition Ω_{RF}, the microwave transition $\Omega_{\mu W}$, and the one-photon detuning δ_{mid} from the middle state. In the limit of large detuning, i.e. $\delta_{mid} \gg \Omega_{RF}, \Omega_{\mu W}$, the two-photon Rabi frequency is given by the equation $\Omega_{2-\gamma} = \dfrac{\Omega_{RF}\Omega_{\mu W}}{2\delta_{mid}}$ [84].

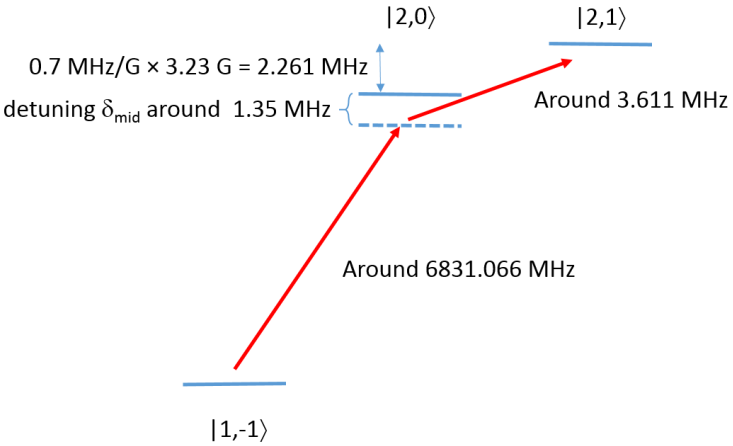

FIG. 6.14: Diagram of the frequencies and spin states involved in the two-photon transition.

6.4.1 Microwave scan

In order to use the two-photon transition, we must first find the two-photon resonance associated with it by conducting a microwave frequency scan, or an RF frequency scan. Since the exact position of this resonance drifts on a daily basis (e.g. due to magnetic field drift, ODT power drift, or master oscillator drift), we conduct such a frequency scan every day in the morning to find the best resonance frequency for that day.

The microwave scan experiment keeps constant one of the frequencies of the microwave or RF and scans the other one. Since the scan range is from a few hundred Hz to a few kHz in scale, it will not dramatically change the detuning.

The microwave scan experiment starts from the condition that all the atoms are in the $|1,-1\rangle$ state. At each frequency in the scan, the two-photon driving fields are applied for a few milliseconds so that the Rabi flopping has time to decohere. When operated exactly at the two-photon resonance, the spin population ratio decoheres to a 50/50 ratio.

Fig. 6.15 shows an example of the spin population ratio as function of microwave frequency for a two-photon resonance scan. We fit the curve with Lorentzian distribution: the center of the Lorentzian is the resonance frequency, and the width of the Lorentzian is the Rabi flopping frequency (if no other broadening mechanism are present). Since the Rabi flopping frequency is proportional to driving strength, the width of the Lorentzian is a good indicator of both the microwave and RF driving field strengths. Based on the plot in Fig. 6.15, the uncertainties on the resonance frequency and the resonance width are both about 10 Hz. The microwave scan experiment error on the resonance frequency makes it hard to set the $\frac{\pi}{2}$ pulse frequency exactly on the resonance, which guarantees that the Ramsey interferometer will always be operating at a finite detuning.

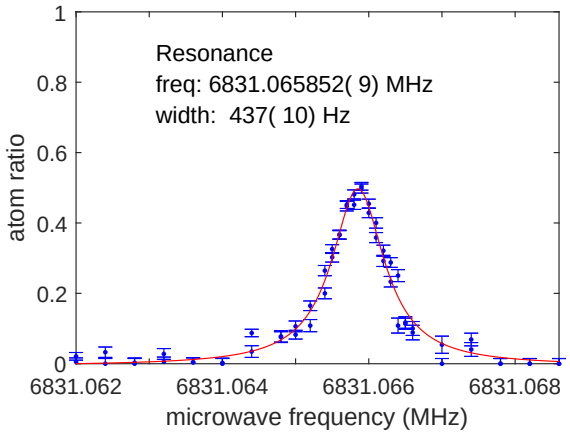

FIG. 6.15: Microwave scan to find the resonance frequency of the two photon transition. The peak frequency of the Lorenzian distribution is the resonance frequency for the microwave transition part of the two-photon transition. In the absence of other broadening mechanisms, the width of the Lorenztian gives the Rabi frequency. The RF frequency in this experiment is fixed at 3.61120459 MHz, i.e we set the DDS Prince Charming at 53.61120459 MHz. *Data gathered on Feb.13.2020*

6.4.2 Rabi flop

Once we have the resonance frequency for the two-photon transition, the next step is to conduct a Rabi flopping measurement to determine the $\frac{\pi}{2}$ pulse duration time. As shown in Fig. 6.16, the atomic spin population ratio oscillates with the two-photon driving field time and eventually decays to a 50/50 spin ratio after a few oscillations. It will completely decay after about 5 ms. In our daily experiment, we do not need to scan the time until full decay, as shown in Fig. 6.16. Instead, we only need to scan carefully around the first 50% atom ratio position for our $\frac{\pi}{2}$ pulse time (i.e. less than 1 ms).

6.4.3 Shift of resonance frequency with microwave power

The shape of the $\frac{\pi}{2}$ pulse can potentially affect the quality of the atom interferometer experiment. As shown in Fig. 6.17, a square RF pulse or microwave pulse will generate sidebands around the central frequency. Using a $\frac{\pi}{2}$ pulse with a smoother shape will tend to suppress these sidebands. but in practice, we found the

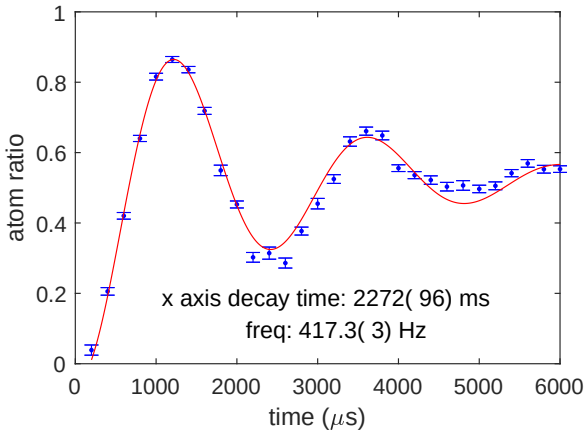

FIG. 6.16: Rabi flopping for the two-photon transition between $|2,1\rangle \leftrightarrow |1,-1\rangle$. The flopping has largely decayed after three flops. The decay may be due to the spatial variation of the RF and microwave driving fields, which largely originate from the nearby chip wires: The result is a spatially varying Rabi frequency that can tend to wash out the oscillations over the spatially distributed atomic cloud. The atom ratio is $\frac{N_{|2,1\rangle}}{N_{|2,1\rangle}+N_{|1,-1\rangle}}$. *Data gathered on Feb.10.2020*

square pulses easier to generate and use, since the smooth variation of the microwave and RF power proved to be problematic on its own.

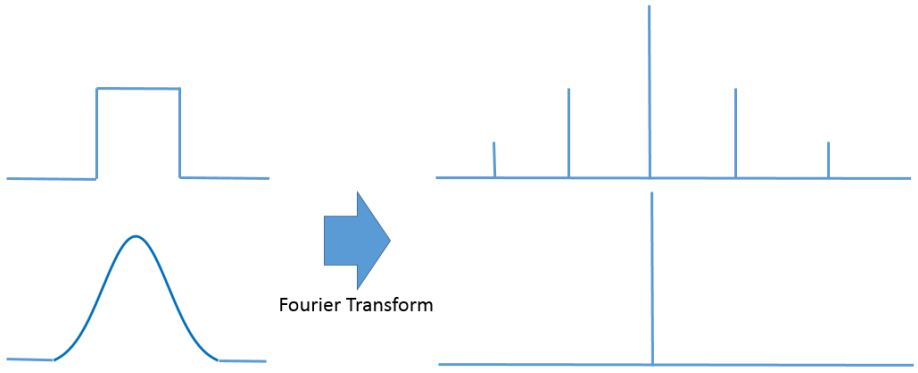

FIG. 6.17: A square pulse for the two-photon driving field will generate sidebands. A smoother pulse will suppress these sidebands.

Unfortunately, as shown in Fig. 6.18, we found that the microwave and RF fields that drive the two-photon transition can also shift the transition resonance frequency. Hence, the resonance frequency will shift with the power of the two-

driving fields. Fig. 6.18 shows the microwave scan resonance versus the microwave driving field power for the two-photon transition: The resonance clearly depends on the power and empirically has a quadratic dependence.

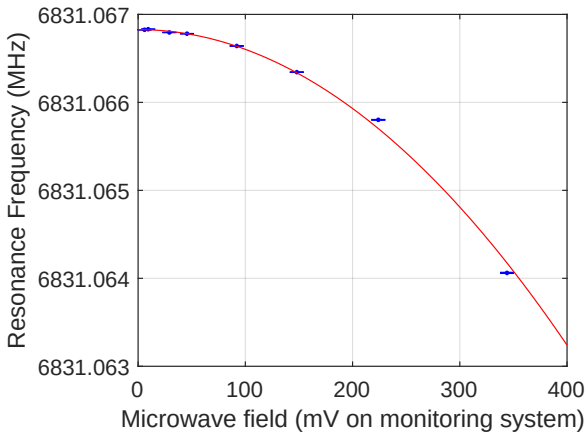

FIG. 6.18: Plot of the microwave scan resonance as a function of the microwave power. The data points are in blue. The red curve is a parabolic fit to the data that shows an empirical quadratic dependence. This effect is due to the microwave power that shifts the energy level and the transition frequency will shift with it. Due to this effect, we have to run our transition microwave with a square pulse, even if it will generate some sideband frequencies from the Fourier transform, rather than smoothly changing the power, which will cause unwanted ARPing of the atoms. *Data gathered on Feb.17.2020*

The resonance frequency shifts with two-photon transition power means the resonance frequency for a smooth-shaped $\frac{\pi}{2}$ pulse will also shift during the pulse. Since the driving frequency will not change during the $\frac{\pi}{2}$ pulse (i.e. chirping the frequency during the pulse is much more difficult), the shift in resonance frequency will act as effective ARP and lower the quality of the atom interferometer.

The ideal solution is to sweep the driving frequency with the $\frac{\pi}{2}$ power to ensure that the driving frequency always matches the resonance frequency. However, this approach is not realistic for now. First, the resonance frequency for the same $\frac{\pi}{2}$ pulse power will drift day by day, and we are not sure the resonance frequency shift with the $\frac{\pi}{2}$ pulse power will stay the same every day. Second, we cannot run the microwave scan experiment for all the different two-photon transition powers to make a curve like Fig. 6.18 every day. Finally, even if we did have such a daily

curve, our apparatus is not configured currently for accurate simultaneous power and frequency changes to chirp the frequency in a quadratic manner for a smooth $\frac{\pi}{2}$ pulse.

As a compromise, we choose our $\frac{\pi}{2}$ pulse to be a square pulse, even if it will generate sidebands. A square pulse is the best choice for the $\frac{\pi}{2}$ pulse based on our current experimental capabilities.

6.5 Ramsey interferometer

This section presents our results for the basic trapped atom Ramsey interferometer, which is the cornerstone for the atom interferometer. For reference, the basic operation of the Ramsey interferometer is described in section 6.3.

Fig. 6.19 shows the Ramsey interferometer fringes as the Ramsey time is varied: The atomic spin population ratio oscillates as the Ramsey time is varied. The Ramsey interferometer fringes largely maintain their amplitude for at least 500 ms with limited loss of contrast. However, the fringe frequency's stability starts to worsen around 100 ms, which hints that we have some yet-to-be-determined frequency noise source that appears on this time scale.

The data shown in Fig. 6.19 is taken in order from the small Ramsey time to the larger Ramsey time with a experiment cycle for each data point. The error bar on each data point is the uncertainty of 1-D Gaussian fitting from the camera program, which is described in section 2.2.7. The red fitting line shows the sinusoidal fitting result based on data in each Ramsey time segment of that box (e.g. 0 ms to 10 ms for the left top plot).

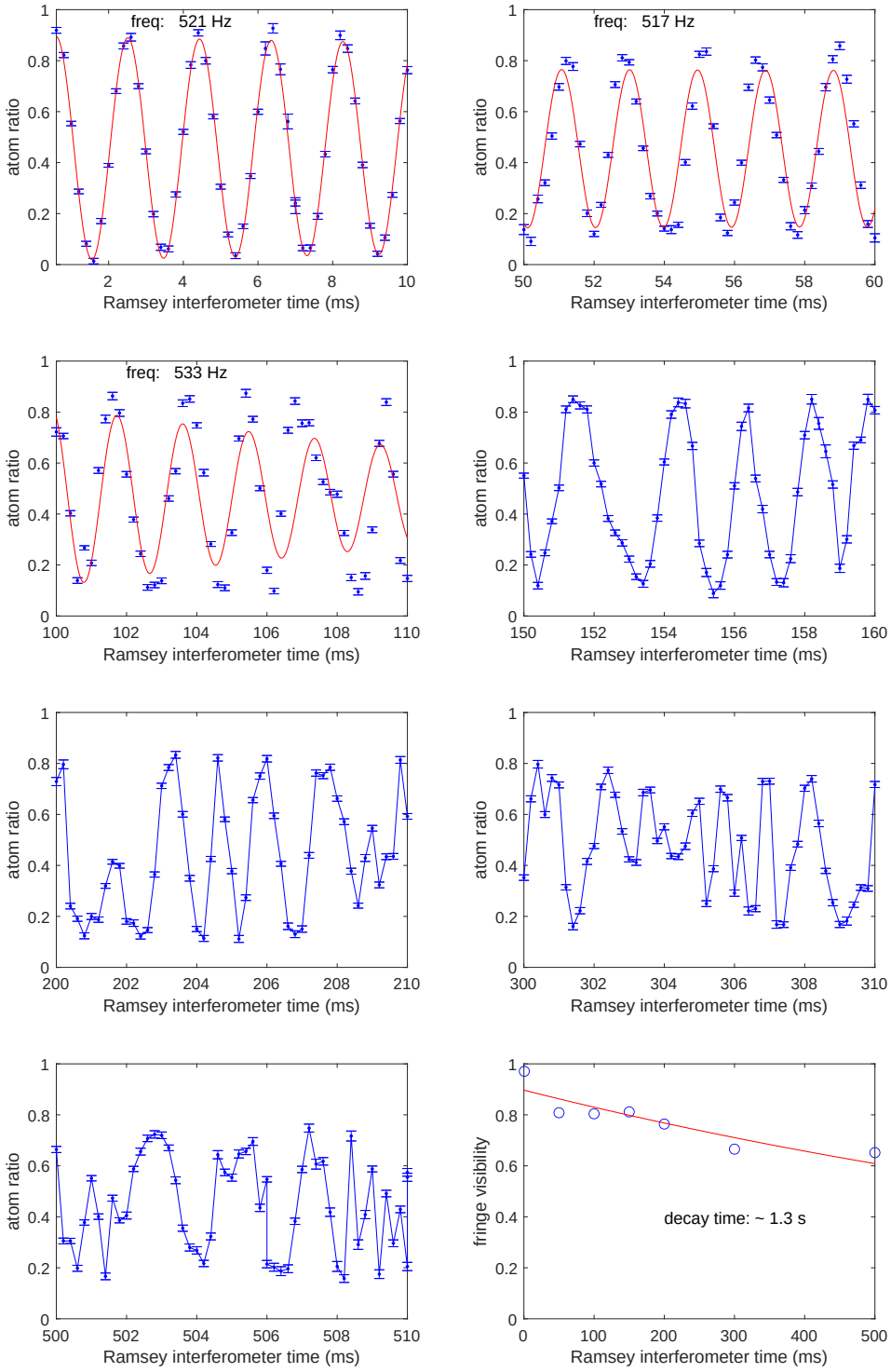

FIG. 6.19: Ramsey interferometer signal. All seven plots show the Ramsey signal (atomic spin population ratio) versus the Ramsey time for different Ramsey time segments. The data points are in blue, and their error bars are the result of Gaussian fit of a single image for each point. In the first three plots, the red line is a least squares sinusoidal fit to the data with an exponential decay envelop: the fit parameters are independent for each plot. The last figure is the decay rate of the fringe visibility. *Data gathered on Jul.12.2019*

These Ramsey fringe measurements show that we have successfully operated the Ramsey interferometer, even if the performance is limited and needs to be improved in the future. Since most of the initial spatial atom interferometer tests will use Ramsey times of less than 100 ms, the present performance is quite sufficient for initial proof-of-principle work.

Base on the data, we can extract the fringe visibility from each time segment, which is defined by $\text{FringeVisibility} = \dfrac{(\text{MaxRatio} - \text{MinRatio})}{(\text{MaxRatio} + \text{MinRatio})}$. The decay time for this fringe visibility is around 1.3 s, which should roughly represent the coherence time t_c for this Ramsey interferometer experiment.

6.5.1 Ioffe calibration

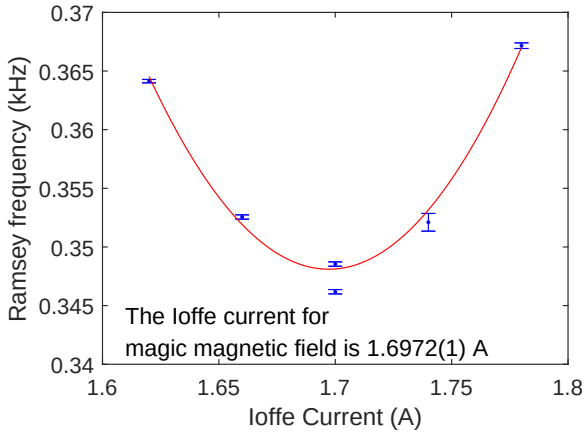

FIG. 6.20: Ramsey fringe frequency versus Ioffe magnetic field. We calibrate the Ioffe current to the magic magnetic field (nominally 3.23 G) by running the Ramsey interferometer experiment with different Ioffe currents and then finding the bottom of the quadratic curve. In this experiment, the Ramsey interferometer fringe frequency is the same as the detuning of the two-photon driving field from the total transition energy. The zero derivative point on the quadratic fit (i.e. the bottom of the parabola) gives the current setting for the "magic" magnetic field, which is the field at which the interferometer is the least sensitive to magnetic instabilities (noise, deviation, drift). There are two data points at 1.7 A, but the error bar of the two data points did not overlap each other: this discrepancy indicates that the shot-to-shot uncertainties are larger than those from a single image fit. *Data gathered on Jul.08.2019*

The Ramsey interferometer provides us a new tool to precisely probe the DC magnetic Ioffe field. One of the applications is to calibrate our Ioffe field to the

magic magnetic field value of 3.23 G.

The Ioffe calibration experiment works by running the Ramsey interferometer experiment for different Ioffe currents for the same two-photon transition driving frequency. As we discussed in section 6.1, the Ramsey interferometer fringe frequency is the frequency difference between the transition energy and the two-photon transition, i.e. the detuning for the transition. If we keep the two-photon transition driving frequency the same, then the Ramsey interferometer fringe frequency shows how the transition energy changes with the Ioffe current. The magic magnetic field is where the transition energy has the highest stability to magnetic noise and Ioffe current noise, i.e. the magnetic field at which a small change in field value results in zero first order change to the Ramsey fringe frequency.

Fig. 6.20 shows the results of the Ioffe calibration measurements. The data and the associated empirical quadratic fit clearly show that the Ramsey fringe frequency bottoms out at a Ioffe magnetic field current of about 1.6972 A with error bar 9.5×10^{-5} A (this error bar is statistical error). This current is the magic magnetic field setting for our Ioffe current.

6.6 Energy detector experiments

This section presents both the DC and AC Zeeman energy detector experiments. The DC magnetic Ioffe field and the microwave near field generated by Dr. Watts are the DC and AC magnetic fields, respectively, that we detect in the energy detector experiments. We generate an interferometric signal by scanning the duration the magnetic field pulse (DC or AC field), which is pulsed on during the Ramsey time, i.e. between the two $\frac{\pi}{2}$ pulses (green and red signals, respectively, in Fig. 6.13). The interferometric fringe frequency, generated by the energy detector scheme, is the DC or AC Zeeman energy shift: $\Delta E_{DC}/h$ or $\Delta E_{AC}/h$.

6.6.1 DC Zeeman energy detector

Fig. 6.21 shows the basic interference fringe generated by the DC Zeeman energy detector scheme. The energy detector shows an obvious oscillating fringe signal, but the frequency is not very stable. The frequency stability is worse than the Ramsey interferometer on the same time scale. This instability has three possible causes. The first possibility is that the Ioffe field might have an overshoot right after we change its value for the pulse. The second possibility is that the timer of the Adwin system, which controls the Ioffe current pulse, is not sufficiently stable. The last possibility is that the change in the Ioffe magnetic field means that the atoms are no longer at the "magic" magnetic field condition, and so the fringe signal will be more sensitive to magnetic field noise and drift.

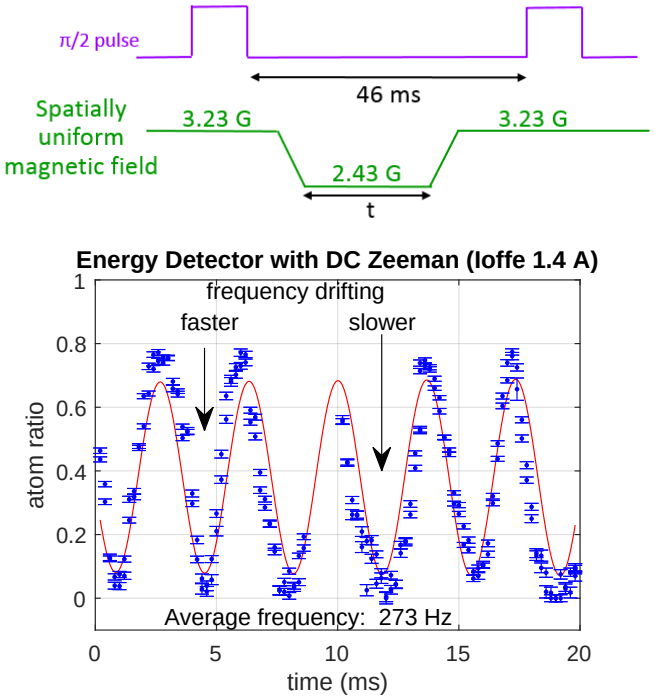

FIG. 6.21: Interferometric fringes for the DC Zeeman energy detector. The fringes are generated by shifting the DC magnetic Ioffe field to 1.4 A (from the standard 1.6972 A) for the time listed on the x-axis. The fringe frequency is not very stable and clearly drifts over the course of the measurements. These data are taken in sequence from 0 ms to 20 ms with one experiment cycle for each data point. In this experiment the Ramsey time is set as 46 ms, which left enough time for the DC Zeeman shift pulse. *Data gathered on Feb.28.2020*

Fig. 6.22 shows the DC Zeeman energy detector fringes on a longer time scale. The red sinusoidal curve (with an exponential envelope) is a fit to the first 30 ms of data, while the dashed blue curve is a fit to the data in the 100 - 130 ms time segment. The sinusoidal curve fit with the equation $Ae^{-Bx}\sin(Cx + D) + E$. This data is well fit by the sinusoid curve out to 30 ms, but the data in the 100 - 130 ms time segment is clearly out-of-phase with the initial fringes (data and red fit). However, the signal still has fringes of comparable amplitude at 100 ms as at 10 ms, which means that the atoms have not decohered after 100 ms, and that the main problem with our apparatus is the instability in the fringe frequency. Notably, the data in Fig. 6.21 and Fig. 6.22 are taken in different days, but the resulting frequencies are almost the same, which indicates our apparatus is very stable.

Theoretical prediction: The current setting in our Adwin control system for 3.23 G is 1.698 A, and the Ioffe field changes with the current by 2.6817 G/A (measured by Charlie Fancher [57]). Then, we know the magnetic field at 1.4 A should be 2.4309 G (there is an environmental offset magnetic field). The theoretical transition frequency for $|2, 1\rangle \leftrightarrow |1, -1\rangle$ for 3.23 G is 6834.678383 MHz, while for 2.4309 G is 6834.678105 MHz. The transition frequency difference under these two magnetic field conditions is the differential DC Zeeman energy shift (278 Hz), which is close to our experimental measurement of 273 Hz.

6.6.2 AC Zeeman energy detector

The AC Zeeman energy detector result is quite different from the DC Zeeman energy detector result. We follow the same procedure as in the DC Zeeman energy detector, but instead use a microwave pulse from Dr. Watts during the Ramsey time, while keeping the Ioffe magnetic field constant. The microwaves have a detuning of $\delta = -2\pi \times 2.5$ MHz with respect to the single-photon $|1, -1\rangle \leftrightarrow |2, -2\rangle$ transition.

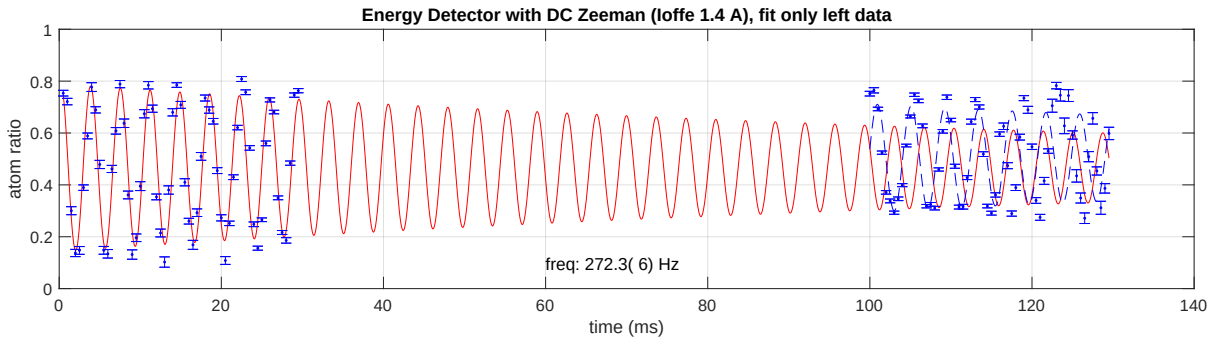

FIG. 6.22: Evolution of interferometric fringes for a long DC magnetic pulse (similar experiment to that in Fig. 6.21) but for longer times). As in Fig. 6.21, the fringes are generated by shifting the DC magnetic Ioffe field to 1.4 A (from the standard 1.6972 A) for the time listed on the x-axis. The red sinusoid is fit to the 0 - 30 ms data, while the dashed blue sinusoid is fit to the 100 - 130 ms data. The sinusoid function includes an exponential envelope. The red and blue curves clearly show that the phase has slipped (or the frequency has shifted) between 30 ms and 100 ms. Similar to Fig. 6.21, the data is taken in sequence from 0 ms to 30 ms and 100 ms to 130 ms with one experiment cycle for each data point. *Data gathered on Mar.02.2020*

We direct the microwaves into U wire 1 to produce an AC Zeeman near field potential for the atoms in the ODT, which shifts the energy of the $|1,-1\rangle$ state level down. Again, we look at the interferometric fringe when we scan the microwave pulse time. As shown in Fig. 6.23, the fit to the fringe oscillation is better for the DC energy detector (e.g. Fig. 6.21), and the fringe oscillation frequency is faster for higher microwave power, as expected.

The AC magnetic field in this experiment comes from "Dr. Watts", and the "Dr. Watts" VVA is different from the Amaterasu and Baku. The "Dr. Watts" VVA has different control voltage setting as Amaterasu. The "Dr. Watts" VVA has full attenuation at 5V and full pass at 0 V, so in our data, the 3.5 V VVA has higher power than 4V VVA.

Even though the AC Zeeman energy detector has a relatively clean fringe signal (i.e. single frequency sinusoid), as compared to the DC Zeeman energy detector, it also features a detrimental coherence decay rate. The AC Zeeman energy detector has a very high decay rate, and the decay rate will be faster for higher power on

Dr. Watts. This behavior indicates that the atoms are decohering very quickly under the effect of Dr. Watts. Since the DC Zeeman energy detector has a longer coherence time, the reason for the fast decoherence should be due to some aspect of the microwave magnetic near field from the Dr. Watts.

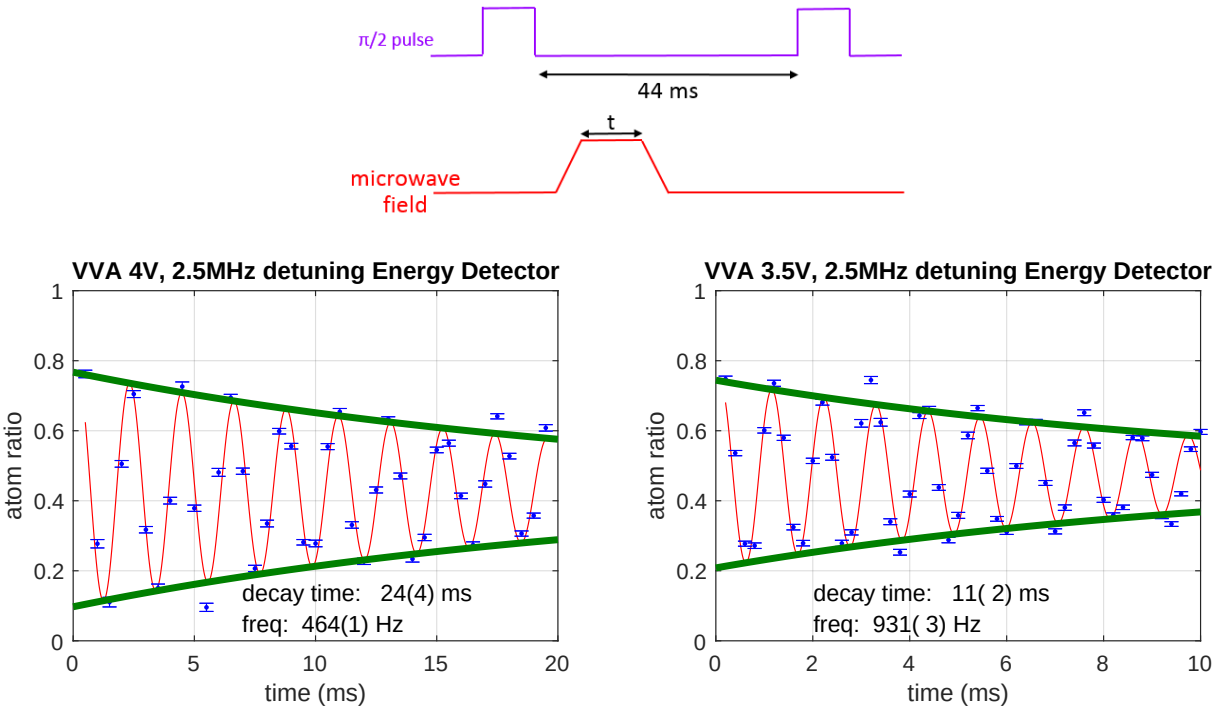

FIG. 6.23: Interferometric fringes for the AC Zeeman energy detector. The AC Zeeman potential is generated by U wire 1, which is driven by Dr. Watts and targets the $|1,-1\rangle \leftrightarrow |2,1\rangle$ transition with microwaves at a red detuning of $\delta = -2\pi\times$ 2.5 MHz. The atoms are trapped in the ODT at a distance of about 100 μm from the chip Z wire, and thus experience substantial gradient in the AC Zeeman potential generated by U wire 1. The red curve is a least square fit to the data with a sinusoid function with an exponential envelope. The green envelop shows the amplitude of the interferometer signal, which decay very fast. The decay time is around 10 ms for the 3.5 V case, and 20 ms for the 4 V case. The frequency of interferometer signal performs as we expect, the higher power (3.5V VVA) has higher frequency than lower power (4V VVA). However, the decay time also gets faster with the power increase. The reason for this effect is not clear yet, it might because the curvature of the microwave or the separation of the atom spin states. *Data gathered on Mar.03.2020*

One hypothesis for the fast decoherence comes from the curvature of the microwave (AC) magnetic near field. The AC magnetic field in the AC Zeeman energy detector experiment connects to the atom chip U wire 1, as shown in Fig. 6.6. The

U wire is very close to the ODT trap, and the AC magnetic field has a high curvature and high gradient for the trapped atoms. As shown in Fig. 6.24, the high curvature distorts the harmonic ODT trapping potential for atom in the $|1,-1\rangle$ state and modifies the trap frequency (or distorts it away from harmonic), thus shifting the energy of the trapped atoms in the $|1,-1\rangle$ state. The trapping potential energy adds to the transition energy (and depends on the energy of trapped atoms) and thus atoms of different energies will have slightly different interferometric fringe frequencies, thus leading to decoherence.

The decoherence time base on the change of trap frequency have a equation $t_c = \frac{\omega}{|\delta\omega|}\frac{\hbar}{kT}$ [85], where the ω is the trap frequency, $\delta\omega$ is the change of trap frequency, k is the Boltzman constant, and T is the atom cloud temperature. If we assume the trap frequency has shift by 0.1% with the atom temperature at 300 μK, the decoherence time will be only around 25 ms. This equation shows the small change on the trap frequency effect a lot on the decoherence time.

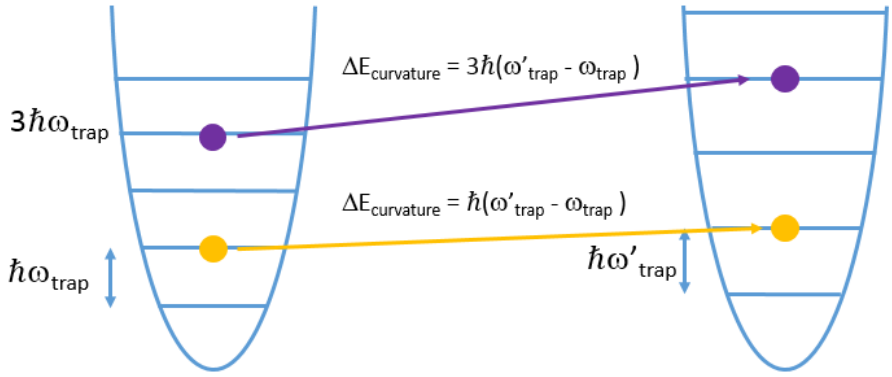

FIG. 6.24: The curvature of AC Zeeman force distorts the trap, and hence modifies the trap frequency. Atoms in different trap state suffer a different energy shift from this distortion, thus decoherence happens.

Another hypothesis for the fast decoherence is based on the gradient of the microwave near field. The high gradient will generate a force and could spatially separate the atoms' $|1,-1\rangle$ from the $|2,1\rangle$ state, which is necessary for the spatial

atom interferometer. However, if we operate the second $\frac{\pi}{2}$ pulse without spatial overlap of the $|1,-1\rangle$ and $|2,1\rangle$ states, then the spatial part of the interferometer is not closed, and the interference cannot happen. In other words, the final position of an atom (and its state) will indicate which path it took, thus eliminating the interference, or in the case of partial overlap resulting in decoherence.

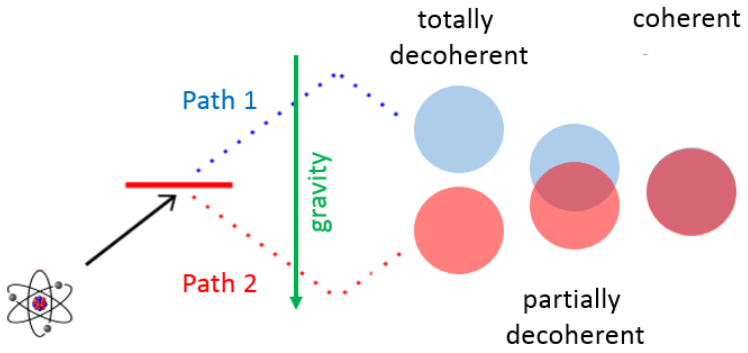

FIG. 6.25: The gradient of AC Zeeman potential (i.e. force) separates the atoms based on their spin states, the atom slosh back after the force turned off. If the second $\frac{\pi}{2}$ pulse operate without the atom clouds overlap, then there is a open atom interferometer, and the atom population fringes will disappear.

We use ultracold thermal atoms for all the atom interferometer experiments, and the atom cloud has a relatively large size. The high gradient of the AC magnetic field causes the different parts of the atom cloud to feel the varying strength of the AC magnetic field. Thus, atoms at different positions in the cloud will produce different interferometric fringe frequencies due to the high gradient, and thus the combined fringe signal will tend to wash out quickly. This problem is most acute when the AC near field is applied abruptly to an extended cloud.

One way to reduce the size of the atomic cloud is to cool it further. A colder cloud has a smaller size, which will reduce the change in AC Zeeman potential across it due to a gradient, and which can also limit in part the effect of potential curvature. However, based on our experience, it is hard to further cool our atoms from where

we are.

In the case off the gradient pushing the $|1,-1\rangle$ state to follow a different path, we can adjust the Ramsey time so as to control the time between turn off the AC Zeeman potential and the time of the second $\frac{\pi}{2}$ pulse. This idea is to wait for the atom cloud to oscillate in the ODT, and then apply the $\frac{\pi}{2}$ pulse when the two clouds for the $|1,-1\rangle$ state and $|2,1\rangle$ state overlap. However, this test also faces a problem that our ODT does not have the same trap frequency for the x and y direction, which we will discuss in section 6.8. Since the "Dr. Watts" source is on the U wire, which is positioned at an angle of 45° away from the ODT, and the ODT is elliptic in shape, the $|1,-1\rangle$ atom cloud will not necessarily return to its original position along both axes at the same time, once we push it. We either need to make the ODT potential symmetric in the xy-plane or move the ODT under U wire 1 so that any push from the potential gradient is along the vertical axis, which is a principal axis of the ODT trapping potential. However, once we positioned the ODT directly below U wire 1, we discovered an issue with the two-photon transition, which is discussed in subsection 6.8.1.

In the longer term, the curvature of the near field potential can be suppressed by using multiple wires (with well picked phases) to generate a nearly linear potential. The successful interferometery experiment with a BEC by Böhi and co-workers [51] used three wires (and a ground plane) as a co-planar waveguide, which generates a roughly linear near field potential. The Ph.D. thesis of Andrew Rotunno explains and demonstrates multi-wire phase manipulation that should be able to achieve a linear potential or a flat one (at a near field saddle point) [54]. However, based on our lab schedule, the multi-wire phase manipulation of a near field potential experiments (to produce an RF AC Zeeman trap) began immediately after the atom interferometer experiment, so we leave this idea for future lab members. Finally, since the long-term objective is to have spatially separated traps for $|1,-1\rangle$ and

$|2,1\rangle$ to create a spatial atom interferometer, the use of AC Zeeman traps for moving the atoms in a spin-dependent manner should mitigate the gradient and curvature problems encountered here.

6.7 Data fitting

This section discusses the data fitting used in this chapter. The data fitting includes the atom number determination based on the camera absorption image, sine wave fitting for the interferometer signal, and the Lorentzian curve fitting for the microwave scan.

The spin state population ratio data (generally abbreviated as "atom ratio" in the plots) comes from the camera images. The camera CCD images contain digital counts for each CCD pixel. The digital count number is proportional to the number of photoelectrons generated in the pixel (determined by the camera amplifier gain) and thus the number of photons incident on the CCD pixel. The radial imaging camera (used for all the image data in this chapter) has 640 $\times$ 480 pixels, spaced 7.4 μm center-to-center. We choose a rectangular region of interest (ROI) around each of the atom clouds in an image; each cloud corresponds to a spin state, after the Stern-Gerlach separation effected upon releasing the atoms from the ODT.

The details of the absorption imaging process were introduced in Chapter 2, and we follow a similar process to calculate the atom number for each pixel.

The cross-section of each atom cloud is close to a Gaussian distribution, so we fit the data with a Gaussian curve and calculate the atom number based on its amplitude and width. Since it is hard to automate reliable 2D Gaussian fits, instead, we sum the pixel atom number counts along one axis of the ROI (x or y depending on the fit) to generate a 1D Gaussian representation of the atomic cloud (with the same width). In this manner, we analyze all of our image data with 1D Gaussian

fits.

In our experiment, there is an additional complication brought about by the presence of an explained "dark spot" in the processed atom number image (i.e. $N_{atom}(x, y)$), which is possibly due to a thermal effect from the ODT laser beam (we use high quality optical filters to prevent the ODT beam from entering the camera). We suspect that the ODT laser heats some mirror or the glass cell section that is shared with the imaging probe and that this heating in turn distorts the probe laser beam somewhat (there is about a 0.5 s time gap between image with atoms and the background laser image during which some of the heated optical elements could cool locally). Solving this problem from the apparatus side requires some additional labor, so we dealt with it through an analytical method. We took several images without atoms and gathered the dark spot information from these. We then compensate for the pixels in the "dark spot" region of the background laser image.

After we have the atom count for each pixel, we use the MatLab built-in "fit" function to fit using a 1D-Gaussian equation: $Ae^{-(x-C)^2/(2W^2)} + D$ where A is the amplitude, C is the center of the Gaussian curve, W is the width of the Gaussian curve, and D is the offset. Then the total atom number for the target state can be calculated by the equation $N_{atom,TargetState} = \sqrt{2\pi} \times A \times W$.

The 1D-Gaussian fitting works well when there are a lot of atom in the ROI. However, the fitting quality is terrible when there is almost no atoms. The program will fit the Gaussian to the random background noise, and the fitting curve might be ridiculous and even fit to a negative atom number. To improve the fitting quality, we take the average center position and width from images with enough atoms for good fits, and fix these two parameter for the Gaussian curve, and set the amplitude of the fitting parameter as A^2 to prevent a negative amplitude, i.e. Amplitude = A^2. When the amplitude is very close to zero, in which case there is a significant risk of getting a negative amplitude without the A^2 method, the uncertainty on the

width of the Gaussian can be unphysically large. In order to avoid this issue, we fix the width (i.e. it is not a fit parameter) of the Gaussian to be the average value for the width obtained from regular fits of images with large atom clouds.

The error for the atom number is obtained by using the error calculation method described in the book by Bevington and Tobinson [86], and for the errors for the χ^2 calculation we use the standard deviation of the residuals. The uncertainties on the fit parameters are determined from the curvature of the χ^2 function at its minimized value, which then gives us the errors on the amplitude and width parameters of the Gaussian fit: $\sigma_{amplitude}$ and σ_{width}, respectively (1-sigma errors). From these fit parameters and associated uncertainties, we can compute the error on the atom number in a fitted atom cloud: $\sigma_{AtomNumber} = \sqrt{2\pi} \times (\text{Amplitude} \times \sigma_{Width} + \sigma_{Amplitude} \times \text{Width})$.

Once we have the atom number for both the $|2,1\rangle$ and $|1,-1\rangle$ states, we can calculate the atom ratio as $\text{AtomRatio} = \dfrac{N_{|2,1\rangle}}{N_{|2,1\rangle} + N_{|1,-1\rangle}}$. Hence the error of the atom ratio is given by

$$\sigma_{AtomRatio} = \text{AtomRatio} \times (1 - \text{AtomRatio}) \times \sqrt{(\frac{\sigma_{|2,1\rangle}}{N_{|2,1\rangle}})^2 + (\frac{\sigma_{|1,-1\rangle}}{N_{|1,-1\rangle}})^2} \qquad (6.1)$$

Finally, for the sinusoid fits of the interferometer fringe signal and the Lorentzian fits of the microwave scan data, we use the same built-in MatLab "fit" function. However, we use a weighted fit with the weight for each data point given by $\dfrac{1}{\sigma^2_{AtomRatio}}$, where in these cases $\sigma_{AtomRatio}$ is the error on the atom ratio computed from eq. 6.1.

6.8 Experimental issues

This section discusses some of the unsolved issues that remain in our atom interferometer experiment. These problems are critical to improving the quality of our atom interferometer.

6.8.1 Two-photon transition sidebands

When we lowered the microwave and RF power to reduce the frequency shift on the two-photon transition (see Fig. 6.18), the transition width became very narrow (< 100 Hz), and we observed sidebands when doing the microwave frequency scan. The sidebands showed up after moving the ODT under the U wire and lowering the $\frac{\pi}{2}$ pulse power.

As shown in Fig. 6.26, there are three peaks in the single microwave scan data. The middle peak is highest and is the main transition peak, and the peaks on both sides are relatively more minor, and we refer to them as sidebands.

If we assume that the main peak and the sidebands follow Lorentzian distributions, then we can fit the data with an equation that is the sum of three Lorentzian. However, there are few data points on the sidebands, and the fitting quality is not that good. When we constrain the widths of both sidebands to be the same value, then the fitting quality improves.

The sidebands are separated by about 150 Hz from the center peak. If we compare the separation width with higher power microwave scans experiment before, e.g. in Fig. 6.15, which has a peak width around 2 kHz, then the sidebands may be present but would be hidden within the central peak. We have looked for a technical origin for the sidebands, i.e. from the microwave and RF sources (and associated VVAs, switches, amplifiers), but the spectrum analyzer shows no evidence of sidebands in the RF or microwave fields directed at the atoms.

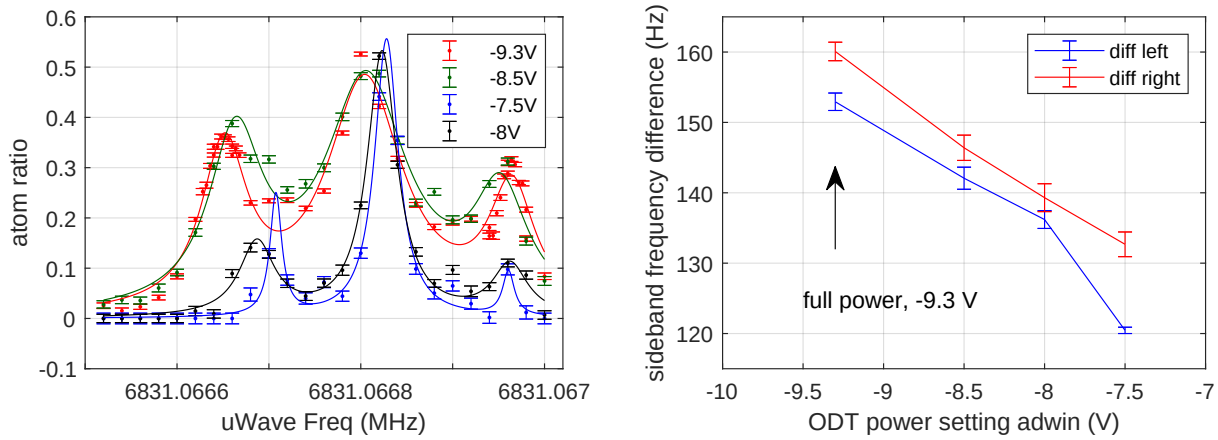

FIG. 6.26: Sidebands in a microwave scan with very low microwave power (around 50 Hz width). The sidebands are around 150 Hz away from the center peak, which is around the ODT trap frequency. If we lower the ODT power (indicated by the voltage: more negative voltage indicates higher ODT power), the trap frequency also get smaller and the sidebands get closer to the center peak. This behavior hints that the sidebands comes from a mechanism that related to the motion of atoms in the ODT. The widht of the peak seems to depend on the ODT power as well, we need more data to confirm this hypothesis, but it might indicates the peak of the sidebands are related to the temperature or the position of the atom cloud, which could be effected by the ODT power. *Data gathered on Mar.19.2020*

We have looked for a connection between the sidebands and the ODT. We changed the ODT power and ran the microwave scan experiment to check whether the sidebands change. As shown in Fig. 6.26 (right), the frequency separation of the sidebands from the central peak drops with the ODT power. The ODT power at -9.3 V is the highest power and the experiment setting value for the atom interferometer experiments discussed above. The ODT power is lower with a less negative voltage, and the -7.5 V setting is the lowest ODT power in this set.

This result hints that the sidebands are related to the ODT in same way. We have two hypotheses for the origin of the sidebands: 1) Classically, if the atoms are sloshing around in the trap while embedded in a microwave or RF near field with a gradient, then in the frame of the atom the strength of the fields will vary at the sloshing frequency ω_{trap}, i.e. the atoms will see an amplitude modulated (AM) field, which in frequency space has sidebands at the AM frequency (the trap sloshing

frequency). 2) Quantum mechanically, the two-photon transition could also add or remove one quantum of trap mechanical energy, i.e. $\hbar\omega_{trap}$, so that the transition moves atoms from trap energy level n to $n \pm 1$ in addition to the internal hyperfine energy change, similar in spirit to what happens in resolved sideband cooling in trapped ions [87]. In principle, $\Delta n = \pm 2, 3, etc$ transitions are also possible, but though possibly less likely (Franck-Condon principle): however, experimentally, we do not see any 2nd or 3rd order sidebands, only first orders ones, though we did not conduct a dedicated search for these. Notably, the lower frequency sideband consistently has a larger amplitude than the higher frequency sideband, though we are not sure what to make of this difference. However, to further research the role of the ODT in the sideband generation process, we need to improve the ODT quality, and the first thing we should do is fix the shape of the ODT so that it is round (see section 6.8.2.

Furthermore, the frequency separation for the left sideband (lower frequency) is smaller than for the right sideband (higher frequency), i.e. the left sideband is closer to the central peak. The possible cause could be: 1) the curvature of the microwave or RF near field, or 2) the power shift of two-photon transition in a near-field gradient. We need further research to confirm this hypothesis.

6.8.2 ODT shape issue

One issue that was discovered part way through the interferometry experiments is that the ODT has a transverse elliptic shape, i.e. the vertical and horizontal trap frequencies are quite different.

This anisotropy is not intentional. Initially, the ODT was relatively isotropic in the transverse directions [53], but it must have been deformed during a realignment. There is a big realignment process happens when we replace the optical platform [54]

around end of 2019. If we assume this realignment is the cause of the elliptic shape ODT, the Ramsey interferometer experiment and the Ioffe calibration experimen (section 6.5) was not effected, but the Energy detector experiments (section 6.6), including DC and AC Zeeman energy detector, and two-photon transition sidebands experiment (subsection 6.8.1) were effected.

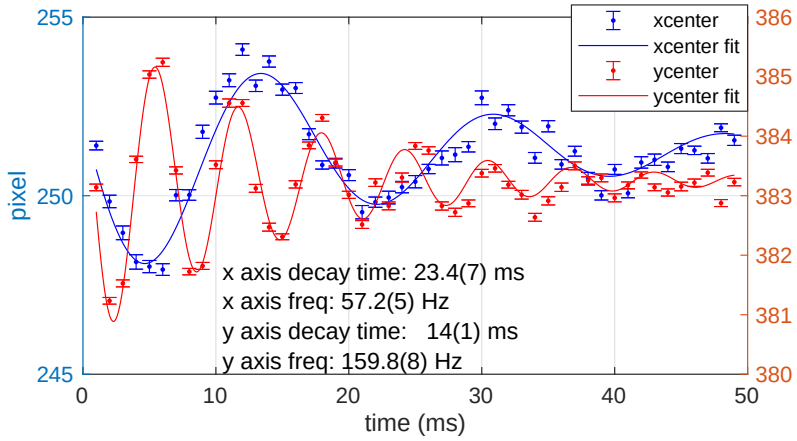

FIG. 6.27: Optical dipole trap sloshing test at full laser trapping power. This plot shows that our ODT is elliptic in shape since the trap frequencies are not the same in the x and y directions. The sidebands shown in Fig. 6.26 at full power are about the same as the y-axis trap frequency. Since the ODT frequency in x axis is in the same level as the width of the peak in Fig. 6.26, we do not know whether the ODT frequency in the x-axis does not generate sidebands or just hidden in the main peak. The ODT frequency difference in the x and y directions means that atoms will not return to its original x and y positions at the same time in interferometer experiment if the AC Zeeman force is not along the x or y axes. *Data gathered on Mar.09.2020*

Fig. 6.27 shows the trapping frequency for the x and y directions, which differ by a little less than a factor of three. The x-axis is the horizontal axis, which has a trap frequency around 57 Hz, and the y-axis is the vertical axis, which has a frequency around 160 Hz. We took this data at the -9.3 V ODT power setting, and its y-axis trap frequency roughly matches the sideband frequency difference for the right peak (high frequency side sideband). The different trap frequencies between these two axes show that the ODT has an in elliptic shape (in transverse plane). The long axis is the x-axis (horizontal) and the short axis is the y-axis (vertical). The elliptic ODT means that the atom cloud will not slosh along the force axis if

we push it from 45° above, i.e. push from U wire 1 in Fig.6.6.

We run this ODT trap frequency experiment (data in Fig. 6.27) by activating the Stern-Gerlach coil (x-axis) or the vertical push coil (y-axis) to push the atoms in ODT. We turn off the ODT before the atoms stop sloshing in the ODT for time-of-flight (TOF) imaging. Then, we take an image after a few ms of TOF, letting the atom cloud expand to a density suitable for the image. Since there is TOF before the image, the atom sloshing distance in pixel number shown in Fig. 6.27 is not the actual pushing distance in the ODT, but the oscillation frequency should be the atom sloshing frequency in the ODT, i.e. the trap frequency of the ODT.

6.8.3 Temperature drift issue

Another issue that was uncovered during the interferometry research is the time varying room temperature of the lab, and how it affects the interferometry signal.

In order to investigate the role of room temperature dirft, we set up the Ramsey interferometer and gathered data while keeping the interferometer Ramsey time the same. Normally, since experimental parameters are being delibrately modified, Ramsey fringe spin population ratio should maintain the same value.

Fig. 6.28 shows the result of this experiment. The blue data on the upper plot is the lab temperature, which we took with an Omega TC1-10052 temperature recorder. We set the thermocouples of Omega TC1-10052 on the apparatus platform next to the science vacuum cell (where the atom chip is located). The mirrors that guide the ODT laser and image probe laser are on this platform, so the platform temperature is relevant to the experiment. The red data is the spin population ratio from the Ramsey interferometer. The top plot of Fig. 6.28 does not show us solid evidence about the correlation between the temperature and the atom ratio drifting. However, we can see that the overall trend of the temperature and the atom ratio are

somewhat correlated. Moreover, the turning points for the atom ratio correlate well with the turning points for the temperature, so the data indicate that there may be a correlation between the temperature and the interferometer signal. The bottom plot of the Fig. 6.28 shows the correlation between the lab temperature and the atom ratio. The correlation is not very strong, but we can calculate the correlation coefficient with equation $\rho(x,y) = \frac{\mathrm{cov}(x,y)}{\sigma_x \sigma_y}$, where the $\mathrm{cov}(x,y)$ is the covariance and the σ is the standard deviation. The correlation coefficient is a value range from -1 to 1, and 0 represent x and y are entirely not correlated, while ± 1 represent x and y are completely correlated in a relation of the sign. The correlation coefficient for the data shown in Fig. 6.28 (bottom) is -0.523, which shows that the temperature has some correlation with the atom ratio, and could be one of the causes for the atom ratio drifting.

The plots in Fig. 6.28 show that, the lab temperature has only varied over the range of 22.35 °C to 22.15 °C, which is only 0.2 °C temperature variation. This drifting value is much smaller than the lab's HVAC system stability, which is specified at ± 1°C. The large metal mass of the platform (i.e. large thermal mass) likely reduces the temperature drift, but it is still not enough for our experiment. Furthermore, it might be hard to improve the HVAC system for the lab. Instead, reducing the temperature dependence for each critical part in the apparatus could be a useful strategy.

There are several possible parts in our apparatus that might be affected by the temperature. For example, we know that the position of the ODT (with respect to the atom chip) various with room temperature (see disscussion the Ph.D. thesis of Dr. Andrew Rotunno [54]). Alternatively, the microwave and RF power and frequency could be affected by the lab temperature.

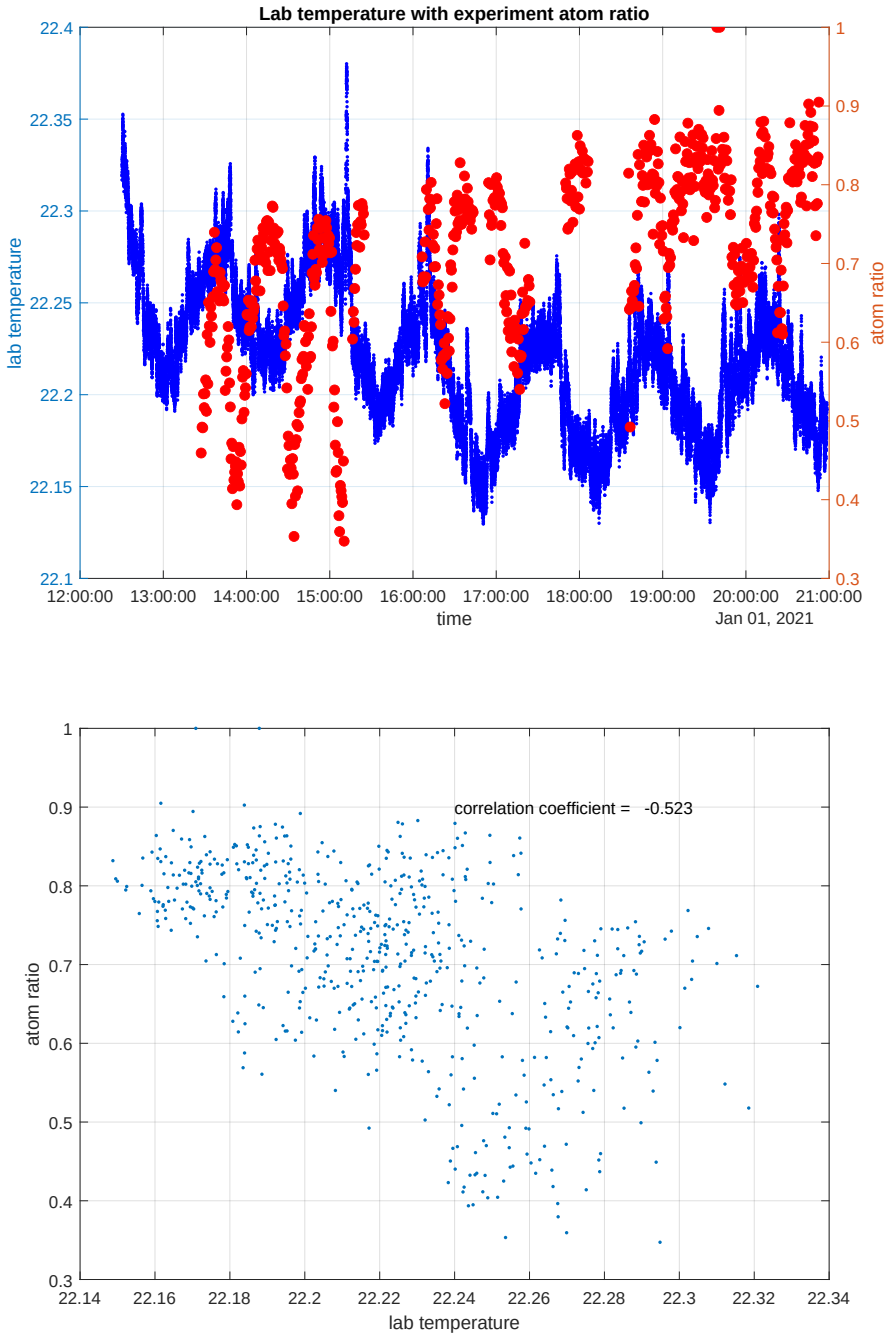

FIG. 6.28: Effect of room temperature on atom interferometer operation. We run the Ramsey interferometer experiment and keep all the settings the same. Top: Lab temperature and Ramsey spin population ratio versus time. Bottom: Ramsey spin population ratio versus lab temperature (same data as in top plot) that shows some anti-correlation. *data gathered on Feb.27.2020*

6.8.4 Quality of the main clock

In this subsection, we discuss the stability of our main clock, i.e. master frequency reference. The main clock will be the standard clock for almost all the apparatus related to the atom interferometer, including the Holzworth, Dr. Watts, DDS units, SRS DG535 pulse generator, and Siglent SDG 5122 arbitrary function generators. The evap RF system does not connect to the main clock, but the evap RF will only work for ARP sweeps from $|1,1\rangle$ to $|1,-1\rangle$, which are robust to modest frequency noise and drift.

The Adwin system is also not connected to the main clock, and this might cause some problems in the AC and DC energy detector experiments. The $\frac{\pi}{2}$ pulse is controlled by the SRS DG535 pulse generator, whose timing is independent of the Adwin (except for the start trigger). However, in the energy detector experiments, the Ioffe field (DC) and Dr. Watts (AC) are controlled by the Adwin system, so Adwin timing noise can show up on the interferometer signal.

Since the main clock is connected to most of the apparatus frequency source, the clock's quality is critical to the atom interferometer. We started our atom interferometer project with a Premium 10 MHz-SC Streamline Crystal Oscillator wenzel associates, but then replaced it with the PRS10 Low phase noise Rb oscillator Stanford Res. system. The latter one has a higher long term stability than the first one based on comparison of datasheets. We do not have a better source to check the quality of the PRS10 clock, but we can use it to check the quality of the former crystal oscillator clock (wenzel). As shown in Fig. 6.29, we measure the beatnote between these two clocks over a day, and the beatnote drifts by around 30 mHz, larger than the aging described in datasheets. The wenzel source was located in an area that increases with temperature after the apparatus is turned on. The PRS10 is located in an area of the lab that experience little temperature change after the

main apparatus is turned on. We began to gather the data right after we turned on the apparatus, and the beatnote increased with time. After we turned off the apparatus, the beatnote starts to drop. This curve hints that the clock frequency drifting is caused by the temperature. The beatnote drift of 30 mHz out of 10 MHz corresponds to around 15 Hz out of 6.8 GHz, around our Ramsey interferometer coherence time. However, after we replaced the clock, the quality of the Ramsey interferometer does not obviously improve. This might be because the clock is not the main problem for the Ramsey interferometer coherence time, or perhaps the PRS10 does not meet it specifications.

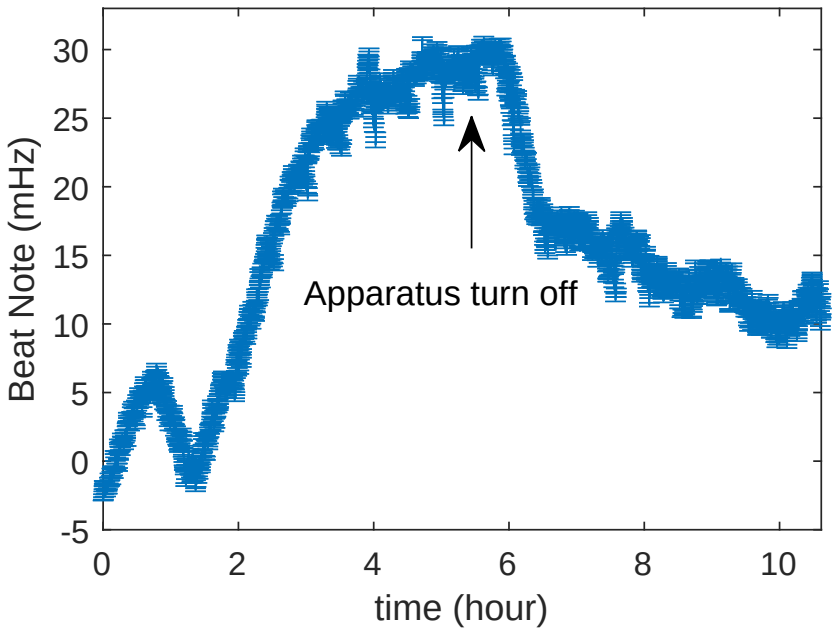

FIG. 6.29: Clock beatnote drifting over a day. The data begins with the apparatus turn on, and the lab temperature should start to increase at this time. The beatnote drifts higher after the apparatus turn on, and then drifts back down after the apparatus turn off. This data shows the the old main clock likely has a temperature dependence. *Data gathered on Oct.04.2019. In folder \Shuangli\programs\SiglentScopeProgram\ClockData\Oct.04.2019*

6.8.5 Microwave amplifier turn-on

In our tests on the Amaterasu microwave amplifier, we found that the Amaterasu needs to be un-muted very early before we input the microwave signal in order to have a constant amplitude output. This problem shows up on the Amaterasu 6.8 GHz two-photon transition source, and possibly the same for Baku amplifier, which use the same model of microwave amplifier.

The first reason is that if we turn on the amplifier at the same time with switch, there will be an overshoot on the output microwave power. Fig. 6.30 shows the Amaterasu output when we turn on the amplifier and switch at the same time. We expect the power output should be a square pulse, but the output power grows up slowly and then overshoots the target power: The power then oscillates after the overshoot for few μs before setting at the target power. This overshoot problem can be solved if we unmute the amplifier for at least 5 μs before the switch turn on.

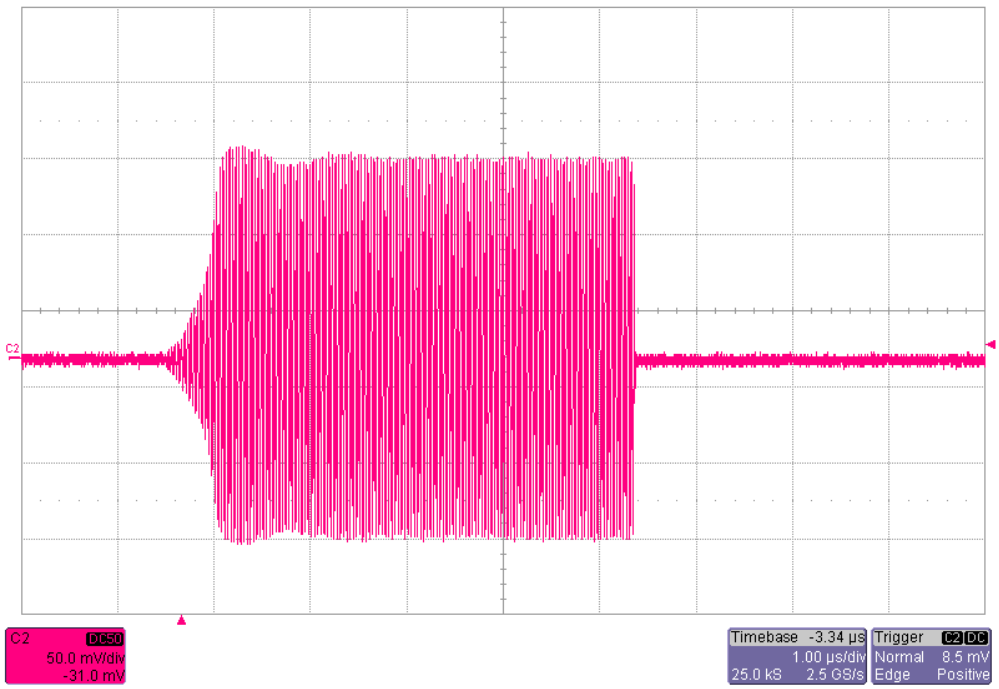

FIG. 6.30: Microwave overshoot when the switch and amplifier turn on at the same time. The vertical axis is proportional to the microwave field (volts) not power.

Furthermore, the amplifier has a decay in output power, which needs a longer unmuting time to solve. As shows in Fig. 6.31, the microwave power will gradually decay with time,even though the input keeps the same power. The power decay during the $\frac{\pi}{2}$ pulse has the same problem we discussed in subsection 6.4.3 since it can act as an ARP. This decay problem relates to the microwave amplifier (CTT inc. GaN Amplifier 6.4-8.5 GHz, Psat=43 dBm, Part # AGW/085-4346) because we found that the decay problem improves if we unmute the amplifier a few seconds before the $\frac{\pi}{2}$ pulse. However, there will be two $\frac{\pi}{2}$ pulses in a single atom interferometer experiment. The unmuting to the second $\frac{\pi}{2}$ pulse will be the same as keeping the amplifier on for the entire experiment. However, if we keep the amplifier on for the entire experiment it will increase the risk of microwave leakage. We have a daisy chain of two VVA that provides 33 dB of attenuation for each VVA and a switch for further attenuation. The frequency doubler (mini-circuits ZX90-2-36-S+) will also strongly attenuate its output if the input power is too small. Even if we have multiple levels of attenuation, it is still possible that there is a tiny amount of microwave leakage through, which is then amplified before going to the chip.

In our current experiment setting, we choose to keep the amplifier on for the entire interferometer experiment because of the power decay problem.

6.8.6 Antenna-chip coupling problem

In the ideal scenario, the antenna should provide a locally flat microwave plane wave incident on the atoms. However, in studying the $|2,2\rangle \rightarrow |1,1\rangle$ transition, we found that the field emitted by the antenna can also push the atoms in a vertical direction. This transition only requires a microwave field and the antenna is the only source. Furthermore also the microwaves push the atoms in a vertical direction, which means their is gradient in the microwave field.

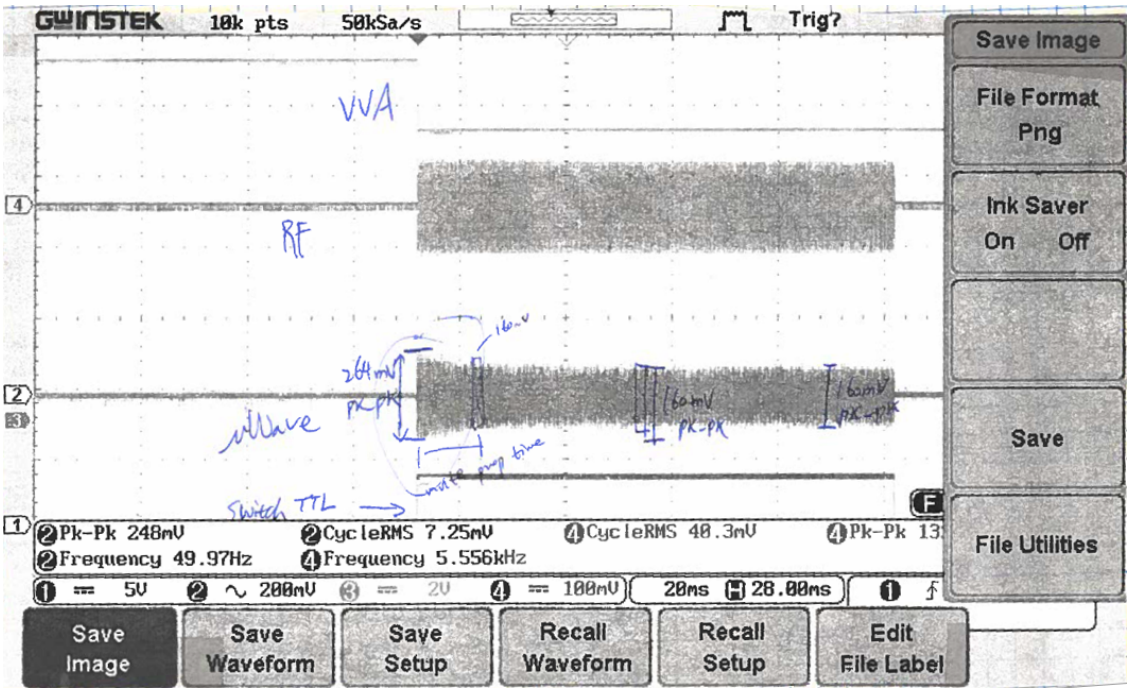

FIG. 6.31: Microwave decay issue. The microwave power will decay after turn on from a signal amplitude of 264 mV to 140 mV.

The most likely reason for this phenomenon is that the microwaves from the antenna couple to one or more chip wires, and the induced current in the chip wire generates a high gradient microwave near field that is strong enough to push the atoms.

This antenna coupling problem is hard to solve right now, because it is depends on the chip itself. If the AC Zeeman trap idea for the atom interferometer experiment works well, and we can generate a flat two-photon transition near field from the chip, then we can bypass this issue. Otherwise, we should design the new atom chip to minimize such unwanted coupling.

Other than the microwave antenna, we also tried to use a loop antenna located outside of the vacuum chamber for the RF transition. However, the loop antenna when excited by frequency lower than 10 MHz will somehow couple to our apparatus temperature interlock and generate a false alarm. Given the chip-antenna coupling problem, it is not worthwhile to solve the RF loop antenna-interlock coupling prob-

lem for now.

6.8.7 ODT laser beam broadband emission

The ODT beam has another problem: the 1064 nm ODT laser beam contains significant spectral component in the 750-950 nm range (probably from laser crystal excitation lamp). Fortunately, this extra light does not pass through the delivery fiber and does not directly impact our atoms much. However, we are using a photo-detector within a "noise eater" feedback system to control and stabilize the ODT power, and the photo-detector is located before the delivery fiber. This apparatus layout causes the photo-detector to adjust the total laser power, based on both the main 1064 nm laser power and the extra 750-950 nm spectral components. In this case, the total optical power (integrated over all wavelengths) is stabilized, leaving the main 1064 nm components less stabilized. This problem causes the ODT to be less stable than it could be even the noise eater signal shows good performance. We temporarily solved this problem by adding a 1064 nm narrow pass band filter just in front of photodiode. However, after installing the filter, the laser power was not sufficient to lock on the regular -9.7 V setting on the noise eater, and we had to lower the power setting to stabilize the noise eater.

6.9 Conclusion and future plan

In the atom interferometer project, we have successfully made a Ramsey interferometer, a DC Zeeman energy detector, and an AC Zeeman energy detector. The Ramsey interferometer generates good interferometric fringes with a stable frequency in the first 10 ms, but with growing phase slip around 100 ms. The DC Zeeman energy detector signal shows some instability on the frequency at 5 ms, and the phase slip shows up around 100 ms, but the fringe visibility of the DC Zeeman

energy detector signal is still relatively high at 100 ms. The AC Zeeman energy detector signal has a stable frequency, but the fringe visibility decays very fast (10-20 ms).

One of the assumptions for the fast decay of the AC Zeeman energy detector fringe signal is that the high gradient AC microwave field could be pushing one state of the atom and thus separating the spin states of the atom clouds. If this assumption is accurate, then we are very close to the spatial atom interferometer, but there is no evidence to prove it due to the elliptic shape of ODT.

The future plan for the atom interferometer project is to achieve the spatial interferometer by solving the problems we discussed above, such as the sideband problem, ODT elliptic shape, and the temperature drifting. However, if the reason for the AC Zeeman energy detector fringe fast decay is not the atom cloud separation, the one option will be to use AC Zeeman trapping potentials, which are discussed in the Ph.D. thesis of Andrew Rotunno [54], to instead create an AC magnetic field with a relatively flat saddle point at the atom cloud. We can use this flat saddle point field to perform the AC Zeeman energy detector experiment without a field gradient and curvature.

CHAPTER 7

Curved Microstrip Traces

7.1 Motivation

During my time in the lab, the atom chip that we are using has shown its limitations and cannot support further experiments. The main limitation of this atom chip is that the wires are only designed for DC current. This chip still works for RF frequency current (10 MHz level and below), but if the frequency reaches microwave level (GHz level), then only a small percentage of the current will be able to travel through the wire, especially around 6.8 GHz.

Our trapped atom interferometer will use the AC Zeeman force to separate atoms in different spin states. This approach requires a very strong microwave current running in the atom chip wires. In order to meet the microwave current requirement, we built a microwave amplifier to provide up to 20 W of microwave power for the atom chip. However, the high-power microwave source brings another risk to our system. We cannot ensure that most of the microwave power is transmitted instead of being reflected. Furthermore, there might be a significant amount of microwave power that is consumed in the chip, transferred to heat. This microwave

heating effect could cause irreversible damage to our atom chip. Moreover, the vacuum environment increases the cost of chip replacement to a very high level. As a result, we need a new atom chip design to support our future experiments.

The new microwave chip trap will be a three-microstrip system. Three straight parallel microstrips are placed next to each other with center-to-center separation around 100 μm. Our earlier research shows that this structure with a specific current ratio and phase difference should provide an AC magnetic field minimum point. Furthermore, the phase difference between the traces can be used to control the trap position and even generate the separated magnetic field minimum point with the different spin states [54, 88].

The microstrip traces are very close together, so it is difficult to install an SMA connector port for the microwaves. To install the SMA connector port, the microstrip needs to be curved and separated from each other at the edge of the chip. However, the effect of a curved trace on the transmission and reflection is not well researched for our specific microstrip size and frequency.

Also, we will run the current in microstrip with multiple frequencies, from DC for regular Ioffe trap, MHz level for radio-frequency transitions, and around 6.8 GHz for microwave-frequency transitions. We still want to keep the possibility of running the current for an even higher frequency, so the minimum goal for this model will be broadband performance from DC to 10 GHz. We will also consider running a standing wave trap to separate the atom along the length of the microstrip, and this needs a broadband frequency up to 20 GHz, which will be our step-up goal.

The ideal microstrip design should have the following features. First, the microstrip should have a high transmission coefficient to maximize microwave power efficiency. Second, the microstrip should have a low reflection coefficient. The reflection will generate a detrimental standing wave along the microstrip. The standing wave could be helpful in the experiment, but if the shape of chip will determine the

phase of this standing wave, then we can not control. The standing wave that we cannot controlled will only add extra force to the atom, constraining experimental performance and capability. Third, the reflection and transmission should be stable for the different frequencies. The stability of transmission is essential for microwave power control when we scan the driving frequency. The stability of reflection is also necessary, for we will monitor the microwave power via the reflection.

To research the problem above, we will use FEKO, an electronic magnetic simulation software, to simulate the S_{11} (reflection coefficient) and S_{21} (transmission coefficient) parameters of the curved trace model. We will compare the results for different microstrip parameters, such as the radius and curve angle, to find the best design for it.

In conclusion, we need a curved microstrip trace model with optimized transmission and minimum reflection. The microstrip should be broadband from DC to at least 10 GHz, which has a stable high transmission rate and low reflection rate.

This chapter will start with the two types of basic straight microstrip model in section 7.2, the canonical model in subsection 7.2.1, the foxhole model in subsection 7.2.2 and the comparison between them in subsection 7.2.3. Then optimize these two model in section 7.3, for feedline length in subsection 7.3.1, and for trace width in subsection 7.3.2. Next, we will study the curved trace model in section 7.4. The types of curved trace model we study includes: the single curve model in subsection 7.4.1, the S-shaped model in subsection 7.4.2, the U-shaped model in subsection 7.4.3, the double S-shaped model in subsection 7.4.4, and the three-microstrip model in subsection 7.4.5.

7.2 Basic straight microstrip models

The most basic building block of the microwave atom chip is a straight segment of microstrip transmission line. In order to accurately simulate our atom chip design, we have built two model types that simulate a microstrip transmission line.

Fig .7.1 shows a cross-section of the microstrip model: the microstrip transmission line includes a copper trace, an aluminum nitride (AlN) substrate, and a copper ground plane. The AlN substrate is 50 μm thick. The copper trace is set above the AlN substrate and has 54 μm as width and 5 μm thickness, which results in a broadband transmission line impedance of 50 Ω. Under the AlN substrate, a 5 μm thick copper ground plane covers the entire bottom surface (see Fig. 7.3).

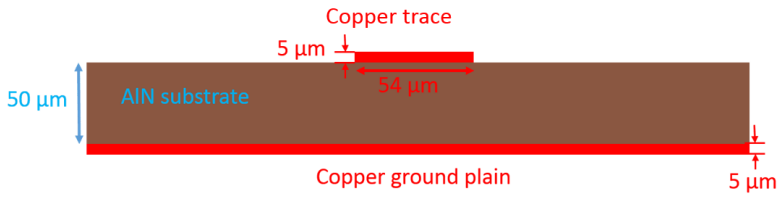

FIG. 7.1: Cross-section of our 50 Ω microstrip transmission line building block.

7.2.1 Canonical model

The first model is called the "canonical model". This model is very straightforward. The AlN substrate has the same length as the transmission line, and the copper trace extends out somewhat from the substrate board and bends down perpendicularly to connect to the ground plane as shown in Fig. 7.2. We call the sections that stick out of the substrate the feedlines (see Fig. 7.4). The feedline can host a source port or load port, which FEKO requires to simulate the model.

In the actual atom chip, the size of the substrate is much bigger than 54 μm, which is the width of the transmission line. However, in the FEKO simulation, it is

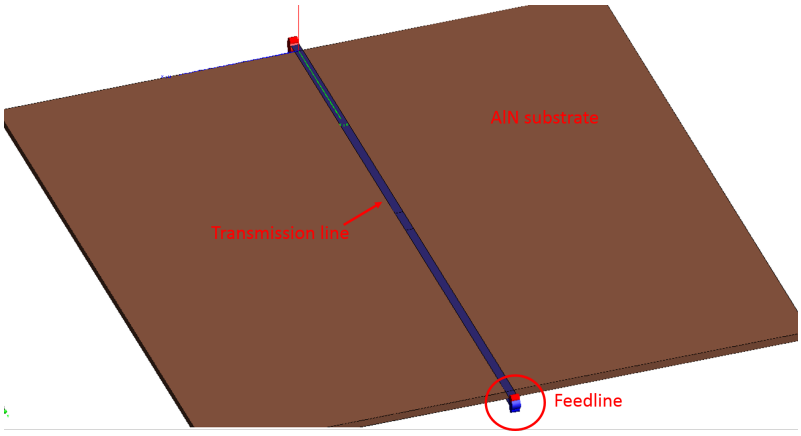

FIG. 7.2: Canonical Model top view. The blue line on the top is the copper trace, and the brown plane is the AlN substrate. Feedlines are set at both ends of the copper trace.

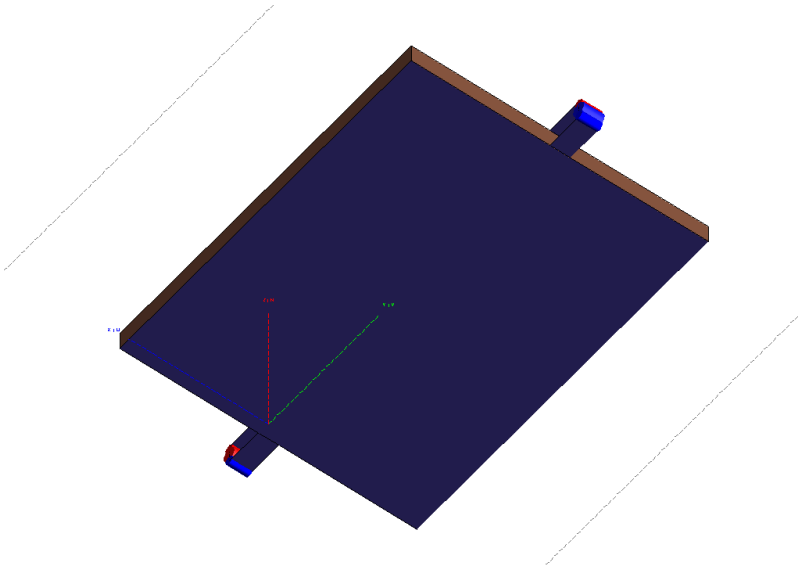

FIG. 7.3: Canonical Model bottom view. The entire bottom of the substrate is covered by a copper ground plane.

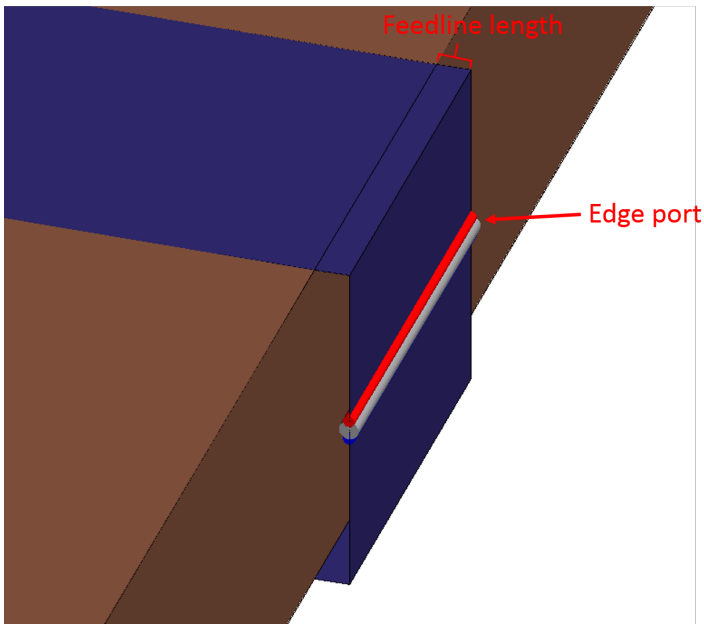

FIG. 7.4: Canonical Model feedline close view. The feedline extends out of the substrate and bends down perpendicularly to connect to the ground plane on the bottom side. The cylindrical line with red, white and blue colors in the middle of the feedline, is the Edge port, which can be defined as a source port or a load port.

not a good idea to set the width of the substrate as large as the actual case because the FEKO simulation requires a lot of computing power. Even simulating with a small substrate might affect the result, it is still better to limit the substrate size and leave more computing power to the most critical part, such as the copper trace. So we set the width of the substrate to be at least 1 cm wide, which guarantees that the strength of the microwave near field is small enough when it reaches the edge.

One of the important features of the microstrip is that its near field is a quasi-TEM mode, i.e. the electric and magnetic near fields are transverse to the propagation direction. Since the microstrip should provide a TEM near field, we can use the transversality of the electric and magnetic fields as a quality check for our straight microstrip model to ensure our FEKO model is reliable. Fig. 7.5 shows the magnetic near field above the microstrip. The right figure shows that all the magnetic components are in the transverse direction, as expected for a TEM mode.

The canonical model is straightforward and similar to the actual chip, except that we alter the SMA connection port into a feedline. However, the canonical model has its limitations. First, the canonical model requires the length of substrate to be the same as the length of the transmission line. In the simulation, there could be a cavity effect that significantly affects the reflection coefficient, which will vary a lot with a small change of a chip parameter. To research the effect of the transmission line length, we want to separate the substrate length and the transmission line length, which is impossible for the canonical model. The second limitation is that the canonical model can only simulate a straight trace or a curved trace exactly at 90 degrees, and cannot be used to research arbitrary curve angles. This limitation is because we use a cuboid to build our substrate, and the shape of substrate and feedline needs to be comparable for each simulation group.

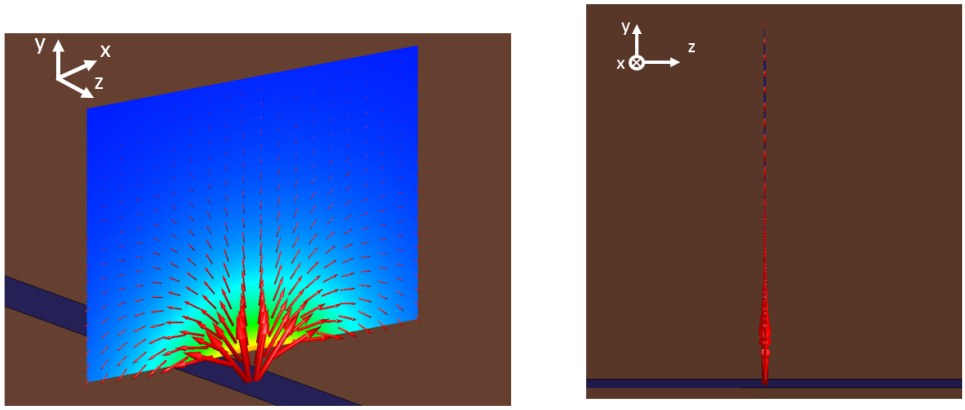

FIG. 7.5: Canonical Model Straight, show near field from main trace.

7.2.2 Foxhole model

The foxhole model was designed to deal with these limitations of canonical model: the microstrip trace ports are decouple from the substrate edges and geometry. As shown in Fig. 7.6, the foxhole model has a substrate that is bigger than

the transmission line, and the transmission line is located roughly in the middle of the substrate. At the end of the transmission line, there are holes in the substrate, and the feedline will go through the hole to the ground plane: we call this hole the "foxhole".

This foxhole model breaks the bounding between the length of substrate and transmission line. And the foxhole trace can be at any arbitrary angle to research the effect of a curved trace.

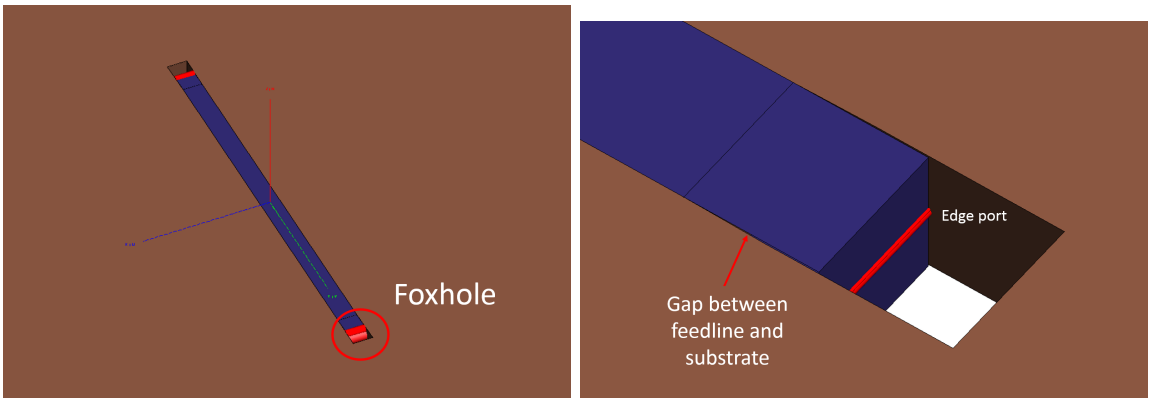

FIG. 7.6: Foxhole Model. The size of the foxhole is bigger than in the simulation model for illustration purpose.

7.2.3 Comparison between canonical and foxhole model

The canonical model and foxhole model are both useful for our simulations. However the model comparison is not the main research focus. Instead, the result of simulations coming from the different models should be similar. We run a model with a 2 cm length of transmission line for both canonical and foxhole models to check how different the result will be.

As shown in Fig. 7.7, the result of the canonical model and the foxhole model S_{11} parameter, the reflection coefficient, stay in the same scale, around 1%. And also for most of the frequency range, the trend of the parameter is the same, except around 4 GHz where the foxhole model has a peak, while the canonical model is

much flatter.

The canonical model shows a more stable result than the foxhole model. This stability might be because the foxhole model will generate some cavity effect inside of the foxhole, between the foxholes, or between the foxhole and the edge of the substrate. Since we are simulate the most simple straight microstrip model, there should not be such irregular behavior as the 4 GHz of the foxhole model. This peak indicates that the canonical model may be more reliable. So we will choose the canonical model as our primary model, and the foxhole will only be used in arbitrary angle research, which cannot be simulated by the canonical model.

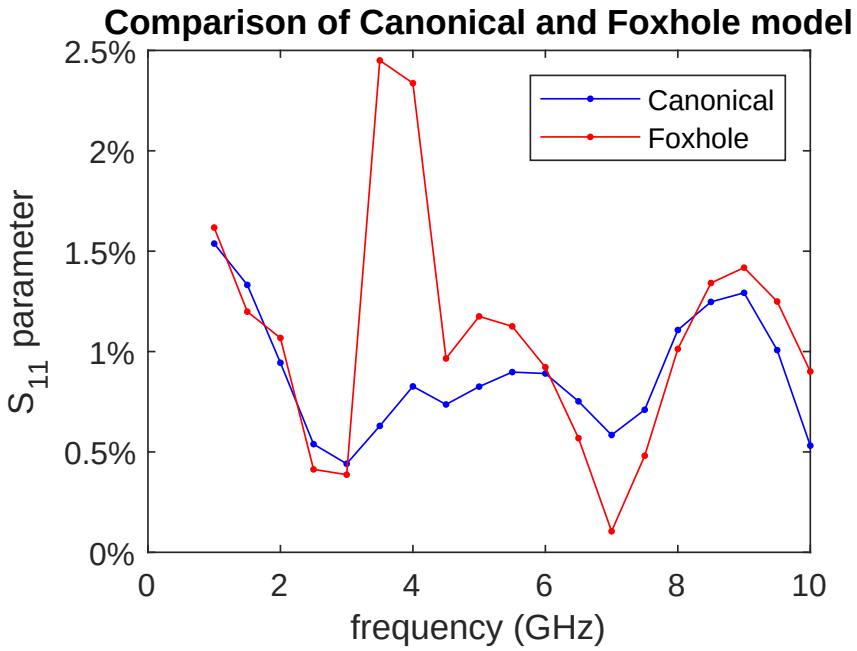

FIG. 7.7: Comparison of canonical and foxhole models for a simple 2 cm trace test case. The result is on the same scale, and most of the reflection coefficient (S_{11}) shows the same trend, except around 4 GHz, where the foxhole model result has a peak, while the canonical model result is relatively flatter.

7.3 Optimization of straight trace models

The first step of our simulation is working on a straight model. There are three benefits to starting our simulations with a straight model. First, there is a quasi-analytic solution for the infinite straight microstrip [89], which can provide us the initial design parameters. Second, the straight model is easier to build in FEKO. Starting with a simple model will help us to ramp up this simulation project. The last reason is that the curved part of the microstrip will more likely show a negative effect on the entire model quality, so having a good straight model will provide a baseline against which the simulations of curved traces can be compared.

Table. 7.1 shows the main parameters of our model. There are two different types of parameters, chip parameters and simulation parameters. The chip parameters will be used in our actual chip design, while the simulation parameters will not be used in our actual chip, and are only used for simulation purposes.

We analytically estimate the chip parameters, and then optimize the width of transmission line with FEKO. For simulation parameters, we set the length of the microstrip as 2 cm, which is the same as our current chip, and optimize the length of the feedline with FEKO simulations.

chip parameter	value
thickness of the substrate	50 μm
thickness of the transmission line	5 μm
width of the transmission line	54 μm
simulation parameter	**value**
length of the transmission line	2 cm
width of the substrate	1 cm
length of feedline	5 μm

TABLE 7.1: Straight trace model parameters. We get these parameters from analytic calculation and previous simulations.

The optimization process of the width of transmission line and the length of

the feedline are presented in the following sections.

7.3.1 Feedline length optimization

The length of the feedline is an important simulation parameter. Since the feedline is not a part of our actual chip design and not a part of the microstrip, it might contribute sufficiently to the reflection coefficient and taint simulation result. If the feedline is too long, it will increase the reflection of the entire model. Meanwhile, we set the "edge port" on the feedline to be the source and load of the current. According to FEKO, the "edge port" can only be inserted in a metal plane with no dielectric in contact with it. This requirement prevents us from setting the length of the feedline to be zero.

We need to find the feedline length that has a minimum effect on our simulation. Thus, we select the feedline length that minimizes the reflection coefficient over a range of frequencies.

For the canonical model, as shown in Fig. 7.8, the reflection coefficient (S_{11} parameter) level is minimum when the feedline length is 5 μm. The worst data point in our simulation is 100 μm feedline length at 9 GHz, which is around 6.5% of the reflection coefficient. When comparing this high reflection coefficient in the 100 μm feedline length to the reflection coefficient with the 5 μm example, the 5 μm feedline length performs about three times better. Based on this result, we use 5 μm as our feedline length for canonical model simulation.

The foxhole model has one more parameter, the size of the hole. In our simulations, we keep the size of the hole always two times the feedline length and set the feedline at the middle of the hole. For the foxhole model, as shown in Fig. 7.9, the smaller feedline length still shows better performance than the longer one. The 5 μm and 10 μm S_{11} curve have a similar performance, and the 5 μm S_{11} curve is

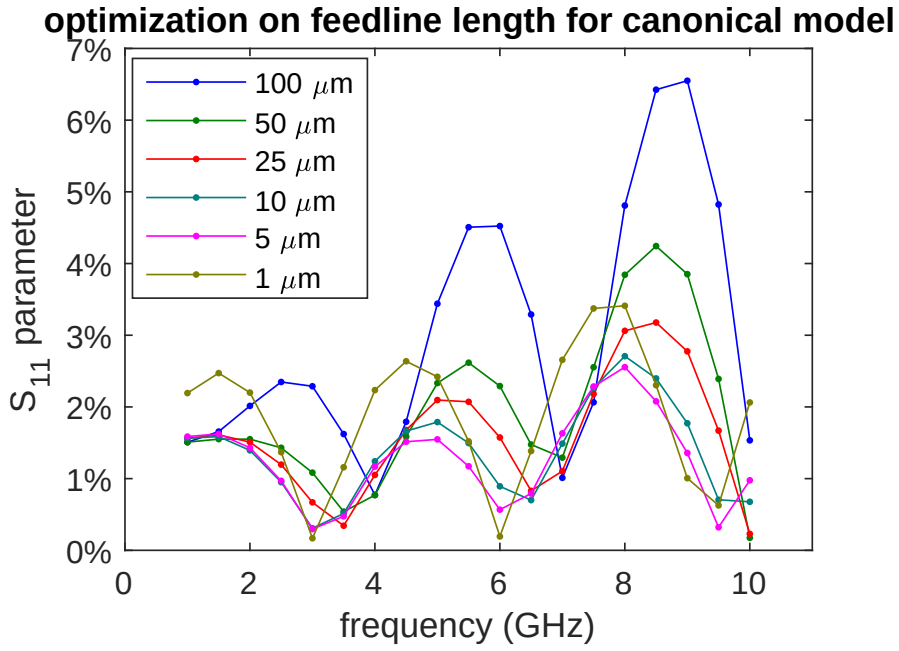

FIG. 7.8: The relation between feedline length and S_{11} parameter for the canonical model. The S_{11} parameter shows a period behavior that suggests the existance of a cavity. The S_{11} parameter basically gets smaller with a shorter feedline length and reaches the minimum at 5 μm. When the length reaches 1 μm, the S_{11} parameter gets higher again.

slightly smaller. The 5.5 GHz point in 5 μm S_{11} curve is a little bit distorted from the trend of the curve and might have a stranger behavior hidden in it. Therefore, just in case, we choose 10 μm for the feedline length of the foxhole model.

7.3.2 Trace width optimization

Next, we optimize the width of the trace so that the microstrip has a 50 Ω impedance, i.e. minimize the reflection coefficient (S_{11}) over as large a frequency range as possible. As shown in Fig. 7.10, the best candidate is 54 μm and 53.5 μm. They both have small reflection coefficients. Notably, the 53.5 μm case performs better around 8 GHz. However, considering the stability around 6.8 GHz, i.e. the frequency that we mainly operate at, the 54 μm case has a smaller reflection than

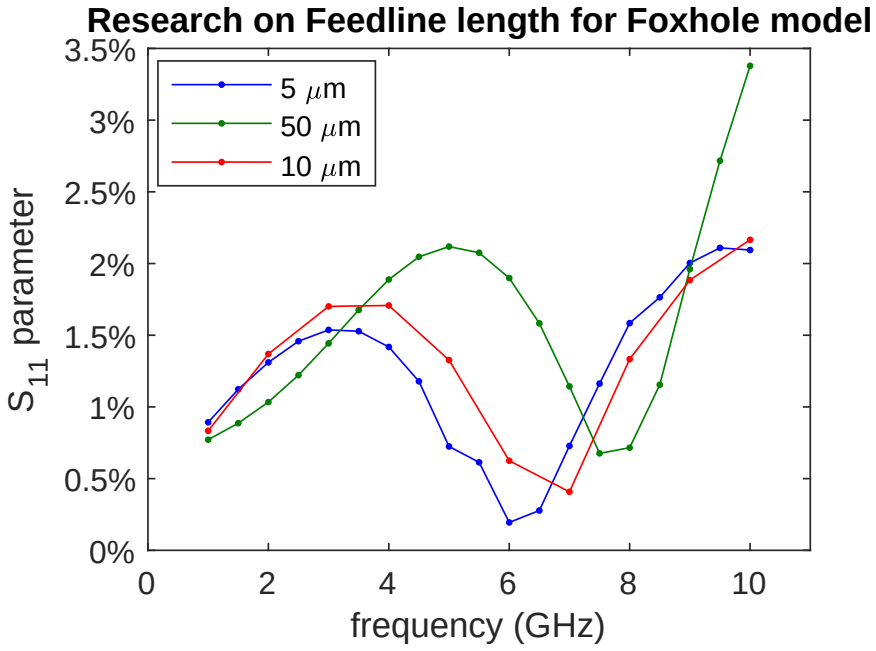

FIG. 7.9: The relation between feedline length and the S_{11} parameter for the foxhole model. The curves show that a smaller feedline length gives a smaller S_{11} parameter.

53.5 μm. Thus, we choose 54 μm as our width for the microstrip transmission line.

7.4 Curved trace models

Now that the straight trace model has been optimized, we investigate curved traces. We choose the most straightforward design for a curved trace that keeps the width of the transmission line the same throughout the turn: intuitively, this geometry is the most likely to minimize the reflection coefficient, so it is a good starting point for optimization.

We consider four different curved trace models: 1) a single curve model, 2) a S-shaped model, 3) a U-shaped model, and 4) a double S-shaped model.

We start with the single curve model and the S-shaped model (S model) and study the dependence of the reflection coefficient with the turn radius and curve

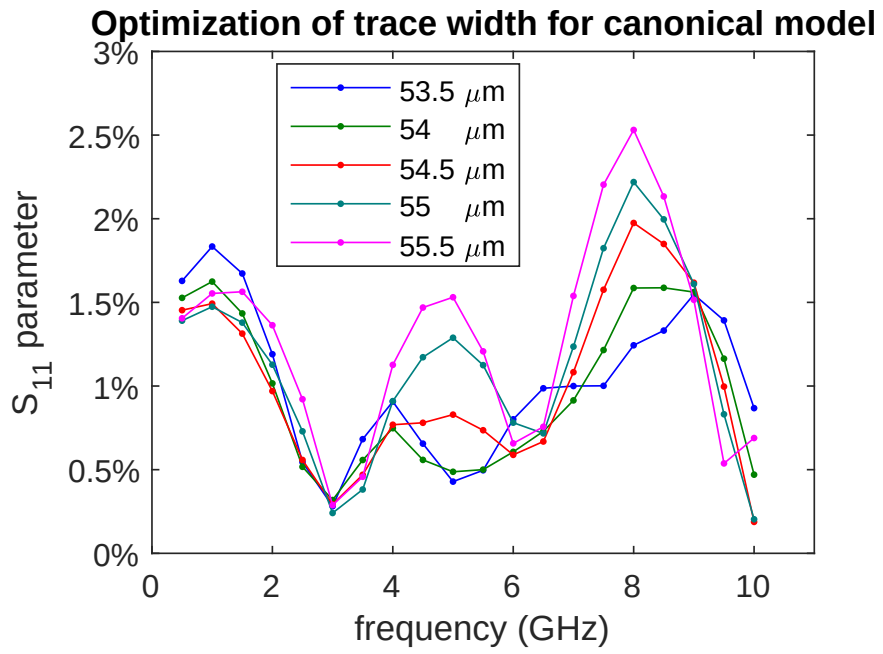

FIG. 7.10: The reflection coefficient for different trace width for the microstrip transmission line. The best candidates are 53.5 μm and 54 μm.

angle. The single curve and S-shaped models will help us better understand the curved microstrip. We will not use the single curve and S-shaped models as the final design, but they are the fundamental parts of the potential final design. The U-shaped model (U model) and the double S-shaped model (DS model), will be used in a candidate atom chip design, which we present at the send of this section.

7.4.1 Single curve model

For the single curve model, we use the canonical model with a single 90 degrees bend to research the effect of turn radius on the S parameters (Fig. 7.11).

As shown in Fig. 7.12 and Fig. 7.13, the radius of the curved trace has limited effect to the microstrip S parameters. The larger radius yields better S parameter performance (low reflection high transmission), but the advantage is not large. In the actual chip design, a larger radius requires a larger substrate, while the size

of the substrate will be limited by the experimental apparatus. In the future chip design, ideally we would set the radius as large as possible without affecting other chip features. We also note that reflection coefficient is quite large in Fig. 7.12.

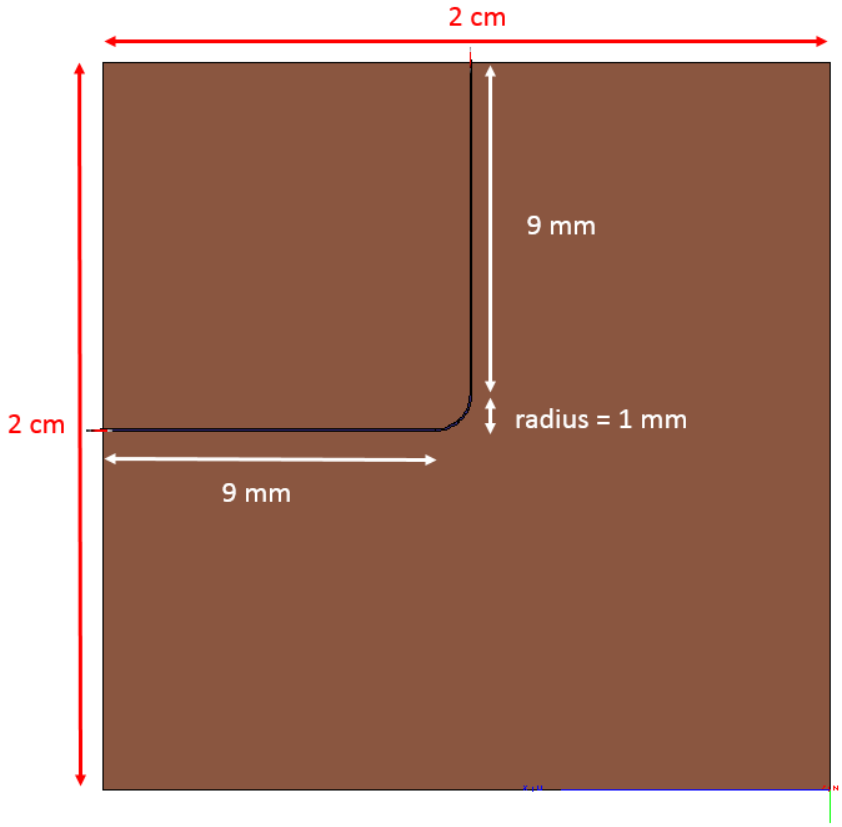

FIG. 7.11: Canonical single curve model. The substrate dimensions are independent of the turn radius.

Next, we move on to the angle of the curve. In order to keep the shape of the substrate, we will use the foxhole model. Fig. 7.14 is the diagram of the foxhole model with arbitrary turn angle. Since the radius is set as 200 μm, the curved microstrip will get longer with a larger angle. In order to keep the entire microstrip length the same, we compensate by adjusting the length of the straight microstrip on both sides.

As shown in Fig. 7.15, the angle of the curved trace also has a limited effect on

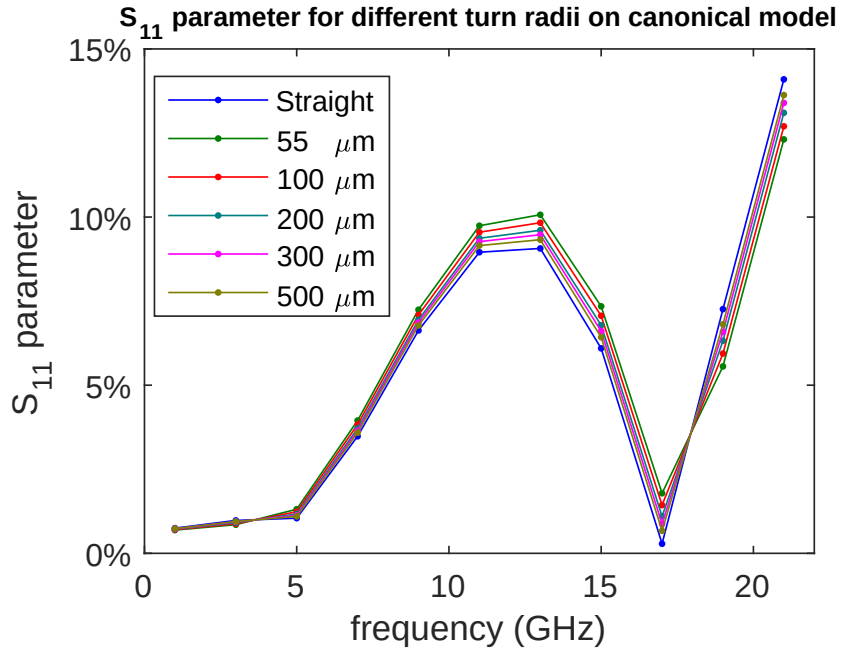

FIG. 7.12: S_{11} parameter with different turn radii for a single 90 degree curve in the canonical model. The simulation uses a 50 μm feedline, and was conducted before we optimized it, so the S_{11} parameter is much higher than other simulations.

the S_{11} parameter. The larger angle has a larger S_{11} parameter, but the advantage is relatively small. The smaller angle has a smaller reflection, but it needs more space to separate the transmission line a same distance. Like with the radius, ideally, we would design the angle of the curved microstrip to be as small as possible without affecting other chip features. However, we note that the foxhole models have a substantially smaller relection coefficient than the canonical model. (Fig. 7.12 vs. Fig. 7.15)

Since the best design for the curved trace does not converge to a specific number, these simulations do not decide the radius and angle for the curved microstrip. However, we will investigate them when we are working with the actual chip design.

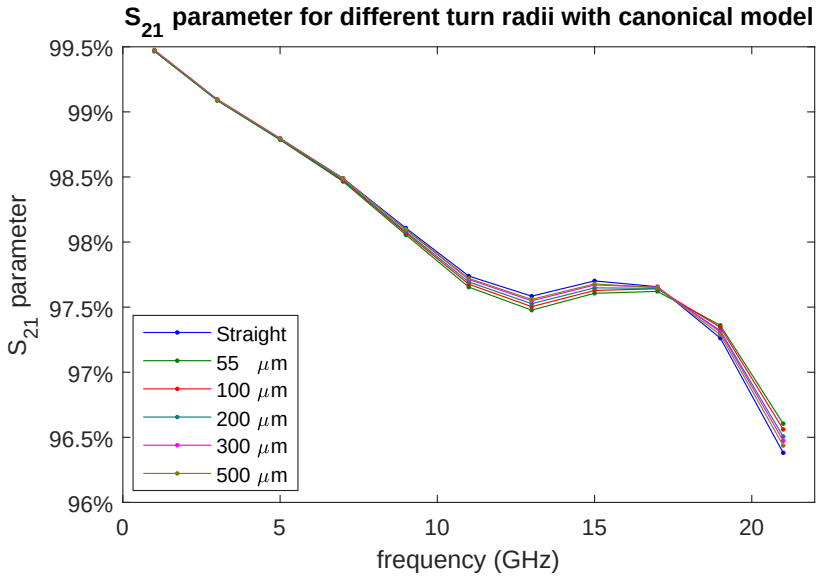

FIG. 7.13: S_{21} parameter with different turn radii for the 90 degree single curve canonical model.

7.4.2 S-shaped model

Next, we move one more step ahead to the S-shaped model to see how multiple curves affect the S parameters. The S model is also a building block of the Double-S model, which is discussed later in section 7.4.4.

From the research on the single curve model, we know that a larger angle performs worse on the S parameter but saves chip surface area. In the S model research, we will continue with the lower limit design on the S parameter and use 90 degree turns for the curves. In future designs, if we have sufficient chip size, we could decrease the angle, and the S parameter performance should increase.

In this S model, we want to study how the turn radius of the curve will affects the S parameters, i.e. reflection and transmission coefficients. To simplify the design, we set the turn radius of both curves to be the same.

As shown in Fig. 7.17 and Fig. 7.18, there is a peak in the S parameters around 3.5 GHz and 7 GHz, and this peak will be significant if the radius is smaller than

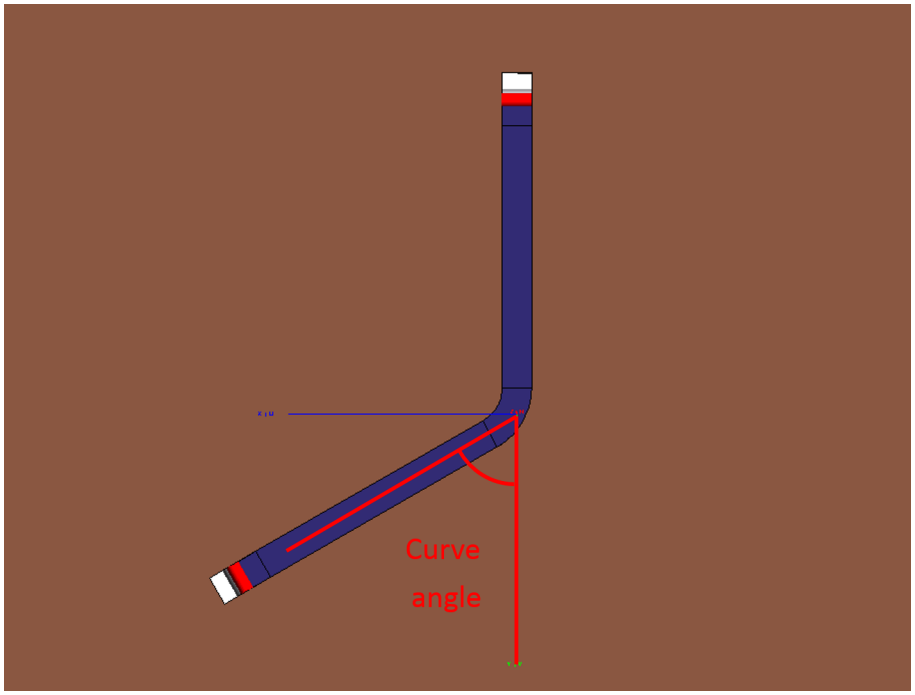

FIG. 7.14: Foxhole model with arbitrary angle

300 μm. For radii exceeding 300 μm, the performance continues to improve, but the improvement is more limited.

For larger turn radii case, the S_{11} parameter curve stays below 1% for intermediate frequencies (2 GHz to 8 GHz), and increases to around 2% at both edges (DC and 10 GHz). The S_{21} parameter curve keeps dropping from 98% at DC to 93% at 10 GHz.

This result shows we should set the radius of the S shape curve larger than 300 μm in our chip design.

7.4.3 U-shaped model

Since we already have a basic understanding of the single curve microstrip and the S-shaped model, we are ready to build some models that will be used in our actual chip design. The U-shaped model is one of our candidates.

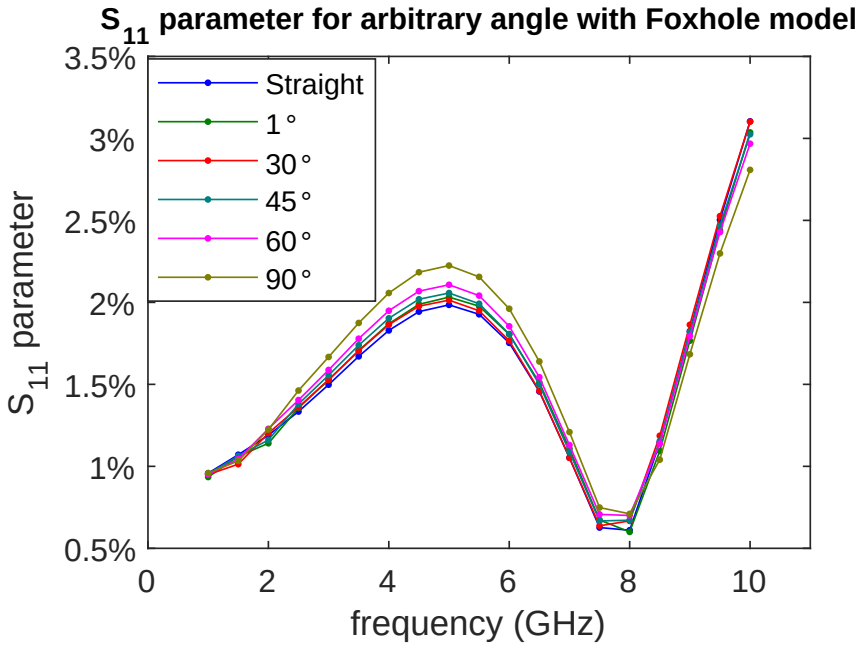

FIG. 7.15: S_{11} parameter with arbitrary angle for a 200 μm turn radius. These simulations were done before optimizing the feedline and the microstrip width, so the S_{11} level will show higher, but the relationship between different angles will still available. This research chooses 100 μm as radius.

The U model, shown in Fig. 7.19, has two curve bends in the same direction and reaches the edge of the substrate on the same side. The U model uses the minimum number of curves to separate the microstrip distance. However, this model will take up all the space on one side of the substrate and limits the room for extra microstrips on that side. This geometry limits the flexibility of the design because there is no space for an extra microstrip to act as an additional microwave source or simply as backup in case we burn the main microstrip.

Since we know that the angle of the curved trace has a limited effect, we choose 90 degrees for the same reasons as those in the S-shaped model. We also based this choice on our study of the effect of turn radius on the S parameters.

As shown in Fig. 7.20, the S_{11} parameter for different turn radii is on the same scale — around 1% — from 2 GHz to 8 GHz. At low frequency, the S_{11} parameter

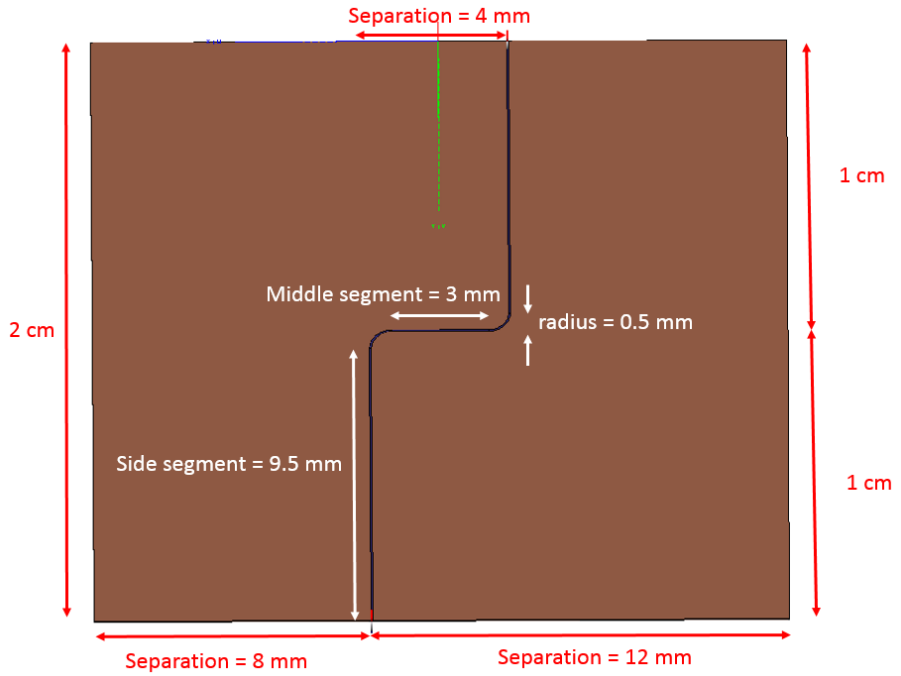

FIG. 7.16: S-shaped model. The microstrip transmission line turns twice along the chip to form an S shape. To isolate the cavity effect between the two side segment, we fix the separation and adjust the length of the middle segment for different turn radii.

increases to 2% for all radii. The main difference shows up at 9 GHz for a radius smaller than 200 μm: the S_{11} parameter jumps to 2%. For larger radii, there is still a peak, but the S_{11} parameter only jumps to 1.5%. Thus larger turn radii are preferable to the smaller radii.

In the Fig. 7.20, the 4 mm case shows a better performance than other radii, especially at 9 GHz, where all the other radii have a peak in their S_{11} curve.

However, from our earlier studies, we know there might be a periodical behavior in the S_{11} curve, due to a cavity type effect. The frequency sampling rate in Fig. 7.20 might be sufficiently dilute to cause aliasing that is hiding the 4 mm radius' peak.

In order to determine whether the 4 mm radius case does have a peak around 9 GHz that goes to 2% in S_{11} curve, we run with a finer frequency step for this case.

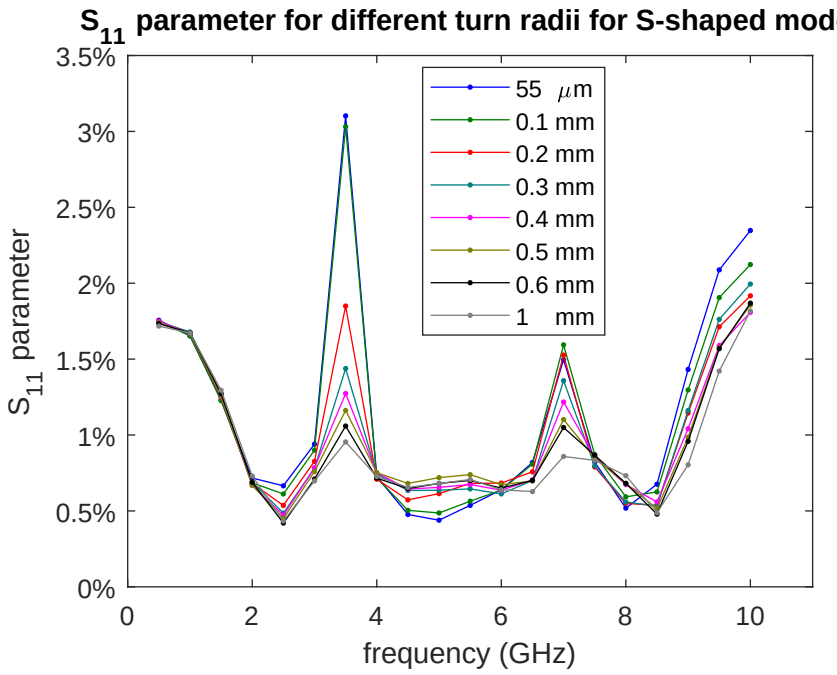

FIG. 7.17: S_{11} with different turn radii for S-shaped model. This S-shaped model uses a 54 μm trace width and 5 μm feedlines.

These simulation results are shown in Fig. 7.21, and prove that the 4 mm radius case has periodic behavior for its S_{11} curve. The oscillation has a smaller amplitude at low frequency (except for the first peak from DC); its amplitude starts to increase after this peak. The peak closest to 9 GHz goes up to 1.5%, which is smaller than 2% S_{11} parameter of smaller radii. These simulations show an obvious advantage for using a larger radius in the U-shaped model. We gathered data from frequencies up to 20 GHz; the oscillation amplitude increased with the frequency and reaches 2.5% at 20 GHz, which is the same level as the first peak at DC.

For the S_{21} curve shown in Fig. 7.22, there is not much difference between different turn radii; it also does not have the large, anomalous spike of the S-shaped model in Fig. 7.18.

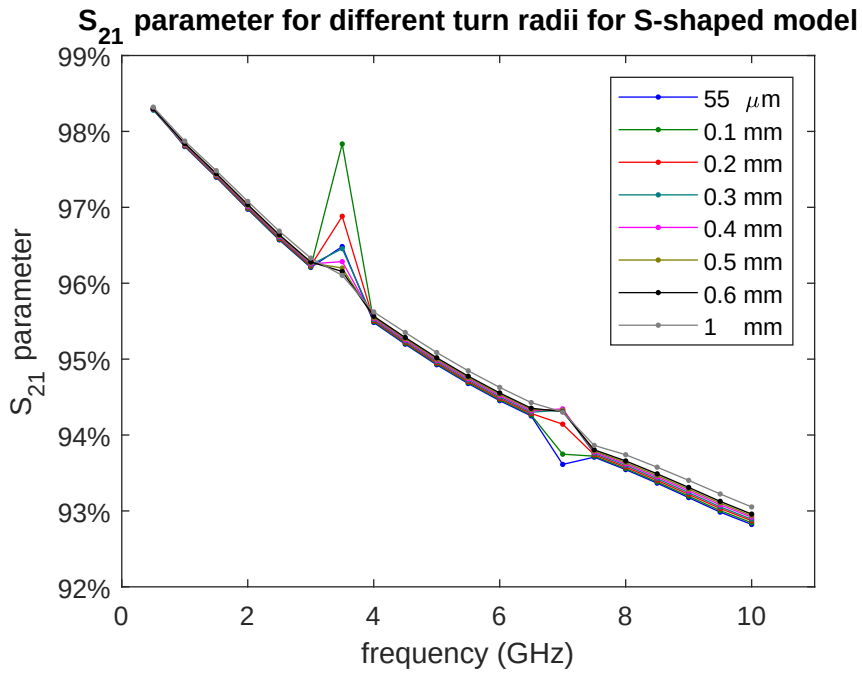

FIG. 7.18: S_{21} parameter for S-shaped model. These curves are calculated with the same model as the S_{11} curve shows in Fig. 7.17

7.4.4 Double S-shaped model

The double S-shaped model connects two S-shaped microstrips in opposite directions as shown in Fig. 7.23. This geometry is another potential candidate for the final design of the atom chip. The double S-shaped model has two more curved section than the U-shaped model; these additional curves might cause it to suffer from a higher S_{11} parameter. However, the double S-shaped model keeps the connection port on the same side of the straight microstrip, which allows us to adjust the width of the substrate as needed or even add an extra trace to the double S-shaped model.

As shown in Fig. 7.24, the S_{11} curves for different radii shows similar oscillation on a similar scale. However, for the 1 mm radius case, there are two large spikes below 4 GHz. Lowest frequency one reaches 6%. The 2 mm and the 4 mm radius cases do not have such spikes and look very similar from DC to 20 GHz.

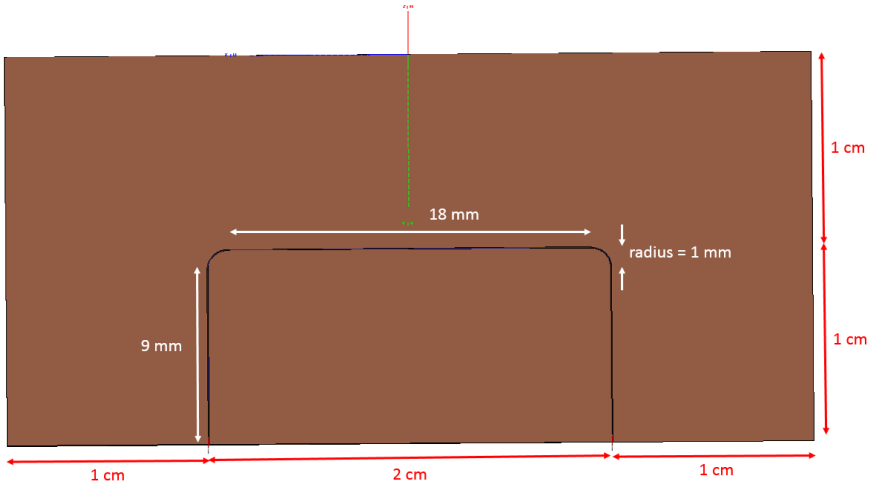

FIG. 7.19: U-shaped model.

The average S_{11} level for the double S-shaped model is around 2% before 10 GHz and increases to 3% at 20 GHz. This result demonstrates that the double S-shaped model suffers rom a 20% to 30% larger S_{11} parameter than the U-shaped model.

7.4.5 Three-microstrip model: prototype atom chip design

The three-microstrip model simulation moves beyond our studies of curved microstrips, so this subsection is a proof-of-principle check on whether our double S-shaped model works within an atom chip design. This model can be used to investigate cross-talk between the three traces and to determine whether there will be a trap. Also, the model building for this three-microstrip model will be a good starting point for future atom chip designs.

The three-microstrip model based on the double S-shaped microstrip, shown in Fig. 7.25, has a straight microstrip in the middle and two double S-shaped microstrips along the sides. In the middle of the chip, there are three 2 cm long

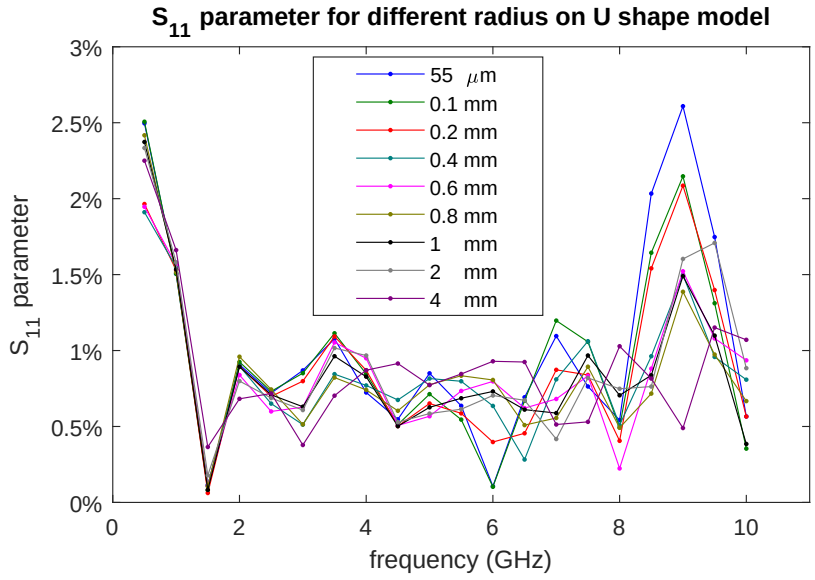

FIG. 7.20: S_{11} parameter for the U-shaped model with different turn radii. Each curve of the U-shaped model is 90 degrees. The distinction between different radii's S_{11} parameter curves occurs at around 9 GHz in frequency. All radii display a peak at this point, but this peak is much larger for radii smaller than 200 μm.

straight parallel microstrips set up next to each other. These three parallel straight microstrips will generate a magnetic minimum in their near field, which can be used to trap atoms. Conveniently the curves of the outside microstrips separate the microstrips far enough to set up an SMA connection ports on either end of each microstrip.

Fig. 7.26 shows the near field generated by the three-microstrip model. The currents in the double S-shaped microstrips on both sides share the same phase and are around 180° out-of-phase with the current in the middle straight microstrip. The voltage setting for the two microstrips on the side are 1 V, while the middle microstrip has half of its value, 0.5 V. Under these conditions, magnetic minimum point appears above the center microstrip, which can then be used to trap atoms in weak-field seeking AC Zeeman states.

Table 7.2 shows the S parameters for this three-microstrip model at 6.8 GHz.

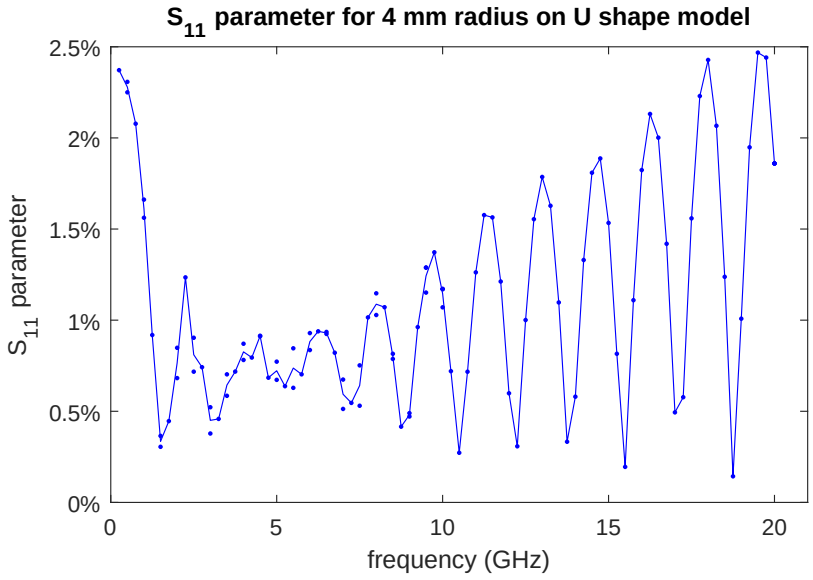

FIG. 7.21: S_{11} parameter for the U-shaped model with a 4 mm turn radius. This data was obtained under the same conditions as those in Fig. 7.20. For some frequencies below 10 GHz, there are two data points with different values at the same frequency: the data is generated by 2 different mesh patterns. This difference in value can be treated as a kind of error bar for the simulation.

The port labels are shown in Fig. 7.25. In the table, we can see that the transmission (S_{61} and S_{42}), the reflection (S_{11} and S_{22}), and the cross-talk (S_{21}, S_{31}, S_{41}, S_{51}, S_{12}, S_{32}, S_{52} and S_{62}) improve with large trace separation as compared to a small separation. The cross-talk is quite large in this simulation and reaches 30% for 100 μm center-to-center separation and 16% for 200 μm center-to-center separation. The larger separation shows better on the cross-talk, but still significant. We need further research on the three-microstrip model to improve it.

7.5 Conclusion for curved traces studies

Base on the studies presented in this chapter, we have a basic understanding about the behavior of the curved microstrip. When implemented correctly, the curved microstrip has a limited effect on the overall reflection coefficient. For most

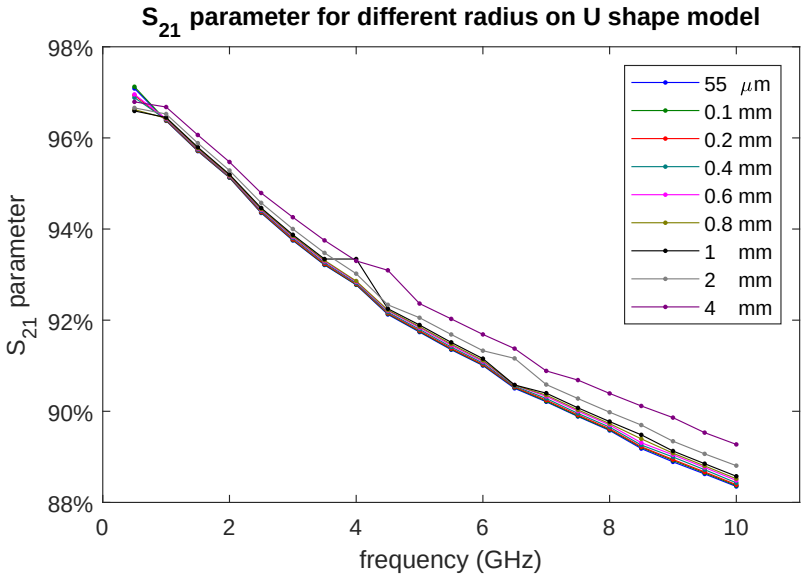

FIG. 7.22: S_{21} parameter for different radius. The S_{21} parameter does not show much difference between different turn radii. The data are on the same scale and follow the same trend. For a larger radius, such as the 4 mm case, the S_{21} parameter is slightly higher than other cases, but this advantage is quite small.

of the simulations in this chapter, the reflection coefficients are smaller than 3% and the transmission coefficients are higher than 93%; from these quantitieswe estimate that roughly 13% of the power will be converted to heat.

Our maximum microwave power is 20 W, so a 13% loss is around 2.6 W, not a small number. If necessary, we can add a protection interlock to limit the "on" time for microwave power into the chip.

For the parameters of microstrip, basically the smaller the curve angle and the bigger the turn radius, the better the performance is. These conditions require us to balance the reflection coefficient and the size of our chip. As a rule of thumb, the turn radius should be larger than 0.3 mm, to limit the increase in the reflection coefficient. However, if we use the double S-shaped model, the turn radius should be larger than 1 mm.

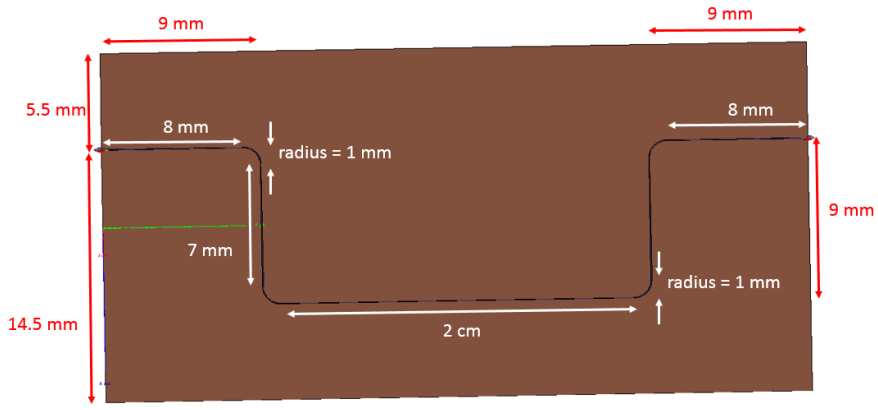

FIG. 7.23: Double S shape model

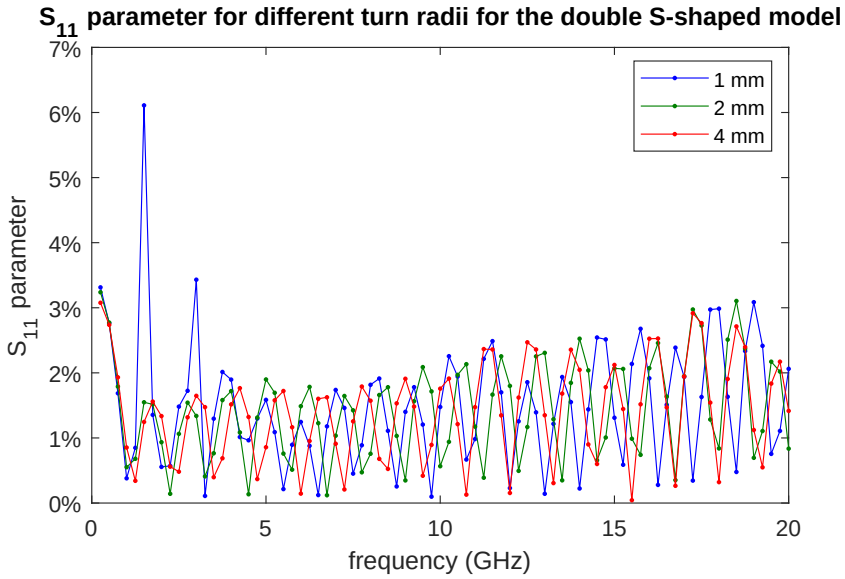

FIG. 7.24: S_{11} parameter for double S-shaped model with different turn radii. This double S-shaped model ran with 90 degree angle for each curve, and the separation between the middle straight line and the straight line on both side was kept at 22 mm.

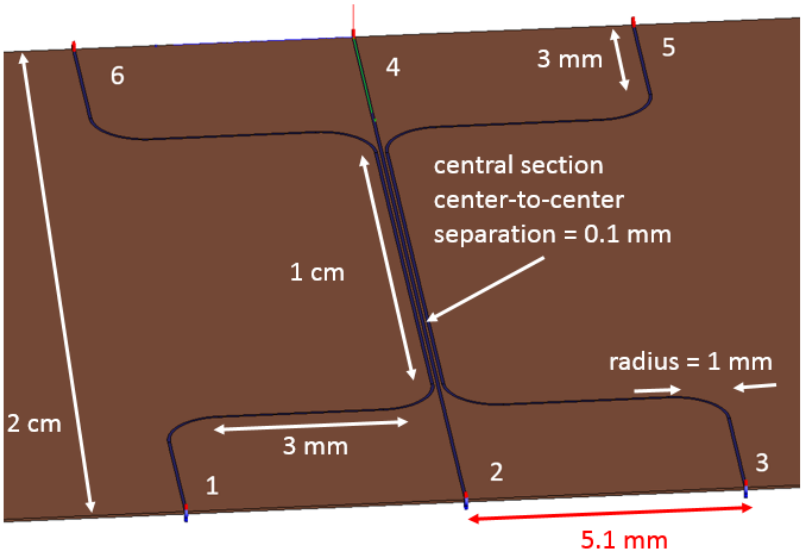

FIG. 7.25: Three-microstrip model. This model is constructed by 2 double S-shaped microstrip on both side, and a straight trace in the middle. In the central section, the parallel traces are separated by 100 μm center-to-center. The length of the middle straight line is 1 cm, the turn radius of the curves is 1 mm, and the distance between the trace edge ports at the substrate edge is 5 mm.

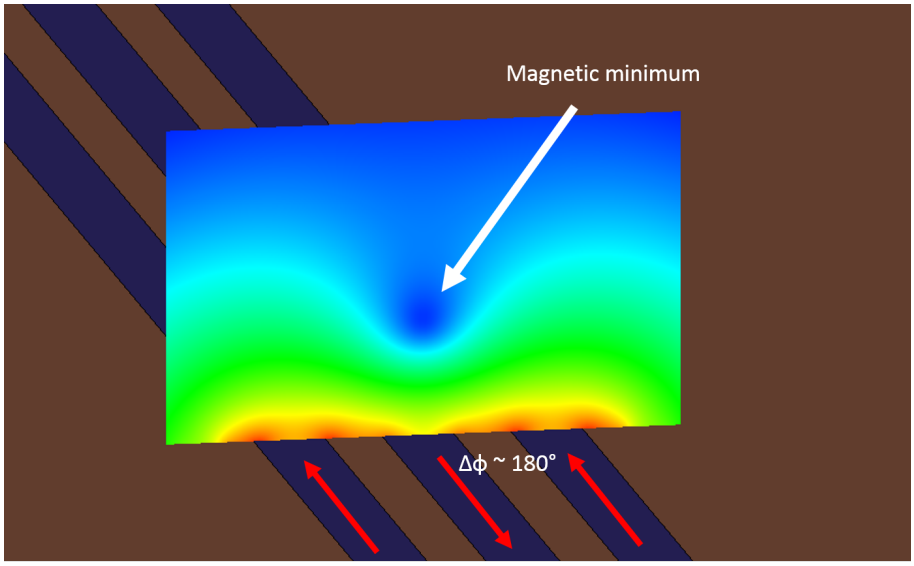

FIG. 7.26: Microwave atom chip trap for 6.8 GHz. The three microstrip traces generate a microwave magnetic field minimum, which serves as a trap for atoms. This trap point is produced when setting the phase of the middle current 180 degrees from the side traces.

	100 μm center-to-center separation	200 μm center-to-center separation	type
S11	3.9%	1.3%	reflection
S21	8.8%	2.6%	cross talk
S31	4.1%	0.7%	cross talk
S41	29.7%	16.2%	cross talk
S51	13.8%	4.6%	cross talk
S61	84.1%	89.2%	transmission
S12	8.8%	2.6%	cross talk
S22	6.2%	1.6%	reflection
S32	8.8%	2.6%	cross talk
S42	81.1%	90.0%	transmission
S52	29.6%	16.2%	cross talk
S62	30.0%	16.2%	cross talk

TABLE 7.2: S parameters for three-microstrip model. This table is simulated by FEKO. The cross talk between the microstrips can be significant. For 100 μm center-to-center separation case, the cross talk could reaches 30%, while for the 200 μm center-to-center case, the cross talking will drop to 16%.

CHAPTER 8

Conclusion

In conclusion, this thesis presented the results of four research projects during my Ph.D. career. These projects are targeted at the long-term lab goal: constructing a spin-dependent trapped atom interferometer.

The introduction in chapter 1 introduced traditional ballistic atom interferometers, the opportunities and challenges of trapped atom interferometers, and the logic chain on the choice of AC Zeeman traps and potentials as the main tools for the trapped atom interferometer. The main difficulty for trapped atom interferometry is atom-atom interactions, and we plan to use ultracold fermions and thermal bosons for multi-mode atom interferometer to reduce these interactions. The multi-mode atom interferometer has a high requirement for keeping the trap shape during the Ramsey time, especially with the spatial separation. A spin-dependent trap is suitable for this requirement, and the AC Zeeman effect is the handiest tool for constructing a the spin-dependent trap in our lab.

The apparatus chapter (chapter 2) presents the apparatus and experiment cycle for the rubidium system, which previous Ph.D. researchers in our lab mainly constructed. Chapter 3 discussed my first project, the potassium laser cooling and

chip trapping sysytem. This chapter discusses the benefits of potassium isotopes the trapped atom interferometer experiment, and shows how the potassium cooling system is integrated to the rubidium cooling system, along with some potassium specific additions to improve the cooling and trapping quality. However, due to some unexpected inelastic collisions between the rubidium and potassium atoms in the chip trap, we failed to obtain a potassium BEC in this project. Nevertheless, the data shows that our potassium gas conditions are not far from those groups who have successfully reached a potassium BEC in the chip trap. Further improvements to the potassium system require some new instruments to be set up.

The trapping theory chapter (chapter 4) focuses on the atom chip trap physics for the DC Zeeman trap and the AC Zeeman trap. The theory chapter supports chapter 5, which discusses a theoretical and computational research project on the chip trap magnetic potential roughness suppression in AC Zeeman traps as compared to DC Zeeman traps. This project uses two methods: numerical simulations with a distorted single 1D wire model and FEKO electromagnetic simulations on a microstrip model with a conductivity patch or an edge defect. The result shows that for a single distorted wire, the AC Zeeman trap suppresses the magnetic roughness with the maximum suppression factor from 10 to 10^8. We find that the suppression factor increases with the trap height h, and number of defects, but decreases with the bump length l. The FEKO simulations shows that for a conductivity variation patch on the edge of the microstrip the AC skin effect suppresses the defect for high frequency currents. For the edge defect case, the high frequency currents perform slightly worse than low-frequency currents, since the skin effect tends to push the current into the edge defect at high frequency. Therefore, it will be important to fabricate chips with very clean trace edges (i.e. very few edge defects).

Chapter 6 introduces the basic theory of atom interferometry with Ramsey interferometer and presents progress on a rubidium atom interferometer with a spin-

dependent AC Zeeman force. This project has achieved significant progress: a fully operational Ramsey interferometer with coherence out to 0.5 s, "magic" magnetic field calibration, a DC Zeeman energy detector, and an AC Zeeman energy detector. In the AC Zeeman energy detection experiment, we found a fast decay on the atom interferometer signal, which might be because of the curvature or the gradient of the AC magnetic near field. The gradient might add an extra force to separate the atom clouds, which we plan to do for the spatial atom interferometer.

Chapter 7 presents microwave simulation research on the curved microstrip traces. This project resulted in preliminary broadband atom chip design based on low reflection with curved trace.

The above projects have significantly progressed the atom interferometer experiment. However, the experimental projects, notably the potassium chip trap cooling and atom interferometer projects, left some unsolved problems: the lab temperature drifting issue and microwave amplifier power decay issue are both possible to cause a phase slip in the atom interferometer experiment. Continuing the experiment with these issues might require to solve them in the middle of a project. Therefore, solving these problems before the next project starts will be helpful for future project progress.

In my opinion, the potassium system should construct the ODT moving system for further cooling before loading the potassium into the chip trap. Meanwhile, we should research a more reliable shutter system because the potassium system is very sensitive to shutter timing. Moreover, the shutter is fragile and often breaks, and it takes around a day to fix. Therefore, having a reliable shutter system will greatly improve the experiment efficiency.

For the atom interferometer project, I am very interested in the two-photon transition sidebands. There might be some interesting physics hidden in it. We should also continue some of the paused projects, such as the Ioffe current stabiliza-

tion system with a high-precision current sensor. These supportive projects will be helpful for our experiment, but we need more time on them. At last, the number of instruments for the atom interferometer project increases a lot during the atom interferometer project. They are not very well integrated, making some difficulty to the experiment, such as experiment control, logging, and problem detection. The set up of an integrated, automated, centralized control and monitoring system will improve the experiment's reliability and efficiency. Moreover, it will also release the researcher from babysitting the instruments and thus focusing on physics.

I hope this thesis will be helpful for future Ph.D. researchers in the lab as well as those who will work on the AC Zeeman effect and microwave atom chip trap design.

APPENDIX A

FEKO tips

This appendix presents tips on how to conduct simulations relevant to microwave atom chip design.

A.1 SEP solution

In FEKO, there are several types of solution methods that we can choose: mainly method of moments (SEP and VEP), and FEM solution.

VEP and FEM solution will consider all the volume in the model and the mesh number will be huge, while SEP will only consider the surface. SEP will lose some precision in the simulation, but in our simulation models, this loss is generally acceptable. Because our models run at a high frequency, most of the current will feel a strong skin effect. The SEP solution considers most of the current that contributes to the results.

A.2 Regular configuration and S parameter configuration

FEKO has two type of configurations: regular configuration and S parameter configuration. We use both of them.

The regular configuration is use to calculate the current distribution on the trace, magnetic near field above the trace, and the reflection to the voltage source. The S parameter configuration, as its name implies, is used to calculate the S parameter result, but it cannot be used for near field calculations.

These two type of configurations, unfortunately, cannot be used simultaneously, because they need slightly different model settings.

The regular configuration needs to add a source port and load port on to the edge ports of the model. In contrast, the S parameter configuration will automatically consider all the edge ports into its S parameter calculation, and we only need to activate at least one of the port to be the source. If we run these two type of configurations at the same time, the edge ports will have a "double definition", and FEKO will treat the port as two sources/loads in parallel, and the impedance setting will totally messed up!

A.3 Local mesh size

Another way to run simulations more efficiently is to set the mesh size in the transmission line as big as possible, while verifying that the result do not change too much.

The first thing we are looking for is the skin effect. As shown in Fig. A.2, there will be 4 triangles across the trace if we set the mesh size to be widthtrace/2. However, this mesh size fails to show any skin effect in the trace (see Fig. A.1).

For the mesh size of widthtrace/3, there will be some skin effect visible in the current distribution result (Fig. A.3). If we have a look at the mesh pattern, Fig. A.4, it has 8 triangles across the trace, double the time of the case when the mesh size is widthtrace/2.

If we compare the triangle number for different mesh size under the same model, the case of mesh size at widthtrace/2 has 22974 triangles, while the case of mesh size at widthtrace/3 has 36702 triangles, which has 50% more triangles than the case of widthtrace/2. Since for the MOM solusion, the running time will increase with cube of the triangle number, and the memory requirement will square the triangle number, running with widthtrace/3 will need longer simulation time and more computing resource.

Even though, in the current distribution, the mesh size of widthtrace/2 does not show any skin effect, there is still a possibility that the simulation already considers the skin effect, but did not display the result, due to the coarse mesh size. To test this possibility, we run a simple straight microstrip model with different mesh sizes to check how the mesh size affects the S parameters. As shown in Fig. A.5, the smaller the mesh size is, the higher the S_{11} parameter. This result means that the coarse mesh size causes an underestimate of the S_{11} parameter. Even though the mesh size has an effect on the S_{11} parameter, it is not too significant. From mesh sizes at widthtrace/2 to widthtracce/5, the S_{11} parameter only increases by 0.4%. Considering the extra running time and memory requirements, running the simulation with widthtrace/2 provides good balance between accuradcy and run time.

A.4 How to make a uniform width curving trace.

To make a curved trace with a uniform width in FEKO, we need to use the path sweep tool. As shown in Fig. A.6, the curved trace is constructed by two lines, shown in yellow. The straight line is the width of the curve, and the curved line is the path. We set the straight line to sweep through the curved line with the path sweep tool to build the curved trace used in our simulations.

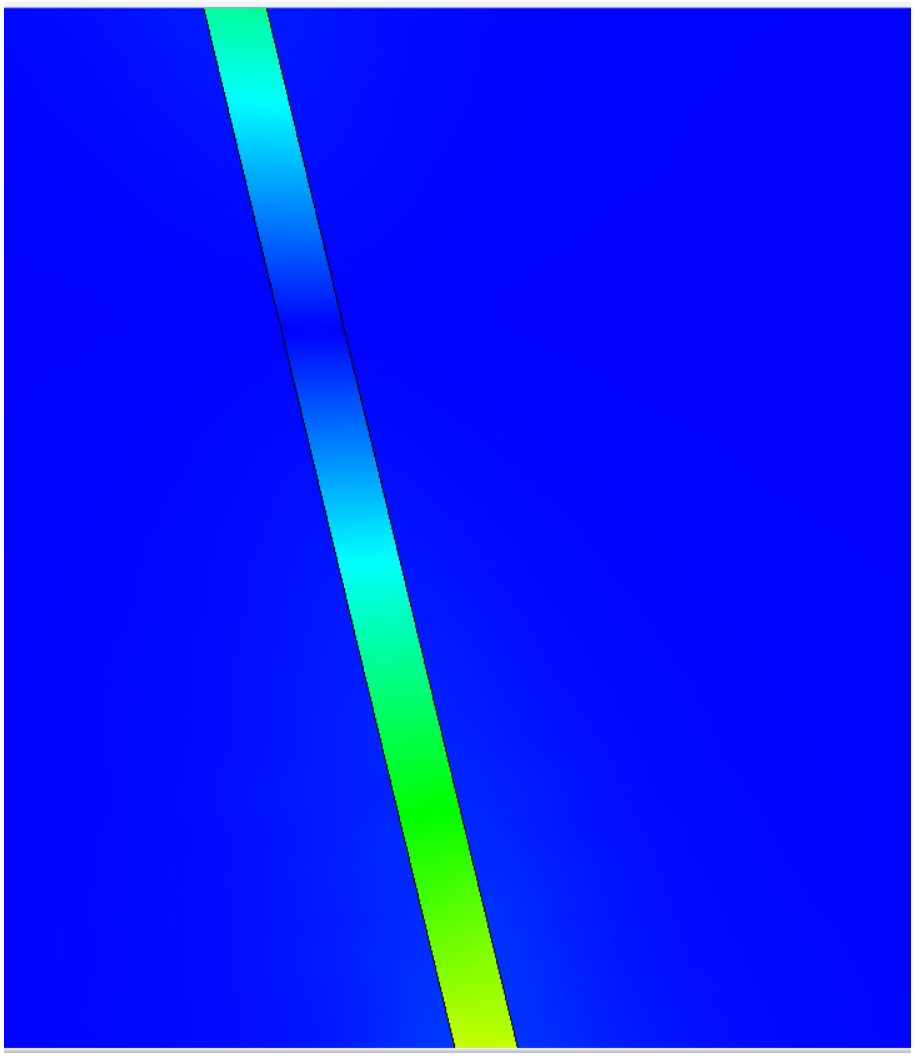

FIG. A.1: Current distribution in the trace when the mesh size is widthtrace/2. At this mesh setting, the current distribution does not show any skin effect.

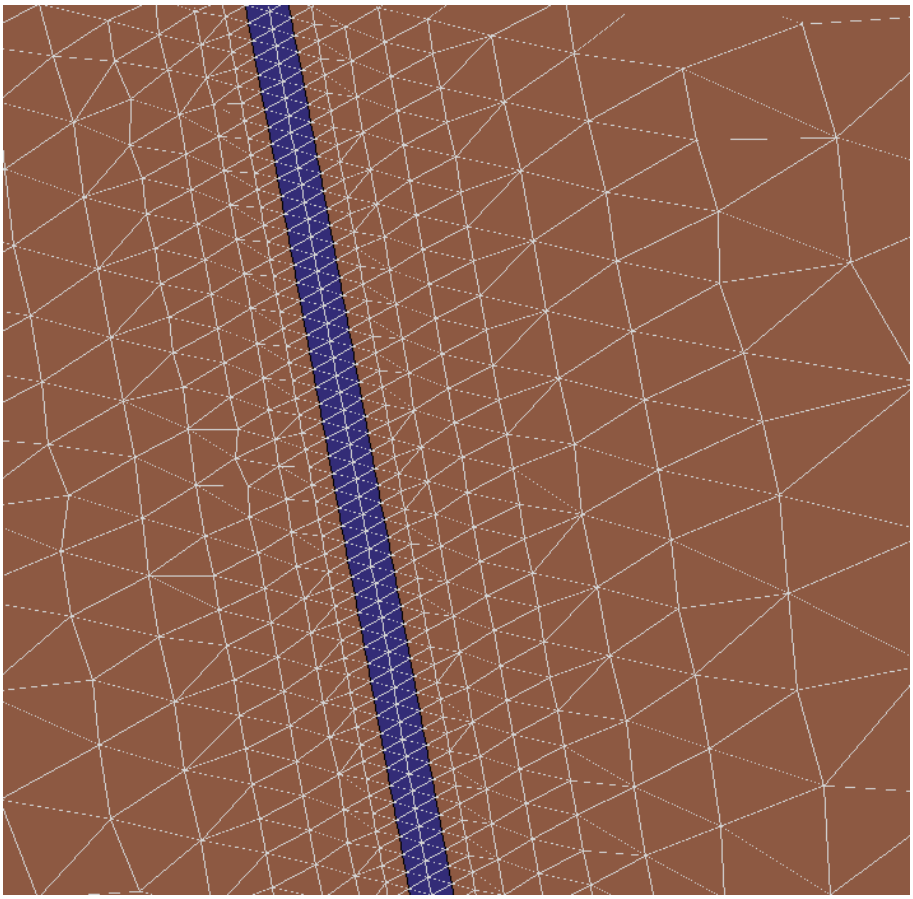

FIG. A.2: Mesh pattern when the mesh size is widthtrace/2. Under this condition the model has a total of 22974 triangles.

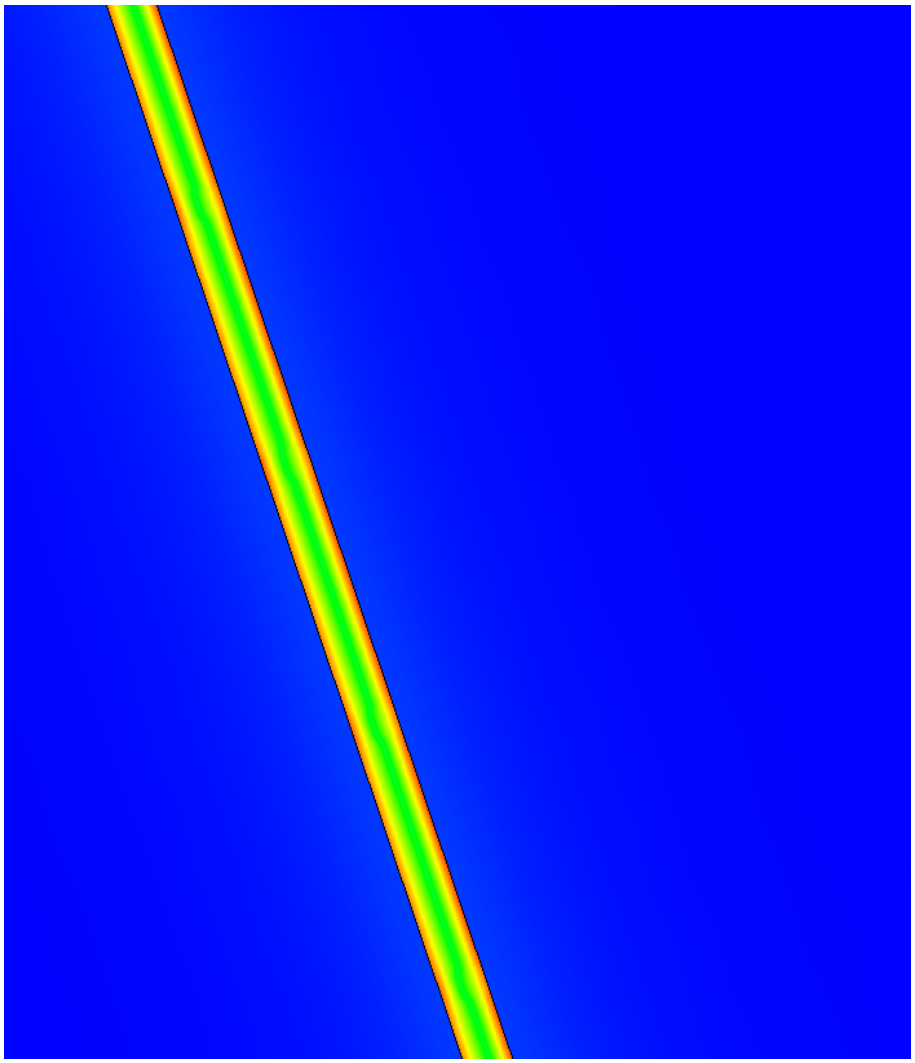

FIG. A.3: Current distribution in the trace when the mesh size is widthtrace/3. At this mesh setting, the current distribution shows the skin effect.

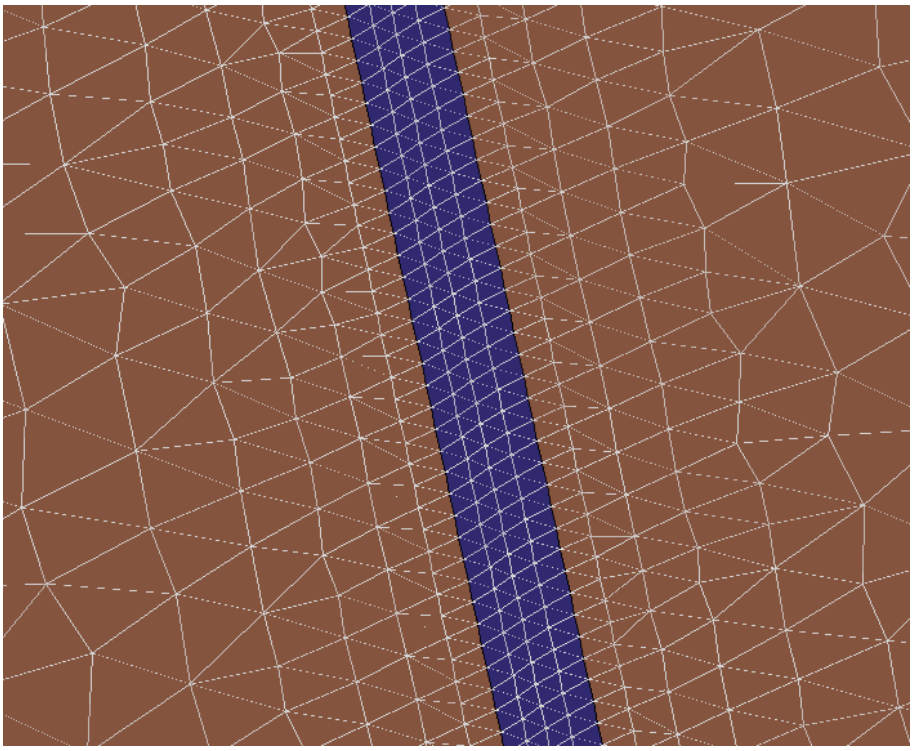

FIG. A.4: Mesh pattern when the mesh size is widthtrace/3. Under this condition, the model has a total of 36702 triangles.

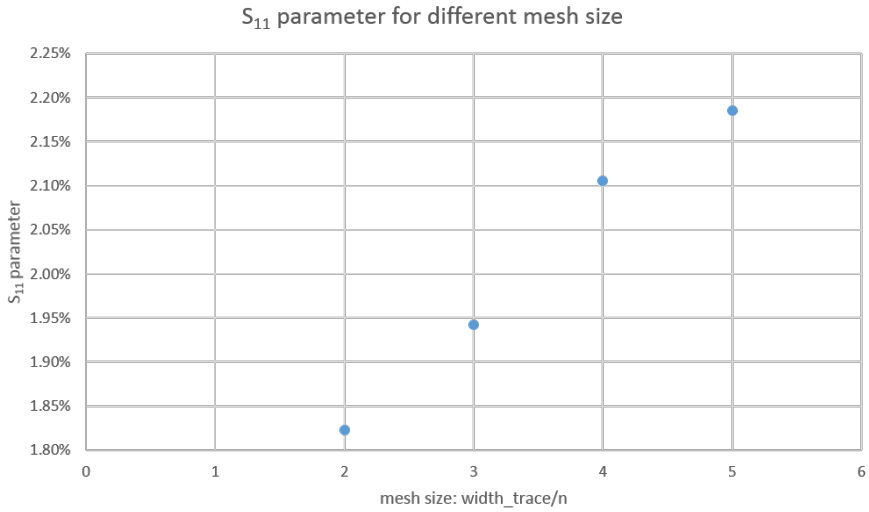

FIG. A.5: S_{11} parameter for different mesh sizes.

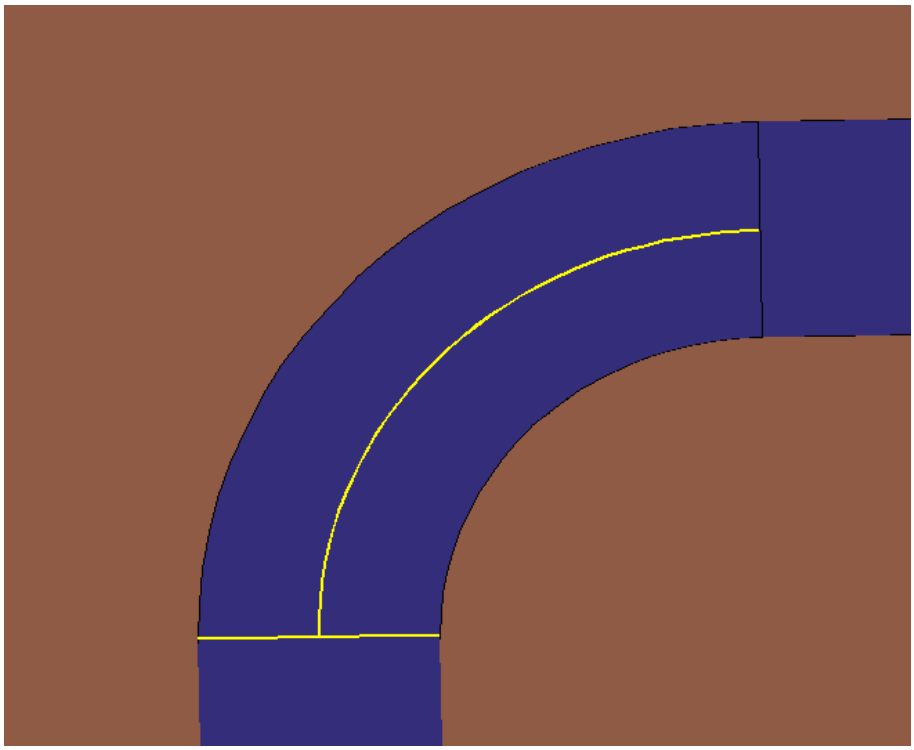

FIG. A.6: Close view of the microstrip curve

APPENDIX B

Atom interferometer resonance scan sideband peak width

This appendix provide extra information for the sideband effect in resonance scan, which we described in subsection 6.8.1. The figure B.1 shows the change of the peak width with the ODT power. Generally, the peak width drop with the ODT power, but the peak width at -8.5 V is largest.

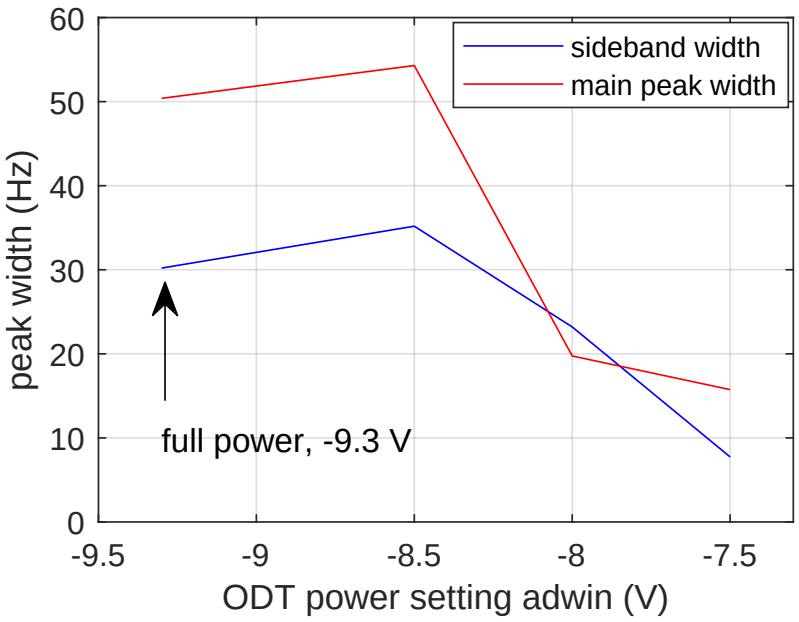

FIG. B.1: Peak width for atom interferometer resonance scan sidebands.

BIBLIOGRAPHY

[1] C. Ospelkaus, U. Warring, Y. Colombe, K. Brown, J. Amini, D. Leibfried, and D. J. Wineland, "Microwave quantum logic gates for trapped ions," *Nature*, vol. 476, no. 7359, pp. 181–184, 2011.

[2] T. Harty, D. Allcock, C. J. Ballance, L. Guidoni, H. Janacek, N. Linke, D. Stacey, and D. Lucas, "High-fidelity preparation, gates, memory, and readout of a trapped-ion quantum bit," *Physical review letters*, vol. 113, no. 22, p. 220501, 2014.

[3] C. F. Ockeloen, R. Schmied, M. F. Riedel, and P. Treutlein, "Quantum metrology with a scanning probe atom interferometer," *Phys. Rev. Lett.*, vol. 111, p. 143001, Oct 2013.

[4] R. Folman, P. Kruger, J. Schmiedmayer, J. Denschlag, and C. Henkel, "Microscopic atom optics: from wires to an atom chip," *arXiv preprint arXiv:0805.2613*, 2008.

[5] M. F. Riedel, P. Böhi, Y. Li, T. W. Hänsch, A. Sinatra, and P. Treutlein, "Atom-chip-based generation of entanglement for quantum metrology," *Nature*, vol. 464, no. 7292, pp. 1170–1173, 2010.

[6] T. Schumm, S. Hofferberth, L. M. Andersson, S. Wildermuth, S. Groth, I. Bar-Joseph, J. Schmiedmayer, and P. Krüger, "Matter-wave interferometry in a double well on an atom chip," *Nature physics*, vol. 1, no. 1, pp. 57–62, 2005.

[7] S. Du, M. B. Squires, Y. Imai, L. Czaia, R. A. Saravanan, V. Bright, J. Reichel, T. Hänsch, and D. Z. Anderson, "Atom-chip bose-einstein condensation in a portable vacuum cell," *Physical Review A*, vol. 70, no. 5, p. 053606, 2004.

[8] S. Schneider, A. Kasper, C. Vom Hagen, M. Bartenstein, B. Engeser, T. Schumm, I. Bar-Joseph, R. Folman, L. Feenstra, and J. Schmiedmayer, "Bose-einstein condensation in a simple microtrap," *Physical Review A*, vol. 67, no. 2, p. 023612, 2003.

[9] B. Canuel, F. Leduc, D. Holleville, A. Gauguet, J. Fils, A. Virdis, A. Clairon, N. Dimarcq, C. J. Bordé, A. Landragin, *et al.*, "Six-axis inertial sensor using cold-atom interferometry," *Physical review letters*, vol. 97, no. 1, p. 010402, 2006.

[10] A. Lenef, T. D. Hammond, E. T. Smith, M. S. Chapman, R. A. Rubenstein, and D. E. Pritchard, "Rotation sensing with an atom interferometer," *Physical review letters*, vol. 78, no. 5, p. 760, 1997.

[11] F. Riehle, T. Kisters, A. Witte, J. Helmcke, and C. J. Bordé, "Optical ramsey spectroscopy in a rotating frame: Sagnac effect in a matter-wave interferometer," *Physical review letters*, vol. 67, no. 2, p. 177, 1991.

[12] T. Gustavson, P. Bouyer, and M. Kasevich, "Precision rotation measurements with an atom interferometer gyroscope," *Physical review letters*, vol. 78, no. 11, p. 2046, 1997.

[13] A. Peters, K. Y. Chung, and S. Chu, "High-precision gravity measurements using atom interferometry," *Metrologia*, vol. 38, no. 1, p. 25, 2001.

[14] J. B. Fixler, G. Foster, J. McGuirk, and M. Kasevich, "Atom interferometer measurement of the newtonian constant of gravity," *Science*, vol. 315, no. 5808, pp. 74–77, 2007.

[15] M. Snadden, J. McGuirk, P. Bouyer, K. Haritos, and M. Kasevich, "Measurement of the earth's gravity gradient with an atom interferometer-based gravity gradiometer," *Physical review letters*, vol. 81, no. 5, p. 971, 1998.

[16] M. G. Tarallo, T. Mazzoni, N. Poli, D. Sutyrin, X. Zhang, and G. Tino, "Test of einstein equivalence principle for 0-spin and half-integer-spin atoms: search for spin-gravity coupling effects," *Physical review letters*, vol. 113, no. 2, p. 023005, 2014.

[17] D. Schlippert, J. Hartwig, H. Albers, L. L. Richardson, C. Schubert, A. Roura, W. P. Schleich, W. Ertmer, and E. M. Rasel, "Quantum test of the universality of free fall," *Physical Review Letters*, vol. 112, no. 20, p. 203002, 2014.

[18] M. Jaffe, P. Haslinger, V. Xu, P. Hamilton, A. Upadhye, B. Elder, J. Khoury, and H. Müller, "Testing sub-gravitational forces on atoms from a miniature in-vacuum source mass," *Nature Physics*, vol. 13, no. 10, pp. 938–942, 2017.

[19] G. Rosi, G. D'Amico, L. Cacciapuoti, F. Sorrentino, M. Prevedelli, M. Zych, Č. Brukner, and G. Tino, "Quantum test of the equivalence principle for atoms

in coherent superposition of internal energy states," *Nature communications*, vol. 8, no. 1, pp. 1–6, 2017.

[20] V. Xu, M. Jaffe, C. D. Panda, S. L. Kristensen, L. W. Clark, and H. Müller, "Probing gravity by holding atoms for 20 seconds," *Science*, vol. 366, no. 6466, pp. 745–749, 2019.

[21] N. Hinkley, J. A. Sherman, N. B. Phillips, M. Schioppo, N. D. Lemke, K. Beloy, M. Pizzocaro, C. W. Oates, and A. D. Ludlow, "An atomic clock with 10–18 instability," *Science*, vol. 341, no. 6151, pp. 1215–1218, 2013.

[22] A. Wicht, J. M. Hensley, E. Sarajlic, and S. Chu, "A preliminary measurement of the fine structure constant based on atom interferometry," *Physica scripta*, vol. 2002, no. T102, p. 82, 2002.

[23] R. H. Parker, C. Yu, W. Zhong, B. Estey, and H. Müller, "Measurement of the fine-structure constant as a test of the standard model," *Science*, vol. 360, no. 6385, pp. 191–195, 2018.

[24] L. Morel, Z. Yao, P. Cladé, and S. Guellati-Khélifa, "Determination of the fine-structure constant with an accuracy of 81 parts per trillion," *Nature*, vol. 588, no. 7836, pp. 61–65, 2020.

[25] D. Hanneke, S. Fogwell, and G. Gabrielse, "New measurement of the electron magnetic moment and the fine structure constant," *Physical Review Letters*, vol. 100, no. 12, p. 120801, 2008.

[26] J. Prodan, A. Migdall, W. D. Phillips, I. So, H. Metcalf, and J. Dalibard, "Stopping atoms with laser light," *Physical review letters*, vol. 54, no. 10, p. 992, 1985.

[27] M. A. Kasevich, "Coherence with atoms," *Science*, vol. 298, no. 5597, pp. 1363–1368, 2002.

[28] H. J. Metcalf and P. Van der Straten, "Laser cooling and trapping of neutral atoms," *The Optics Encyclopedia: Basic Foundations and Practical Applications*, 2007.

[29] J. Reichel, W. Hänsel, and T. Hänsch, "Atomic micromanipulation with magnetic surface traps," *Physical Review Letters*, vol. 83, no. 17, p. 3398, 1999.

[30] S. Leslie, J. Guzman, M. Vengalattore, J. D. Sau, M. L. Cohen, and D. Stamper-Kurn, "Amplification of fluctuations in a spinor bose-einstein condensate," *Physical Review A*, vol. 79, no. 4, p. 043631, 2009.

[31] K. B. Davis, M.-O. Mewes, M. R. Andrews, N. J. van Druten, D. S. Durfee, D. Kurn, and W. Ketterle, "Bose-einstein condensation in a gas of sodium atoms," *Physical review letters*, vol. 75, no. 22, p. 3969, 1995.

[32] M. W. Zwierlein, C. A. Stan, C. H. Schunck, S. M. Raupach, S. Gupta, Z. Hadzibabic, and W. Ketterle, "Observation of bose-einstein condensation of molecules," *Physical review letters*, vol. 91, no. 25, p. 250401, 2003.

[33] J. Ensher, D. S. Jin, M. Matthews, C. Wieman, and E. A. Cornell, "Bose-einstein condensation in a dilute gas: Measurement of energy and ground-state occupation," *Physical Review Letters*, vol. 77, no. 25, p. 4984, 1996.

[34] J. R. Anglin and W. Ketterle, "Bose–einstein condensation of atomic gases," *Nature*, vol. 416, no. 6877, pp. 211–218, 2002.

[35] S. M. Dickerson, J. M. Hogan, A. Sugarbaker, D. M. S. Johnson, and M. A. Kasevich, "Multiaxis inertial sensing with long-time point source atom interferometry," *Phys. Rev. Lett.*, vol. 111, p. 083001, Aug 2013.

[36] M. Abe, P. Adamson, M. Borcean, D. Bortoletto, K. Bridges, S. P. Carman, S. Chattopadhyay, J. Coleman, N. M. Curfman, K. DeRose, T. Deshpande, S. Dimopoulos, C. J. Foot, J. C. Frisch, B. E. Garber, S. Geer, V. Gibson, J. Glick, P. W. Graham, S. R. Hahn, R. Harnik, L. Hawkins, S. Hindley, J. M. Hogan, Y. Jiang, M. A. Kasevich, R. J. Kellett, M. Kiburg, T. Kovachy, J. D. Lykken, J. March-Russell, J. Mitchell, M. Murphy, M. Nantel, L. E. Nobrega, R. K. Plunkett, S. Rajendran, J. Rudolph, N. Sachdeva, M. Safdari, J. K. Santucci, A. G. Schwartzman, I. Shipsey, H. Swan, L. R. Valerio, A. Vasonis, Y. Wang, and T. Wilkason, "Matter-wave atomic gradiometer interferometric sensor (magis-100)," 2021.

[37] D. Becker, M. D. Lachmann, S. T. Seidel, H. Ahlers, A. N. Dinkelaker, J. Grosse, O. Hellmig, H. Mntinga, V. Schkolnik, T. Wendrich, A. Wenzlawski, B. Weps, R. Corgier, T. Franz, N. Gaaloul, W. Herr, D. Ldtke, M. Popp, S. Amri, H. Duncker, M. Erbe, A. Kohfeldt, A. Kubelka-Lange, C. Braxmaier, E. Charron, W. Ertmer, M. Krutzik, C. Lmmerzahl, A. Peters, W. P. Schleich, K. Sengstock, R. Walser, A. Wicht, P. Windpassinger, and E. M. Rasel, "Space-borne bose-einstein condensation for precision interferometry," *Nature*, vol. 562, pp. 391–395, 2018.

[38] D. C. Aveline, J. R. Williams, E. R. Elliott, C. Dutenhoffer, J. R. Kellogg, J. M. Kohel, N. E. Lay, K. Oudrhiri, R. F. Shotwell, N. Yu, and R. J. Thompson, "Observation of bose-einstein condensates in an earth-orbiting research lab," *Nature*, vol. 582, pp. 193–197, 2020.

[39] P. Treutlein, P. Hommelhoff, T. Steinmetz, T. W. Hänsch, and J. Reichel, "Coherence in microchip traps," *Phys. Rev. Lett.*, vol. 92, p. 203005, May 2004.

[40] C. Deutsch, F. Ramirez-Martinez, C. Lacroûte, F. Reinhard, T. Schneider, J. N. Fuchs, F. Piéchon, F. Laloë, J. Reichel, and P. Rosenbusch, "Spin self-rephasing and very long coherence times in a trapped atomic ensemble," *Phys. Rev. Lett.*, vol. 105, p. 020401, Jul 2010.

[41] J. M. Obrecht, R. J. Wild, M. Antezza, L. P. Pitaevskii, S. Stringari, and E. A. Cornell, "Measurement of the temperature dependence of the casimir-polder force," *Phys. Rev. Lett.*, vol. 98, p. 063201, Feb 2007.

[42] D. J. Kapner, T. S. Cook, E. G. Adelberger, J. H. Gundlach, B. R. Heckel, C. D. Hoyle, and H. E. Swanson, "Tests of the gravitational inverse-square law below the dark-energy length scale," *Phys. Rev. Lett.*, vol. 98, p. 021101, Jan 2007.

[43] E. R. Moan, R. A. Horne, T. Arpornthip, Z. Luo, A. J. Fallon, S. J. Berl, and C. A. Sackett, "Quantum rotation sensing with dual sagnac interferometers in an atom-optical waveguide," *Phys. Rev. Lett.*, vol. 124, p. 120403, Mar 2020.

[44] M. O. Scully and J. P. Dowling, "Quantum-noise limits to matter-wave interferometry," *Phys. Rev. A*, vol. 48, pp. 3186–3190, Oct 1993.

[45] S. Aubin, S. Myrskog, M. H. T. Extavour, L. J. LeBlanc, D. McKay, A. Stummer, and J. H. Thywissen, "Rapid sympathetic cooling to fermi degeneracy on a chip," *Nature Phys.*, vol. 2, p. 384, 2006.

[46] C. Gross, T. Zibold, E. Nicklas, J. Estve, and M. K. Oberthaler, "Nonlinear atom interferometer surpasses classical precision limit," *Nature*, vol. 464, pp. 1165–1169, 2010.

[47] M. Bloom and K. Erdman, "The transverse stern–gerlach experiment," *Canadian Journal of Physics*, vol. 40, no. 2, pp. 179–193, 1962.

[48] M. Bloom, E. Enga, and H. Lew, "Observation of the transverse stern–gerlach effect in neutral potassium," *Canadian Journal of Physics*, vol. 45, no. 4, pp. 1481–1495, 1967.

[49] C. Agosta, I. Silvera, H. Stoof, and B. Verhaar, "Trapping of neutral atoms with resonant microwave radiation," *Physical Review Letters*, vol. 62, no. 20, pp. 2361–2364, 1989.

[50] R. J. C. Spreeuw, C. Gerz, L. S. Goldner, W. D. Phillips, S. L. Rolston, C. I. Westbrook, M. W. Reynolds, and I. F. Silvera, "Demonstration of neutral atom trapping with microwaves," *Phys. Rev. Lett.*, vol. 72, pp. 3162–3165, May 1994.

[51] P. Böhi, M. F. Riedel, J. Hoffrogge, J. Reichel, T. W. Hänsch, and P. Treutlein, "Coherent manipulation of bose-einstein condensates with state-dependent microwave potentials on an atom chip," *Nature Phys.*, vol. 5, p. 592, 2009.

[52] C. Xin-zhao, L. Shu-qin, and D. Tai-qian, "Experimental study of ac zeeman effect in 87rb atomic frequency standard," *Acta Physica Sinica (Overseas Edition)*, vol. 5, no. 6, p. 423, 1996.

[53] C. Fancher, A. Pyle, A. Rotunno, and S. Aubin, "Microwave ac zeeman force for ultracold atoms," *Phys. Rev. A*, vol. 97, no. 4, p. 043430, 2018.

[54] A. P. Rotunno, *Radiofrequency AC Zeeman Trapping for Neutral Atoms*. PhD thesis, College of William and Mary, 2021.

[55] M. K. Ivory, *Experimental Apparatus for Quantum Pumping with a Bose-Einstein Condensate*. PhD thesis, College of William and Mary, 2016.

[56] A. R. Ziltz, *Ultracold rubidium and potassium system for atom chip-based microwave and RF potentials*. PhD thesis, College of William and Mary, 2015.

[57] C. T. Fancher, *AC Zeeman Force with Ultracold Atoms*. PhD thesis, College of William and Mary, 2016.

[58] A. J. Pyle, *Scattering of a Bose-Einstein Condensate off a Modulated Barrier*. PhD thesis, College of William and Mary, 2016.

[59] D. A. Steck, "Rubidium 87 d line data," 2001.

[60] D. M. Harber, H. J. Lewandowski, J. M. McGuirk, and E. A. Cornell, "Effect of cold collisions on spin coherence and resonance shifts in a magnetically trapped ultracold gas," *Phys. Rev. A*, vol. 66, p. 053616, Nov 2002.

[61] G. Barontini, *Ultracold Bose-Bose mixtures with tunable interspecies interactions*. PhD thesis, University of Firenze, 2009.

[62] G. Modugno, G. Ferrari, G. Roati, R. J. Brecha, A. Simoni, and M. Inguscio, "Bose-einstein condensation of potassium atoms by sympathetic cooling," *Science*, vol. 294, no. 5545, pp. 1320–1322, 2001.

[63] T. Kishimoto, J. Kobayashi, K. Noda, K. Aikawa, M. Ueda, and S. Inouye, "Direct evaporative cooling of ^{41}K into a bose-einstein condensate," *Phys. Rev. A*, vol. 79, p. 031602, Mar 2009.

[64] G. Thalhammer, G. Barontini, L. De Sarlo, J. Catani, F. Minardi, and M. Inguscio, "Double species bose-einstein condensate with tunable interspecies interactions," *Phys. Rev. Lett.*, vol. 100, p. 210402, May 2008.

[65] A. Burchianti, C. D'Errico, S. Rosi, A. Simoni, M. Modugno, C. Fort, and F. Minardi, "Dual-species bose-einstein condensate of ^{41}K and ^{87}Rb in a hybrid trap," *Phys. Rev. A*, vol. 98, p. 063616, Dec 2018.

[66] M. Ivory, A. Ziltz, C. Fancher, A. Pyle, A. Sensharma, B. Chase, J. Field, A. Garcia, D. Jervis, and S. Aubin, "Atom chip apparatus for experiments with ultracold rubidium and potassium gases," *Rev. Sci. Instrum.*, vol. 85, no. 4, p. 043102, 2014.

[67] T. Tiecke, "Optical transitions of the d1 and d2-lines of ^{39}k, ^{40}k and ^{41}k," 2019.

[68] Y.-J. Lin, A. R. Perry, R. L. Compton, I. B. Spielman, and J. V. Porto *Phys. Rev. A*, vol. 79, p. 063631, 2009.

[69] S. Du, A. Ziltz, and S. Aubin, "Suppression of potential roughness in atom chip ac zeeman traps," *will be published on pra*, 2021.

[70] J. Fortágh and C. Zimmermann, "Magnetic microtraps for ultracold atoms," *Rev. Mod. Phys.*, vol. 79, pp. 235–289, Feb 2007.

[71] W. Hänsel, P. Hommelhoff, T. W. Hänsch, and J. Reichel, "Bose-einstein condensation on a microelectronic chip," *Nature*, vol. 413, pp. 498–501, 2001.

[72] J. Esteve, J.-B. Trebbia, T. Schumm, A. Aspect, C. I. Westbrook, and I. Bouchoule, "Observations of density fluctuations in an elongated bose gas: Ideal gas and quasicondensate regimes," *Phys. Rev. Lett.*, vol. 96, p. 130403, Apr 2006.

[73] Y.-J. Wang, D. Z. Anderson, V. M. Bright, E. A. Cornell, Q. Diot, T. Kishimoto, M. Prentiss, R. A. Saravanan, S. R. Segal, and S. Wu, "Atom michelson interferometer on a chip using a bose-einstein condensate," *Phys. Rev. Lett.*, vol. 94, p. 090405, Mar 2005.

[74] Y.-j. Lin, I. Teper, C. Chin, and V. Vuletić, "Impact of the casimir-polder potential and johnson noise on bose-einstein condensate stability near surfaces," *Phys. Rev. Lett.*, vol. 92, p. 050404, Feb 2004.

[75] E. R. Elliot, M. C. Krutzik, J. R. Williams, R. J. Thompson, and D. C. Aveline, "Nasa's cold atom lab (cal): system development and ground test status," *npj Microgravity*, vol. 4, p. 16, 2018.

[76] P. Krüger, L. M. Andersson, S. Wildermuth, S. Hofferberth, E. Haller, S. Aigner, S. Groth, I. Bar-Joseph, and J. Schmiedmayer, "Potential roughness near lithographically fabricated atom chips," *Phys. Rev. A*, vol. 76, p. 063621, Dec 2007.

[77] S. Groth, P. Krüger, S. Wildermuth, R. Folman, T. Fernholz, J. Schmiedmayer, D. Mahalu, and I. Bar-Joseph, "Atom chips: Fabrication and thermal properties," *Appl. Phys. Lett.*, vol. 85, p. 2980, 2004.

[78] J.-B. Trebbia, C. L. Garrido Alzar, R. Cornelussen, C. I. Westbrook, and I. Bouchoule, "Roughness suppression via rapid current modulation on an atom chip," *Phys. Rev. Lett.*, vol. 98, p. 263201, Jun 2007.

[79] S. Aigner, L. D. Pietra, Y. Japha, O. Entin-Wohlman, T. David, R. Salem, R. Folman, and J. Schmiedmayer, "Long-range order in electronic transport through disordered metal films," *Science*, vol. 319, no. 5867, pp. 1226–1229, 2008.

[80] M. A. Schneider, M. Wenderoth, A. J. Heinrich, M. A. Rosentreter, and R. G. Ulbrich, "Current transport through single grain boundaries: A scanning tunneling potentiometry study," *Appl. Phys. Lett.*, vol. 69, p. 1327, 1996.

[81] O. Cherry, J. D. Carter, and J. D. D. Martin, "An atom chip for the manipulation of ultracold atoms," *Can. J. Phys.*, vol. 87, p. 633, 2009.

[82] Y. Japha, O. Entin-Wohlman, T. David, R. Salem, S. Aigner, J. Schmiedmayer, and R. Folman, "Model for organized current patterns in disordered conductors," *Phys. Rev. B*, vol. 77, p. 201407, May 2008.

[83] T. Schumm, J. Estève, C. Figl, J.-B. Trebbia, C. Aussibal, H. Nguyen, D. Mailly, I. Bouchoule, C. I. Westbrook, and A. Aspect, "Atom chips in the real world: the effects of wire corrugation," *Eur. Phys. J. D*, vol. 32, p. 171, 2005.

[84] P. Treutlein, *Coherent manipulation of ultracold atoms on atom chips*. PhD thesis, Ludwig Maximilians Universität München, 2008.

[85] M. Dupont-Nivet, R. Demur, C. I. Westbrook, and S. Schwartz, "Experimental study of the role of trap symmetry in an atom-chip interferometer above the bose-einstein condensation threshold," *njp*, vol. 20, Apr 2018.

[86] P. R. Bevington and K. D. Robinson, *Data reduction and error analysis for the physical sciences*. Boston: McGraw-Hill, 2003.

[87] F. Diedrich, J. C. Bergquist, W. M. Itano, and D. J. Wineland, "Laser cooling to the zero-point energy of motion," *Phys. Rev. Lett.*, vol. 62, pp. 403–406, Jan 1989.

[88] W. Miyahira, A. Rotunno, S. Du, and S. Aubin, "Microwave atom chip design," *"submitted to MDPI Atoms"*, 2021.

[89] S. J. Orfanidis, *Electromagnetic Waves and Antennas*. 2016.

VITA

Shuangli Du

Shuangli Du was born in China and then moved to Japan with his parents. He spent his happy childhood in Nagoya, Aichi prefecture in Japan, and enjoyed baseball every day. He then moved back to Beijing, China, at the age of 8, and lived there for the next 14 years. In China, he gradually showed his interest in science and finally choses physics as his major for his undergraduate education at Renmin University in China. As an undergraduate researcher, he mainly worked on Angle-Resolved photoemission spectroscopy in condensed matter physics with Prof. Shancai Wang to fabricate the MoS2 crystals and measure their energy structure and electron density. In the third year of his undergraduate studies, he learned of cold atom physics in a seminar and developed a strong interest in it, which led him to his graduate studies in the Lab of Seth Aubin at the College of William and Mary. During his Ph.D. research, he developed a lot of experience in engineering physics and improved the lab apparatus, including microwave amplifiers, apparatus monitoring systems, and the potassium laser cooling and trapping system. He also made a lot of progress on physics research, including theoretical research on microstrip transmission lines and experimental research on atom interferometers. During his theoretical research, he developed an interest and talent for programming and will work on the electronic design automation software at Cadence Inc. after graduating. The experience in physics research, especially on the atom chip, will be beneficial

for his new career.